Reconstructing Miocene Climate Dynamics in the Ili Basin (SE Kazakhstan) Using Rock Magnetic Studies

Dissertation

der Mathematisch-Naturwissenschaftlichen Fakultät

der Eberhard Karls Universität Tübingen

zur Erlangung des Grades eines

Doktors der Naturwissenschaften

(Dr. rer. nat.)

vorgelegt von

Dipl.-Phys. Verena Rajtschan

geb. Verestek

aus Stuttgart

Tübingen

2019

Gedruckt mit Genehmigung der Mathematisch-Naturwissenschaftlichen Fakultät der Eberhard Karls Universität Tübingen.

Tag der mündlichen Qualifikation:	30.04.2019
Dekan:	Prof. Dr. Wolfgang Rosenstiel
1. Berichterstatter:	Prof. Dr. Erwin Appel
2. Berichterstatter:	Prof. Dr. Silke Voigt

Abstract

The reconstruction of Central Asia's climate during the Neogene is important in order to understand present and future climate dynamics in the Asian inland. Central Asia witnessed increased aridification during the Cenozoic, resulting in ongoing desertification of the region today. Factors such as global cooling and uplift of the Tibetan Plateau blocking the moisture supply from the south mainly controlled the progressive aridification. Furthermore, the advance and retreat of the Paratethys largely influenced the moisture supply to Central Asia. To unravel these influencing factors on the Neogene climate evolution in Central Asia, a well-exposed paleoclimatic archive is studied in the Ili Basin in southeast Kazakhstan. The studied terrestrial succession of the Aktau Mountains exposes alluvial, playa and lacustrine deposits of middle to late Miocene age. A robust age model that allows detailed correlation to trans-regional and global tectonic and climatic processes during the Neogene is fundamental for paleoclimatic interpretation of the proxy record. Thus, the focus of the present doctoral thesis is on rock magnetic studies for magnetostratigraphic dating and for a paleoclimatic proxy record. Sedimentological studies such as bulk-sediment mineralogy, geochemistry and palynology further assist the interpretations of the magnetic signal and provide additional paleoclimatic proxies.

A chronostratigraphy of the studied succession is achieved by magnetostratigraphic dating and using biostratigraphic markers. Widespread remagnetization constrained the established magnetostratigraphy to the 90 m-thick Bastau Formation, which is dated to an age of 15.3 to 13.9 Ma. Secondary magnetizations are likely related to post-depositional magnetic alterations and authigenic formation of magnetite. With the age model, the middle Miocene succession can be put in the context of the Middle Miocene Climate Transition. Global cooling is associated with changes of magneto-mineralogical properties above 55 m in the Bastau Formation concomitant with increasing salinization and lithology changes to saline mudflats and further up to an ephemeral playa lake.

In order to validate the use of rock magnetic parameters as proxies and their sensitivity to climate, the driving mechanisms behind the formation of magnetic minerals and magnetic alteration processes, and their correlation to environmental changes are assessed. A 4.5 m-thick playa cycle in the middle Miocene Koktal Formation is studied in high-resolution. Rock magnetic parameters together with geochemical element content

are used to reconstruct changes in water availability and aridity during the playa cycle. It is shown that rock magnetic parameters such as χ, ARM, SIRM, HIRM, ARM/SIRM and s-ratio are potentially effective proxies for a detailed paleo-environment reconstruction not only in the middle Miocene Ili Basin but also in comparable floodplain/playa lake settings.

Combining magnetic susceptibility data with studies of bulk-sediment mineralogy, geochemistry, sediment color and palynology from the Bastau Formation revealed that moisture availability, the intensity of sediment discharge, weathering and pedogenesis in the middle Miocene Ili Basin are climatically forced. Time series analysis of magnetic susceptibility and chemical weathering indices such as the Ti/Al ratio suggest that the changes in moisture availability and the mudflat deposits are orbitally forced by long eccentricity.

Zusammenfassung

Die Rekonstruktion des Klimas in Zentralasien während des Neogen ist von großer Bedeutung, um die gegenwärtige und zukünftige Klimadynamik im asiatischen Innenland zu verstehen. Im Känozoikum erlebte Zentralasien eine zunehmende Aridifizierung, die heute zu einer verstärkten Wüstenbildung in der Region führt. Zu den Hauptfaktoren für diese progressive Aridifikation zählt globale Abkühlung und die Hebung der Tibetischen Hochebene, welche die Feuchtigkeitszufuhr aus dem Süden blockierte. Weiter beeinflusste die Ausdehnung und der Rückgang der Paratethys die Feuchtigkeitszufuhr in Zentralasien. Um diese Einflussfaktoren auf die neogene Klimaentwicklung in Zentralasien zu verstehen, wurde ein Palöklimaarchiv im Ili Becken in Südostkasachstan erforscht. Die untersuchte terrestrische Gesteinsabfolge der Aktau Berge zeigt alluviale, Playa- und lakustrine Sedimentablagerungen aus dem Mittel- bis Spätmiozän. Ein robustes Altersmodell, das deren detaillierte Korrelation zu transregionalen und globalen tektonischen und klimatischen Prozessen im Neogen ermöglicht, ist fundamental für die paläoklimatische Interpretation der Proxydaten. Daher liegt das Hauptaugenmerk der vorliegenden Arbeit auf gesteinsmagnetischen Untersuchungen für die magnetostratigraphische Datierung und für paläoklimatische Proxydaten. Sedimentologische Studien wie Sedimentmineralogie, Geochemie und Palynologie stützen dabei die Interpretation des magnetischen Signals und ergeben gleichzeitig weitere paläoklimatische Proxies.

Eine Chronostratigraphie der untersuchten Gesteinsabfolge wurde durch magnetostratigraphische Datierung und mit Hilfe von biostratigraphischen Markern erstellt. Weitverbreitete Remagnetisierung limitierte die aufgestellte Magnetostratigraphie auf die 90 m dicke Bastau Formation, der ein Alter von 15,3 bis 13,9 Millionen Jahre zugeordnet wurde. Die sekundären Magnetisierungen wurden wahrscheinlich durch Alterationseffekte nach der Sedimentablagerung und authigene Magnetitbildung hervorgerufen. Mit dem in dieser Arbeit entwickelten Altersmodell kann die Bastau Formation in Zusammenhang mit dem mittelmiozänen Klimawandel gebracht werden. Globale Abkühlung geht mit Änderungen der magneto-mineralogischen Eigenschaften oberhalb von 50 m in der Bastau Formation einher sowie einer steigenden Versalzung und Lithologieänderungen hin zu Salztonebenen und später zu einem ephemeren Playasee.

Um die Verwendung von gesteinsmagnetischen Parametern als Proxies und deren Klimasensitivität zu validieren, wurden die treibenden Faktoren für die Bildung magnetischer Minerale und magnetische Alterationsprozesse sowie deren Korrelation zu Umweltveränderungen evaluiert. Ein 4,5 m mächtiger Playazyklus in der mittelmiozänen Koktal Formation wurde dafür detailliert untersucht. Gesteinsmagnetische Parameter wurden zusammen mit geochemischen Elementgehalten verwendet um die Änderungen der Wasserverfügbarkeit und Aridität während des Playazyklus zu rekonstruieren. Es konnte gezeigt werden, dass gesteinsmagnetische Parameter wie χ, ARM, SIRM, HIRM, ARM/SIRM und s-ratio potentielle Proxies für eine detaillierte Rekonstruktion der Paläoumwelt sind, nicht nur im mittelmiozänen Ili Becken sondern auch in vergleichbaren Überschwemmungs- bzw. Playaseegebieten.

Weiter konnte mit der magnetischen Suszeptibilität und Studien zur Sedimentmineralogie, Geochemie, Sedimentfarbe und Palynologie an der Bastau Formation gezeigt werden, dass die Verfügbarkeit von Feuchte, die Intensität des Sedimenttransportes, Verwitterung und Pädogenese im mittelmiozänen Ili Becken durch das Klima gesteuert werden. Zeitreihenanalysen der magnetischen Suszeptibilität und chemischer Verwitterungsindizes wie dem Ti/Al-Verhältnis deuten darauf hin, dass Änderungen der Feuchteverfügbarkeit und die Tonebenen von orbitalen Einflüssen wie der langen Exzentrizität gesteuert werden.

Contents

Chapter 1

Thesis organization and list of publications

This doctoral thesis is organized in a cumulative manner. Chapter 2 presents an introduction covering the context and the main ideas of the thesis. In Chapter 3-5 research articles are presented which were written in the framework of the research for this doctoral thesis. Related research articles are outlined in Chapter 6. Chapter 7 summarizes the conclusions and Chapter 8 addresses open research questions.

List and status of publications that are included in this doctoral thesis:

Verestek, V., Appel, E., Voigt, S., Frisch, K. 2018. Constrained Magnetostratigraphic Dating of a Continental Middle Miocene Section in the Arid Central Asia. *Front. Earth Sci.* 6(49). doi: 10.3389/feart.2018.00049.

Verestek, V., Appel, E., Frisch, K., and Voigt, S. (in review). Rock magnetic signature of a playa cycle in Central Asia and environmental implications. *Int. J. Earth Sci.*

Voigt, S., Weber, Y., Frisch, K., Bartenstein, A., Hellwig, A., Petschick, R., Bahr, A., Pross, J., Koutsodendris, A., Voigt, T., **Verestek, V.**, Appel, E. 2017. Climatically forced moisture supply, sediment flux and pedogenesis in Miocene mudflat deposits of southeast Kazakhstan, Central Asia. *Deposit. Rec.* 3. doi: 10.1002/dep2.34.

More publications emerged within the research project of this doctoral thesis in collaboration with the Goethe University Frankfurt:

Frisch, K., Voigt, S., Voigt, T., Hellwig, A., **Verestek, V.**, and Weber, Y. 2019. Extreme aridity prior to lake expansion deciphered from facies evolution in the Miocene Ili Basin, south-east Kazakhstan. *Sedimentology.* accepted. doi: 10.1111/sed.12556.

Frisch, K., Voigt, S., Voigt, T., **Verestek, V.**, Appel, E., Albert, R., Gerdes, A., Raddatz, J., Weber Y., Arndt, I. (in preparation). Astronomical forced aridity during the Miocene Climate Transition in Central Asia.

Chapter 2

Introduction

In a world where extreme weather conditions like droughts and floods occur more and more frequent and where regional but also global weather patterns are changing, understanding the world's climate dynamics becomes an important task. Today the Earth's climate is observed in many ways. For an understanding of the present and future climate evolution, it is essential to unravel the climate dynamics of the past. Reconstructing paleoclimate and its regional and global dynamics on geological timescales is the key to this important task. Scientists of various disciplines work together to understand the Earth's past climate.

Rock magnetism is an important tool to date paleoclimatic archives such as sedimentary sequences and together with bulk-sediment mineralogy, geochemistry and palynology may provide proxy indices that allow the reconstruction of paleoclimate. With paleomagnetic studies and rock magnetic parameters one can identify tectonic events such as block rotations, date rock sequences, investigate secular variations of the geomagnetic field and assess environmental changes in lake catchments e.g due to erosion or industrialization – just to name a few of its applications.

Sedimentary records reflect a wide variety of environmental processes that occurred not only in the water column but also in the catchment area, e.g. the Tibetan Plateau (Dupont-Nivet et al., 2007; Zhang et al., 2012) and Lake Baikal (Peck et al., 1994; Williams et al.,

1997). One advantage of terrestrial sediments and in particular lacustrine sediments is the typically higher sedimentation rate compared to marine sediments and thus the potential for a high-resolution record of the paleoenvironmental conditions.

Aim of the study

The main objective of this study is to reconstruct the middle Miocene climate dynamics in the Ili Basin from orbital to tectonic time scales with a focus on magnetostratigraphic dating of the sedimentary succession of the Aktau Mountains in southeast Kazakhstan. A well-calibrated chronostratigraphy provides the required temporal framework for paleoclimatic and paleoenvironmental reconstructions. The sedimentary succession of the Aktau Mountains is a highly promising terrestrial archive for paleoclimatic research, ideally located in order to elucidate Central Asia's climate evolution during the Cenozoic. In order to establish a reliable, detailed chronostratigraphy, magnetostratigraphy is the preferred technique because of the lack of volcanic horizons and paucity of index fossils. The likely stratigraphic position is in the Middle Miocene, i.e. in a period with frequent reversals (~10 polarity zones) and a relatively characteristic polarity pattern with predominantly reverse polarity. These are favorable preconditions for magnetostratigraphic dating.

In a second step, rock magnetic parameters are used together with bulk-sediment mineralogy, geochemistry and palynology to compile a proxy data record to assess the water availability as well as the source and timing of increased moisture supply in Central Asia in connection with Miocene mountain uplift and the retreat of the Eastern Paratethys.

Central Asia and the Aktau Mountains

The Asian inland is the world's largest arid region in the temperate zone and in particular Central Asia is one of the most arid areas on Earth. Located in a climatic transition zone between the Asian monsoons and westerly airflow, Central Asia is very sensitive to climate variability (Chen et al., 2009).

During the Cenozoic, progressive aridification was prevailing throughout Central Asia (Guo et al., 2002; Tang et al., 2011; Caves et al., 2015). The Cenozoic climate evolution in Central Asia has been studied using sedimentary archives and general circulation

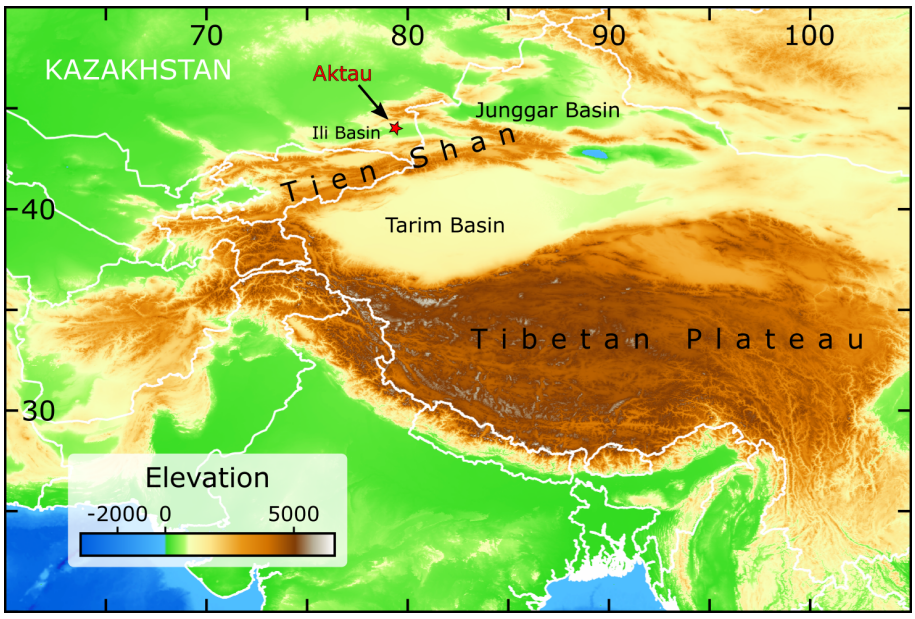

Figure 1: Topographic map of Central Asia showing the location of the Ili Basin and the Aktau Mountains (adapted after Amante and Eakins, 2009).

models. Multiple key factors have been proposed to control the climate dynamics. While uplift of the Tibetan Plateau blocked the moisture supply from the south (Kutzbach et al., 1993; Guo et al., 2002; Zhang et al., 2007; Miao et al., 2012; Bosboom et al., 2014), also global climate changes correlate well with Central Asia's progressive aridification (Dupont-Nivet et al., 2007; Lu et al., 2010; Miao et al., 2012; Licht et al., 2014). The atmospheric moisture supply in Central Asia was mainly driven by the extent of the Paratethys and its advance and retreat (Fluteau et al., 1999; Bosboom et al., 2011, 2014). To further constrain these influencing factors, a well-exposed paleoclimatic archive in the Aktau Mountains is studied in this doctoral thesis.

The Aktau Mountains are located in the Ili Basin, a triangular foreland basin of the Tien Shan Mountains (44°00′20.3″N 79°14′40.9″E, Fig. 1). The Ili Basin is bounded on the north by the Dzhungarian Alatau and the Borohoro Mountain ranges and on the south by the central Tien Shan Mountains. The depression of the Ili Basin gradually descends westward with a semi-arid desert, the Ili River and steppe vegetation dominating today's landscape (Fig. 2). High-altitude westerly winds are prevailing in the basin throughout the year (Song et al., 2014). The basin is filled with Eocene to Quaternary clastic deposits, with predominating fluvial, alluvial and lacustrine sediments of a large lake system (Lucas

Figure 2: Today's semi-arid landscape of the Ili Basin

et al., 2000; Kober et al., 2013). The Aktau Mountains formed during the Pleistocene by progressive compression of the Ili Basin's sedimentary fill (Kober et al., 2013). The resulting asymmetrical anticline with a steep southern limb and a gently dipping northern flank well exposes a quasi-continuous succession of Eocene/Oligocene to early Pleistocene sediments (Bazhanov and Kostenko, 1961; Voigt et al., 2017).

The Aktau succession, its lithology and abundant fossil records have been documented before (Bazhanov and Kostenko, 1961; Bodina, 1961; Lucas et al., 1997; Kordikova and Mavrin, 1996). An overview over the different proposed stratigraphic schemes can be found in Kober et al. (2013). In this doctoral thesis, the lithostratigraphic description of the Aktau Mountains is based on the formation names of Bodina (1961) and the thicknesses from Bazhanov and Kostenko (1961) and Kordikova and Mavrin (1996). The succession is divided in seven formations (abbreviated Fm, Fig. 3). The Arasan Fm at the base of the succession is comprised of reddish fluvial deposits of a river system that grade into red alluvial mudstone deposits (Alakul Fm). In the Aidarly Fm yellow, cross-bedded fluvial sandstone deposits of a meandering river occur, followed by reddish-brown mudflat deposits of the Bastau Fm. The Koktal Fm is characterized by ephemeral playa lake

Figure 3: Aktau succession with the Cenozoic stratigraphic formations after Bodina (1961) (adapted from Voigt et al., 2017).

deposits that grade into perennial lacustrine deposits (Kokterek Fm). The top of the succession is comprised of mudflat deposits with intermittent lacustrine and fluvial deposits from a connected river-freshwater-lake system (Ili Fm).

Parent rocks of the alluvial deposits of the Arasan, Alakul, Bastau, Koktal and Kokterek formations are Permo-Carboniferous volcanics (andesites, rhyolites and trachytes) from the Palaeozoic accretionary arc complex of the Central Asian Orogenic belt (Jahn et al., 2004; Kröner et al., 2014; Li et al., 2015). Today, these volcanic rocks are exposed in the Katutau, Suattau, Dzhungarian Alatau and Borohoro Mountain ranges at the northern rim of the Ili Basin. The provenance of the sandstones in the Arasan, Aidarly and Ili formations is a distant gneissic, quartz-rich and mica-rich source, partly mixed with volcanics from local sources (Lucas et al., 1997; Kober et al., 2013).

Biostratigraphic data of the Aktau succession have been documented by a series of studies on the fluvial deposits of the Arasan Fm and Aidarly Fm and the lacustrine mudflats of the Ili Fm, which are summarized by Lucas et al. (2000). The Arasan Fm is dated to the late Eocene (Ergilian) based on hyracodontid *Ardynia* sp. and Brontotheriidae bones (Lucas et al., 1997). Mammal bones of the giant rhinoceros *Paraceratherium* place the lower Aidarly Fm to the late Oligocene (Tabenbulukian) (Lucas et al., 1997). Abundant plant and mammal records in the upper Aidarly Fm (xerophytes, turtles, insectivores, rodents, carnivores, ruminantia such as the *Lagomeryx*, the odd-toed *Gomphotherium* and *Brachypotherium*) are from the early to middle Miocene mammal zones MN4 to MN5 (late Burdigalian to Langhian) (Rayushkina, 1993; Lucas et al., 1997; Kordikova, 2000; Kordikova and de Bruijn, 2001). The charophytes date the lower Ili Fm to the late Miocene to early Pliocene (Nikolskaya, 1990; Dzhamangaraeva, 1997), while excavated bones of

the gomphotere *Anancus avernensis* provide a late Miocene to early Pleistocene age frame for the Ili Fm (Bazhanov and Kostenko, 1961; Voigt et al., 2017).

Methods

Rock magnetism together with bulk-sediment mineralogy, geochemistry and palynology of the Aktau succession were studied within this doctoral thesis. The focus is on paleomagnetic studies for magnetostratigraphic dating and and the use of rock magnetic parameters as paleoenvironmental proxies. Bulk-sediment mineralogy, geochemistry and palynology further assist the interpretations of the magnetic signal. The research for this doctoral thesis was conducted in close collaboration with the project partners at the Goethe University Frankfurt.

The approx. 370 m-thick Bastau Fm, Koktal Fm and Kokterek Fm were lithologically logged by the team from Goethe University Frankfurt on a centimeter-to-decimeter-scale resolution (Fig. 4). Based on diagnostic lithological features, observations on evaporite morphology and mineralogy, a groundwater table respectively lake level-sensitive facies model was developed for the alluvial-lacustrine part of the middle to late Miocene of the Ili Basin (Frisch et al., 2019).

Rock magnetic investigations excel due to fast, sensitive and nondestructive measurement procedures facilitating high-resolution records. Consequently, rock magnetic parameters are widely used as proxies for paleoclimate in both terrestrial and marine sequences (e.g. Dearing et al., 1981; Bloemendal et al., 1992; Peck et al., 1994; Thouveny et al., 1994; Hu et al., 2002; Channell et al., 2013). In order to validate the use as proxies and their sensitivity to climate, the driving mechanisms behind the formation of magnetic minerals and magnetic alteration processes, and their correlation to environmental changes need to be assessed. In sediments, allogenic and authigenic processes need to be considered, i.e. processes during eolian or fluvial transport and processes during and after deposition such as dissolution, recrystallization, authigenesis and oxidation (Thompson and Oldfield, 1986; Bloemendal et al., 1992; Herb et al., 2013). Comparison of magnetic proxies with other climate or environmental proxies such as pollen is necessary for calibration and to validate the sensitivity of the magnetic record to climate. In the Aktau Mountains, magnetic proxies are used together with bulk-sediment mineralogy, geochem-

ical element contents and palynology to constrain paleoclimatic indications (Voigt et al., 2017, Chapter 5; Verestek et al., 2018, Chapter 3; Verestek et al., in review, Chapter 4). Concentration dependent parameters and in particular magnetic susceptibility are commonly inferred as climate proxies (Peck et al., 1994; Thouveny et al., 1994; Evans and Heller, 2003; Herb et al., 2013). Magnetic proxies used in this doctoral thesis are magnetic susceptibility (χ), anisotropy of susceptibility (AMS), anhysteretic remanent magnetization (ARM), saturation isothermal remanent magnetization (SIRM), hard isothermal remanent magnetization (HIRM) and derived ratios such as s-ratio and ARM/SIRM (Voigt et al., 2017, Chapter 5; Verestek et al., in review, Chapter 4). The magnetic measurements were all performed at the University Tübingen.

Because of the mentioned advantages of rock magnetic measurements, magnetic polarity stratigraphy has become a common tool in chronostratigraphic dating of not only of volcanic rock sequences but also of terrestrial and marine successions (Johnson et al., 1975; Alvarez et al., 1977; Tauxe and Opdyke, 1982; Opdyke and Channell, 1996). Here, the stability and origin of the magnetic remanence have to be investigated to provide a reliable age model. Detailed rock magnetic studies help to identify the magnetic carriers, to assess magnetic alteration processes and to recognize possible remagnetization effects and secondary overprints. Paleomagnetic directions from primary magnetizations are combined to a polarity profile that is compared to the General Polarity Time Scale (GPTS). Additional time constraints (e.g. biostratigraphic markers or radiometric dating) are often needed to correlate polarity profiles to the GPTS. In the Aktau Mountains, the biostratigraphic age of MN4-MN5 from the Aidarly Fm is used as an anchor for the correlation of the polarity sequence from the Bastau Fm (Verestek et al., 2018, Chapter 3).

Cyclostratigraphy is based on the sensitive response of the Earth's climate to variations in the Earth's orbital geometry (Hays et al., 1976). In cyclostratigraphic studies, cyclic variations of lithology or physical rock properties are tied to orbitally forced changes in global climate (Kodama and Hinnov, 2015). The cyclic variations of solar insolation are called Milankovic cycles and are caused by precession, obliquity and eccentricity of the Earth. Milankovic cycles can be identified in sedimentary records using time series analyses and filtering. By comparison with reference curves (e.g. the marine oxygen isotope record from Lisiecki and Raymo (2005)) or wiggle matching (e.g. using the orbital solution from Laskar et al. (2004)), the observed proxy record can be orbitally tuned. The

fluvial-floodplain and lacustrine deposits of the Aktau Mountains show a remarkable color banding. The lithologic cyclicity is highly promising for cyclostratigraphic analysis, in particular with a robust age model from magnetostratigraphy. A combined magneto- and cyclostratigraphic approach has the potential to establish a high-resolution chronostratigraphy of the Aktau succession and therewith a detailed temporal framework for paleoclimatic and paleoenvironmental reconstructions and assessment of potential orbital forcing mechanisms.

In three field campaigns, over 900 oriented samples were collected from the middle to late Miocene deposits of the Aktau succession (Bastau Fm, Koktal Fm, Kokterek Fm and lower Ili Fm) for rock magnetic and paleomagnetic investigations. Additionally, a 4.5 m-thick playa cycle in the Koktal Fm was sampled continuously. First, the natural remanent magnetization (NRM) was measured and stepwise demagnetized to isolate paleo-directions. Subsequent rock magnetic measurements were performed to analyze the magneto-mineralogical properties, in particular the origin of the magnetic minerals, possible magnetic alteration processes and the sensitivity to paleoenvironmental changes. Conducted measurements include thermomagnetic runs and frequency dependence of magnetic susceptibility, hysteresis measurements, ARM and AMS measurements, IRM acquisition and subsequent thermal demagnetization of the IRM.

Complex magneto-mineralogical signature

The study of the magneto-mineralogical properties revealed magnetite and hematite as the magnetic remanence carriers with stable remanences throughout the sampled formations of the Aktau Mountains. Although thermal and alternating field demagnetizations of the NRM showed a partly complex and multicomponent behavior, the characteristic directions were consistent with those expected for the middle Miocene in Central Asia. However, the determined paleo-directions were clearly dominated by normal directions. Only in the Bastau Fm, the paleomagnetic results revealed a typical sequence of polarity zones but remagnetization effects and partial secondary overprints were also observed. Thus, the paleo-directions that were less likely affected by secondary magnetization were selected based on rock magnetic parameters and a reliable magnetostratigraphy could be established for the Bastau Fm (Verestek et al., 2018, Chapter 3). According to the age

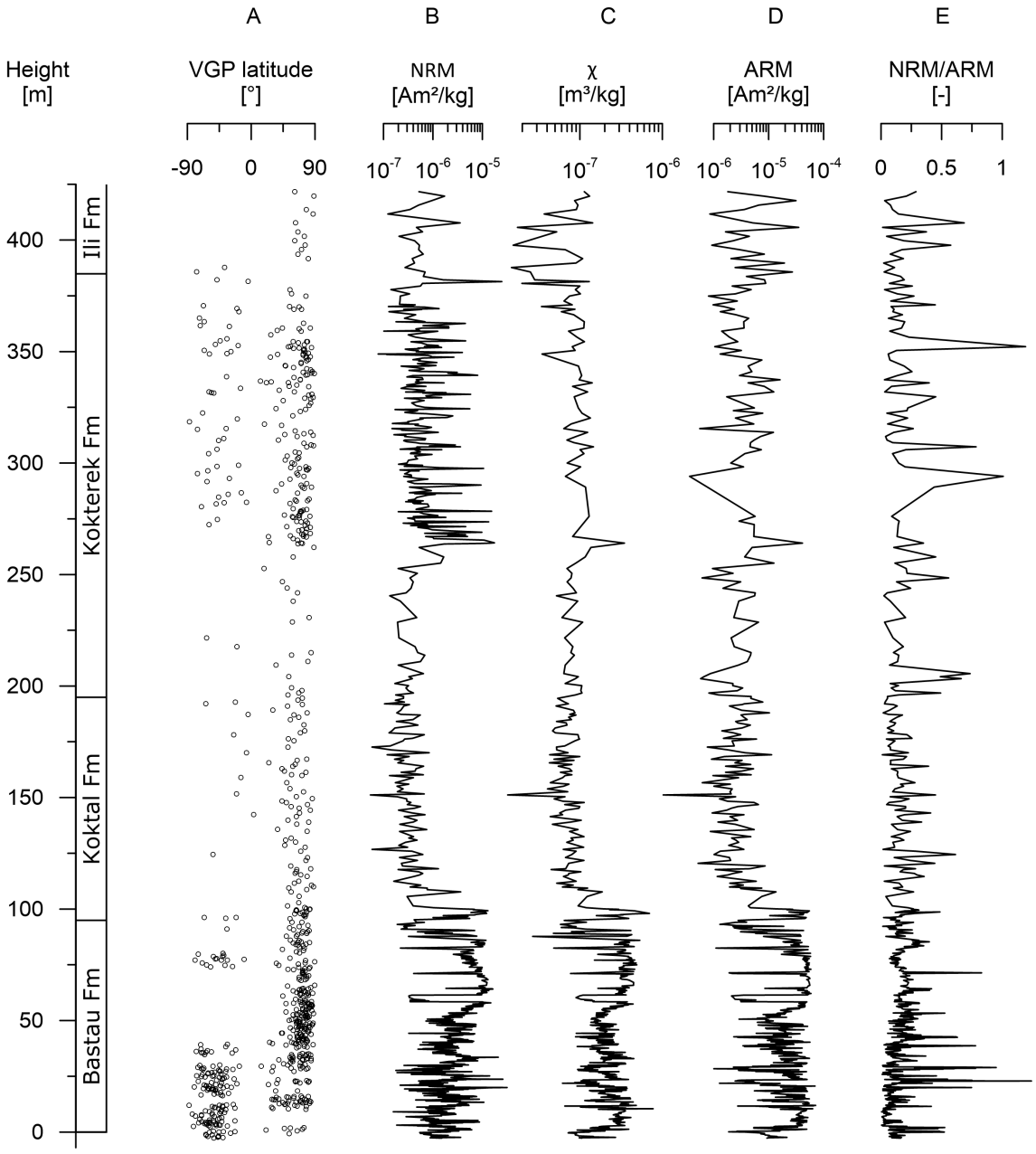

Figure 4: Rock magnetic record of the studied Aktau succession: (A) VGP latitude, (B-D) concentration dependent parameters (NRM, χ, ARM), (E) natural remanence type indicator NRM/ARM.

model established within in this doctoral thesis and biostratigraphic data from the lower Ili Fm (Nikolskaya, 1990; Dzhamangaraeva, 1997), reverse paleo-directions should occur in the overlying Koktal, Kokterek and Ili formations, in particular the reverse polarity dominated chrons C3B, C3A and C2. However, reverse paleo-directions (determined from over 400 samples collected from these formations) are rare and scattered inhibiting further magnetostratigraphic dating and indicating widespread remagnetization (Fig. 4 A). Not only the NRM intensities are lower above the Bastau Fm but also all other concentration dependent parameters (Fig. 4 B-D). Throughout the sampled formations, high NRM/ARM ratios are observed repeatedly (Fig. 4 E) that are interpreted as indicative of a chemical remanent magnetization and possible remagnetizations (Verestek et al., 2018, Chapter 3; Verestek et al., in review, Chapter 4). The origin of the remagnetizations remains an open question that is further addressed in Chapter 8.

In the present doctoral thesis, a magnetostratigraphy is established for the middle Miocene Bastau Fm in the Aktau Mountains (Verestek et al., 2018, Chapter 3) that serves as a basis for age estimations for the overlying formations. The rock magnetic signature of a playa cycle from the middle Miocene Koktal Fm is investigated with a focus on paleoenvironmental proxies (Verestek et al., in review, Chapter 4). Orbital forcing mechanisms are assessed for the Bastau Fm by studying bulk-sediment mineralogy, geochemistry, magnetic susceptibility, sediment color and palynology (Voigt et al., 2017, Chapter 5).

References

Alvarez, W., Arthur, M. A., Fischer, A. G., Lowrie, W., Napoleone, G., Silva, I. P., and Roggenthen, W. M. 1977. Upper Cretaceous-Paleocene magnetic stratigraphy at Gubbio, Italy V. Type section for the Late Cretaceous-Paleocene geomagnetic reversal time scale. *Geol. Soc. Am. Bull.*, 88:383–389. doi: 10.1130/0016-7606(1977)88<383:UCMSAG>2.0.CO;2.

Amante, C. and Eakins, B. W. 2009. ETOPO1 1 Arc-Minute Global Relief Model: procedures, data sources and analysis. *NOAA Technical Memorandum NESDIS NGDC-24, Nat. Geophys. Data Center, NOAA*. doi: 10.7289/V5C8276M.

Bazhanov, V. S. and Kostenko, N. N. 1961, Geologicheskiy razrez Dzhungarskogo Alatau i ego paleozoologicheskoye obosnovanie [Geological section of Dzhungarian Alatau and its paleontological basis]. In Galuzo, I. G., editor, *Materialy po Istorii Fauny i Flory Kazakhstana*, pages 47–52. Akademiya Nauk Kazakskoi SSR.

Bloemendal, J., King, J. W., Hall, F. R., and Doh, S.-J. 1992. Rock magnetism of late Neogene and Pleistocene deep-sea sediments - Relationship to sediment source, diagenetic processes, and sediment lithology. *J. Geophys. Res.*, 97:4361–4375. doi: 10.1029/91JB03068.

Bodina, L. E. 1961. Ostrakody tretichnykh otlozhenii zaisanskoi i iliiskoi depressi [ostracods of tertiary deposits in the zaisan and ili depressions]. *Trudy VNIGRI*, 170:43–153.

Bosboom, R., Dupont-Nivet, G., Houben, A., Brinkhuis, H., Villa, G., Mandic, O., Stoica, M., Zachariasse, W., Guo, Z., Li, C., and Krijgsman, W. 2011. Late Eocene sea retreat from the Tarim Basin (west China) and concomitant Asian paleoenvironmental change. *Palaeogeogr. Palaeoclimatol. Palaeoecol.*, 299:385–398. doi: 10.1016/j.palaeo.2010.11.019.

Bosboom, R., Abels, H., Hoorn, C., van den Berg, B., Guo, Z., and Dupont-Nivet, G. 2014. Aridification in continental Asia after the Middle Eocene Climatic Optimum (MECO). *Earth Planet. Sci. Lett.*, 389:34–42. doi: 10.1016/j.epsl.2013.12.014.

Caves, J. K., Winnick, M. J., Graham, S. A., Sjostrom, D. J., Mulch, A., and Chamberlain, C. P. 2015. Role of the westerlies in Central Asia climate over the Cenozoic. *Earth Planet. Sci. Lett.*, 428:33–43. doi: 10.1016/j.epsl.2015.07.023.

Channell, J. E. T., Hodell, D. A., Margari, V., Skinner, L. C., Tzedakis, P. C., and Kesler, M. S. 2013. Biogenic magnetite, detrital hematite, and relative paleointensity in Quaternary sediments from the Southwest Iberian Margin. *Earth Planet. Sci. Lett.*, 376: 99–109. doi: 10.1016/j.epsl.2013.06.026.

Chen, F., Holmes, J., Wunnemann, B., and Yu, Z. 2009. Holocene climate variability in arid Asia: Nature and mechanisms. *Quaternary International*, 194(1):1–5. doi: 10.1016/j.quaint.2008.07.019.

Dearing, J. A., Elner, J. K., and Happey-Wood, C. M. 1981. Recent sediment flux and erosional processes in a Welsh upland lake-catchment based on magnetic susceptibility

measurements. *Quater. Res.*, 16:356–372. doi: 10.1016/0033-5894(81)90016-8.

Dupont-Nivet, G., Krijgsman, W., Langereis, C., Abels, H., Dai, S., and Fang, X. 2007. Tibetan Plateau aridification linked to global cooling at the Eocene-Oligocene transition. *Nature*, 445:635–638. doi: 10.1038/nature05516.

Dzhamangaraeva, A. K. 1997. Pliocene charophytes from Aktau Mountain, southeastern Kazakhstan. *Geobios*, 30:475–479. doi: 10.1016/S0016-6995(97)80115-5.

Evans, M. and Heller, F. 2003. *Environmental Magnetism: Principles and Applications of Enviromagnetics*. Int. Geophys. Academic Press.

Fluteau, F., Ramstein, G., and Besse, J. 1999. Simulating the evolution of the Asian and African monsoons during the past 30 Myr using an atmospheric general circulation model. *J. Geophys. Res.*, 104:11995–12018. doi: 10.1029/1999JD900048.

Frisch, K., Voigt, S., Voigt, T., Hellwig, A., Verestek, V., and Weber, Y. 2019. Extreme aridity prior to lake expansion deciphered from facies evolution in the Miocene Ili Basin, south-east Kazakhstan. *Sedimentology*, accepted. doi: 10.1111/sed.12556.

Guo, Z., Ruddiman, W., Hao, Q., Wu, H., Qiao, Y., Zhu, R., Peng, S., Wei, J., Yuan, B., and Liu, T. 2002. Onset of Asian desertification by 22Myr ago inferred from loess deposits in China. *Nature*, 416:159–163. doi: 10.1038/416159a.

Hays, J. D., Imbrie, J., and Shackleton, N. J. 1976. Variations in the Earth's Orbit: Pacemaker of the Ice Ages. *Science*, 194:1121–1132. doi: 10.1126/science.194.4270.1121.

Herb, C., Zhang, W., Koutsodendris, A., Appel, E., Fang, X., and Pross, J. 2013. Environmental implications of the magnetic record in Pleistocene lacustrine sediments of the Qaidam Basin, NE Tibetan Plateau. *Quater. Int.*, 313:218–229. doi: 10.1016/j.quaint.2013.06.015.

Hu, S., Deng, C., Appel, E., and Verosub, K. L. 2002. Environmental magnetic studies of lacustrine sediments. *Chin. Sci. Bull.*, 47:613–616. doi: 10.1360/02tb9141.

Jahn, B. M., Windley, B., Natalin, B., and Dobretsov, N. 2004. Phanerozoic continental growth in central Asia – Preface. *J. Asian Earth Sci.*, 23:599–603. doi: 10.1016/S1367-9120(03)00124-X.

Johnson, N. M., Opdyke, N. D., and Lindsay, E. H. 1975. Magnetic Polarity Stratigraphy of Pliocene-Pleistocene Terrestrial Deposits and Vertebrate Faunas, San Pedro Valley, Arizona. *Geol. Soc. Am. Bull.*, 86:5–12. doi: 10.1130/0016-7606(1975)86<5:MPSOPT>2.0.CO;2.

Kober, M., Seib, N., Kley, J., and Voigt, T. 2013. Thick-skinned thrusting in the northern Tien Shan foreland, Kazakhstan: structural inheritance and polyphase deformation. *Geol. Soc. Spec. Publ.*, 377:19–42. doi: 10.1144/SP377.7.

Kodama, K. P. and Hinnov, L. A. 2015. *Rock magnetic cyclostratigraphy*. Wiley-Blackwell.

Kordikova, E. G. 2000. Insectivora (Mammalia) from the Lower Miocene of the Aktau Mountains, South-Eastern Kazakhstan. *Senckenberg. lethaea*, 80:67–79. doi: 10.1007/BF03043665.

Kordikova, E. G. and de Bruijn, H. 2001. Early miocene rodents from the Aktau Mountains (South-Eastern Kazakhstan). *Senckenberg. lethaea*, 81:391–405. doi: 10.1007/BF03042791.

Kordikova, E. G. and Mavrin, A. V. 1996. Stratigraphy and Oligocene-Miocene mammalian biochronology of the Aktau Mountains, Dzhungarian Alatau range, Kazakhstan. *Palaeovert.*, 25:141–174.

Kröner, A., Kovach, V., Belousova, E., Hegner, E., Armstrong, R., Dolgopolova, A., Seltmann, R., Alexeiev, D. V., Hoffmann, J. E., Wong, J., Sun, M., Cai, K., Wang, T., Tong, Y., Wilde, S. A., Degtyarev, K. E., and Rytsk, E. 2014. Reassessment of continental growth during the accretionary history of the Central Asian Orogenic Belt. *Gondwana Res.*, 25:103–125. doi: 10.1016/j.gr.2012.12.023.

Kutzbach, J., Prell, W., and Ruddiman, W. 1993. Sensitivity of Eurasian Climate to Surface Uplift of the Tibetan Plateau. *J. Geol.*, 101:177–190. doi: 10.1086/648215.

Laskar, J., Robutel, P., Joutel, F., Gastineau, M., Correia, A. C. M., and Levrard, B. 2004. A long-term numerical solution for the insolation quantities of the Earth. *Astron. Astrophys.*, 428:261–285. doi: 10.1051/0004-6361:20041335.

Li, D., He, D., D.and Maa, Tang, Y., Kong, Y., and Tang, J. 2015. Carboniferous-Permian tectonic framework and its later modifications to the area from eastern Kazakhstan to southern Altai: Insights from the Zaysan-Jimunai Basin evolution. *J. Asian Earth Sci.*,

113:16–35. doi: 10.1016/j.jseaes.2014.09.017.

Licht, A., van Cappelle, M., Abels, H. A., Ladant, J.-B., Trabucho-Alexandre, J., France-Lanord, C., Donnadieu, Y., Vandenberghe, J., Rigaudier, T., Lécuyer, C., Terry, D., Jr., Adriaens, R., Boura, A., Guo, Z., Soe, A. N., Quade, J., Dupont-Nivet, G., and Jaeger, J.-J. 2014. Asian monsoons in a late Eocene greenhouse world. *Nature*, 513:501–506. doi: 10.1038/nature13704.

Lisiecki, L. E. and Raymo, M. E. 2005. A Pliocene-Pleistocene stack of 57 globally distributed benthic δ^{18}O records. *Paleoceanography*, 20:PA1003. doi: 10.1029/2004PA001071.

Lu, H., Wang, X., and Li, L. 2010. Aeolian sediment evidence that global cooling has driven late Cenozoic stepwise aridification in central Asia. *Geological Society of London Special Publications*, 342:29–44. doi: 10.1144/SP342.4.

Lucas, S. G., Bayshashov, B. U., Tyutkova, L. A., Zhamangara, A. K., and Aubekerov, B. Z. 1997. Mammalian biochronology of the Paleogene-Neogene boundary at Aktau Mountain, eastern Kazakhstan. *Paläontol. Z.*, 71:305–314. doi: 10.1007/BF02988498.

Lucas, S. G., Aubekerov, B. Z., Dzhamangaraeva, A. K., Bayshashov, B. U., and Tyutkova, L. A. 2000, Cenozoic lacustrine deposits of the Ili basin, southeastern Kazakhstan. In Gierlowski-Kordesch, E. and Kelts, K. R., editors, *Lake Basins Through Space and Time*, pages 59–64. AAPG Studies in Geology.

Miao, Y., Herrmann, M., Wu, F., Yan, X., and Yang, S. 2012. What controlled Mid-Late Miocene long-term aridification in Central Asia?– Global cooling or Tibetan Plateau uplift: A review. *Earth Sci. Rev.*, 112:155–172. doi: 10.1016/j.earscirev.2012.02.003.

Nikolskaya, V. D. 1990. Pozdneneogenovye kharovye vodorosli gor Aktau i Koibyn (Ilinskaya vpadina) [Late Neogene charophytes from Aktau Mountain and Koibyn (Ili basin)]. *Fauna Pozvonochnykh i Flora Mezozoya i Kainozoya Kazakhstana*, 2:80–104.

Opdyke, N. and Channell, J. 1996. *Magnetic Stratigraphy*. International Geophysics Series. Academic Press.

Peck, J., King, J., Colman, S., and Kravchinsky, V. 1994. A rock-magnetic record from Lake Baikal, Siberia: Evidence for Late Quaternary climate change. *Earth Planet. Sci. Lett.*, 122(1):221–238. doi: 10.1016/0012-821X(94)90062-0.

Rayushkina, G. S. 1993, Miotsyenovaya flora Dzhungarsovo Aktau (Iliiskaya vpadina) [Miocene flora from Dzhungarian Aktau (Ili depression). In *Matyerialy po Istorii Fauny i Flory Kazakhstan*, volume 12, pages 116–131. Akademiya Nauk Kazakskoi SSR.

Song, Y., Chen, X., Qian, L., Li, C., Li, Y., Li, X., Chang, H., and An, Z. 2014. Distribution and composition of loess sediments in the Ili Basin, Central Asia. *Quat. Int.*, 334-335: 61–73. doi: 10.1016/j.quaint.2013.12.053.

Tang, Z., Ding, Z., White, P., Dong, X., Ji, J., Jiang, H., Luo, P., and Wang, X. 2011. Late Cenozoic central Asian drying inferred from a palynological record from the northern Tian Shan. *Earth Planet. Sci. Lett.*, 302:439–447. doi: 10.1016/j.epsl.2010.12.042.

Tauxe, L. and Opdyke, N. D. 1982. A time framework based on magnetostratigraphy for the siwalik sediments of the Khaur area, Northern Pakistan. *Palaeogeogr. Palaeoclimat. Palaeoeco.*, 37:43–61. doi: 10.1016/0031-0182(82)90057-8.

Thompson, R. and Oldfield, F. 1986. *Environmental Magnetism*. Allen & Unwin. doi: 10.1007/978-94-011-8036-8.

Thouveny, N., de Beaulieu, J.-L., Bonifay, E., Creer, K. M., Guiot, J., Icole, M., Johnsen, S., Jouzel, J., Reille, M., Williams, T., and Williamson, D. 1994. Climate variations in Europe over the past 140 kyr deduced from rock magnetism. *Nature*, 371:503–506. doi: 10.1038/371503a0.

Verestek, V., Appel, E., Voigt, S., and Frisch, K. 2018. Constrained Magnetostratigraphic Dating of a Continental Middle Miocene Section in the Arid Central Asia. *Front. Earth Sci.*, 6:49. doi: 10.3389/feart.2018.00049.

Verestek, V., Appel, E., Frisch, K., and Voigt, S. in review. Rock magnetic signature of a playa cycle in Central Asia and environmental implications. *Int. J. Earth Sci.*

Voigt, S., Weber, Y., Frisch, K., Bartenstein, A., Hellwig, A., Petschick, R., Bahr, A., Pross, J., Koutsodendris, A., Voigt, T., Verestek, V., and Appel, E. 2017. Climatically forced moisture supply, sediment flux and pedogenesis in Miocene mudflat deposits of southeast Kazakhstan, Central Asia. *Deposit. Rec.*, 3(2):209–232. doi: 10.1002/dep2.34.

Williams, D. F., Peck, J., Karabanov, E. B., Prokopenko, A. A., Kravchinsky, V., King, J., and Kuzmin, M. I. 1997. Lake Baikal Record of Continental Climate Response to Orbital Insolation During the Past 5 Million Years. *Science*, 278(5340):1114–1117. doi:

10.1126/science.278.5340.1114.

Zhang, W. L., Appel, E., Fang, X. M., Yan, M. D., Song, C. H., and Cao, L. W. 2012. Paleoclimatic implications of magnetic susceptibility in Late Pliocene-Quaternary sediments from deep drilling core SG-1 in the western Qaidam Basin (NE Tibetan Plateau). *J. Geophys. Res.*, 117(B06). doi: 10.1029/2011JB008949.

Zhang, Z., Wang, H., Guo, Z., and Jiang, D. 2007. What triggers the transition of palaeoenvironmental patterns in China, the Tibetan Plateau uplift or the Paratethys Sea retreat? *Palaeogeogr. Palaeoclimatol. Palaeoeco.*, 245(3):317–331. doi: 10.1016/j.palaeo.2006.08.003.

Chapter 3

Constrained Magnetostratigraphic Dating of a Continental Middle Miocene Section in the Arid Central Asia

Author	Author position	Scientific ideas	Data generation	Analysis & interpretation	Paper writing
Verena Verestek	1	50%	100%	50%	70%
Erwin Appel	2	30%	-	25%	20%
Silke Voigt	3	10%	-	15%	5%
Konstantin Frisch	4	10%	-	10%	5%
Status in publication process:		published			

frontiers in Earth Science

ORIGINAL RESEARCH
published: 08 May 2018
doi: 10.3389/feart.2018.00049

Constrained Magnetostratigraphic Dating of a Continental Middle Miocene Section in the Arid Central Asia

Verena Verestek[1], Erwin Appel[1], Silke Voigt[2] and Konstantin Frisch[2]*

[1] Department of Geosciences, University Tübingen, Tübingen, Germany, [2] Institute of Geosciences, Goethe University Frankfurt, Frankfurt, Germany

The Neogene succession of the Aktau Mountains in the Ili Basin, southeast Kazakhstan, is a terrestrial archive well suited for researching the role of Central Asia in Miocene climate evolution. We present an integrated approach for dating the well-exposed Bastau Formation, based on magnetostratigraphy and constraints from cyclostratigraphy and biostratigraphy. Stepwise demagnetization yielded characteristic remanence directions that are consistent with those expected for the Miocene in Central Asia. The reddish-colored alluvial floodplain deposits and gray lacustrine deposits show partly complex magnetic behavior with magnetite and hematite as the main magnetic carriers, with variable demagnetization behavior and non-dipolar normal and reverse polarity directions. The observed magnetic properties are best explained by depositional variability and magneto-mineralogical alteration effects of both dissolution and neo-formation of magnetite, including significant secondary magnetization. The mean of reverse polarity directions is flatter than the expected Middle Miocene Earth magnetic field, which is an indicator for the existence of inclination shallowing that supports a primary origin. Detailed rock magnetic analyses are used to analyze the nature of the characteristic remanent magnetization and to discriminate primary and secondary remanence directions in order to obtain a reliable magnetostratigraphic result. The proposed age of 15.3–13.9 Ma for the Bastau Formation corresponds to the known biostratigraphic setting, matches with typical sedimentation rates of foreland basins in Central Asia, and coincides with spectral analysis of geochemical proxies of that section. The resulting age model serves as a robust framework for paleoclimate reconstruction of Neogene climate dynamics in Central Asia.

Keywords: magnetostratigraphy, Miocene, paleoclimate, rock magnetism, sedimentary rocks

OPEN ACCESS

Edited by:
Kenneth Philip Kodama, Lehigh University, United States

Reviewed by:
Anne-Christine Da Silva, University of Liège, Belgium
Josep M. Pares, National Research Center on Human Evolution, Spain

****Correspondence:***
Verena Verestek
verena.verestek@uni-tuebingen.de

Specialty section:
This article was submitted to Geomagnetism and Paleomagnetism, a section of the journal Frontiers in Earth Science

Received: *05 October 2017*
Accepted: *16 April 2018*
Published: *08 May 2018*

Citation:
Verestek V, Appel E, Voigt S and Frisch K (2018) Constrained Magnetostratigraphic Dating of a Continental Middle Miocene Section in the Arid Central Asia. Front. Earth Sci. 6:49. doi: 10.3389/feart.2018.00049

INTRODUCTION

Central Asia's climate dynamics during the Cenozoic, with a general trend of aridification (Guo et al., 2002; Tang et al., 2011; Caves et al., 2015), was mainly driven by global cooling and uplift of the Tibetan plateau (Zhisheng et al., 2001; Lu et al., 2010; Miao et al., 2012). The extent of the Paratethys, together with its advance and retreat largely influenced the atmospheric moisture supply in Central Asia (Fluteau et al., 1999; Bosboom et al., 2011). To investigate these influencing factors, we study a

well-exposed paleoclimatic archive, the Neogene sedimentary succession in the Aktau Mountains (SE Kazakhstan). A robust age model that allows detailed correlation to trans-regional and global tectonic and climatic processes during the Neogene is fundamental for paleoclimatic interpretation of the proxy record. Several biostratigraphic studies provide a first rough temporal framework for the succession (e.g., Kordikova and Mavrin, 1996; Dzhamangaraeva, 1997; Lucas et al., 2000). However, the paucity of index fossils and lack of volcanic horizons compromise a detailed age model for the Aktau Mountains.

Sedimentary rocks and sediments can provide high-quality continuous magnetic polarity records contributing to the understanding of environmental processes. The source and primacy of the magnetic minerals in the sedimentary deposits are crucial for paleomagnetic studies. Secondary magnetic overprints due to viscous remanences, new formation of magnetic minerals and magneto-mineralogical alteration associated with burial, diagenesis, exhumation and exposure may complicate the analysis of characteristic remanences. Magnetostratigraphic dating of continental sediments is often more complex than for marine sequences due to a highly variable lithology causing varying rock magnetic properties, alteration and remagnetization processes (Hounslow and Nawrocki, 2008; Roberts et al., 2010; Kodama, 2012). However, under favorable conditions, one can link lithologic variations to cyclic variations in the depositional environment, i.e., precession, obliquity and eccentricity (Hays et al., 1976; Olsen and Kent, 1996; Kodama and Hinnov, 2015). Use of other approaches such as biostratigraphy and cyclostratigraphy can help to substantiate complex magnetostratigraphic dating (Krijgsman et al., 1995; Hu et al., 2005; Abels et al., 2010; Herb et al., 2015).

The studied section largely consists of red beds. Albeit the controversy on the reliability of red beds (Butler, 1992), previous studies show that red beds can carry a reliable primary detrital remanent magnetization (Tauxe et al., 1980; Tauxe and Kent, 1984; Krijgsman et al., 1999; Kruiver et al., 2003). Red beds might not be good recorders of precise paleo-remanence directions due to syn-depositional effects as inclination shallowing, but they can acquire and preserve a primary remanence and are thus a promising target lithology for recording the polarity of the Earth magnetic field. Because of the possible influencing factors mentioned above, it is essential to verify the reliability of each red bed record. Fold tests and reversal tests can yield important information about the timing of remanence acquisition and possible remagnetization processes. Moreover, rock magnetic methods are necessary to investigate remanence stability, the origin of the natural remanence magnetization and to identify possible secondary magnetizations (Kodama, 2012).

The Neogene is a period of frequent magnetic polarity reversals favoring a magnetostratigraphic approach to develop a detailed age model for the Aktau succession. In this paper, we present a detailed magnetostratigraphy of the Bastau Formation (Fm) as a fundamental basis for better understanding the Neogene climate dynamics in Central Asia. The Bastau Fm, with its depositional variability and magneto-mineralogical alteration effects, is an example of a complex continental setting. Detailed rock magnetic analyses, together with other constraints such as geochemical and cyclostratigraphic results, are required to develop a reliable temporal framework.

GEOLOGICAL SETTING

The studied succession is located in the Aktau Mountains situated in the Ili Basin, a triangular foreland basin in southeast Kazakhstan (44°00′20.3″N 79°14′40.9″E, **Figure 1**). A semi-arid desert, steppe vegetation and the Ili River dominate the today's landscape. The basin is surrounded by the foothills of the Dzhungarian Alatau Mountains to the north and the foothills of the Tien Shan Mountains to the south.

The Aktau Mountains provide an exceptionally well-exposed, long and continuous succession of Cenozoic sediments. They result from an asymmetrical anticline with a gently dipping northern flank mainly comprising lake deposits and mudflats. Bedding is fairly constant throughout the section with an average dip direction of 314° and dip angle of 10°. We did not identify any sedimentary unconformity as cemented surfaces or abrupt changes in grain size, which suggests that the sedimentary sequence is relatively continuous.

The Neogene stratigraphy of the 1,500 m-thick Aktau succession is divided into five formations (**Figure 2**; Voigt et al., 2017). Fluvial sandstones of a meandering river (Aidarly Fm) are overlain by cyclically bedded mudflats with sheet-flood deposits and paleosols (Bastau Fm). Higher up, the succession grades into ephemeral playa lake deposits (Koktal Fm), and perennial lacustrine limestones and marls (Kokterek Fm). The overlying Ili Fm roughly resembles the underlying Kokterek Fm but with more organic rich horizons (Bodina, 1961; Voigt et al., 2017). Biostratigraphic data provide a low resolution temporal framework that is useful as age marker for magnetostratigraphic dating of the Aktau Mountains (**Figure 2C**). The plant and mammal fossils (rodents, *Gomphotherium*, *Stephanocemas* and *Lagomeryx*) found at the top of the Aidarly Fm were correlated to the European mammalian biozones MN4-MN5 (Kordikova and Mavrin, 1996; Lucas et al., 1997, 2000; Kordikova, 2000; Kordikova and de Bruijn, 2001). Charophytes and the occurrence of the gomphotere *Anancus avernensis* in the lower Ili Fm suggested a Pliocene age (Bazhanov and Kostenko, 1961; Dzhamangaraeva, 1997). Accordingly, the Bastau Fm is of late Early to Middle Miocene age.

The lithology of the 90 m-thick Bastau Fm can be divided into three lithofacies based on water availability, with smooth transition between facies: alluvial fan, dry mudflat and wet mudflat (Voigt et al., 2017). The alluvial fan facies is characterized by unbedded, reddish or grayish bleached sandstone. Massive red (sandy) mudstones with occasional calcretes are typical for the dry mudflat facies. The wet mudflat facies is represented by reddish, yellow and greenish, mostly layered sandy and silty marls, often with color mottling. Additionally, with the occurrence of displacive gypsum, an increasing salinization above 55 m is observed, indicating high evaporation rates (Voigt et al.,

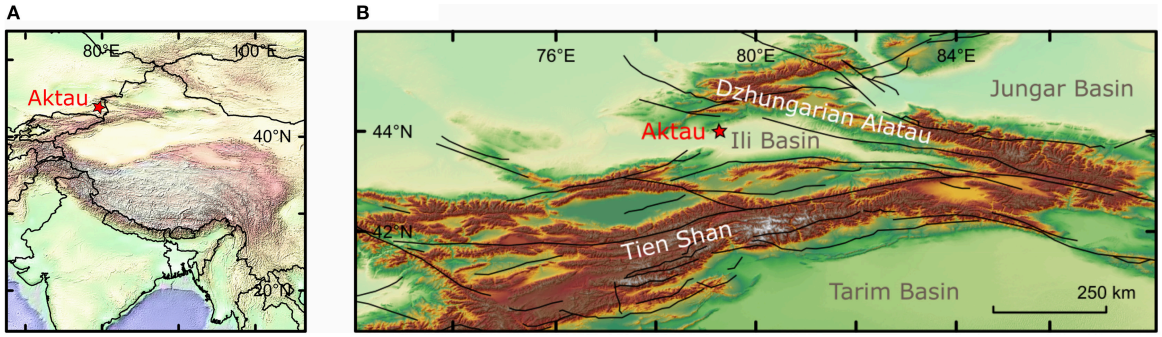

FIGURE 1 | (A) Overview map of Central Asia and the Tibetan Plateau (red star marking the location of the studied Aktau Mountains), **(B)** topographic map of the Ili Basin and the Tien Shan belt with major fault zones after Jolivet et al. (2010).

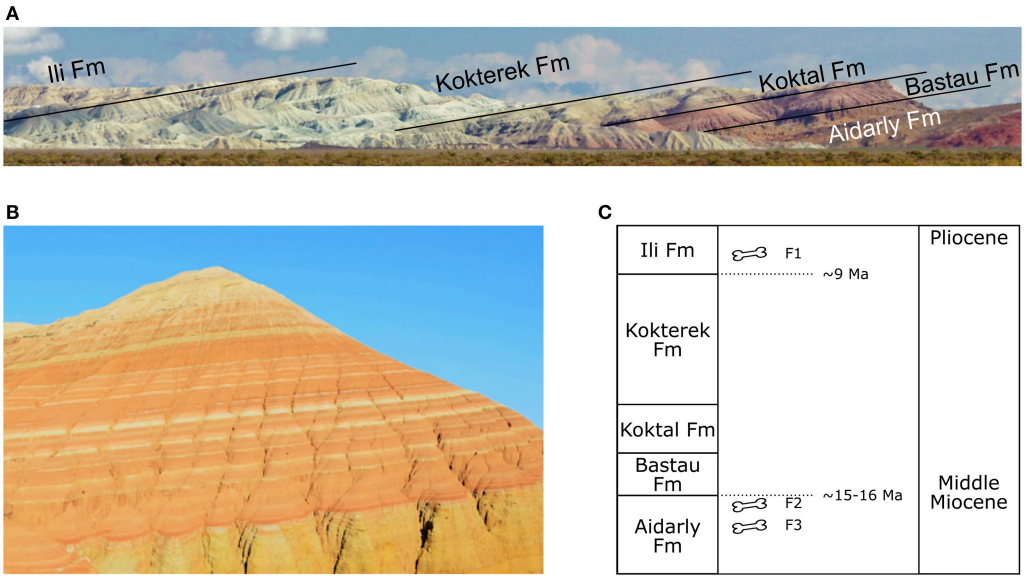

FIGURE 2 | (A) Cenozoic succession of the Aktau Mountains with the stratigraphic formations after Voigt et al. (2017), **(B)** image of the 90 m-thick Bastau Fm with the dominant red siltstones (photo by J. Pross), **(C)** biostratigraphic overview with marker fossil records: F1 after Bazhanov and Kostenko (1961), and Dzhamangaraeva (1997), F2 and F3 after Lucas et al. (1997).

2017). Further details on the lithology and facies including a detailed facies zone matrix is in progress.

SAMPLING AND METHODS

The studied sequence is characterized by small-scale heterogeneities along the sequence. Lithological heterogeneities exist even at the same stratigraphic level (e.g., small-scale variation of mottled parts), equally pronounced as between neighboring sampling levels. Thus, a dense sampling scheme was preferred over site-level sampling to ensure consistency by checking subsequent samples along the sequence. After removing the weathered surface layer, we collected samples from 503 levels (one sample per level) from fresh rock along the entire Bastau Fm. We applied a dense sampling scheme with a mean of ca. 20 cm distance between sampling levels, and partly prepared twin specimens for testing different demagnetization procedures. For sampling, we used a battery driven drill or a double-blade cutter. Drilled cylindrical samples (2.5 cm in diameter) were cut into standard specimens of 2.2 cm sides; cut samples were prepared into cubes of 2.2 cm sides. Since the content of clay is very high in all samples, we used a cordless compressor for air drilling instead of water flushing. The samples were oriented with a magnetic compass and an inclinometer.

All magnetic parameters were measured in the laboratory of Tübingen University. Full vector magnetization measurements

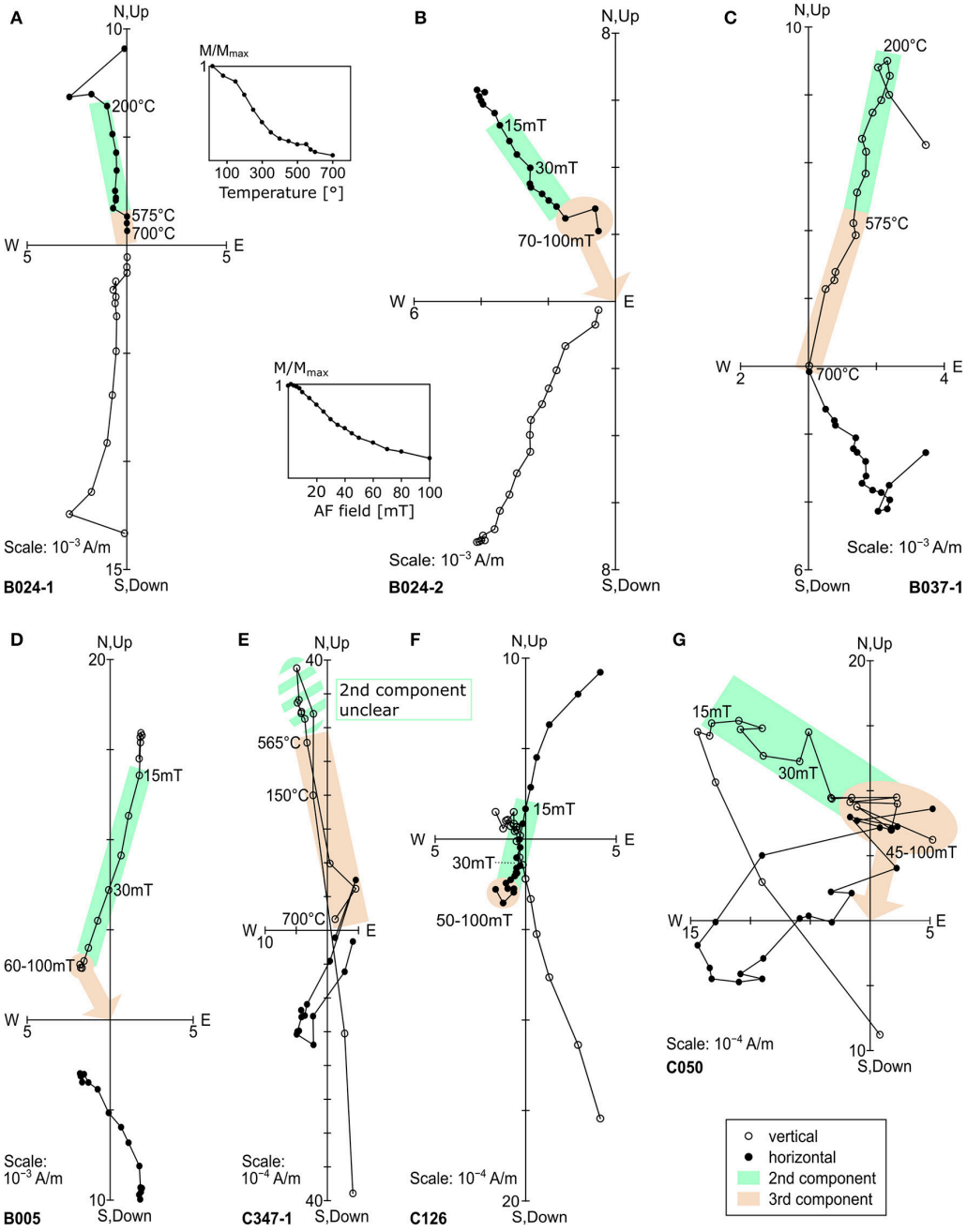

FIGURE 3 | Orthogonal end-vector projections of thermal and alternating field demagnetization data (stratigraphic coordinates) for representative samples from the Bastau Fm. Sample names are in bold. The determination of the second and third components is demonstrated in green and red (first component removed below 15 mT or below 200°C not marked). For the third component, clustering directions at high AF steps are forced to the origin (arrows, in F omitted for clarity).

of stepwise demagnetization of natural remanent magnetization (NRM) were performed on a 2G Enterprises DC-SQUID magnetometer. Alternating field (AF) demagnetization was applied in steps of 3 mT up to 45 mT and then in progressively larger steps up to 100 mT. For thermal (TH) demagnetization, the specimens were consecutively heated to temperatures

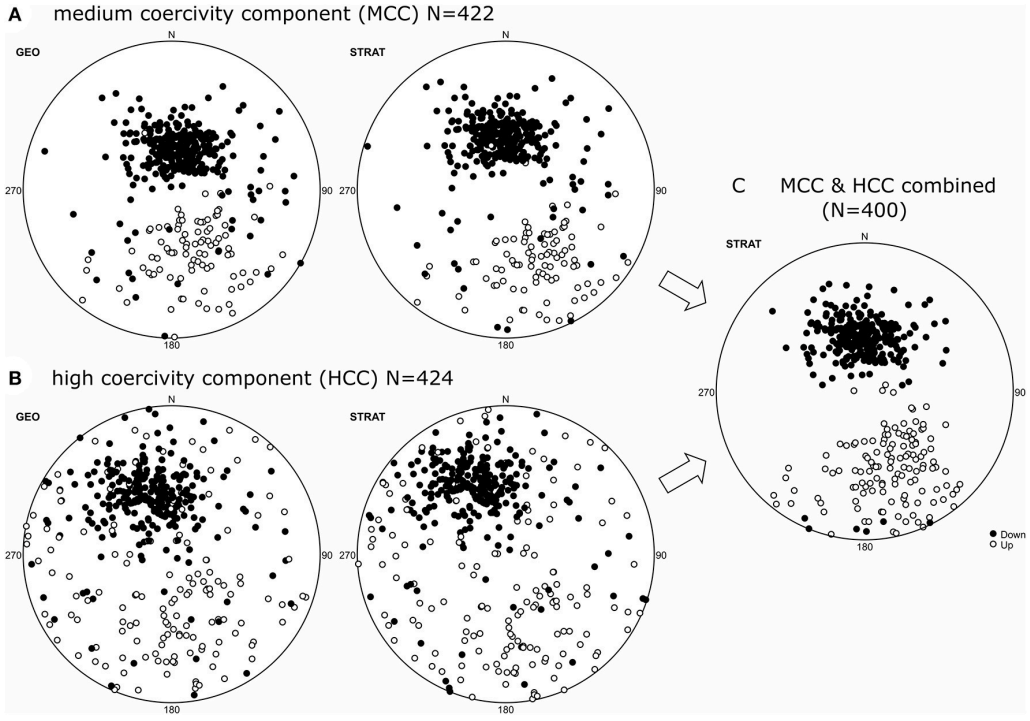

FIGURE 4 | Equal area projections of remanence directions determined from NRM demagnetization in geographic (left) and stratigraphic (middle) coordinates: **(A)** medium coercivity component (MCC) and **(B)** high coercivity component (HCC); **(C)** MCC & HCC combined data set in stratigraphic coordinates obtained from A and B (see text in section Characteristic Remanent Magnetizationfor explanation).

between 100 and 700°C in steps of 50°C (plus one step at ∼570°C). For remanence analysis from the demagnetization path we used principle component analysis (Kirschvink, 1980). For determining the high coercivity component and high temperature component the directions are forced through the origin. Mean directions of remanence populations were calculated by Fisher statistics (Fisher, 1953).

Anhysteretic remanent magnetization (ARM) was produced and measured using the SQUID magnetometer with an integrated degausser, applying a 100 mT peak alternating field and a biasing 50 μT direct field. Isothermal remanent magnetization (IRM) was imparted with a Magnetic Measurements PM9 pulse magnetizer and IRM intensity was measured with a Molspin spinner magnetometer. The IRM acquired in a 1.0 T field is taken as saturation IRM (SIRM). From SIRM and reverse IRM in a −300 mT field we calculated the high-coercivity IRM (HIRM) and the s-ratio (after Bloemendal et al., 1992). For selected samples we obtained full IRM acquisition curves (28 steps from 10 mT to 2.8 T), and decomposed the curves by log-Gaussian analysis after Kruiver et al. (2001) in order to characterize the different ferro(i)magnetic phases by their medium acquisition field ($B_{1/2}$) and to determine their contribution to the IRM signal.

Susceptibility measurements were performed with an AGICO MFK1-FA Kappabridge. Bulk susceptibility expressed in mass-specific units (χ) and its frequency dependence (kfd) were determined from bulk samples at two different operating frequencies (976 Hz and 15,616 Hz). High-temperature susceptibility runs were done by heating sample powder (∼0.2 g) to 700°C in air at low heating rate (11°C/min) and measuring susceptibility during the full heating and cooling cycle. Anisotropy of susceptibility (AMS) was measured with a 3D-rotator and analyzed in volume-specific units (k). AMS parameters P_j and T (Jelinek, 1981) were calculated to describe the degree of anisotropy and the shape of the AMS tensors. Hysteresis loops were obtained on small sub-samples (∼2 mg) with a PMC MircoMag 2900 (max. field 500 mT), extracting the ratios of saturation remanence to saturation magnetization (M_{rs}/M_r) and coercivity of remanence to coercivity (H_{cr}/H_c).

PALEOMAGNETIC AND ROCK MAGNETIC RESULTS

Remanence Analysis

A subset of 10 samples (each one divided into twin specimens) was chosen as pilot samples and subjected

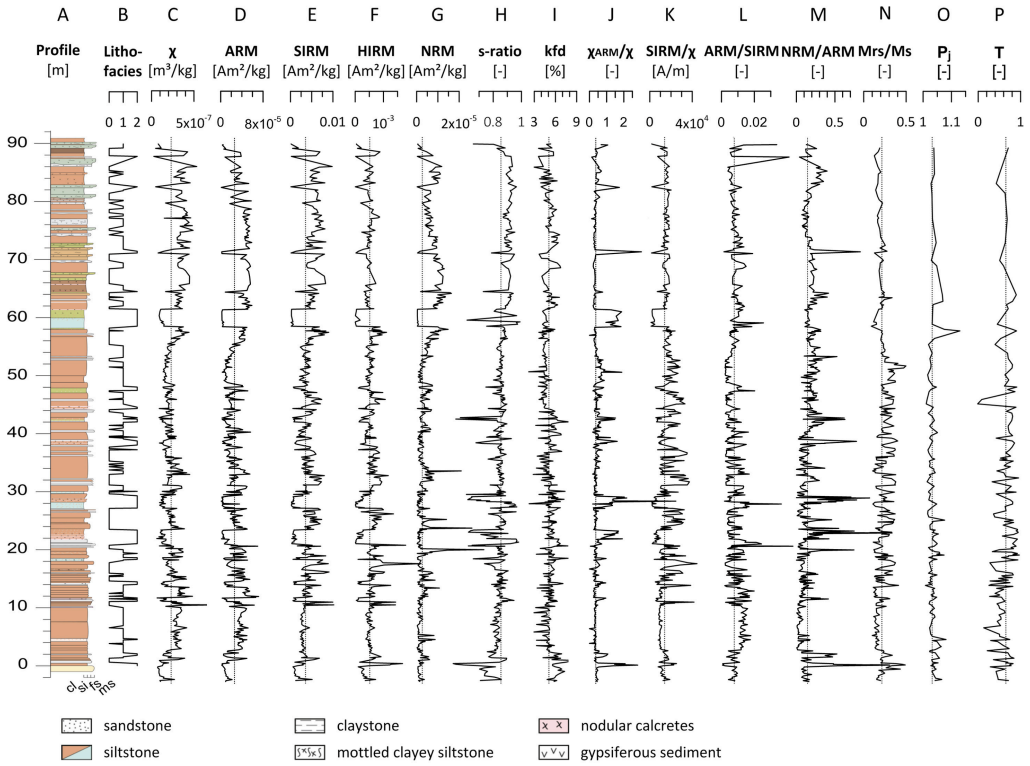

FIGURE 5 | Rock magnetic parameters measured along the section with median values indicated by dashed lines: **(A)** profile with simplified color chart and grain size indication on the right (cl, claystone; si, siltstone; fs, fine sandstone; ms, medium sandstone), **(B)** lithofacies (0–alluvial fan, 1–dry mudflat, 2- wet mudflat), **(C-G)** concentration-dependent parameters (χ, SIRM, ARM, HIRM, NRM), **(H)** magnetic mineral indicator (s-ratio), **(I-L)** grain size dependent ratios (kfd, χ_{ARM}/χ, SIRM/χ, ARM/SIRM), **(M)** NRM/ARM as an indicator for natural remanence intensity to remanence capacity, **(N)** magnetic grains size (i.e. domain-state) indicative ratio M_{rs}/M_s, **(O,P)** parameters of degree and shape of anisotropy of magnetic susceptibility (P_j, T). For explanation of abbreviations, see section Sampling and Methods.

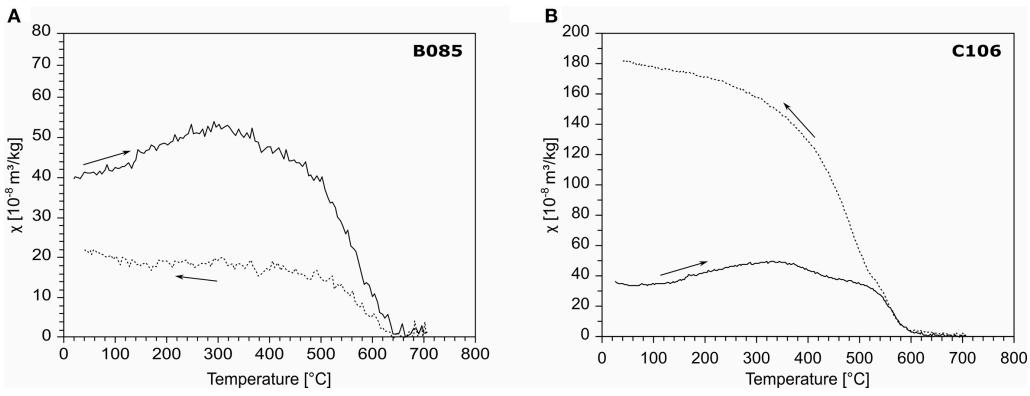

FIGURE 6 | Bulk susceptibility vs. temperature curves of representative samples of the Bastau Fm. Both curves show the typical decrease around 580°C, corresponding to the Curie temperature of magnetite, and non-reversible behaviors; in **(A)** magnetite is destroyed at high temperature whereas in **(B)** new magnetite is produced.

to AF and TH demagnetization. AF demagnetization adequately resolved magnetic components for samples from all lithologies, and we thus chose AF treatment as the standard demagnetization procedure for the bulk of the specimens. In total, 503 specimens were treated with AF demagnetization. For control, additional 73 specimens

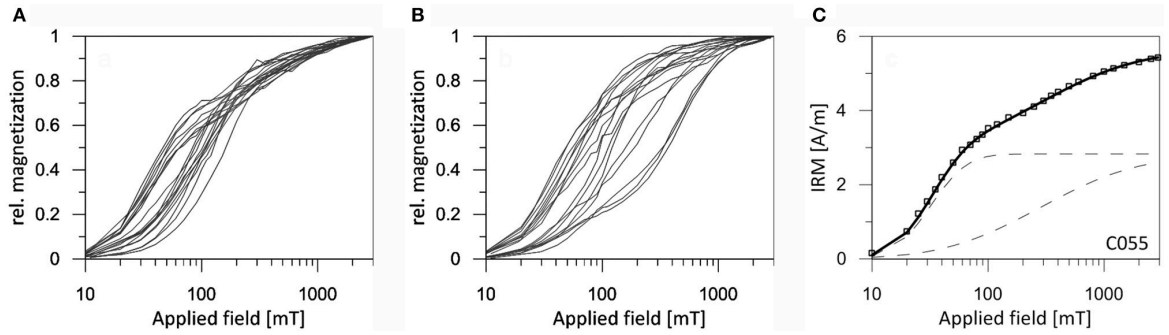

FIGURE 7 | Isothermal remanence magnetization acquisition curves: **(A)** alluvial fan and dry mudflat facies types, **(B)** wet mudflat facies type, **(C)** end member modeling for sample C055 (dry mudflat facies type) after Kruiver et al. (2001) with the two end member components magnetite and hematite indicated with dashed lines.

(twin specimens from same levels) were analyzed with TH demagnetization.

Both AF and TH demagnetization yield similar results (e.g., twin specimens of sample B024 in **Figures 3A,B**). The majority of specimens show three components of remanent magnetization. The remanence removed at low AF fields <15 mT or at low temperatures <200°C shows highly scattered direction with a slight tendency toward the present Earth magnetic field direction. This soft magnetic or viscous remanence will not be further discussed. A medium coercivity component (MCC) is isolated using AF demagnetization data from 15 to 30 mT or higher. At the maximum AF field (100 mT) the specimens are not completely demagnetized. The residual remanence from 60 to 70 mT onward shows relatively constant intensities and clustering remanence directions, which are predominantly quite stable (**Figures 3D,F**), though partly also noisy cases occur (**Figure 3G**). This residual remanence indicates a high coercivity component (HCC) which is immune against AF demagnetization. It can only be demagnetized to the origin by TH treatment. However, a more detailed analysis of the final (TH) demagnetization path is not possible because of the relatively low intensity of the residual remanence compared to the NRM intensity (**Figures 3B,D,F**). As a reasonable approximation of the HCC, we determined its direction by averaging the clustering residual directions anchoring them to the origin. TH demagnetization results give a hint about the remanence carriers. Most of the NRM is unblocked below 600°C, but part of it survives until temperatures between 600 and 700°C (**Figures 3A,C,E**). This points out that magnetite and hematite are the likely carriers of the MCC and HCC, respectively.

For most specimens, the MCC and HCC show directions of the same polarity. However, for 7% of the samples, the HCC exhibits a reverse polarity direction while the MCC indicates a normal polarity direction (**Figure 3F**). The contrary, i.e., a reverse polarity MCC paired with a normal polarity HCC, never occurs. **Figure 4** displays the dispersions of all extracted remanence directions of the MCC (**Figure 4A**) and HCC (**Figure 4B**) in separate plots. Both components show roughly antipodal remanence directions, and thus are potential

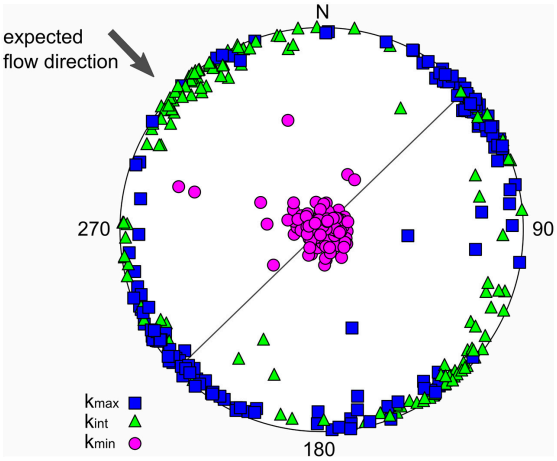

FIGURE 8 | Anisotropy of susceptibility principle axes (tilt-corrected coordinates): minimum principle axes (k_{min}, circles) group perpendicular to the bedding plane, maximum principle axes (k_{max}, squares) group in the strike direction (gray line) of the bedding plane.

carriers of a characteristic paleo-remanence. The HCC scatters much more than the MCC, which is likely due to the approximative determination of this component. Normal and reverse polarity directions of the HCC tend to be antiparallel (normal polarity mean D/I = 334.0°/41.4°, reverse polarity mean D/I = 171.2°/−48.8°) and both polarity directions show relatively similar scatter, whereas for the MCC the normal polarity directions (mean D/I = 355.8°/62.5°) are clearly steeper and more clustered than the reverse polarity directions (mean D/I = 155.7°/−40.5°).

Magnetic Mineralogy

Rock magnetic properties provide further information on the stability and the origin of magnetic remanences. Below, we separate these results into their indication for magnetic

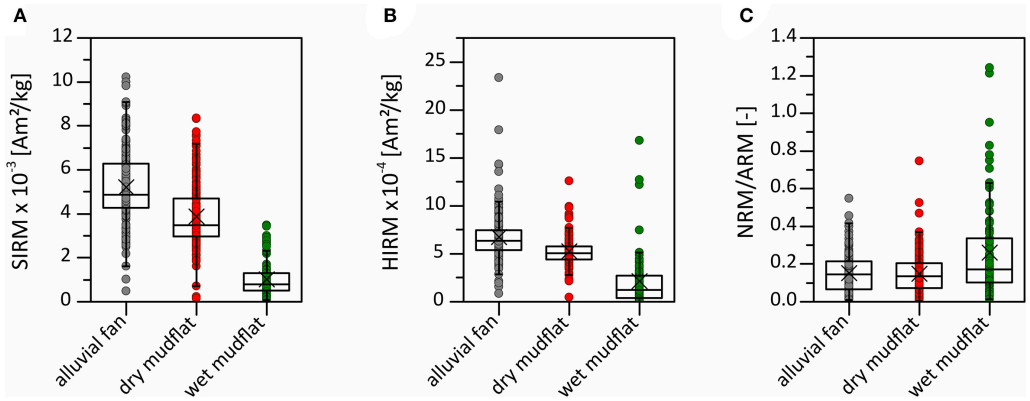

FIGURE 9 | Lithofacies and rock magnetic characteristics: box plots of the concentration-dependent parameters **(A)** SIRM, **(B)** HIRM, and **(C)** NRM/ARM ratio with means indicated by crosses, quartiles boxes and whiskers with a factor of 1.5. All consistently indicate statistically different mean values for the wet mudflat facies, supporting alteration of the primacy magnetic mineralogy in this facies.

concentration, magnetic mineral type, magnetic grain-size, and magnetic fabric.

Concentration-Dependent Parameters

The concentration-dependent magnetic parameters vary with lithology. Bulk magnetic susceptibility χ (**Figure 5C**) shows an increase above 55 m. Samples from the alluvial fan and dry mudflat facies show higher values than wet mudflat samples. A similar pattern is observed for the intensities of ARM (**Figure 5D**), SIRM (**Figure 5E**) and NRM (**Figure 5G**). Also HIRM values (**Figure 5F**) are lower in the wet mudflat facies; however, there is no increase above 55 m.

Magnetic Minerals

Temperature dependent results suggest the existence of at least two magnetic phases in all lithologies of the Bastau Fm. In all studied samples, a marked decrease around 550–580°C is seen in high-temperature susceptibility runs, which clearly reveals the presence of magnetite (**Figure 6**). Most samples show a decrease around 350–450°C which can be attributed to the inversion of maghemite to hematite. Hematite is not observed in the thermomagnetic curves as the presence of magnetite overrides its very low susceptibility. In most samples, strongly enhanced values appear in the cooling curves accompanied by a continuous increase during cooling (**Figure 6B**). We explain this observation with new formation of ultrafine superparamagnetic magnetite particles (with a range of different grain sizes) at high temperatures during heating, which transform from the fully unblocked state to the state of higher susceptibility during cooling (Bowles et al., 2009). The new formation of magnetite during heating is more pronounced in the mudflat layers.

The s-ratio (**Figure 5H**) varies between 0.52 and 0.99 (median 0.86) implying a high fraction of hematite in most of the samples. Like the concentration-dependent parameters, s-ratios change above 55 m, showing higher values in the upper part.

Unmixing of IRM acquisition curves (Kruiver et al., 2001) for representative samples of all three facies types (**Figures 7A,B**, in total 28 samples) indicate the presence of both magnetite and hematite. The lower coercivity end member component has mean $B_{1/2}$-values between 30 and 100 mT, which can be related to magnetite. This first end member component has relatively lower $B_{1/2}$-values for alluvial fan and dry mudflat samples compared to wet mudflat samples. The $B_{1/2}$-values of the second end member component varies between 100 and 700 mT, which according to maximum unblocking temperatures during TH demagnetization of the SIRM (**Figure 7C**) represents hematite. Occasionally a third end member component with $B_{1/2}$-values >1,500 mT is identified contributing <20% to the SIRM signal. This third component could be interpreted as a second hematite fraction with relatively higher coercivity. Contributions of goethite can be excluded based on TH demagnetization of IRM. The contributions of the first and second end member components are relatively equal in the alluvial fan and dry mudflat samples. In wet mudflat samples, the contributions are more variable, with 30–90% for the first component, indicating a relatively higher magnetic fraction than in the other two facies types. Interestingly, for those samples from the wet mudflat facies showing striking color mottling, the first component either contributes relatively less to the total SIRM (<45%) with $B_{1/2}$-values around 35–75 mT, or has higher coercivities ($B_{1/2}$-values around 100 mT) contributing up to 89% to the total SIRM.

Magnetic Grain-Size Characteristics

The frequency dependent susceptibility kfd is generally low with an average value of 5% (**Figure 5I**). Thus, non-superparamagnetic grains dominate the ferro(i)magnetic mineral assemblage.

The lower values of χ_{ARM}/χ and SIRM/χ (**Figures 5J,K**) in the wet mudflat layers are likely caused by a decrease of the magnetite fraction and reflect a relatively higher paramagnetic contribution. The ARM/SIRM ratio (**Figure 5L**) is a more

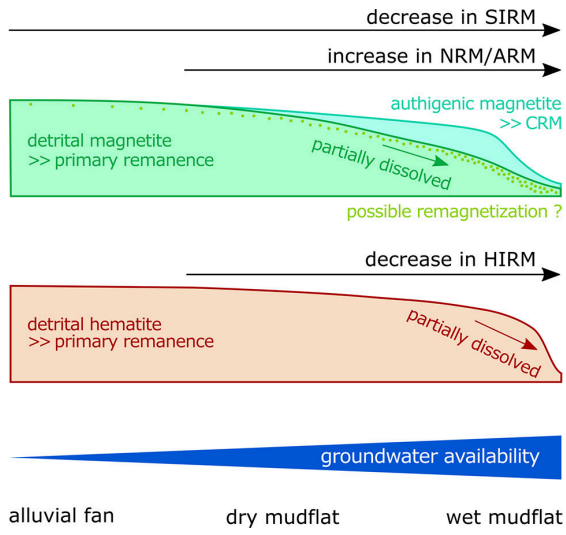

FIGURE 10 | Principle sketch of the interpreted magnetic alteration scenario of the ferro(i)magnetic phases, comprising dissolution and neo-formation of magnetite and dissolution of hematite, causing secondary chemical remanent magnetization (CRM) of authigenic magnetite and possibly also partial remagnetization of the detrital fraction.

suitable magnetic grain size indicator as it only depends on the ferro(i)magnetic phases. Its strong fluctuation between stratigraphic levels of 10 m and 50 m suggests a complex magnetic behavior in this part.

Hysteresis loops are dominated by low coercivity values, they close around maximum 300 mT, and they are not a wasp-waisted, highlighting the magnetite fraction (i.e., the existing hematite fraction is obviously hidden in these curves). The hysteresis parameters are rather variable. Saturation magnetization values (M_s) are low in samples from the wet mudflat facies and range from high to low in samples of the alluvial fan and dry mudflat facies. The magnetic grain size dependent ratios M_{rs}/M_s (**Figure 5N**) and H_{cr}/H_c do not resemble the stratigraphic pattern of the ratios χ_{ARM}/χ, SIRM/χ and ARM/SIRM. The samples used for hysteresis measurements are likely too small (2 mg) to average on the internal heterogeneity of the sediment while χ_{ARM}/χ, SIRM/χ and ARM/SIRM were obtained from larger bulk samples of several grams. The reliability of the hysteresis results is obviously limited, and thus, we omit the results of hysteresis for further interpretations.

Anisotropy of Magnetic Susceptibility

We measured the AMS of 152 samples along the Bastau Fm. **Figures 5O,P** shows changes in AMS parameters (Jelinek, 1981) with stratigraphic position. The degree of anisotropy P_j varies from 1.008 to 1.130 with an average of 1.035. The shape parameter T ranges from −0.013 to 0.969 with a mean of 0.637 and clearly indicates an oblate shape. Variations of P_j and T throughout the stratigraphic section show no relationship with the variation of the concentration-dependent parameters. The k_{max} and k_{min} principle axes (**Figure 8**) are well grouped, with a bedding parallel fabric after tilt correction. The k_{max} directions are preferentially aligned NE-SW, i.e., in the strike direction of the bedding planes, and the k_{min} directions group very well perpendicular to the bedding plane, supporting a primary sedimentary fabric.

DISCUSSION AND MAGNETOSTRATIGRAPHY

Main Magnetic Carriers and Salinity

Detailed rock magnetic analyses revealed magnetite and hematite as the main magnetic carriers in samples from the Bastau Fm. We interpret the trend of higher values of the s-ratio (**Figure 5H**) and the concentration-dependent parameters χ, ARM and SIRM (**Figures 5C,D,E**) above 55 m as an increase in the absolute magnetite content. The mean level of HIRM values (**Figure 5F**) indicates a fairly constant hematite content throughout the section, i.e., no increasing or decreasing trend. Relatively similar residual magnetization intensities after AF demagnetization also support this interpretation. Higher magnetite concentration above 55 m is likely related to lithological changes with higher groundwater levels, higher fluctuations and salinity and intensified authigenic mineral formation (Voigt et al., 2017), including possible new formation of magnetite. For this upper part, Voigt et al. (2017) propose increasing evaporation rates in a progressively hydrologic restricted basin above 50 m.

Source of Sedimentary Input

AMS has been widely used in rock magnetic studies to understand the hydrologic regime, transport and depositional conditions of sediments or tectonic effects, also in the foreland basins of the nearby Tien Shan (Gilder et al., 2001; Charreau et al., 2005; Tang et al., 2012). The distribution of the principle AMS axes (**Figure 8**) is typical for sedimentary fabric with hydromechanical and/or gravitational processes that influence the alignment of (magnetic) grains during deposition (Tarling and Hrouda, 1993; Charreau et al., 2006; Itoh et al., 2013). The clustering of k_{max} is perpendicular to the transport direction proposed by Voigt et al. (2017). Detrital sedimentary discharge, e.g., by mudflows, coming from the foothills of the Altyn Emel and Dzhungarian Alatau in the north-west likely aligned the (geometrical) long axis of particles in NE-SW direction, indicating a fast paleocurrent flow (Tarling and Hrouda, 1993; Felletti et al., 2016).

Lithofacies Dependence of Rock Magnetic Mineralogy

The contribution of the magnetic phases to the magnetic signal varies with lithofacies. All concentration-dependent parameters (**Figures 5C-G**) show lower values for the wet mudflat facies, i.e., SIRM and HIRM are highest in the alluvial fan facies and lowest in the wet mudflat facies (**Figures 9A,B**). We interpret these variations as a concentration variation of both magnetite and hematite in the samples. The concentration of ferro(i)magnetic minerals is obviously decreasing with increasing groundwater availability.

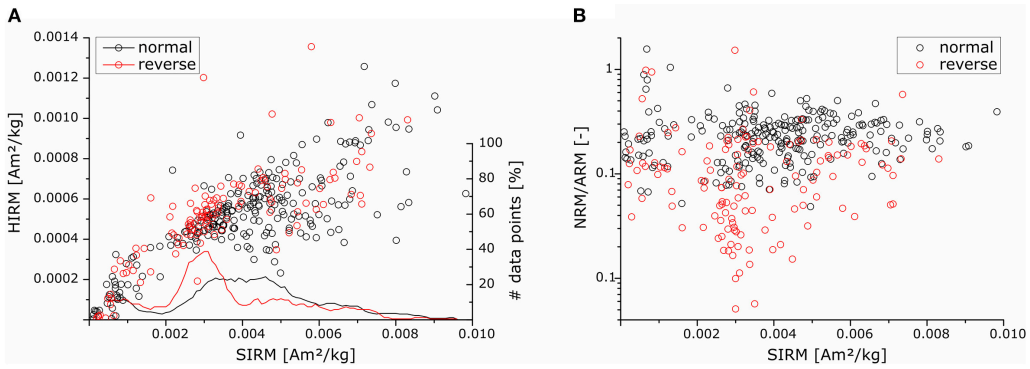

FIGURE 11 | (A) HIRM vs. SIRM and **(B)** NRM/ARM vs. SIRM scatter plots. In black (red) are the data points for samples with normal (reverse) polarity directions. The solid curves in A indicate the relative distribution of data points calculated from running means of 0.001 Am²/kg-windows for samples with normal (black) and reverse (red) polarity directions.

The three facies types are characterized by different intensities of pedogenic reworking under arid conditions evident from the neo-formation of Mg-rich clay minerals as palygorskite (Voigt et al., 2017). Authigenic mineral formation favorably occurs in the capillary fringe by evaporative groundwater rise (Deocampo, 2015) and is most pronouncedly developed in the wet mudflat facies.

New formation of magnetite during high temperature thermomagnetic runs (**Figure 6B**) is more pronounced in the wet mudflat layers. This supports the interpretation of enhanced soil formation in this facies by Voigt et al. (2017) as magnetite formation during high temperature runs is typical for soil and paleosols (Zhang C. et al., 2012; Jordanova, 2016; Sun et al., 2017).

The ratio of the NRM and ARM (**Figure 5M**) represents the natural remanence intensity (NRM) normalized to the remanence acquisition capability (given by the ARM). The NRM/ARM-ratio is higher in the wet mudflat facies and shows much higher variation in this facies type (**Figure 9C**). A higher NRM/ARM-ratio may indicate the presence of a secondary chemical remanent magnetization, which often carries a strong remanence intensity (Deng et al., 2007).

One has to note that classification of samples into the three facies types is not straightforward (see **Figure 5B** for their interpreted distribution along the section), and thus the differences of the considered rock magnetic parameters are certainly larger than indicated by the results in **Figure 9**.

Characteristic Remanent Magnetization

The time-averaged dipole field direction at the Aktau location has an inclination I = 62.6° (ambient present-day field direction: declination/inclination D/I = 4.9°/64.4°). The expected direction during the Middle Miocene calculated from the apparent polar wander path of Torsvik et al. (2012) is quite similar to the present one, i.e., D/I = 351.2°/64.4° with a corresponding virtual geomagnetic pole (VGP) at latitude/longitude = 83.4°/57.9°. The bedding planes are uniformly tilted at a low angle of 10°. Thus, recent or earlier overprints are difficult to identify and to discriminate from normal paleo-directions of primary origin.

In a first step, we combine the MCC and HCC (**Figures 4A,B**) into a common characteristic remanent magnetization (MCC & HCC combined) data set. Principle criteria for rejecting specimens are a mean angular deviation (MAD) >15°, and directions strongly deviating from the expected paleo-direction (used threshold: VGP latitude <30°). The accuracy in the determination of the MCC is usually better than for the HCC. For most specimens showing the same polarity for both components, we thus used the MCC in the MCC & HCC combined data set. Only in 54 cases for which the MCC does not meet the MAD and VGP threshold, but the HCC does, we selected the latter one. Specimens with dual polarities of both components (7 % of all samples) all show a normal polarity direction for the MCC. This indicates a secondary origin of the MCC in these samples, and we thus regarded the reverse polarity HCC as the valid paleo remanence direction (if it meets the MAD and VGP criteria). According to this procedure and the rejection criteria, 103 from the 503 sample levels were excluded.

Figure 4C shows an equal area projection of the accepted MCC & HCC combined directions consisting of 320 MCC data (236 and 84 of normal and reverse polarity, respectively) and 80 HCC data (26 and 54 of normal and reverse polarity, respectively). Reverse polarity directions show a higher dispersion than normal polarity directions, which can be explained by three reasons, all of them based on the fact that the normal polarity directions include a much higher part of the MCC than the reverse polarity directions (90 and 61%, respectively). First, the HCC often contributes relatively little to the total NRM signal, and thus its determined remanence direction (from stable end points during AF demagnetization) is noisier than for the MCC. Second, hematite particles (the likely carrier of the HCC) have a weaker magnetostatic interaction with the Earth magnetic field during their deposition. Third, the normal polarity MCC is likely contaminated to some degree by secondary chemical magnetizations, which are better clustered.

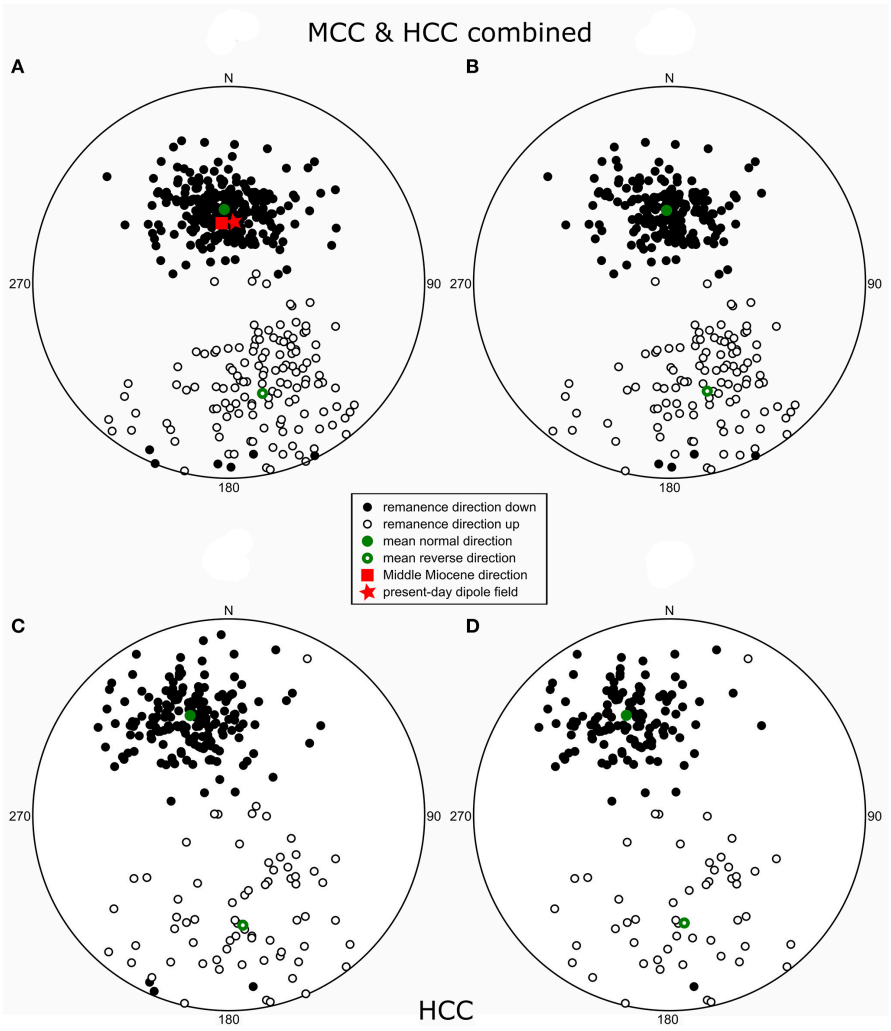

FIGURE 12 | Equal area projection of remanence directions (in stratigraphic coordinates) determined from demagnetization of NRM (mean directions of normal and reverse polarities are indicated by green circles): **(A)** directions from the MCC & HCC combined data set as shown in **Figure 4C** with expected Middle Miocene (red square) and present-day (red star) Earth magnetic field directions; **(B)** MCC & HCC combined data retained after rock magnetic selection (used for the final magnetostratigraphy; see **Figure 13E**); **(C)** HCC directions only and **(D)** HCC directions filtered by the same rock magnetic criteria.

Normal polarity directions clearly dominate the combined MCC & HCC data set. This may be due to the dominating normal polarity intervals during the time of deposition of the Bastau Fm, but also secondary magnetization effects could add to the imbalance of polarities. The interpreted alteration scenario and its possible relationship with magnetic overprinting is further discussed in the following section Magnetic Alterations and Remagnetization.

Magnetic Alterations and Remagnetization

Secondary overprinting is a common process in sedimentary rocks (McCabe and Elmore, 1989; van der Voo and Torsvik, 2012; Roberts, 2015). Transformation, low-temperature oxidation, dissolution and neo-formation could lead to changes in coercivity, e.g., due to a change of the effective particle size and inhomogeneities generated within particles (Zhang W. L. et al., 2012; Hu et al., 2015). The directions in our MCC & HCC combined data set (**Figure 4C**), particularly the normal polarity ones, are likely contaminated by secondary magnetizations due to new formation and partial remagnetization of ferro(i)magnetic phases during diagenetic processes and later alteration. Samples from the wet mudflat facies are preferred candidates for the presence of secondary magnetizations as they show lower NRM values with partially normal polarity directions in stratigraphic

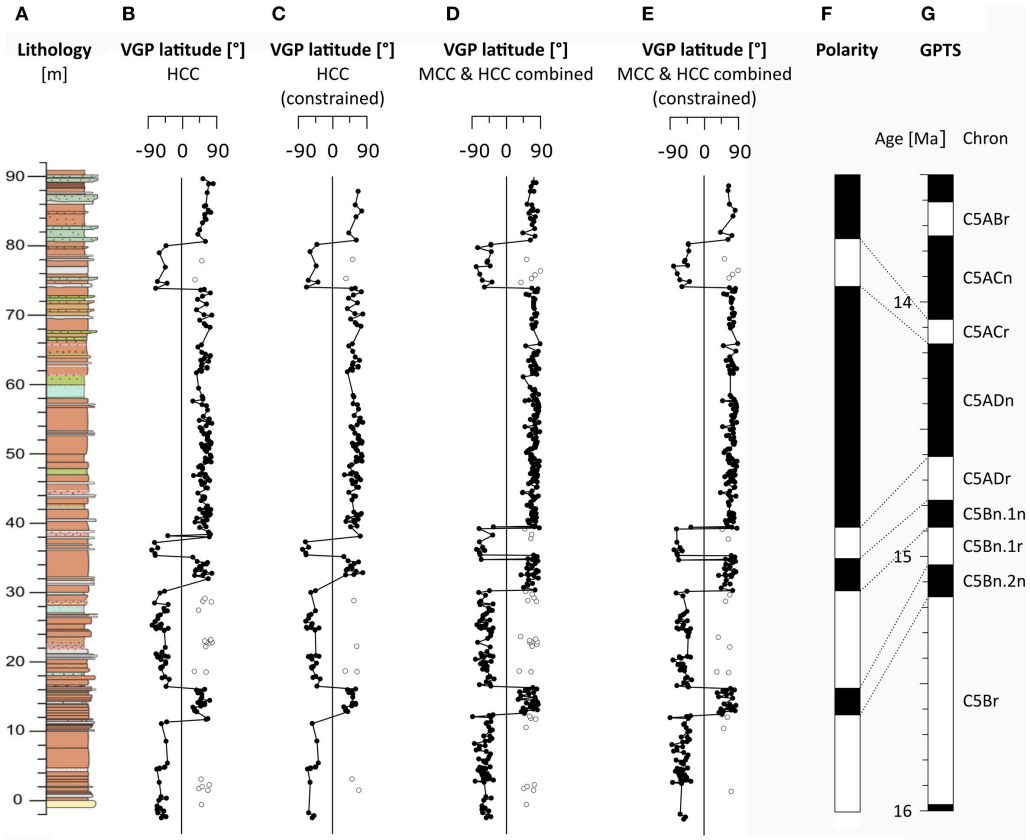

FIGURE 13 | Magnetostratigraphic results for the Bastau Fm based on the rock magnetic data-selection criteria: **(A)** stratigraphic column (as in **Figure 5A**), **(B,C)** VGP (North poles) latitude plots based on the HCC only and **(D,E)** based on the MCC & HCC combined data set (selections correspond to **Figures 12B,D**, respectively), open circles indicate still remaining questionable normal polarity directions within reverse polarity intervals (see text for further explanation), **(F)** resulting polarity pattern correlated to **(G)** the GPTS after Gradstein et al. (2012).

intervals where specimens from other facies types suggest a reverse polarity.

Chemical alteration in arid and semiarid settings responds sensitively to changes in the hydrologic system of a basin. Voigt et al. (2017) used bulk-sediment geochemistry to derive weathering indices and studied changes in the intensity of weathering and pedogenesis in the Bastau Fm. They observed elevated weathering intensities as a result of pronounced pedogenesis in periods of driest climatic conditions in settings when the regional evaporation rate was high and the alluvial sedimentary discharge was low. Elevated values of weathering indices (i.e., Mg-enrichment by authigenic formation of Mg-rich clay minerals) as well as low Ti/Al ratios occur in the wet mudflat facies, i.e., in horizons that are characterized by mottling and associated color changes from pedogenic reworking (**Figures 15A,B**). These horizons formed during times of intensified evaporation, higher groundwater table and associated capillary groundwater rise. Gale et al. (2006) attributes color mottling in clay rich sediments to repeated drying and wetting of soils and the non-uniform process of ferrous iron to ferric iron reduction. The presence of rutile in wet mudflat layers (Voigt et al., 2017) also suggests reductive conditions. Rock magnetic parameters suggest syn- and post-depositional alteration of magnetite, linked with secondary magnetic overprinting and poorer remanence conservation. The dry mudflats were deposited during periods of higher hinterland precipitation and accordingly higher detrital sediment production. These wet conditions are less seasonal with continuous sedimentary input, more stable aggradation of mudflats and pedogenesis with well drained descendent soils (Voigt et al., 2017) favoring conservation of primary ferro(i)magnetic phases.

The variations of the concentration dependent magnetic parameters with lithofacies and the different coercivities and contributions in the end-members from IRM decomposition samples of the wet mudflat facies are indicative for an alteration of the ferro(i)magnetic fraction. The wet mudflat facies is characterized by an elevated groundwater table wherefore reducing conditions are dominating the diagenesis in these

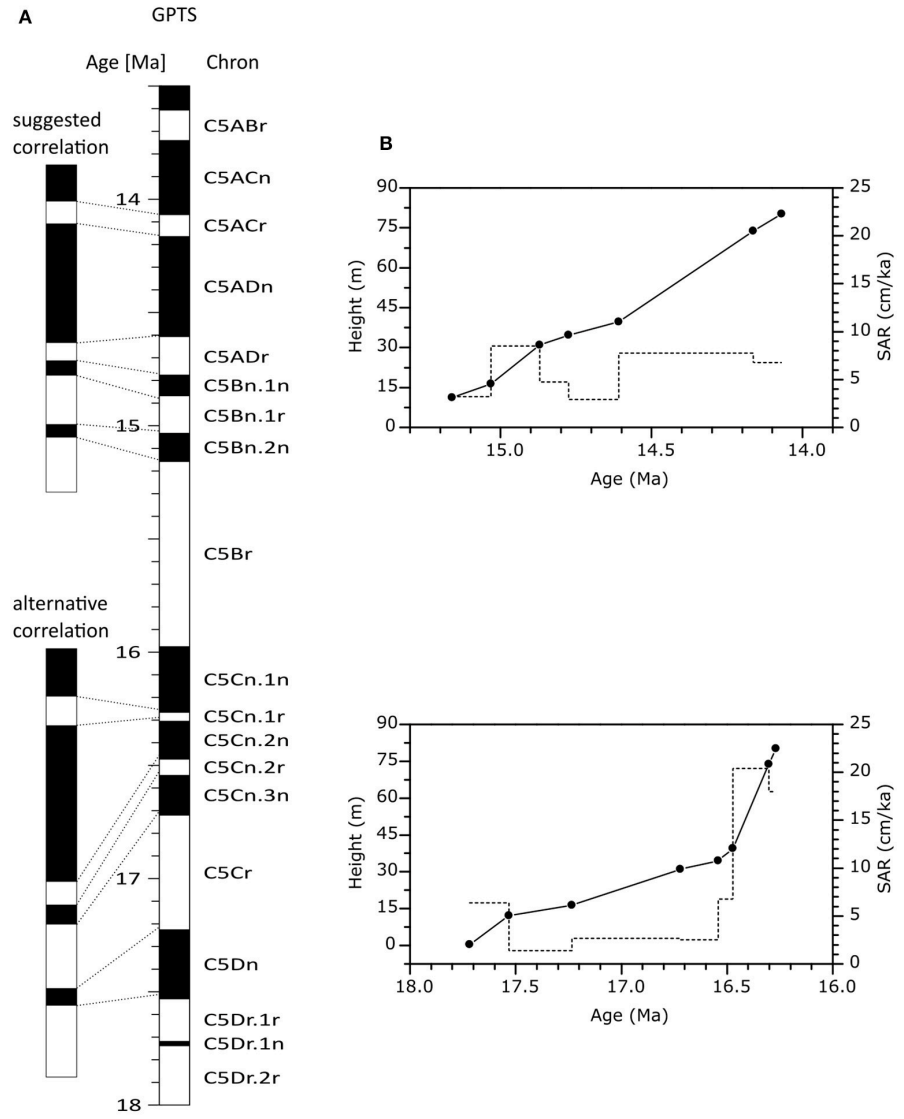

FIGURE 14 | (A) Suggested and possible alternative magnetostratigraphic correlation of the polarity pattern retrieved from the VGP latitude to the GPTS after Gradstein et al. (2012), **(B)** corresponding height vs. age plots (black line) with sediment accumulation rates (SAR, dashed line) calculated for each fully resolved chron.

horizons (Voigt et al., 2017). We propose dissolution and neo-formation of magnetite as the main alteration processes (see principle scenario in **Figure 10**), which we explain in the following paragraphs.

In the Bastau Fm the paleo-remanence is likely carried by fine and coarse magnetite and hematite grains. Multi-domain grains are susceptible to remagnetization and less effective recorders of paleo magnetizations than fine single domain grains (Butler, 1992). Certainly, remagnetization of soft magnetic particles may also be present in all facies types of the Bastau Fm (**Figure 10**).

Magnetite dissolution has been studied in laboratory experiments (Karlin and Levi, 1985; Canfield and Berner, 1987) and found to have profound influence on remanence stability (Roberts et al., 2013). Dissolution of magnetite is well known from water-logged sediments (Florindo et al., 2003; Demory et al., 2005; Taylor et al., 2014). Partial dissolution of magnetite in the Bastau section is indicated by lower concentration-dependent values (**Figures 5C,D,E**), and a decrease of the χ_{ARM}/χ and SIRM/χ ratios (**Figures 5J,K**) that is likely related to a stronger contribution of paramagnetic minerals to χ. The proposed dissolution process, which most affected the

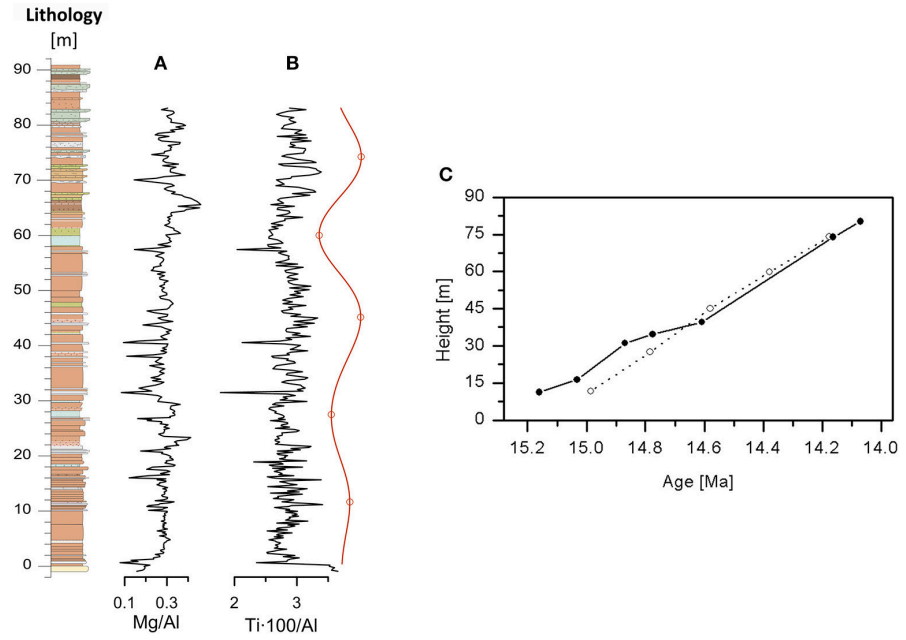

FIGURE 15 | Geochemical proxies along the profile (as in **Figure 5A**): **(A)** Mg/Al ratio and **(B)** Ti/Al ratio with long eccentricity filter output in red (both from Voigt et al., 2017), and **(C)** height vs. age correlation from magnetostratigraphy (black line) and time-series analysis of the Ti/Al ratio (dotted).

wet mudflat facies, likely dissolved the magnetite particles partially (**Figure 10**), shifting the magnetic grain assemblage toward smaller magnetite grains (still larger than SP grains). This change in magnetic grain size is supported by slightly higher ARM/SIRM ratios (**Figure 5L**) in the wet mudflat facies. Dissolution in the water-logged sediment may alter the magnetic grain assemblage and cause poorer remanence preservation and unreliable paleo-directions in the wet mudflat facies.

Hematite dissolution has been observed under reductive conditions (Bloemendal et al., 1993; Liu et al., 2004; Hu et al., 2013), and Yamazaki et al. (2003) found hematite to be more resistive to dissolution than magnetite. The lower HIRM values for the wet mudflat facies (**Figure 5F**) imply the occurrence of partial dissolution of hematite in this facies (**Figure 10**). The steeper slope of the data trend in the HIRM-SIRM-plot at lower SIRM values (**Figure 11A**) supports a higher stability of the hematite fraction compared to magnetite.

SIRM values in **Figure 11A** show a high variability. In principle, the variability could be explained by pronounced variation of detrital input, but this is unlikely the main process (Voigt et al., 2017). Interestingly, the SIRM distribution of specimens with normal polarity directions is shifted to higher SIRM values compared to the specimens with reverse polarity directions (solid curves in **Figure 11A**). Therefore, dissolution of magnetite and hematite grains cannot be the only alteration effect causing secondary magnetizations. The fact that normal polarity samples have higher SIRM values points out the presence of authigenic magnetite that carries a chemical remanent magnetization. Meijers et al. (2016) observed post-depositional partial magnetic overprinting in lacustrine sediments on the Central Anatolian Plateau, associated with removal of primary magnetic grains, neo-formation of magnetite in grayish rocks and precipitation of pigmentary hematite in red and pink clay-rich layers, caused by fluid flow. Magnetite authigenesis may be associated with diagenesis of smectite and illitization (Katz et al., 2000; Tohver et al., 2008). Although much of the illite in the Bastau Fm is of detrital origin (Voigt et al., 2017), pronounced pedogenesis and repeated drying and wetting processes in the wet mudflat facies is highly favorable for slow low-temperature illitization of smectite. The higher NRM/ARM ratio in samples with normal polarity directions compared to the samples with reverse polarity directions (**Figure 11B**) can be explained by authigenic magnetite, which acquired a chemical remanence parallel to the Earth's magnetic field when surpassing the critical grain size (Larson and Walker, 1975). A chemical remanent magnetization of newly formed small magnetite grains is most probably significantly higher than the primary detrital remanent magnetization (Katz et al., 2000). The higher NRM/ARM values are thus interpreted to be indicative for newly formed magnetite (**Figure 10**).

Based on our data, we cannot specify the alteration effect in more detail. However, we can conclude that dissolution and neo-formation of magnetite are likely the key processes in the alteration scenario as indicated by the low concentration dependent parameters in the wet mudflat facies and the higher NRM/ARM ratio in samples with normal polarity directions (**Figure 10**). How and under which conditions the two processes occur in detail, remains an open question that requires further studies.

Because of the interpreted magnetic alteration of the remanence carriers, we suggest to use three criteria (SIRM, HIRM and NRM/ARM ratio) for the selection of the MCC & HCC combined directions, which are less likely affected by (partial) secondary magnetizations. Doing so, one has to notice that the complex interplay and heterogeneity on a small scale compromises the unambiguous identification and selection of samples affected by alteration effects.

Magnetostratigraphy

In order to establish a reliable magnetostratigraphic sequence, we used selection criteria based on the results of remanence analysis and rock magnetic characteristics. Equal area plots of the selections are shown in **Figure 12**.

The results of VGP latitudes along the section based on the HCC only (**Figure 13B**) and the combined MCC & HCC data set (**Figure 13D**) are quite similar (in both plots only specimens meeting the MAD and VGP criteria are included). For further analysis, we use the combined larger data set shown in **Figure 12A** (identical to the one shown in **Figure 4C**). The open circles denoting normal directions within longer intervals of reverse polarity raise issues of the primary origin of these remanences. These remanences mainly correspond to layers of the wet mudflat facies. Since the assignment of the samples into the different facies types is partly difficult (see section Lithofacies Dependence of Rock Magnetic Mineralogy), a general rejection of a facies such as the wet mudflat facies is inappropriate. Thus, in a next step, a selection approach based rock magnetic properties is presented in order to reduce the influence of magnetic alterations and remagnetization.

According to our proposed alteration scenario (**Figure 10**) dissolution and neo-formation of magnetite as well as partial dissolution of hematite caused partial magnetic overprinting in horizons with elevated groundwater availability. Thus, we used rock magnetic properties to identify samples that are likely more affected by secondary magnetization. Based on the assumption that the magnetic alteration caused lower concentration values (SIRM, HIRM) and a higher NRM/ARM ratio (see rock magnetic analyses in section Lithofacies Dependence of Rock Magnetic Mineralogy), samples with the following properties were rejected (**Figures 12B,D**): (1) SIRM $< 1.38 \times 10^{-3}$ Am²/kg below 50 m and SIRM $< 2.53 \times 10^{-3}$ Am²/kg above 50 m; (2) HIRM $< 2.43 \times 10^{-4}$ Am²/kg (3) NRM/ARM > 0.29. The thresholds were determined by median-1σ (SIRM, HIRM) and median $+ 1\sigma$ (NRM/ARM) values. For SIRM two criteria were used for data selection to take into account the higher SIRM values in the upper part of the section. The selection according to NRM/ARM ratios is also in line with the trend of normal and reverse polarity samples shown in **Figure 11B** (i.e., normal polarity samples showing higher NRM/ARM values). The rock magnetic selection criteria remove 93 samples from the MCC & HCC combined data set (**Figures 12B**, **13E**), mostly samples with normal polarity direction (72%) and samples from the wet mudflat facies (56%). Normal polarity samples are suspected to be prime candidates for magnetic overprinting, and thus the higher number of rejected normal polarity samples supports the validity of the rock magnetic selection criteria.

The mean inclination of the reverse polarity directions is $\sim 24^\circ$ lower than the expected Middle Miocene dipole field direction and thus indicate a paleo-remanence influenced by inclination shallowing. Another possible selection approach may employ this interpretation, i.e., the assumption that the reverse polarity directions represent remanences of predominantly primary origin, while normal polarity directions are stronger contaminated by partial secondary magnetization. However, it is difficult to set appropriate criteria for corresponding filtering.

The rock magnetic selection criteria could also be applied to the HCC only. This results in the rejection of 71 samples (179 of 250 samples remaining, see **Figures 12C,D**). Likewise, the selection is effective in reducing the influence of secondary magnetization. The corresponding VGP latitudes in **Figures 13B,C** show a very similar pattern than the MCC & HCC combined data set, with just the reverse polarity interval C5ADr appearing to be shorter. Due to the higher quality and quantity of the MCC & HCC combined data set, we use the MCC & HCC combined result for further interpretations.

With the rock magnetic selection criteria applied to the MCC & HCC combined data set and based on 307 samples, we establish a final magnetostratigraphic sequence, which shows 3 normal and 3 reverse intervals (**Figure 13F**), each interval defined by at least 7 samples. The mean normal direction of all 307 included samples in stratigraphic coordinates is D/I $= 350.3^\circ/53.5^\circ$ ($k = 11.32$, $\alpha_{95} = 2.5^\circ$). We correlate the resulting polarity sequence to the geomagnetic polarity time scale (GPTS) by Gradstein et al. (2012) using the biostratigraphic age of MN4-MN5 (early Miocene, Lucas et al., 2000) at the top of the underlying Aidarly Fm as an anchor. The best match with the reference scale is from the polarity boundary C5Br/C5Bn.2n (15.16 Ma) to the polarity boundary C5ACr/C5ACn (14.07 Ma), as shown in **Figure 13G**.

The sediment accumulation rates (SARs) resulting from this correlation are shown in **Figure 14B** (top). The SAR varies between 3 and 8 cm/ka. Higher SARs occur in intervals where the lithology varies more and coarser grained layers are more pronounced. The mean SAR for the section (6.3 cm/ka) is used to extrapolate the temporal framework of the section at either end.

Out of the 307 samples used to constrain the magnetostratigraphy for the Bastau Fm, 195 are of normal polarity and 112 are of reverse polarity. The mean normal polarity direction is $\sim 19^\circ$ steeper than the mean reverse polarity direction, and the mean declinations differ by $\sim 17^\circ$ from antipodality (**Figure 12B**). Consequently, the reversal test of McFadden and McElhinny (1990) is negative. This indicates still existing unremoved partial magnetic overprinting in the normal polarity directions causing steeper inclinations and declinations tending toward 0° for normal polarity directions (i.e., tending toward the present Earth magnetic field). This effect is known from other continental sedimentary sequences and in the surrounding basins (in the Junggar Basin, Charreau et al., 2005; Subei, Gilder et al., 2001; Tarim Basin, Charreau et al., 2006).

Correlation to the GPTS

The proposed correlation to the GPTS suggests a long reverse interval before the first reversal at the base of the Bastau

Fm. To support this interpretation, we collected additional paleomagnetic samples at the top of the underlying Aidarly Fm (weakly consolidated yellow sandstone). Most layers are much less consolidated and compromise a reliable interpretation. TH and AF demagnetization yielded a complex magnetic behavior with mainly normal polarities. Reverse directions also occur, e.g., from a strongly cemented sandstone layer 7 m below the base of the Bastau Fm. Sandstone is prone to remagnetization and recent overprints, especially weakly consolidated sandstone (Jackson et al., 1993; Kodama, 2012), thus the results from the Aidarly Fm are not considered to be conclusive.

The proposed correlation of the polarity pattern of the Bastau Fm from chron C5B2.2n to chron C5ACr as shown in **Figure 13** results in an age of 15.3–13.9 Ma for the Bastau Fm (ages of the lower and upper ends estimated from linear extrapolation of SARs). The SARs of 3–8 cm/ka (**Figure 14B** top) match well with our field observations of quite continuous sedimentation throughout the section. SAR estimates based on biostratigraphic data are in the range of 5–9 cm/ka and time-series analysis of the Bastau Fm by Voigt et al. (2017) suggests similar SARs. Also, SARs in the range of 6–13 cm/ka were found in other foreland basins of the Tien Shan (Huang et al., 2006; Charreau et al., 2009). An alternative magnetostratigraphic correlation (see **Figure 14A** bottom) matching with the biostratigraphic framework would be between 18 and 16 Ma. However, the resulting SARs show large variation between 2 and 20 cm/ka (**Figure 14B** bottom), and especially the abrupt change to high SAR of 20 cm/ka above the stratigraphic level of 40 m contradicts field observations (Voigt et al., 2017). Other correlations to polarity chrons younger than C5B2.2n-C5ACr principally violates coincidence with the fossil findings from Lucas et al. (2000).

Orbital Control

Orbital forcing of paleoenvironments has been well documented for continental settings (Prokopenko et al., 2006; Vollmer et al., 2008; Abels et al., 2010). Voigt et al. (2017) suggest an orbital control on mudflat deposition in the Bastau Fm. The authors found two dominant cycles in their spectral analysis of geochemical proxies, which they interpret as short (100 ka) and long (405 ka) eccentricity based on its cycle-to-frequency ratio. The Bastau Fm comprises only a small number of 405 ka cycles, the interference of high amplitudes of short eccentricity cycles and minima of long eccentricity causes noisy signals in some intervals, and non-linear feedbacks due to complex interactions of climate and depositional processes have to be taken into account (Hilgen et al., 2015). Although this limits the significance of the cyclostratigraphic interpretation, its principle validity seems reliable. Voigt et al. (2017) suggest the correlation of maxima in the Ti/Al ratio filter outputs to long eccentricity minima (**Figure 15B**). Above the stratigraphic level of 40 m, the correlation is straightforward, whereas below 40 m, i.e., where the depositional variability is the highest, it is more problematic due to the complexity of the signal as described above.

From the spectral analysis of Voigt et al. (2017), we calculated the corresponding SARs, and compared them to the SARs suggested by the magnetostratigraphic correlation (**Figure 15C**). The two curves match well above 40 m but deviate below, i.e., for the lowest (oldest) maxima and minima from the long eccentricity correlation. However, these are the least accurately determined extreme values in the suggested correlation of Voigt et al. (2017). Nevertheless, the SARs are in the same order throughout the section. This supports our interpretation of the magnetic polarity sequence and suggests that the age model developed by our magnetostratigraphic correlation is correct. If the short normal polarity directions within the in the longer reverse intervals in the unfiltered combined data (**Figure 13D**) would be interpreted as valid polarity intervals, the resulting much lower SARs would strongly contradict the SARs obtained from orbital analysis.

With the age model, we can put the succession into the context of the Middle Miocene Climate Transition. Global cooling corresponds with the increasing salinization and the change of magneto-mineralogical properties above 55 m where the lithology changes to saline mudflats and further up to a playa lake.

CONCLUSIONS

The Neogene Aktau Mountains in the Ili Basin, SE Kazakhstan, provide a complex sedimentary record typical for a foreland basin of the Tien Shan Mountains. It is well suited for paleoclimatic research and with the presented magnetostratigraphy may elucidate the role of Central Asia in the Middle Miocene climate evolution. The complex sedimentary setting consists of reddish-colored alluvial floodplain deposits and gray lacustrine deposits. The rocks of the studied sections have been subdivided in three main lithofacies to characterize the depositional variability of the Middle Miocene Bastau Fm (alluvial fan, dry mudflat, and wet mudflat).

Rock magnetic properties of the succession well reflect the depositional variability and allow magnetostratigraphic dating of the Bastau Fm. Stepwise demagnetization revealed a partly complex magnetic behavior with magnetite and hematite as the main magnetic carriers. Thus, detailed rock magnetic analyses were used to analyze the nature of the characteristic remanent magnetization. Remagnetization effects were identified and can be related to intensified evaporative rise of capillary groundwater. The facies dependent remagnetization is best explained by magneto-mineralogical alteration effects, i.e., dissolution of magnetite and hematite and remagnetization due to secondary formed magnetite.

To account for remagnetizations and secondary overprints rock magnetic properties are further used to discriminate remanence directions in order to obtain a reliable magnetostratigraphic result. The presented Middle Miocene magnetostratigraphy provides a robust age model for Bastau Fm with an age from 15.3 to 13.9 Ma.

The age correlation indicates sediment accumulation rates between 3 and 8 cm/ka throughout the section. This is in good agreement with estimates based on biostratigraphic data as well as time-series analysis and corresponds with sedimentation rates found in other foreland basins of the Tien Shan Mountains. Anisotropy of susceptibility results confirm

a detrital sedimentary discharge from the foothills of the Dzhungarian Alatau in the north-west.

Future work should focus on the alteration processes of magnetic minerals, i.e., study authigenic mineral transformations and their effects on remagnetization processes.

AUTHOR CONTRIBUTIONS

All authors substantial contributed to the conception of the work, data acquisition, analysis and interpretation, drafting the work and revising it critically. All gave the final approval of the version to be published and agree to be accountable for all aspects of the work in ensuring that questions related to the accuracy or integrity of any part of the work are appropriately investigated and resolved. VV did the main data acquisition and writing. Analysis, interpretation were mainly done by VV and EA.

ACKNOWLEDGMENTS

This study was financially supported by the Deutsche Forschungsgemeinschaft (DFG grant AP 34/41-1 and VO 687/16-1). We further acknowledge support by the Open Access Publishing Fund of the University Tübingen. Three reviewers helped to improve the manuscript with their constructive comments. We also thank the administration and rangers of the State National Park Altyn Emel for providing access to the Aktau Mountains for geological field work, and Konstantin Kossov and Julia Zhilkina for their support in the field.

REFERENCES

Abels, H., Aziz, H. A., Krijgsman, W., Smeets, S. J. B., and Hilgen, F. J. (2010). Long-period eccentricity control on sedimentary sequences in the continental Madrid Basin (middle Miocene, Spain). *Earth Planet. Sci. Lett.* 289, 220–231. doi: 10.1016/j.epsl.2009.11.011

Bazhanov, V. S., and Kostenko, N. N. (1961). "Geologicheskiy razrez Dzhungarskogo Alatau i ego paleozoologicheskoye obosnovanie [Geological section of Dzhungarian Alatau and its paleontological basis]," in *Materialy po Istorii Fauny i Flory Kazakhstana*, ed I. G. Galuzo (Alma Ata: Akademia Nauk Kazakhskoy SSR), 47–52.

Bloemendal, J., King, J., Hall, F. R., and Doh, S.-J. (1992). Rock magnetism of Late Neogene and Pleistocene deep-sea sediments: relationship to sediment source, diagenetic processes, and sediment lithology. *J. Geophys. Res.* 97, 4361–4375. doi: 10.1029/91JB03068

Bloemendal, J., King, J., Hunt, A., Demenocal, P., and Hayashida, A. (1993). Origin of the sedimentary magnetic record at ocean drilling program sites on the owen ridge, western arabian sea. *J. Geophys. Res.* 98, 4199–4219. doi: 10.1029/92JB02914

Bodina, L. E. (1961). Ostrakody tretichnykh otlozhenii zaisanskoi i iliiskoi depressi [ostracods of tertiary deposits in the zaisan and ili depressions]. *Trudy VNIGRI* 170, 43–153.

Bosboom, R. E., Dupont-Nivet, G., Houben, A. J. P., Brinkhuis, H., Villa, G., Mandic, O., et al. (2011). Late Eocene sea retreat from the Tarim Basin (west China) and concomitant Asian paleoenvironmental change. *Palaeogeogr. Palaeoclimatol. Palaeoecol.* 299, 385–398. doi: 10.1016/j.palaeo.2010.11.019

Bowles, J., Jackson, M., Chen, A., and Solheid, P. (2009). Interpretation of low-temperature data, part 1: Superparamagnetism and paramagnetism. *IRM Quart.* 19. 7–11.

Butler, R.F., (1992) *Paleomagnetism: Magnetic Domains to Geologic Terranes*. Boston, MA: Blackwell Publishing.

Canfield, D. E., and Berner, R. A. (1987). Dissolution and pyritization of magnetite in anoxic marine sediments. *Geochim. Cosmochim. Acta* 51, 645–659. doi: 10.1016/0016-7037(87)90076-7

Caves, J. K., Winnick, M. J., Graham, S. A., Sjostrom, D. J., Mulch, A., and Chamberlain, C. P. (2015). Role of the westerlies in Central Asia climate over the Cenocoic. *Earth Planet. Sci. Lett.* 428, 33–43. doi: 10.1016/j.epsl.2015.07.023

Charreau, J., Chen, Y., Gilder, S., Barrier, L., Dominguez, S., Augier, R., et al. (2009). Neogene uplift of the Tian Shan Mountains observed in the magnetic record of the Jingou River section (northwest China). *Tectonics* 28:TC2008. doi: 10.1029/2007TC002137

Charreau, J., Chen, Y., Gilder, S., Dominguez, S., Avouac, J.-P., Sen, S., et al. (2005). Magnetostratigraphy and rock magnetism of the Neogene Kuitun He section (northwest China): implications for Late Cenozoic uplift of the Tianshan mountains, *Earth Planet. Sci. Lett.* 230, 177–192. doi: 10.1016/j.epsl.2004.11.002

Charreau, J., Gilder, S., Chen, Y., Dominguez, S., Avouac, J.-P., Sen, S., et al. (2006). Magnetostratigraphy of the Yaha section, Tarim Basin (China): 11 Ma acceleration in erosion and uplift of the Tian Shan mountains. *Geology* 34, 181–184. doi: 10.1130/G22106.1

Demory, F., Oberhänsli, H., Nowaczyk, N. R., Gottschalk, M., Wirth, R., and Naumann, R. (2005). Detrital input and early diagenesis in sediments from Lake Baikal revealed by rock magnetism. *Glob. Planet. Change* 46, 145–166. doi: 10.1016/j.gloplacha.2004.11.010

Deng, C. L., Liu, Q. S., Wang, W., and Liu, C. C. (2007). Chemical overprint on the natural remanent magnetization of a subtropical red soil sequence in the Bose Basin, southern China. *Geophys. Res. Lett.* 34:L22308. doi: 10.1029/2007GL031400

Deocampo, D. M. (2015). Authigenic clay minerals in lacustrine mudstones. *Geol. Soc. Am. Spec. Paper*. 515, 45–64. doi: 10.1130/2015.2515(03)

Dzhamangaraeva, A. K. (1997). Pliocene charophytes from Aktau Mountain, southeastern Kazakhstan. *Geobios* 30, 475–479. doi: 10.1016/S0016-6995(97)80115-5

Felletti, F., Dall'Olio, E., and Muttoni, G. (2016). Determining flow directions in turbidites: an integrated sedimentological and magnetic fabric study of the Miocene Marnoso Arenacea Formation (northern Apennines, Italy). *Sediment. Geol.* 335, 197–215. doi: 10.1016/j.sedgeo.2016.02.009

Fisher, R. A. (1953). Dispersion on a sphere. *Proc. R. Soc. Lond. A* 217, 295–302. doi: 10.1098/rspa.1953.0064

Florindo, F., Roberts, A., and Palmer, M. R. (2003). Magnetite dissolution in siliceous sediments. *Geochem. Geophys. Geosyst.* 4:1053. doi: 10.1029/2003GC000516

Fluteau, F., Ramstein, G., and Besse, J. (1999). Simulating the evolution of the Asian and African monsoons during the past 30 Myr using an atmospheric general circulation model. *J. Geophys. Res.* 104, 11995–12018. doi: 10.1029/1999JD900048

Gale, A. S., Huggett, J. M., Pälike, H., Laurie, E., Hailwood, E. A., and Hardenbol, J. (2006). Correlation of Eocene-Oligocene marine and continental records: orbital cyclicity, magnetostratigraphy and sequence stratigraphy of the Solent Group, Isle of Wight, UK. *J. Geol. Soc. Lond.* 163, 401–415. doi: 10.1144/0016-764903-175

Gilder, S., Chen, Y., and Sen, S. (2001). Oligo-Miocene magnetostratigraphy and rock magnetism of the Xishuigou section, Subei (Gansu Province, western China) and implications for shallow inclinations in central Asia. *J. Geophys. Res.* 106, 30505–30521. doi: 10.1029/2001JB000325

Gradstein, F. M., Ogg, J. G., Schmitz, M., and Ogg, G. (2012). *The Geologic Time Scale 2012*. Boston, MA: Elsevier B.V.

Guo, Z. T., Ruddiman, W. F., Hao, Q. Z., Wu, H. B., Qiao, Y. S., Zhu, R. X., et al. (2002). Onset of Asian desertification by 22 Myr ago inferred from loess deposits in China. *Nature* 416, 159–163. doi: 10.1038/416159a

Hays, J. D., Imbrie, J., and Shackleton, N. J. (1976). Variations in the Earth's orbit: pacemaker of the ice ages. *Science* 194, 1121–1132. doi: 10.1126/science.194.4270.1121

Herb, C., Appel, E., Voigt, S., Koutsodendris, A., Pross, J., Zhang, W., et al. (2015). Orbitally tuned age model for the late Pliocene–Pleistocene lacustrine

succession of drill core SG-1 from the western Qaidam Basin (NE Tibetan Plateau). *Geophys. J. Int.* 200, 35–51. doi: 10.1093/gji/ggu372

Hilgen, F. J., Hinnov, L. A., Abdul Aziz, H., Abels, H. A., Batenburg, S., Bosmans, J. H. C., et al. (2015). Stratigraphic continuity and fragmentary sedimentation: the success of cyclostratigraphy as part of integrated stratigraphy. *Geol. Soc. Lond. Spec. Publ.* 404, 157–197. doi: 10.1144/SP404.12

Hounslow, M. W., and Nawrocki, J. (2008). Palaeomagnetism and magnetostratigraphy of the Permian and Triassic of Spitsbergen: a review of progress and challenges. *Polar Res.* 27, 502–522. doi: 10.1111/j.1751-8369.2008.00075.x

Hu, P., Liu, Q., Torrent, J., Barrón, V., and Jin, C. (2013). Characterizing and quantifying iron oxides in Chinese loess/paleosols: implications for pedogenesis. *Earth Planet. Sci. Lett.* 369-370, 271–283. doi: 10.1016/j.epsl.2013.03.033

Hu, S. Y., Goddu, S. R., Appel, E., Verosub, K., Yang, X. D., and Wang, S. M. (2005). Palaeoclimatic changes over past one million years derived from lacustrine sediments of Heqing Basin (Yunnan, China). *Quatern. Int.* 136, 123–129. doi: 10.1016/j.quaint.2004.11.013

Hu, S. Y., Goddu, S. R., Herb, C., Appel, E., Gleixner, G., Wang, S. M., et al. (2015). Climate variability and its magnetic response recorded in a lacustrine sequence in Heqing basin at the SE Tibetan Plateau since 900 ka. *Geophys. J. Int.* 201, 444–458. doi: 10.1093/gji/ggv033

Huang, B. C., Piper, J. D. A., Peng, S. T., Liu, T., Li, Z., Wang, Q. C., et al. (2006). Magnetostratigraphic study of the Kuche Depression, Tarim Basin, and Cenozoic uplift of the Tian Shan Range, Western China. *Earth Planet. Sci. Lett.* 251, 346–364. doi: 10.1016/j.epsl.2006.09.020

Itoh, Y., Tamaki, M., and Takano, O. (2013). "Rock Magnetic Properties of Sedimentary Rocks in Central Hokkaido - Insights into Sedimentary and Tectonic Processes on an Active Margin," in *Mechanism of Sedimentary Basin Formation - Multidisciplinary Approach on Active Plate Margins*, ed Y. Itoh (Rijeka: InTech), 233–253.

Jackson, M., Borradaile, G., Hudleston, P., and Banerjee, S. (1993). Experimental deformation of synthetic magnetite-bearing calcite sandstones: effects on remanence, bulk magnetic properties, and magnetic anisotropy. *J. Geophys. Res.* 98, 383–401. doi: 10.1029/92JB01028

Jelinek, V. (1981). Characterization of the magnetic fabrics of rocks. *Tectonophysics* 79, 63–67. doi: 10.1016/0040-1951(81)90110-4

Jolivet, M., Dominguez, S., Charreau, J., Chen, Y., Li, Y., and Wang, Q. (2010). Mesozoic and Cenozoic tectonic history of the central Chinese Tian Shan: Reactivated tectonic structures and active deformation. *Tectonics* 29:TC6019. doi: 10.1029/2010TC002712

Jordanova, N. (2016). *Soil Magnetism: Applications in Pedology, Environmental Science and Agriculture*. Academic Press.

Karlin, R., and Levi, S. (1985). Geochemical and sedimentological control of the magnetic properties of hemipelagic sediments. *J. Geophys. Res.* 90, 10373–10392. doi: 10.1029/JB090iB12p10373

Katz, B., Elmore, R. D., Cogoini, M., Engel, M. H., and Ferry, S. (2000). Associations between burial diagenesis of smectite, chemical remagnetization, and magnetite authigenesis in the Vocontian trough, SE France. *J. Geophys. Res.* 105, 851–868. doi: 10.1029/1999JB900309

Kirschvink, J. L. (1980). The least squares line and plane and the analysis of paleomagnetic data. *Geophys. J. R. Astron. Soc.* 62, 699–712. doi: 10.1111/j.1365-246X.1980.tb02601.x

Kodama, K. P. (2012). *Paleomagnetism of Sedimentary Rocks: Process and Interpretation*. Oxford: Wiley-Blackwell.

Kodama, K. P., and Hinnov, L. A. (2015). *Rock magnetic cyclostratigraphy*. Oxford: Wiley-Blackwell.

Kordikova, E. G. (2000). Insectivora (Mammalia) from the Lower Miocene of the Aktau Mountains, South-Eastern Kazakhstan. *Senckenb. Lethaea* 80, 67–79. doi: 10.1007/BF03043665

Kordikova, E. G., and de Bruijn, H. (2001). Early Miocene Rodents from the Aktau Mountains (South-Eastern Kazakhstan). *Senckenb. Lethaea* 81, 391–405. doi: 10.1007/BF03042791

Kordikova, E. G., and Mavrin, A. V. (1996). Stratigraphy and Oligocene-Miocene mammalian biochronology of the Aktau Mountains, Dzhungarian Alatau range, Kazakhstan. *Palaeovertebrata* 25, 141–174.

Krijgsman, W., Delahaije, W., Langreis, C., and de Boer, P. L. (1999). Paleomagnetism and astronomically induced cyclicity of the Armantes section; a Miocene continental red sequence in the Calatayud-Daroca basin (Central Spain). *Acta Geol. Hispanica* 32, 201–219.

Krijgsman, W., Hilgen, F. J., Langereis, C., Santarelli, A., and Zachariasse, W. J. (1995). Late Miocene magnetostratigraphy, biostratigraphy and cyclostratigraphy in the Mediterranean. *Earth Planet. Sci. Lett.* 136, 475–494. doi: 10.1016/0012-821X(95)00206-R

Kruiver, P. P., Dekkers, M. J., and Heslop, D. (2001). Quantification of magnetic coercivity by the analysis of acquisition curves of isothermal remanent magnetisation. *Earth Planet. Sci. Lett.* 189, 269–276. doi: 10.1016/S0012-821X(01)00367-3

Kruiver, P. P., Langreis, C. G., Dekker, M. J., and Krijgsman, W. (2003). Rock-magnetic properties of multicomponent natural remanent magnetization in alluvial red beds (NE Spain). *Geophys. J. Int.* 153, 317–332. doi: 10.1046/j.1365-246X.2003.01880.x

Larson, E. D., and Walker, T. R. (1975). Development of chemical remanent magnetization during early stages of red-bed formation in Late Cenozoic sediments, Baja, California. *Geol. Soc. Am. Bull.* 86, 639–650. doi: 10.1130/0016-7606(1975)86<639:DOCRMD>2.0.CO;2

Liu, J., Zhu, R., Roberts, A., Li, S., and Chang, J. (2004). High-resolution analysis of early diagenetic effects on magnetic minerals in post-middle-Holocene continental shelf sediments from the Korea Strait. *J. Geophys. Res.* 109:B03103. doi: 10.1029/2003JB002813

Lu, H., Wang, X., and Li, L. (2010). "Aeolian sediment evidence that global cooling has driven late Cenozoic stepwise aridification in central Asia," in *Monsoon Evolution and Tectonics-Climate Linkage in Asia*. ed P. D. Clift, R. Tada, and H. Zheng (Geological Society, Special Publications), 29–44.

Lucas, S. G., Aubekerov, B. Z., Dzhamangaraeva, A. K., Bayshashov, B. U., and Tyutkova, L. A. (2000). "Cenozoic lacustrine deposits of the Ili basin, southeastern Kazakhstan," in *Lake Basins Through Space and Time,* ed E. Gierlowski-Kordesch, K. R. Kelts (AAPG Studies in Geology), 59–64.

Lucas, S. G., Bayshashov, B. U., Tyutkova, L. A., Zhamangara, A. K., and Aubekerov, B. Z. (1997). Mammalian biochronology of the Paleogene-Neogene boundary at Aktau Mountain, eastern Kazakhstan. *Paläontol. Z.* 71, 305–314. doi: 10.1007/BF02988498

McCabe, C., and Elmore, R. D. (1989). The occurrence and origin of Late Paleozoic remagnetization in the sedimentary rocks of North America. *Rev. Geophys.* 27, 471–493. doi: 10.1029/RG027i004p00471

McFadden, P. L., and McElhinny, M. W. (1990). Classification of the reversal test in paleomagnetism. *Geophys. J. Int.* 130, 725–729. doi: 10.1111/j.1365-246X.1990.tb05683.x

Meijers, M. J. M., Strauss, B. E., Özkaptan, M., Feinberg, J. M., Mulch, A., and Whitney, D. L., Kaymakci, N. (2016). Age and paleoenvironmental reconstruction of partially remagnetized lacustrine sedimentary rocks (Oligocene Aktoprak basin, central Anatolia, Turkey). *Geochem. Geophys. Geosyst.* 17, 914–939. doi: 10.1002/2015GC006209

Miao,Y., Herrmann, M., Wu, F., and Yan, X., Yang, S. (2012). What controlled Mid–Late Miocene long-term aridification in Central Asia? - Global cooling or Tibetan Plateau uplift: a review. *Earth Sci. Rev.* 112, 155–172. doi: 10.1016/j.earscirev.2012.02.003

Olsen, P. E., and Kent, D. V. (1996). Milankovitch climate forcing in the tropics of Pangea during the Late Triassic. *Palaeogeogr. Palaeoclimatol. Palaeoecol.* 122, 1–26. doi: 10.1016/0031-0182(95)00171-9

Prokopenko, A. A., Hinnov, L., Williams, D. F., and Kuzmin, M. I. (2006). Orbital forcing of continental climate during the Pleistocene: a complete astronomically tuned climatic record from Lake Baikal, SE Siberia. *Quat. Sci. Rev.* 25, 3431–3457. doi: 10.1016/j.quascirev.2006.10.002

Roberts, A. P. (2015). Magnetic mineral diagenesis. *Earth Sci. Rev.* 151, 1–47. doi: 10.1016/j.earscirev.2015.09.010

Roberts, A. P., Florindo, F., Larrasoaña, J. C., O'Regan, M. A., and Zhao, X. (2010). Complex polarity pattern at the former Plio–Pleistocene global stratotype section at Vrica (Italy): remagnetization by magnetic iron sulfides. *Earth Planet. Sci. Lett.* 292, 98–111. doi: 10.1016/j.epsl.2010.01.025

Roberts, A. P., Tauxe, L., and Heslop, D. (2013). Magnetic paleointensity stratigraphy and high-resolution Quaternary geochronology: successes and future challenges. *Quat. Sci. Rev.* 61, 1–16. doi: 10.1016/j.quascirev.2012.10.036

Sun, M., Zhang, X., Tian, M., Liu, R., He, Z., Qi, L., et al. (2017). Loess deposits since early Pleistocene in northeast China and implications for desert evolution in east China. *J. Asian Earth Sci.* 155, 164-173. doi: 10.1016/j.jseaes.2017.09.013

Tang, Z., Ding, Z., White, P. D., Dong, X., Ji, J., Jiang, H., et al. (2011). Late Cenozoic central Asian drying inferred from a palynological record from the northern Tian Shan. *Earth Planet. Sci. Lett.* 302, 439–447. doi: 10.1016/j.epsl.2010.12.042

Tang, Z., Huang, B., Dong, X., Ji, J., and Ding, Z. (2012). Anisotropy of magnetic susceptibility of the Jingou River section: Implications for late Cenozoic uplift of the Tian Shan. *Geochem., Geophys. Geosyst.* 13:Q03022. doi: 10.1029/2011GC003966

Tarling, D. H., and Hrouda, F. (1993). *The Magnetic Anisotropy of Rocks*. London: Chapman & Hall.

Tauxe, L., and Kent, D. V. (1984). Properties of a detrital remanence carried by haematite from study of modern river deposits and laboratory redeposition experiments. *Geophys. J. R. Astr. Soc.* 77, 543–561. doi: 10.1111/j.1365-246X.1984.tb01909.x

Tauxe, L., Kent, D. V., and Opdyke, N. D. (1980). Magnetic components contributing to the NRM of Middle Siwalik red beds. *Earth Planet. Sci. Lett.* 47, 279–284. doi: 10.1016/0012-821X(80)90044-8

Taylor, S. N., Lagroix, F., Rousseau, D.-D., and Antoine, P. (2014). Mineral magnetic characterization of the Upper Pleniglacial Nussloch loess sequence (Germany): an insight into local environmental processes. *Geophys. J. Int.* 199, 1463–1480. doi: 10.1093/gji/ggu331

Tohver, E., Weil, A. B., Solum, J. G., and Hall, C. M. (2008). Direct dating of carbonate remagnetization by $^{40}Ar/^{39}Ar$ analysis of the smectite–illite transformation. *Earth Planet. Sci. Lett.* 274, 524–530. doi: 10.1016/j.epsl.2008.08.002

Torsvik, T. H., van der Voo, R., Preeden, U., Mac Niocaill, C., Steinberger, B., Doubrovine, P. V., et al. (2012). Phanerozoic polar wander, palaeogeography and dynamics. *Earth Sci. Rev.* 114, 325–368. doi: 10.1016/j.earscirev.2012.06.007

van der Voo, R., and Torsvik, T. H. (2012). "The history of remagnetization of sedimentary rocks: deceptions, developments and discoveries," in *Remagnetization and Chemical Alteration of Sedimentary Rocks*, eds R. D. Elmore, A. R. Muxworthy, M. Aldana, and M. Mena (Geological Society, London, Special Publications), 23–53

Voigt, S., Weber, Y., Frisch, K., Bartenstein, A., Hellwig, A., Petschick, R., et al. (2017). Climatically forced moisture supply, sediment flux and pedogenesis in Miocene mudflat deposits of south-east Kazakhstan, Central Asia. *Deposit. Rec.* 3, 209–232. doi: 10.1002/dep2.34

Vollmer, T., Werner, R., Weber, M., Tougiannidis, N., Röhling, H.-G., and Hambach, U. (2008). Orbital control on Upper Triassic Playa cycles of the Steinmergel-Keuper (Norian): a new concept for ancient playa cycles. *Palaeogeogr. Palaeoclimatol. Palaeoecol.* 267, 1–16. doi: 10.1016/j.palaeo.2007.12.017

Yamazaki, T., Abdeldayem, A., and Ikehara, K. (2003). Rock-magnetic changes with reduction diagenesis in Japan Sea sediments and preservation of geomagnetic secular variation in inclination during the last 30,000 years. *Earth Planets Space* 55, 327–340. doi: 10.1186/BF03351766

Zhang, C., Paterson, G. A., and Liu, Q. (2012). A new mechanism for the magnetic enhancement of hematite during heating: the role of clay minerals. *Stud. Geophys. Geod.* 56, 845–860. doi: 10.1007/s11200-011-9018-4

Zhang, W. L., Appel, E., Fang, X. M., Yan, M. D., Song, C. H., and Cao, L. W. (2012). Paleoclimatic implications of magnetic susceptibility in Late Pliocene-Quaternary sediments from deep drilling core SG-1 in the western Qaidam Basin (NE Tibetan Plateau). *J. Geophys. Res.* 117:B06101. doi: 10.1029/2011JB008949

Zhisheng, A., Kutzbach, J. E., Prell, W. L., and Porter, S. C. (2001). Evolution of Asian monsoons and phased uplift of the Himalaya-Tibetan Plateau since late Miocene times. *Nature* 411, 62–66. doi: 10.1038/35075035

Conflict of Interest Statement: The authors declare that the research was conducted in the absence of any commercial or financial relationships that could be construed as a potential conflict of interest.

Chapter 4

Rock magnetic signature of a playa cycle in Central Asia and environmental implications

Author	Author position	Scientific ideas	Data generation	Analysis & interpretation	Paper writing
Verena Verestek	1	50%	80%	50%	65%
Erwin Appel	2	30%	-	25%	15%
Konstantin Frisch	3	10%	-	15%	15%
Silke Voigt	4	10%	20%	10%	5%
Status in publication process:		in review			

Rock magnetic signature of a playa cycle in Central Asia and environmental implications

Verena Verestek[1]*, Erwin Appel[1], Konstantin Frisch[2], Silke Voigt[2]

[1] *Department of Geosciences, University Tübingen, Hölderlinstraße 12, 72074 Tübingen, Germany*

[2] *Institute of Geosciences, Goethe University Frankfurt, Altenhöferallee 1, 60438 Frankfurt, Germany*

* corresponding author: verena.verestek@uni-tuebingen.de

Abstracts

The increased aridification of Central Asia during the Miocene coincides in time with lake formations and playa evolutions in the region. However, Miocene continental climate dynamics and the forcing of aridification are still not well constrained. Neogene lacustrine mudflat deposits in the Ili Basin in southeast Kazakhstan provide a well-exposed paleoclimate archive. Here, we present a detailed rock magnetic study of a middle Miocene playa cycle deposited in a closed basin. We use high-resolution rock magnetic parameters, lithological studies and geochemistry to reconstruct the playa environment and the depositional conditions. The rock magnetic mineralogy of the playa cycle is controlled by hematite and two fine-grained magnetite phases. Increased magnetic concentrations occur during dry mudflat conditions, with a lower groundwater table and increased aridity. The underlying processes controlling the observed variation in magnetic concentrations are a complex interplay of diagenetic processes during and after deposition. Authigenic formation of both magnetite phases, one formed before and the other after sediment consolidation is supported as the most likely scenario by the data. Early diagenetic formation of fine-grained magnetite by microbial activity is followed by post-depositional formation of a secondary fine-grained magnetite phase. The rock magnetic parameters such as the magnetic concentration dependent parameters, ARM/SIRM and s-ratio indicate a sensitive record of (ground)water availability and aridity changes in the Ili Basin. We suggest that they can serve as effective proxy indices for detailed paleoenvironment reconstruction for playa evolution, not only in the middle Miocene Ili Basin but also in comparable floodplain/playa lake settings.

1 Introduction

Playas are saline shallow water bodies that form in arid and semi-arid basins where evaporation exceeds precipitation (Briere, 2000; Roy et al., 2008). The composition of the playa brine and the precipitated minerals from the brine are controlled by factors such as the catchment lithology, water chemistry, selective precipitation of evaporite minerals with varying evaporation, dissolution and re-precipitation of evaporites, seepage loss and reduction of sulphate during anoxic deposition conditions (Rosen, 1994; Roy et al., 2008 and references therein). Thus in sedimentological studies, playa sediments are widely used to reconstruct paleo-environment and paleo-hydrology, and to study geochemical processes during the formation of evaporites (Bowler and Teller, 1986; Schütt et al., 2000; Roy et al., 2008; Huerta et al., 2010). Rock magnetism of playa deposits

received less attention. Often playa sediments are a small part within the studied section and were not analyzed in much detail, e.g. in Northern Spain (Abdul Aziz et al., 2000), the Tibetan Plateau (Zhang et al., 2012; Fang et al., 2015), the Indian Thar Desert (Deotare et al., 2004), and Death Valley (Liddicoat et al., 1980; Pluhar et al., 1992). In this study, we present combined rock magnetic and geochemical data of a continuously sampled playa cycle from the Neogene succession exposed in the Aktau Mountains in southeast Kazakhstan. During the Cenozoic, Central Asia witnessed a general trend of aridification (Guo et al., 2002; Tang et al., 2011; Caves et al., 2015). Global cooling, Paratethys retreat, India's collision with Asia and associated mountain uplift largely influenced the climate evolution in Central Asia (Ramstein et al., 1997; Guo et al., 2002; Tang et al., 2011; Miao et al., 2012). Loess, alluvial, lacustrine and playa deposits are widespread in Cenozoic deposits around the region. The Aktau Mountains offer a great insight into the paleo-depositional environment of the Neogene. In the middle Miocene Koktal Formation (Fm) recurring playa cycles dominate the lithology revealing cycling water availability conditions during depositions (Frisch et al., 2018). Rock magnetic methods are used to determine concentration, mineralogy and grain-size of the magnetic phases in different stages of the playa cycle. The variations in these parameters can often be used as proxies for paleo-environmental changes in a sedimentary basin and/or the surrounding catchment area (Sagnotti et al., 1998; Hu et al., 2002; Evans & Heller 2003; Rosenbaum & Reynolds 2004; Kodama 2012). Magnetic susceptibility χ has been proposed as a proxy for lake level and drier/wetter conditions under humid conditions, e.g. for Lake Baikal (Peck et al., 1994) and pluvial lakes in Oregon, USA (Rosenbaum et al., 1996; Negrini et al., 2000). The authors reported similar behavior of other magnetic concentration dependent parameters such as anhysteretic remanent magnetization and saturation magnetization. In more arid conditions, it was shown that χ is indicative for past dryness fluctuations in the Qaidam Basin on the Tibetan Plateau (Herb et al., 2013, 2015). An approach to link rock magnetic parameters and depositional environment in a non-evaporative alluvial-palustrine setting can be found in Kruiver et al. (2002). Here, we show that the magnetic concentration dependent parameters are sensitive of the varying groundwater table and lake level fluctuations (referred to as water availability in the following) under semi-arid to arid conditions in a playa cycle.

2 Geologic setting

The Aktau Mountains are located in the Ili Basin at the border of southeast Kazakhstan and Xinjiang Province (China) in Central Asia (44°00′20.3″N 79°14′40.9″E, Fig. 1a). The exceptionally well exposed Cenozoic sediments are associated with an asymmetrical, gently north dipping anticline that mainly comprises alluvial, playa, lacustrine and fluvial deposits (Frisch et al., 2018, Lucas et al., 1997). The Neogene lithology can be divided into five stratigraphic formations (Fm) as shown in Fig. 1b (Voigt et al., 2017). The succession was dated using bio-, cyclo- and magnetostratigraphic constraints (Bazhanov & Kostenko, 1961; Kordikova & Mavrin, 1996; Dzhamangaraeva, 1997; Lucas et al., 1997, 2000; Kordikova, 2000; Kordikova & de Bruijn, 2001; Voigt et al., 2017; Verestek et al., 2018). The parent material of the Neogene alluvial-lacustrine sediments stems from Permo-Carboniferous rocks of the Central Asian Orogenic Belt (Kröner et al., 2014; Frisch et al., 2018).

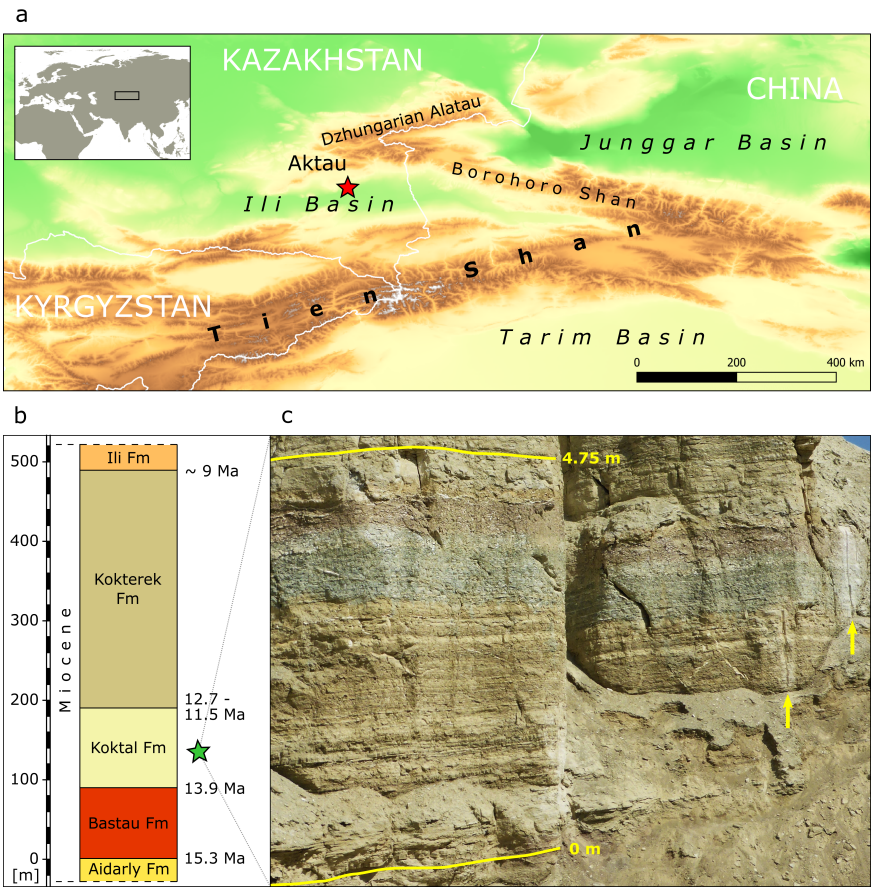

Figure 1: (a) Topographic map of Central Asia showing the location of the Aktau Mountains (red star) and the Ili Basin (modified after Amante & Eakins, 2009). (b) Stratigraphic overview of the Neogene Aktau Mountains and the marked position of the playa cycle (green star). Age constraints are after biostratigraphic data of Bazhanov & Kostenko (1961) and Dzhamangaraeva (1997), sedimentation rate estimates of Voigt et al. (2017) and magnetostratigraphic data of Verestek et al. (2018). (c) Outcrop photograph of the playa cycle (base and top are marked in yellow). Two of the vertical slits from the sample collection are marked with yellow arrows

The studied playa cycle is a 4.5 m-thick succession in the Koktal Fm (Fig. 1c) and mainly composed of mudstones, marls, limestones and gypcretes (Fig. 2a) of middle Miocene age. A detailed description of the lithology of the Koktal Fm can be found in Frisch et al. (2018), where the playa cycle represents the horizon between 136.8 - 141.3 m. A lithologic log of the playa cycle is shown in Fig. 2a. In the lower part of the playa cycle, light brown-gray marls and limestones devoid of evaporites alternate with carbonates yielding abundant sulphate nodules and lenses. Three prominent limestone beds occur between 2.3 - 2.75 m (Beds 5, 7, 9). Above 2.80 m, the stratification alters to thick structureless gray-greenish marls (Bed 4) and reddish mudstone (Bed 3) followed by yellowish-brownish mudstone (Bed 2). Gypsum occurs as lenticular crystals and nodules within the sediment and forms thin beds of massive sulphate (gypsarenites in Bed 23) and a massive gypcrete crust at the top of the playa cycle (Bed 1).

3 Sampling and Methods

A 4.5 m-thick playa succession was sampled. Using a blade cutter, the samples were cut out continuously in the field (in long slits in the outcrop wall, Fig. 1c) and sub-sampled into cubic specimens of ~2 cm sides in the laboratory. A total of 203 samples was obtained covering ~90 % of the entire sequence (~10 % were lost due to cutting).

Natural remanent magnetization (NRM) and anhysteretic remanent magnetization (ARM) were measured with a 2G Enterprises DC-SQUID magnetometer. The ARM was imparted by applying a 100 mT peak alternating field and a biasing 50 μT direct field with an integrated degausser. Isothermal remanent magnetization (IRM) was imparted with a Magnetic Measurements PM9 pulse magnetizer and measured with a Molspin spinner magnetometer. The IRM acquired at fields of 1 T is considered as saturation magnetization (SIRM). The hard IRM (HIRM=(SIRM+IRM$_{-300mT}$)/2) and a s-ratio (s=(1-IRM$_{-300mT}$/SIRM)/2 after Bloemendal et al., 1992) were determined from the SIRM and backfield IRM at -300 mT. IRM acquisition curves of representative 20 samples were measured and analyzed with MAX UnMix (Maxbauer et al., 2016b). In this end-member analysis, different magnetic mineral phases are characterized by their contribution to SIRM, the half-acquisition field $B_{1/2}$ and the width of the distribution (dispersion parameter DP). Magnetic susceptibility (mass-specific χ) was measured at two frequencies (976 Hz and 15,616 Hz) using an AGICO MFK1-FA Kappabridge. The frequency dependence was quantified by the percentage difference (χ_{fd}%) and the absolute difference (χ_{fd}). For thermomagnetic runs of magnetic susceptibility (χ-T curves), sample powder of representative samples was heated up to 700 °C, and then cooled down to room temperature (in air). Anisotropy of magnetic susceptibility (AMS) was determined using a 3D-rotator. The degree of anisotropy (P_j) and the shape (T) of the AMS tensor were calculated after Jelinek (1981). We also performed hysteresis measurements with a PMC MircoMag 2900, but due to the low intensity of small sub-samples (~2 mg) the obtained curves can be hardly interpreted, and are thus not further discussed.

All rock magnetic measurements were conducted in the laboratory of Tübingen University.

The elemental composition of the sediments was measured at Goethe University in Frankfurt with a handheld X-ray fluorescence (XRF) spectrometer (Delta Professional by Olympus NDT). XRF scanning allows non-destructive determination of major and minor elements at the surface of the cubic samples and was performed through a SPEX 3520 Polypropylene® thin film. Data collection was achieved over a 1 cm^2 area using two beams with 20 s count time at 40 kV and 50 s count time at 10 kV, respectively. Raw element concentrations of Si, Ti, Fe, Zr, Ca, S, Cl, Mg, Mo and U are given in percentage or ppm calculated by the internal software using the mode for rock geochemistry. These data are uncorrected for porosity, wherefore only relative abundances and variations are considered for the discussion. The relative standard deviation of repeated standard measurements was less than 5 %. Although this method is semi-quantitative, it provides useful results and implications on deposition and paleo-environmental conditions.

4 Lithofacies

The hydrological conditions in the middle Miocene part of the Aktau succession are assumed to reflect a discharge playa setting (Rosen, 1994). Accordingly, the groundwater table is controlled by the balance between the positive net evaporation in the basin center and the aquifer recharge by groundwater seepage and surface run-off from the nearby mountains (catchment area). Playa lakes are formed either during times of high water availability when the groundwater table rises above the sediment surface and or by ponding of flood water after run-off events. Changing groundwater levels can be recorded sensitively by playa sediments (Frisch et al., 2018). Based on lithology, evaporite occurrences and morphology, three lithofacies types are defined which describe the position of the (ground)water table relative to the sediment surface. The definition of the lithofacies types and the interpretation of the sedimentary features follows the alluvial-lacustrine facies model for the Aktau succession established by Frisch et al. (2018). Here, we differentiate between the dry saline mudflat, wet saline mudflat and ephemeral playa lake facies, the changes in lithofacies are shown in Fig. 2b.

4.1 Lithofacies

The dry saline mudflat facies includes yellowish-brownish, rarely greenish carbonates and red mudstones. Evaporites occur as irregular oriented, whitish single lenses, rosettes and nodules of sulphate, generally less than 5 cm in size, or as massive, grey sulphate beds (gypcretes). Based on the sulphate morphologies, which are indicative for intra-sediment gypsum precipitated above the groundwater table in the capillary zone, this lithofacies reflects the lowest position of the groundwater table. The groundwater table is generally below the sediment surface, however the extent of the capillary zone fluctuated and thus pore water saturation and salinity varied. Frequent sediment infiltration by meteoric water (i.e. flood water or direct precipitation), alternating with a re-establishment of the capillary groundwater rise promoted evaporite alteration (dissolution, recrystallization) and led to nodule and gypcrete formation (Watson, 1985; Frisch et al., 2018). The sulphate content of gypcretes increases with time (Frisch et al., 2018) starting with weakly developed gypcretes (e.g. Beds 14, 19 and 22) and reaching mature crusts (Beds 1 and 2).

The wet saline mudflat facies consists of yellowish-brownish, rarely greenish marls with layered whitish single lenses, rosettes and nodules of sulphate (less than 5 cm in size), partly grading into layers of finely dispersed, diffuse sulphate. Evaporite morphologies indicate a groundwater table close to, or at the sediment surface. Sulphates are mainly precipitated in a shallow capillary zone directly below the sediment surface. The high groundwater table stabilizes the capillary zone, thus infiltration of freshwater during and after floods is less common compared to the dry saline mudflat. This prevents substantial haloturbation and gypcrete formation and preserves layered sulphates. Still ephemeral desiccation or influx of freshwater in the upper-most centimeters of sediment may occur. In this respect, the lower half of Bed 4 is exceptional since sediment crack-filling evaporites, similar to evaporite polygons found on modern salt pan surfaces, indicate a constant feed of saline groundwater up to the sediment surface (Lowenstein & Hardie, 1985).

The ephemeral playa lake facies comprises yellowish-brownish limestones (mostly devoid of sulphates) and thin beds of massive sulphate (gypsarenites). This lithofacies reflects subaqueous deposition in the central parts of the basin. Following heavy rainfall in the catchment area, the surface run-off leaches evaporites at the

basin margin and accumulates in the basin center, where it forms a shallow lake with moderate to high salinity. After the initial settling of suspension load mud, the flood water becomes evaporatively enriched, precipitating first carbonate (as limestones, e.g. Beds 7, 9 and 16), followed by sulphate (as gypsarenites, Bed 23) (Eugster & Hardie, 1978; Hardie et al., 1978, Arenas et al., 1999). However, gypsarenites are not necessarily formed and preserved after every flood event.

4.2 Detrital input and facies belt progradation

In playa settings, highest groundwater tables, respectively lake levels, are found in the center of the basin. Thus, the dry saline mudflat, dominated by capillary and pedogenic sulphates represents the most advanced progradation of marginal facies into the basin, whereas the wet saline mudflat is associated with more or less phreatic conditions (Frisch et al., 2018). The ephemeral playa lake lithofacies represents the wet saline mudflat at times of flooding.

Despite a clear facies belt progradation, the detrital input is constantly low for all lithofacies zones. Sediments of the more marginal dry saline mudflat do not show substantially coarser grain sizes than the deposits of the wet saline mudflat or the ephemeral playa lake. It is inferred, that the sand fraction of sheet floods already settled down on the floodplains of the distal alluvial fan (Nichols & Fisher, 2007). With a constantly low influx of clastic material, the overall lithology throughout the playa cycle is mainly controlled by the rate of authigenic mineral precipitation (clay minerals, carbonates, evaporites) and the groundwater/lake salinity. High water availability increases the rate of authigenic mineral precipitation especially during subaqueous deposition, evident by the precipitation of limestones and gypsarenites in the playa lake facies. Low groundwater tables interrupt or stop the supply of saline water up to the sediment surface and thus hamper the evaporite formation. Additionally, low pore water saturation slows down the formation of authigenic clay minerals (e.g. smectite, sepiolite). To conclude, the proportion of detrital clastics in the sediments is supposed to be largely controlled by the rate of authigenic mineral formation, which in turn depends on the groundwater and lake level. High water availabilities decrease the relative share of clastic material.

5 Rock magnetic results

The rock magnetic results are used to determine concentrations, mineralogy, grain-size (domain-state), relative NRM intensity and magnetic fabric of the magnetic phases in different stages of the playa cycle.

5.1 Concentration dependent parameters

The magnetic concentration dependent parameters χ, ARM, SIRM and HIRM (Fig. 2c-f) all show a similar behavior along the profile. The reddish Bed 3 stands out with its much higher values following on top of a thin light gray layer with a clear minimum. Below 3.5 m the values show only small variations with slightly lower values occurring in lighter colored, carbonate rich layers (in particular Beds 5, 7, 9, 11, 13). Bed 1 and 23 show relatively low concentration dependent values, which can be (partly) attributed to the high gypsum content in

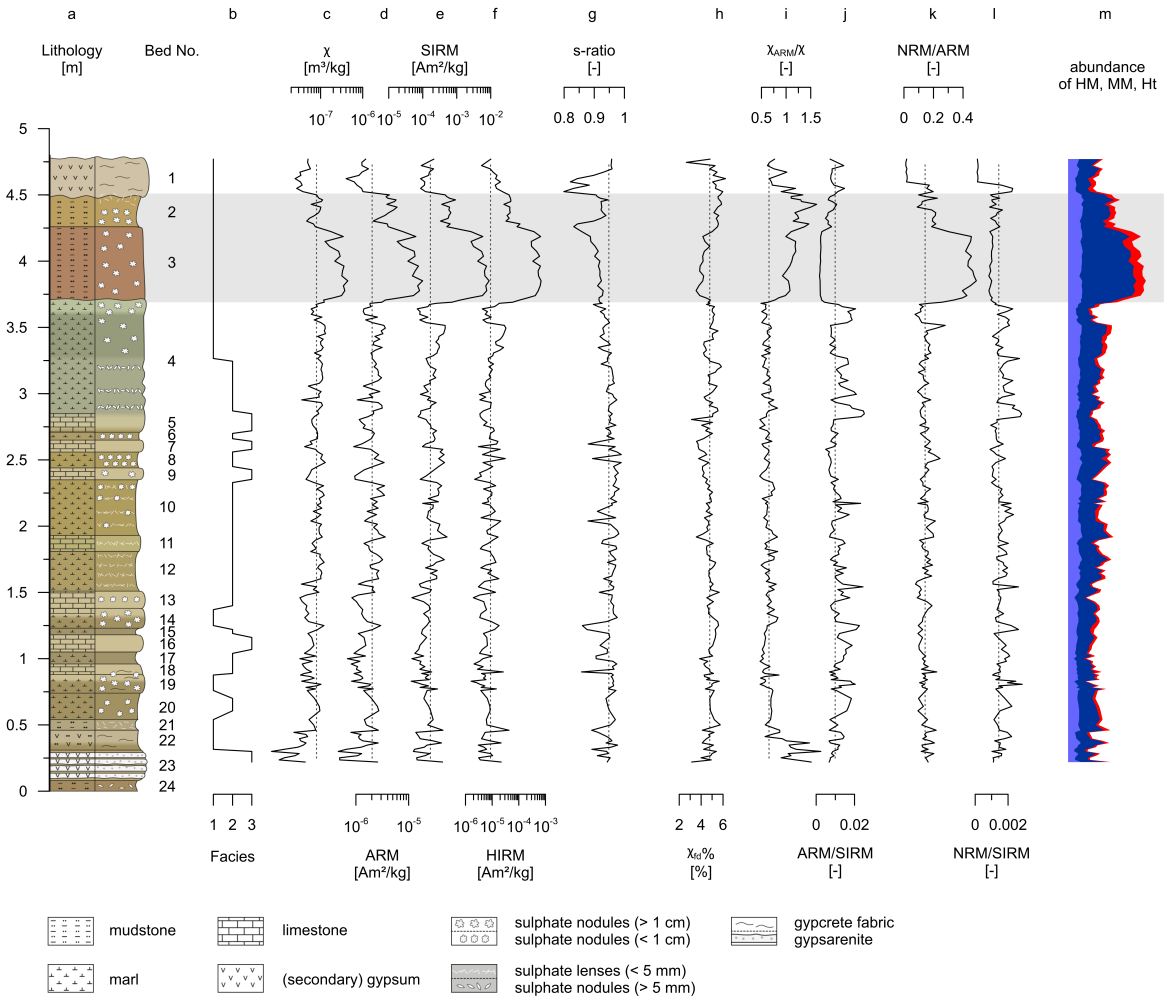

Figure 2: (a) Lithological profile of the studied playa cycle with bed number, and (b) subdivision into three lithofacies types (1 - dry saline mudflat, 2 - wet saline mudflat, 3 - ephemeral playa lake). (c-f) concentration dependent magnetic parameters (χ, ARM, SIRM, HIRM), (g) low-to-high coercivity magnetic mineral indicator s-ratio, (h-j) grain size dependent ratios (χ_{fd}%, χ_{ARM}/χ, ARM/SIRM), (k,l) natural remanence type indicators (NRM/ARM, NRM/SIRM). (m) Schematic overview on the absolute abundance of the three magnetic fractions (HM/light blue: high-coercivity magnetite, MM/dark blue: medium-coercivity magnetite, Ht/red: hematite) as derived from rock magnetic properties SIRM, HIRM and ARM/SIRM; the figure does not displays true contributions but allows recognizing the tendencies of the absolute and relative contents of the three phases. Dashed lines are medians. The gray bar marks the samples with high concentration dependent parameters (HCP)

these layers. Plotting χ versus SIRM (Fig. 3a) reveals a significantly different composition of the magnetic assemblage in Bed 3. The very good correlation (R^2 = 0.98) for the reddish Bed 3 suggests that susceptibility in this part is controlled by the ferro(i)magnetic mineral phases. In the marl and limestone layers below Bed 3 the correlation is much lower and χ/SIRM ratios are higher.

5.2 Magnetic minerals

Thermomagnetic curves generally show a considerable irreversible behavior with strong increase upon cooling (Fig. 4a). Samples from the reddish Bed 3 exhibit a decrease above 300 °C, which can be attributed to the inversion of maghemite to hematite. The drop around 580 °C is characteristic for magnetite. The shape of the cooling curve with increasing susceptibility values over a large temperature range indicate that the newly formed phase consists of fine magnetite particles which transform from superparamagnetic to single domain state during cooling (Bowles et al., 2009). The χ-T curves from samples of the wet saline mudflat and playa lake facies are noisy and do not allow identification of ferro(i)magnetic minerals by their blocking temperature.

The s-ratio (Fig. 2g) was determined to evaluate the relative content of high coercivity components. It varies between 0.80 and 0.99 (mean 0.94) indicating a substantial amount of hematite in most samples. Above ca. 3 m the s-ratio steadily decreases until the top of the reddish Bed 3 at 4.25 m. Low s-ratio values also occur in most parts of Bed 1.

End-member modeling of the twenty measured IRM acquisition curves generally revealed two lower coercivity components (most likely related to magnetite or maghemite) and a high coercivity component shown by incomplete saturation above 300 mT (Fig. 4b,c). According to thermal demagnetization of the IRM the high coercivity component is hematite (which is not observed in the thermomagnetic curves due to its much lower magnetic susceptibility compared to the dominating magnetite). The IRM acquisition curves reach ~90 % of their maximum value at 300 mT indicating that the magnetic remanence is dominated by magnetite (for simplicity we do not further differentiate between magnetite and maghemite). The two lower coercivity components have $B_{1/2}$ values of 31.6 - 78.2 mT (mean 41.9 mT) and 94.1 - 135.6 mT (mean 117.1 mT), the corresponding mean DP values are 0.37 and 0.24, and their contributions to the SIRM are 43.0 - 59.7 % (mean 51.9 %) and 28.6 - 49.1 % (mean 42.5 %), respectively. We label these two components medium coercivity magnetite (MM) and higher coercivity magnetite (HM). In samples from the reddish Bed 3, the contribution of MM is relatively higher than the one of HM (59.5 % and 29.0 %) compared to other samples (51.0 % and 44.4 %). Also the high coercive hematite contributes relatively more to the SIRM than in samples from other beds.

5.3 Magnetic grain size

The frequency dependent susceptibility χ_{fd}% is indicative for superparamagnetic contributions to the magnetic susceptibility. χ_{fd}% values are generally low (Fig. 2h) and range between 2.7 and 6.2 % with an average of 4.8 %. Bed 2 shows the highest χ_{fd}% values, whereas Bed 3 has relatively small values. The ratios χ_{ARM}/χ (Fig. 2i) and ARM/SIRM (Fig. 2j) also show a different magnetic behavior of the reddish Bed 3. The highest χ_{ARM}/χ ratios occur in samples from Bed 2 and 3. The lowest ARM/SIRM ratios are determined for the samples from Bed 3.

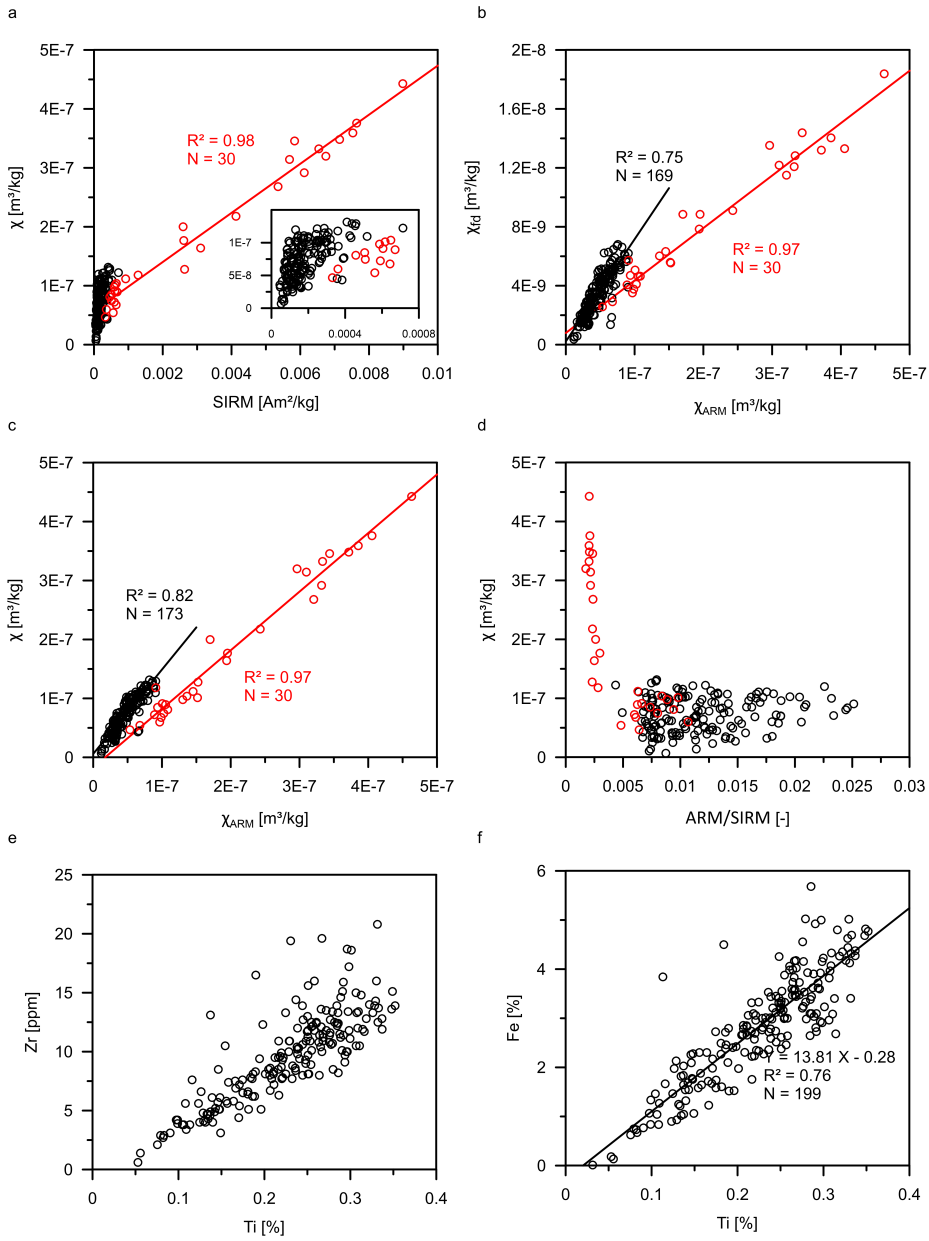

Figure 3: Scatter plots of (a-d) rock magnetic parameters and (f, e) geochemical element with curves and statistic results of linear correlation analysis. Red and black colors discriminate between samples of Beds 2 and 3 with high magnetic concentrations and the rest of the playa cycle

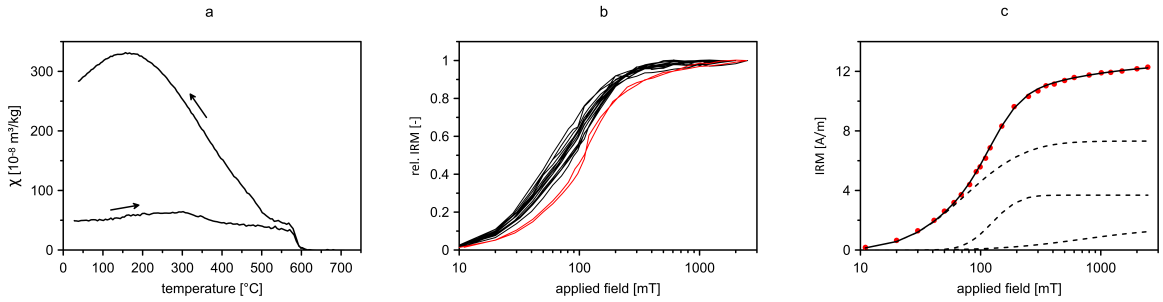

Figure 4: (a) Typical thermomagnetic curve of magnetic susceptibility for a sample from Bed 3. (b) IRM acquisition curves of representative samples (HCP samples marked in red). (c) IRM end-member modeling result of a sample from Bed 3 with three contributing components (dashed lines)

5.4 Relative NRM intensity

The ratios NRM/ARM (Fig. 2k) and NRM/SIRM (Fig. 2l) were determined to evaluate the NRM intensity relative to the remanence capacity. Bed 3 shows the highest NRM/ARM ratios throughout the playa cycle, while NRM/SIRM values are rather small. Both ratios are exceptionally low in Bed 1.

5.5 Anisotropy of magnetic susceptibility

The degree of anisotropy P_j is low and varies from 1.007 to 1.067 (mean 1.032). P_j values are generally lower in carbonate rich horizons, in particular Beds 5, 7, 9 and 11. The variation of the shape parameter T is from -0.143 to 0.959 (mean 0.658). Oblate grains dominate the magnetic fabric. The collected samples were not oriented horizontally but have the same vertical axis. The AMS results indicate a well grouped distribution of the principle minimum axis perpendicular to the bedding plane and thus a primary sedimentary fabric.

6 Geochemical data

To better understand the depositional conditions and its environmental implications, geochemical XRF scans were performed. In Fig. 5, the concentrations of elements are plotted along the profile.

The elements Si, Ti and Fe are indicative for the proportion of clastic input in individual beds (Fig. 5b-d). Lower contents occur in carbonate rich horizons, in particular Beds 5, 7, 9, 11, 13 and 18. Conversely, marls and mudstone horizons, deposited during lower groundwater and lake levels generally show elevated contents. A general trend of clastic input superimposed to the bed variations is not evident.

Ca, S and Cl are interpreted as indicators for water chemistry and the amount of evaporitic mineral precipitation (Fig. 5e-g). The records of S and Ca show a strong positive correlation at the base between 0 and 0.75 m (R^2=0.76) and at the top in the interval from 2.80 m to 4.77 m (R^2=0.69). The middle part is characterized by a weaker correlation (R^2=0.22). Thus, Ca derived from gypsum makes up a large share of the total Ca content in the basal and top part of the cycle, whereas most likely $CaCO_3$ rather than plagioclase must contribute substantially to the Ca content in the more calcareous middle part. Additionally, elevated values of the S

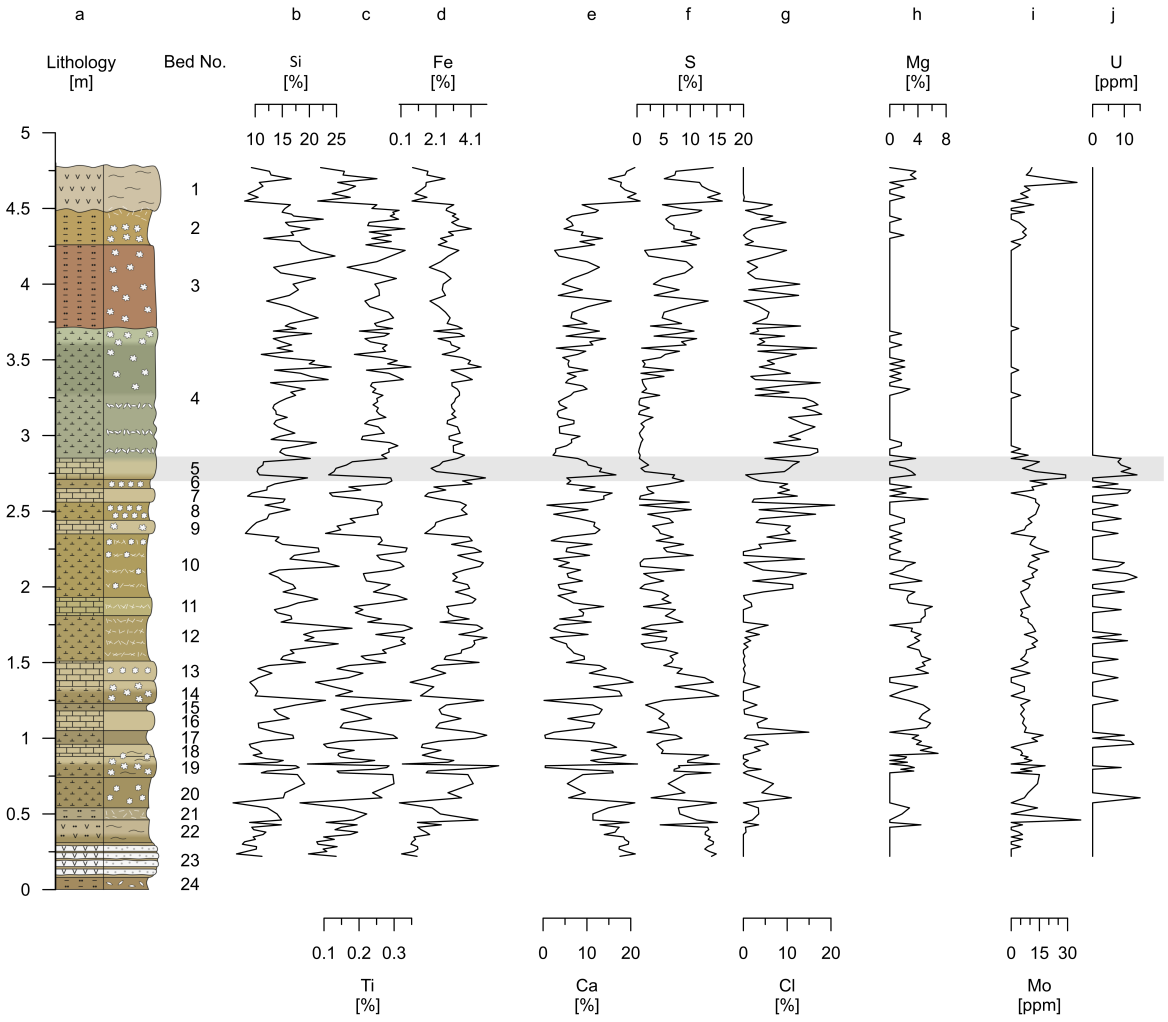

Figure 5: Geochemical element contents plotted along the (a) lithological profile with bed numbers: (b-d) parameters sensitive for clastic input (Si, Ti, Fe), (e-g) evaporation indicators (Ca, S, Cl), (h) possible clay authigenesis indicator (Mg), (i-j), and redox sensitive elements (Mo, U). The gray bar marks the redox boundary between predominantly subaerial and subaquatic deposition conditions

record point also to a higher gypsum content at the base and the top of the playa cycle. Co-occurrence of high Ca and S contents in carbonate rich horizons are observed in Beds 5, 11, 13, 14, 18 and 19. In the lower part (up to ~1.5 m), the Cl content is low while the S content is high, followed by a short interval where the contents of both elements are low. From 1.95 m to 3.25 m, the Cl content increases while the S content decreases.

Mg contents of up to 6 % occur in the horizon between 0.75 - 2.8 m (Beds 5-18), while above 3 m the Mg content is mostly below the XRF detection limit of 1 % (Fig. 5h).

The redox sensitive elements Mo and U indicate a transition around 2.8 m (Bed 5). Mo (Fig. 5i) and U (Fig. 5j) contents are enhanced below this transition and close or below the XRF detection limit above 2.8 m. Mo values increase again in Bed 2 and 1.

7 Discussion

7.1 Sedimentological interpretation of the geochemical and magnetic records

7.1.1 Geochemistry

The assumption of a constant detrital influx throughout the playa cycle is supported by the absence of a long term trend in clastic elements. This, together with the negative correlation of elements of detrital and authigenic origin, suggests a different degree of detritus dilution by authigenic mineral precipitation for each bed, depending on the water availability.

Since $CaCO_3$ and $CaSO_4$ cannot be precipitated simultaneously from the same brine (Eugster & Hardie, 1978), the enrichment of S in carbonate rich horizons argues for an early diagenetic precipitation of gypsum in these beds. Calcareous horizons are likely to originate from ephemeral alkaline playa lakes. Following the complete lake desiccation, saline groundwater infiltrated the calcareous lake sediments, which led to the formation of interstitial gypsum. The Cl record is indicative for the presence of highly soluble evaporites. Its trend is opposed to the sulphur record wherefore the variation is not considered as an indication for late salt formation during present-day meteoric conditions, but instead related to the brine evolution during the playa cycle deposition. The trends in the S and Cl below 3.25 m records suggest a progressive increase in groundwater salinity with sequential saturation and precipitation of sulphates and later chlorides, probably halite. This inference is corroborated by the polygonal, evaporite-filled sediment cracks, which occur at around 3.0 m. Theses cracks are a typical feature of the central part of saltpans. There, halite precipitating brines dominate, whereas sulphate precipitating brines prevail at the basin margin (Eugster & Hardie, 1978; Hardie et al., 1978; Rosen, 1991). These findings suggest a brine expansion from the central basin or a brine accumulation at the location of the Aktau Mountains at the beginning of the deposition of Bed 4. Above 3.25 m, the trends in S and Cl records are reversed indicating that groundwater salinities decreased again allowing only for the precipitation of sulphates. The elements S and Cl elucidate the entire lithofacies evolution of a temporarily water-covered playa lake with a salt flat.

The redox sensitive elements U and Mo show elevated values below Bed 4 (Fig. 5i,j). The oxidation states and mineral solubility of U mainly control the partitioning or release of U and Mo onto or from mineral structures

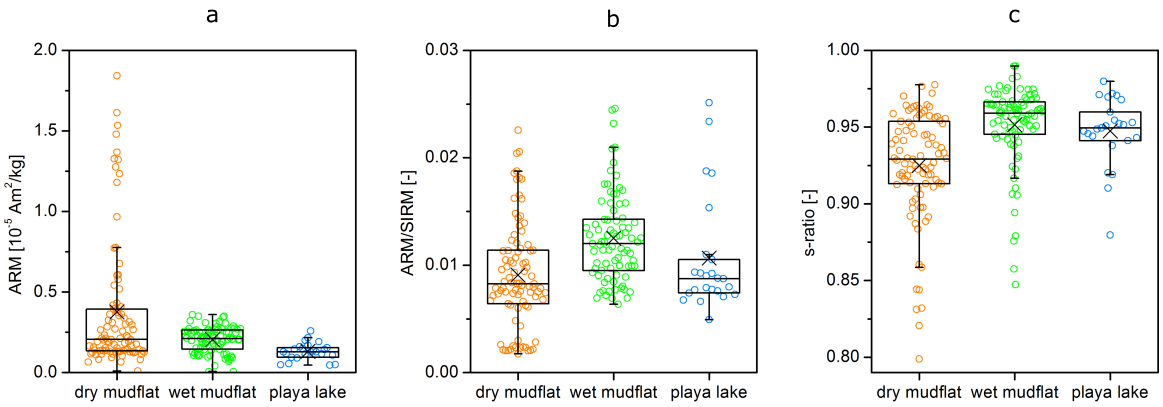

Figure 6: Statistical analysis of the rock magnetic parameters for the three different groups of lithofacies (as classified by lithology): The boxplots of the magnetic concentration dependent parameter ARM (a) generally reflect the increasing water availability, while the grains-size indicating ratio ARM/SIRM (b) and the low-to-hard coercivity magnetic mineral indicator s-ratio (c) show a maximum in the wet saline mudflats, where the groundwater table is the highest. The boxplots show medians, quartiles and maximum/minimum values (1.5 factor whiskers), and means are displayed by crosses

(Maher et al., 2013). In oxic waters, U is readily dissolved as hexahedral uranyl ions (UO_2^{2+}). In its +4 oxidation state U is less soluble and forms more stable compounds such carbonate complexes (Cumberland et al. 2016). Mo occurs as tetrahedral molybdate anions (MoO_4^{2-}) in oxygenous waters, while MoO_4^{2-} is removed from sulfidic waters to form thiomolybate species in reducing conditions (Crusius et al., 1996; Erickson & Helz, 2000). Accordingly, the trace elements U and Mo are indicators of reducing conditions, whereby Mo is the diagnostic element for sulphate reducing conditions (Crusius et al., 1996, Dean et al., 1997). The higher contents of U and Mo thus indicate a redox boundary below between Bed 5 and 4. The redox boundary at Bed 5 is likely an early diagenetic feature. Reducing conditions are probably linked to an almost constant saturation of sediments with saline groundwater until Bed 5, despite small interruptions due to groundwater table lowstands and freshening during and after run-off events. Based on the sedimentological and geochemical interpretations (presence of Cl brines), this condition should have prevailed also in the lower part of Bed 4. It is assumed that the prolonged groundwater table lowstand of Bed 3 affected also the underlying Bed 4 sediments, evident by the early diagenetic precipitation of capillary sulphate nodules in the upper part of Bed 4. The redox boundary at Bed 5 suggests an even more profound oxidation of sediments during this groundwater table lowstand.

Mg fixation is either a result of primary microbial mediated dolomite formation under evaporatic conditions (e.g., Vasconcelos et al., 1995; Warthmann et al., 2005) or of Mg-rich clay authigenesis, i.e. smectite formation under aquatic and highly alkaline (pH ~9) conditions (Deocampo et al., 2009). The latter process has been detected from dry mudflat sediments in the underlying Bastau Fm by the identification of palygorskite (Voigt et al., 2017). The increased Mg values could be indicative of clay authigenesis but a more detailed study on clay mineralogy could provide more insight but is beyond the scope of this study.

7.1.2 Magnetic record

More than half of the playa cycle (from the base until Bed 5) is characterized by low concentration dependent values. Small variations in all the magnetic parameters are predominantly associated with recurring changes in sedimentation from marl (e.g. Beds 20, 15, 12, 10 and 8) to limestone (e.g. Beds 18, 14, 13, 11, 9, 7 and 5) beds. The low variability of the magnetic parameters can be related to the predominant deposition in the wet saline mudflat facies. Sediments of this lithofacies zone were protected against extensive oxidation by the relative high groundwater table. This enabled elevated rates of authigenic mineral formation, which explains also the generally low values of the magnetic concentration dependent parameters due to magnetic mineral dilution. Short-termed groundwater table lowering led to the decreased formation of authigenic sediments whereas ephemeral subaqueous deposition (ephemeral playa lake facies) favored the precipitation of authigenic minerals. The magnetic concentration dependent parameters well reflect these changes of the depositional environment with typical lower values in limestone and gypsarenite beds and higher values in marl layers.

With the transition to Bed 4, the magnetic concentration dependent parameters show even less variability. The brine expansion probably stabilized the groundwater availability and thus caused a more constant sedimentation. However, the s-ratio starts to decline already in the lower part of Bed 4 and indicates a successively oxygenated sediment by the increased oxidation of magnetite to hematite. This trend concurs with the substantial groundwater table lowering possibly during Bed 3 and the early diagenetic alteration of the underlying sediments inferred from evaporite morphologies and geochemistry.

In the upper part of the playa cycle, especially in Bed 3, high values of the magnetic concentration dependent parameters can be observed. This is related to a substantial lowering of the groundwater table with well-oxygenated, reddish sediments. The massive top-down oxidation in Beds 3 indicates reduced sedimentation (low mudflat aggradation) and an increased aridity. The elevated values of the magnetic concentration dependent parameters are likely linked to low rates of authigenic mineral formation (especially low carbonate content), which caused a relative enrichment of the magnetic minerals compared to the remaining part of the playa cycle.

The two top-most Beds 2 and 1 show again decreasing magnetic concentration dependent parameters together with the development of mature gypcrete crusts. The crust formation is accompanied by the accumulation of $CaSO_4$ and thus caused a relative decrease in the proportion of magnetic minerals. This is confirmed by the XRF analysis, which reveals a clear correlation and an increased content of S and Ca in Bed 2 and 1. The yellowish sediment color might suggest a less oxygenated sediment due to a higher groundwater availability, which possibly facilitated the gypcrete formation compared to Bed 3. This is supported by higher s-ratio values in Beds 2 and 1, pointing to less oxidation of magnetite to hematite.

The variations in the magnetic records enable to track changes in the depositional environment, which can be found independently in the sedimentary and geochemical records. The lithofacies dependence of three magnetic parameters are plotted in Fig. 6. The magnetic concentration dependent parameter ARM, the ratio ARM/SIRM that indicates the grain size (domain state) of magnetite, and the s-ratio that estimates the relative contents of magnetite and hematite (low s-ratio values indicate higher relative contributions of hematite), are selected because they well semi-quantify different rock magnetic characteristics of the playa cycle. The

ARM/SIRM ratio is also influenced by the hematite fraction; however, as the ARM/SIRM varies by about one order and hematite generally contributes less than 30 % to the SIRM, this influence will not seriously distort the significance of the ARM/SIRM ratio as an indicator of grain size variation of the magnetite fraction. Thus, higher ratios are indicative for finer magnetite grain sizes.

On average the ARM decreases with increasingly aquatic sedimentation from the dry saline mudflat facies to the playa lake facies, reflecting the amount of clastic detritus relative to authigenic minerals (Fig. 6a). The distribution of individual data points of the dry saline mudflat facies, however, shows a very high variability. This is probably related to a strong variation of authigenic mineral genesis, especially carbonate, which cannot be resolved by the sedimentary facies. In case of the ARM/SIRM ratio, highest values (i.e. magnetite showing more single domain), are found on average in the wet saline mudflat facies (Fig. 6b). Facies zone boxplots (Fig. 6c) show highest values for the s-ratio in the wet mudflat and lowest values with a high scatter in the dry mudflat facies. This could be linked to the constant saturation of sediments with saline groundwater in the wet mudflat facies, which prevents sediment oxidation by infiltration of atmospheric oxygen. Conversely, the dry saline mudflat is characterized by low groundwater table. There, the presence of whitish, altered sulphates indicates that the top of the capillary fringe must have sunk below sediment surface to give way for low salinity meteoric flood or precipitation water. This enables also the infiltration of atmospheric oxygen into the sediments. Therefore, s-ratio values of dry saline mudflat samples are lowest. Intermediate values in the playa lake facies might emphasize the ephemeral character of these flooding events but could also point to well oxygenated floodwater. ARM/SIRM ratios show no direct lithofacies dependence (Fig. 6b).

The boxplots of Fig. 6 confirm that the magnetic concentration dependent parameters can be associated with varying rates of authigenic mineral (i.e. carbonate) precipitation in response to the water availability (ground- and lake water), which controls the proportion of magnetic minerals in the sediment at more or less constant detrital input. The variations within the lithofacies types (in particular the dry saline mudflat facies) indicate that the rock magnetic assemblage of the playa cycle reacted much more sensitive to groundwater level changes than reflected by the lithofacies code. A much higher magnitude of groundwater table lowering is indicated for Bed 3 compared to previous occurrences of dry saline mudflats by the rock magnetic parameters. In particular, the s-ratio gives insights into the redox conditions probably controlled by the infiltration of atmospheric oxygen into the sediments depending on the position of the groundwater table. The s-ratio is however susceptible to (early) diagenetic alteration, whereas post sedimentary groundwater level changes do not affect the concentration depending parameters. In conclusion, the magnetic records seem to allow a more detailed interpretation of the groundwater availability and likely other depositional conditions such as aridity changes. In the following, the rock magnetic signature of the playa cycle is discussed to understand the underlying processes and to elaborate the possible use of magnetic parameters as proxies in paleo-environmental settings as studied.

7.2 Magnetic minerals

The rock magnetic signature of the studied playa cycle indicates distinct variations in the rock magnetic properties throughout the lithologies. The reddish Bed 3 shows notably higher concentrations of ferro(i)magnetic minerals. The variations in the rock magnetic parameters further suggest different contributions of the magnetic minerals in the reddish Bed 3 compared to other beds of the studied playa cycle. The differences in

magnetic minerals of samples with high concentration dependent parameters (HCP), i.e. samples from Bed 3 and 2, and low concentration dependent parameters (LCP) are discussed in the following. In Fig. 2m, the relative and absolute abundance of the ferro(i)magnetic phases in HCP and LCP samples are illustrated.

The concentration of ferro(i)magnetic minerals is rather low, hence the contribution of paramagnetic phases to the signal could be significant. Paramagnetic clay minerals in the sediment matrix such as illite, palygorskite and chlorite are common in Neogene sediments of the Ili Basin (Voigt et al., 2017, Hellwig et al., 2018). However, χ and χ_{fd} correlate well with χ_{ARM} and the linear fit passes through the origin (Fig. 3b,c) indicating the dominance of ferro(i)magnetic minerals and only minor paramagnetic contribution in the magnetic susceptibility signal.

Hematite occurs throughout the playa cycle in varying concentrations as semi-quantified by the HIRM and the s-ratio (Fig. 2f,g), end-member modeling of IRM acquisition curves and thermal demagnetization of the IRM. HIRM values are generally higher and s-ratios are lower in HCP samples, which means that in these samples the absolute concentration of hematite is increased, and also the relatively contribution of hematite is higher.

The dominating magnetic carrier in the studied playa cycle is magnetite. It contributes to the magnetic signal in two phases, a medium coercivity magnetite (MM) phase and a higher coercivity magnetite (HM) (Fig. 4c). The values of χ and ARM/SIRM are not correlated (Fig. 3d). There is a wide range of ARM/SIRM values in LCP samples, while in HCP samples the ARM/SIRM tends to be clearly lower and less variable. The higher ARM/SIRM ratios (Fig. 2j) indicate a relatively higher contribution of the HM phase in LCP samples compared to HCP samples. Nevertheless, the absolute content of the HM phase varies little throughout the playa cycle while the MM phase is causing major variations (Fig. 2m). This is evident from the strong enhancement of concentration dependent parameters overriding the variation of the MM/HM ratio. The ratios χ_{ARM}/χ and χ/SIRM (Fig. 3c,a) are lower in HCP samples. Since the trend of χ vs. χ_{ARM} and χ vs. SIRM are generally different for HCP and LCP samples, control of hematite on these ratios can be excluded, and the relative contributions of the MM and HM fractions must be the cause.

In conclusion, MM and hematite concentrations are higher in HCP samples and the ratio of the MM-to-HM fractions is higher than in LCP samples.

7.3 Origin of magnetic properties variation

To substantiate the use of rock magnetic parameters as paleo-environmental proxies in the playa cycle, it is important to understand how the magnetic mineral assemblage is related to processes in the catchment area, authigenic processes, and effects of post-depositional magnetic alteration.

The NRM/ARM values in the reddish Bed 3 are much higher than in other beds of the playa cycle (Fig. 2k). A high NRM/ARM ratio may indicate a secondary chemical remanent magnetization (CRM) as suggested by e.g. Deng et al. (2007) and Verestek et al. (2018). The simultaneous low NRM/SIRM values (Fig. 2l) suggest that the possible CRM is carried by the relatively lower coercivity ferro(i)magnetic phase, i.e. the MM fraction. The high values of the NRM/ARM ratio in HCP samples and low values of the LCP samples are a strong indication that a CRM is restricted to the MM fraction. The HM fraction may carry a detrital remanent magnetization (DRM), which is usually far lower than a CRM for a given ferro(i)magnetic mineral assemblage.

In the following, we assess the consistency of the observed playa cycle data with different processes to identify the origin of the ferro(i)magnetic minerals and possible alterations.

7.3.1 Possible processes controlling magnetic concentration and grain size

From the sedimentological discussion in 7.1 the low magnetic concentration parameters in LCP samples can be related to elevated rates of authigenic mineral formation and thus magnetic mineral dilution. In Bed 3, authigenic mineral growth (i.e. carbonate and sulphate precipitation) is hampered by increased aridity causing an enrichment of the magnetic minerals. However, concentration dependent parameters vary by almost two (χ, ARM) or more than two (SIRM, HIRM) orders of magnitude. The dilution and enrichment mechanism contributes to the variability in the magnetic signal but the variation as well as the varying MM/HM ratios indicate further controlling processes. Several factors may explain magnetic variations such as changes in provenance, pedogenesis, post-depositional dissolution, low temperature oxidation (LTO), authigenic formation of magnetite, or erosion and transport conditions.

7.3.1.1 Changes in provenance

If the large variation in magnetic mineral concentrations is caused by changes in provenance, it must be associated with varying types of parent rocks serving as sources for eroded material, which mixed up in significantly different portions in the depositional record. At the same time one would expect significant variations in concentrations of those chemical elements that are not sensitive to diagenetic alteration, e.g. Ti and Zr. However, the geochemical data of the studied playa record indicate a high correlation between Ti and Zr (R^2 = 0.77, Fig. 3e), which is typical for detrital input derived from a relatively stable source area (Rosenbaum et al., 1996). Thus, the observed variability in the concentration dependent magnetic properties cannot be explained by changes in provenance.

7.3.1.2 Pedogenesis

In situ formation of superparamagnetic magnetite is common in soils (Maher & Taylor, 1988; Maher et al., 2003; Maxbauer et al., 2016a) and paleosols (Zhou et al., 1990; Geiss & Zanner, 2006; Ahmed & Maher, 2018). The χ_{fd}% values in our record (Fig. 2h) vary between 2.7 and 6.2 % indicating the presence of superparamagnetic particles. However, these χ_{fd}% stand for relatively little superparamagnetic portions, and the variation across the playa sequence is small compared to the variation in concentration dependent magnetic parameters. Hence, we conclude that pedogenically produced ultrafine ferrimagnetic minerals do not play an important role for the observed variations in magnetic concentrations in the studied playa cycle.

7.3.1.3 Dissolution

Post-depositional dissolution of detrital magnetic minerals is common in water-logged sediments (Karlin & Levi, 1985; Canfield & Berner, 1987; Snowball, 1993; Rosenbaum et al., 1996; Florindo et al., 2003; Demory et al., 2005; Ao et al., 2009). Verestek et al. (2018) found magnetic alterations in the Bastau Fm underlying the Koktal Fm, and suggested both dissolution and neo-formation of ferro(i)magnetic phases in these sediments. The gypsum bearing red and greenish layers of the Bastau Fm show the same lithological and sedimentary features and similar rock magnetic properties as the dry saline mudflat facies of the playa cycle (in particular the reddish Bed 3 and Beds 14, 19, 21, 22). Repeated wetting/drying-cycles and saline conditions enhance

reduction and dissolution (Snowball & Thompson, 1988; Sandgren & Risberg, 1990; Ahmed & Maher, 2018). Moreover, reduction is particularly effective in the presence of organic carbon that promotes sulfate reduction and dissolution of magnetite (Channell et al., 2013). Dissolution effects could be expressed by mineral transformations and grain-size selective dissolution. Often dissolution of magnetite is associated with formation of iron sulphides such as pyrite and ferrimagnetic greigite (Karlin & Levi, 1985; Canfield & Berner, 1987; Orgeira et al., 2011; Rowan & Roberts, 2006). However, our results of IRM thermal demagnetization and thermomagnetic χ-T runs show no indication of greigite. If dissolution occurred, it would have been grain-size selective, affecting the finer HM fraction more than the MM fraction due to the higher surface-to-volume ratio (Canfield & Berner, 1987; Liu et al., 2004). Thus, if dissolution was a major driving mechanism of the rock magnetic variations in the studied playa cycle, the larger-sized MM particles in LCP samples would contribute relatively more to the magnetic signal than in HCP samples. However, the higher ARM/SIRM ratios in LCP samples implicates a relatively higher contribution of the finer-grained HM particles in LCP samples (Fig. 2m), and therefore contradicts the expected ARM/SIRM change for a dissolution process in the playa sediments.

The chemical elements records of Fe and Ti also supports the conclusion that dissolution of magnetite was not a major factor. Rosenbaum et al. (1996) inferred post-depositional magnetite dissolution of lacustrine sediments from negative offset of the linear fit line between Fe and Ti contents. However, the studied playa cycle show only a minor offset (0.28 %, Fig. 3f).

7.3.1.4 Low temperature oxidation

LTO is a common alteration process in soil and paleosols (Maher, 1998; van Velzen & Dekkers, 1999; Zhang et al., 2012) and in lacustrine sediments (Wang et al., 2004; Li et al., 2006a; Fang et al., 2015; Hu et al., 2015). Fang et al. (2015) proposed a close relationship of LTO in the catchment area and magnetic properties of the derived lacustrine sediments in the Xining Basin (China), and interpreted it with varying arid conditions. The mudflat and intermittent playa lake deposits in the lower Koktal Fm are a result of changes in the balance of moisture supply in the catchment area and evapotranspiration in the semi-arid to arid Ili Basin (Frisch et al., 2018). A redox boundary at Bed 5 separates the studied playa cycle into a period of high groundwater table preventing a deep infiltration of atmospheric oxygen into the sediment and a period of profound groundwater table lowering, which led to thorough sediment oxygenation (Fig. 5). The driest conditions during the playa cycle occurred during the deposition of Bed 3. The concomitant groundwater table lowstand was likely accompanied by a lowering of the top of the capillary zone. A decline of the capillary fringe enabled the infiltration of atmospheric oxygen into the sediment. The oxygeneous conditions in Bed 3 favored oxidation processes of magnetite to maghemite and hematite (McNeill 1990; Fang et al., 2015) recorded by the s-ratio, which gradually decreases above 3 m in the profile, reaching values as small as 0.83 at the top of Bed 3. The reddish color of Bed 3 also results from pigmentary hematite that is associated with LTO. The relatively higher contribution of hematite in HCP samples as evident from end-member modeling of IRM acquisition curves and the gradual upward decrease of the s-ratio suggest a higher degree of oxidation in HCP samples. Moreover, both magnetite phases show high $B_{1/2}$ values which can be explained by LTO. The high hematite content in HCP samples could be attributed to strong LTO of magnetite. Such a process is only possible if the magnetite concentration has been sufficiently high so that magnetite was partly oxidized to hematite and partly preserved causing the observed high concentration dependent parameters of both magnetite and hematite.

To conclude, LTO is an alteration process that likely occurred in the studied playa cycle, in particular oxidizing magnetite to hematite. However, it cannot explain the variation in the concentration dependent parameters of more than two orders of magnitude and the simultaneously observed higher MM/HM ratio in HCP samples. Therefore, LTO is not the most important control of the variations of magnetic properties.

7.3.1.5 Authigenic formation of magnetite

Authigenic formation of magnetite associated with strong changes in the sediment magnetic properties has been frequently reported (Katz et al., 1998; Dinarès-Turell et al., 2003; Kodama, 2012; Channell et al., 2013; Roberts, 2015). Secondary magnetite formation was linked to late diagenetic processes such as basinal fluid flow associated with orogenesis and clay authigenesis (McCabe et al., 1989; McCabe & Elmore, 1989; Katz et al., 2000; Woods et al. 2002; Tohver et al., 2008). Verestek et al. (2018) reported secondary magnetite and partial magnetic overprint in the underlying Bastau Fm. They suggested clay diagenesis of smectite and illitization as the responsible process resulting in neo-formation of magnetite and secondary chemical remanent magnetizations. Pedogenesis, and also repeated drying and wetting processes, favor slow illitization of smectite at low temperatures (Huggett, 2005). The fluctuating groundwater table as well as the recurrent mudflats in the playa cycle likely facilitated conditions where diagenesis of smectite and illitization occurred. Detailed studies of the clay mineralogy in the playa cycle are needed to check this hypothesis. Other diagenetic processes are also possible, i.e. processes where magnetite forms from ions that were released by decomposition of unstable iron-bearing minerals within the sediment (e.g. Larson & Walker, 1975). Paramagnetic iron sulfides, ferrihydrite and other amorphous ferric iron oxides are likely candidates for such processes (Katz et al., 1998; Moreau et al. 2005). Furthermore, fine single domain magnetite can be formed by anaerobic oxidation of ferric iron such as ferrihydrites (Miot et al., 2014). The small χ_{fd}% values (in Bed 3) and relatively high $B_{1/2}$ values in HCP samples support authigenic magnetite formation represented by the MM fraction, which acquired a CRM when it grew above the critical blocking volume (Larson & Walker, 1975).

Also the HM fraction may have formed by an inorganic process. However, the low DP values of ~0.24 of this phase revealed by end-member modeling of SIRM acquisition curves indicate a narrow grain size range that favors a biogenic origin (Moskowitz et al., 1993; Chang et al., 2013). It may consist of magnetosomes produced by magnetotactic bacteria, and the high $B_{1/2}$ values above 100 mT could be caused by LTO. Because of the high surface-to-volume ratio of these very fine grains, biogenic magnetite is prone to alteration by both oxidation and dissolution. Van Velzen & Zijderveld (1995) reported higher coercivity magnetite with single-domain behavior in marine marls and explain the increased coercivities with internal stress induced by maghemitization (Appel, 1987; Smith, 1987; Housden & O'Reilly 1990). It is well known that in heterogeneously oxidized titanomagnetites, the magnetoelastic anisotropy dominates the magnetic domain state causing an increase in magnetic hardness by particle-internal heterogeneous distribution of magnetic easy axes (Beske-Diehl & Soroka 1984; Appel & Soffel, 1985; Smith, 1987). If the HM fraction consists of magnetosomes, it could have been formed in the playa or in the catchment area. In any case its formation will predate the consolidation of the playa sediments and it will carry a DRM.

In summary, authigenic magnetite formation may occur in manifold ways within sediments, but it is mostly limited to the formation of fine magnetite grains. In principle, the variations in the magnetite fractions could have been caused by authigenic formation of magnetite before and after sedimentation, resulting in a primary DRM

of the HM fraction and a high CRM of the MM fraction, respectively. In such a scenario, the increased aridity and related changes in the depositional environment during the deposition of HCP samples provided more favorable conditions for the authigenic formation of the MM fraction causing the higher MM/HM ratio and the high absolute concentration of the MM fraction in HCP samples. The high NRM/ARM ratio and simultaneously low NRM/SIRM ratio in HCP samples are compatible with a dominance of the NRM by a CRM of the MM fraction.

Further studies such as electron microscopy will be beneficial for assessing the sizes and shapes of magnetite particles and to search for magnetosomes.

7.3.1.6. Sorting during transport

More arid conditions increases erosion and thus the volume of transported material, while reduced erosion during wetter conditions and denser vegetation may be associated with more effective sorting effects during transport (Li et al., 2006b; Wei et al., 2018). Sorting during transport removes coarser grained magnetite more efficiently than fine-grained magnetite particles (Rosenbaum & Reynolds, 2004). Drier conditions with occasional precipitation could have resulted in short strong erosion events and the deposition of dry saline mudflats in the Aktau Mountains with higher MM contributions whereas more humid conditions with more frequent but weaker erosion events could have led to deposition of relatively finer grained magnetite due to sorting effects during transport. The increased aridity during the deposition of HCP samples could have reduced the sorting effect while the more humid conditions during deposition of LCP samples linked with denser vegetation cover could have favored sorting effects. Despite sorting effects could have played a role in the formation of the magnetic signals of the playa sediments, it is unlikely that these effects resulted in the observed high variations of concentration dependent magnetic parameters.

7.3.2 The most likely scenario

The MM concentration is strongly increased in HCP samples, accompanied by a slightly higher amount of the HM fraction, which suggests a common driver or simultaneous favorable conditions for their enhancement. Dilution and enrichment due to changes in the rate authigenic mineral formation controlled by water availability may explain the increased HM concentration in HCP samples. The high variations in the magnetic record are caused by the MM fraction whose concentration variations must be controlled by additional processes. Following the discussion in the previous section, we can exclude several processes as major drivers. These are substantial changes in provenance because it does not match with the geochemical signature, pedogenic magnetite formation because of the generally low χ_{fd}% values, and dissolution because the finer fraction (HM) is making up a relatively higher portion of the total magnetite in LCP samples. LTO is certainly an alteration process, which has to be considered, especially for the formation of hematite through oxidation of magnetite, but it is very unlikely that LTO alone can explain the immense variation of about two orders of magnitude in concentration dependent parameters. Likewise, sorting during transport could have produced some variability in the magnetic record, but by no means the observed concentration changes. Thus, the most likely scenario to explain the magnetic record of the studied playa sequence is a combination of magnetic enhancement by authigenic formation of magnetite and transformation of magnetite to hematite by LTO.

The MM fraction has a mean DP value of 0.37 indicating a wider grain size range as it is typical for detrital fraction. However, the high $B_{1/2}$ values of around 30 - 80 mT are hardly compatible with detrital magnetite grains that are usually in the pseudo-single domain to multi-domain range with corresponding $B_{1/2}$ values lower than observed in the playa sediments. The high coercivities could be caused by extreme heterogeneities in stress distribution within the entire volume of detrital magnetite grains due to LTO, but it is more likely that the high $B_{1/2}$ values are linked to fine magnetite grains. We cannot exclude that the HM fraction consists of small-sized detrital magnetite; however, the much more likely alternative is that the MM magnetite was formed by inorganic processes.

Multiple iron sources for the inorganic formation of magnetite are proposed in 7.2.1. Clay authigenesis and illitization are possible process where magnetite is formed. Elevated Mg contents can be indicative for clay authigenesis. However, the Mg record shows higher contents in the wet saline mudflat and playa lake facies (Fig. 5h). We do not exclude illitization just because of the observed Mg contents but we also fail to provide a more likely explanation of the observed magnetic variations based on inorganic formation of magnetite from other iron sources.

The high NRM/ARM ratios together with simultaneous low NRM/SIRM ratios in HCP samples further support the interpretation of secondary magnetite by indicating a possible CRM in HCP samples carried by the coarser and lower coercivity MM fraction. In order to acquire a high CRM the secondary MM grains must have been formed in a post-depositional stage.

The abundance of the HM fraction is similar throughout the playa cycle (Fig. 2m) which is suggestive of a detrital origin of the HM phase. The low mean DP of 0.24 that means a narrow grain size range is indicative of magnetosomes. However, one could expect that living conditions for magnetotactic bacteria are generally better in wetter conditions. Not only the MM fraction is enhanced but also the HM fraction shows a slight increase in HCP samples, which represent the dry saline mudflat facies and in particular the driest conditions. The proposed dilution and enrichment mechanism could cause the slight increase.

Although a low DP value is commonly associated with magnetosomes, inorganic formation of the HM fraction cannot be excluded. Such a formation process must have occurred in an earlier stage than the MM formation process, i.e. before consolidation of the playa sediments, as the combined information from the NRM/ARM and NRM/SIRM ratios suggests that the HM fraction did not acquire a CRM.

At this point, the biogenic origin of the HM fraction and a post-depositional formation of the MM fraction associated with a CRM are the most likely scenario when considering diagenetic processes. The reason for the magnetic enhancement in HCP samples is still an open question. In the case of a post-depositional MM formation, the more arid depositional conditions during deposition of HCP samples could have facilitated the availability of iron sources. The possible detrital and biogenic origin of the HM fractions need to be further investigated.

The occurrence of hematite are indicative for maghemitization by LTO. The increase in s-ratio and HIRM above 3.5 m could have been caused by enhanced formation of hematite through LTO of magnetite towards the top of Bed 3. Strong LTO could have possibly altered the hematite concentration observed in the playa cycle under the assumption that LTO is more effective under more arid conditions. Simultaneous formation of magnetite and LTO of the magnetite to hematite is highly unlikely. Consequently, a proposed magnetite formation processes

must have occurred at an earlier stage of the diagenesis that is followed by LTO of the magnetite grains and hematite formation at a later stage. Hence, sufficient magnetite has to be formed to explain the magnetite enhancement concomitant with an increased hematite concentration in HCP samples. The occurrence of hematite and high $B_{1/2}$ values of both magnetite phases are indicative for maghemitization of magnetite.

7.4 Magnetic parameters as proxy for water availability

The rock magnetic parameters together with the geochemical proxies allow for a detailed interpretation of the depositional conditions, in particular water availability. The groundwater level is used for the facies classification of the different beds (Fig. 2b). The rock magnetic parameters that depend on magnetic concentration roughly mirror the facies code, i.e. when the water availability is high then magnetic concentration is low (Fig. 2c-f, in particular Beds 5, 7, 9 and 11). Low concentration values coincide with elevated Ca content (Fig. 5e), which is linked to increased rates of authigenic mineral precipitation (i.e. carbonate), which lowers the proportion of magnetic minerals in sediments deposited at higher water availability especially under subaquatic conditions.

Furthermore, the variation of the concentration dependent parameters suggest that magnetic parameter variations allow a more detailed interpretation of the water availability during the deposition of the studied playa cycle than the facies code (Fig. 7). For example, the lighter colored top layer of Bed 4 show lower concentration dependent values indicating short periods of higher groundwater level. Conversely, SIRM and HIRM values increase between 3.25 and 3.5 m suggesting an episode of deposition under drier conditions. Throughout the playa cycle, short-termed groundwater table lowering (dry mudflat facies) or ephemeral subaqueous deposition (ephemeral playa lake facies), led to a varying amount to dilution of clastic sediment by increased carbonate precipitation. The magnetic concentration dependent parameters well reflect these groundwater level changes with typical lower values in limestone beds and higher values in marl layers, and thus seem to be associated with water availability during deposition of the playa sediments in the Aktau Mountains (Fig. 7). Verestek et al. (2018) found a similar relationship for the Bastau Fm, which underlays the Koktal Fm.

It was shown that the s-ratio could be used as a proxy for the oxygenation of the sediment/soil. Enhanced oxidation of magnetite to hematite occurs at groundwater table lowstands, when the top of the capillary zone sinks below the sediment surface, enabling the infiltration of atmospheric oxygen.

The groundwater availability in the Koktal Fm is driven by the balance of moisture supply to the catchment area and water loss by evaporation in the hydrologically closed Ili Basin (Frisch et al., 2018). Regional climate variation controlled the water budget in the semi-arid to arid middle Miocene basin resulting in mudflat and intermittent playa lake deposits in the Aktau Mountains. Thus, the rock magnetic parameters do no only reflect groundwater availability but can also be interpreted as an indicator for aridity changes. In the Aktau Mountains, variations in aridity and groundwater availability caused varying deposition conditions with likely varying availability of iron sources for post-depositional formation of magnetite. We propose that rock magnetic parameters such as χ, ARM, SIRM, HIRM, ARM/SIRM and s-ratio are potentially effective proxy indices for detailed paleo-environment reconstruction not only in the middle Miocene Ili Basin but also in comparable floodplain/playa lake settings.

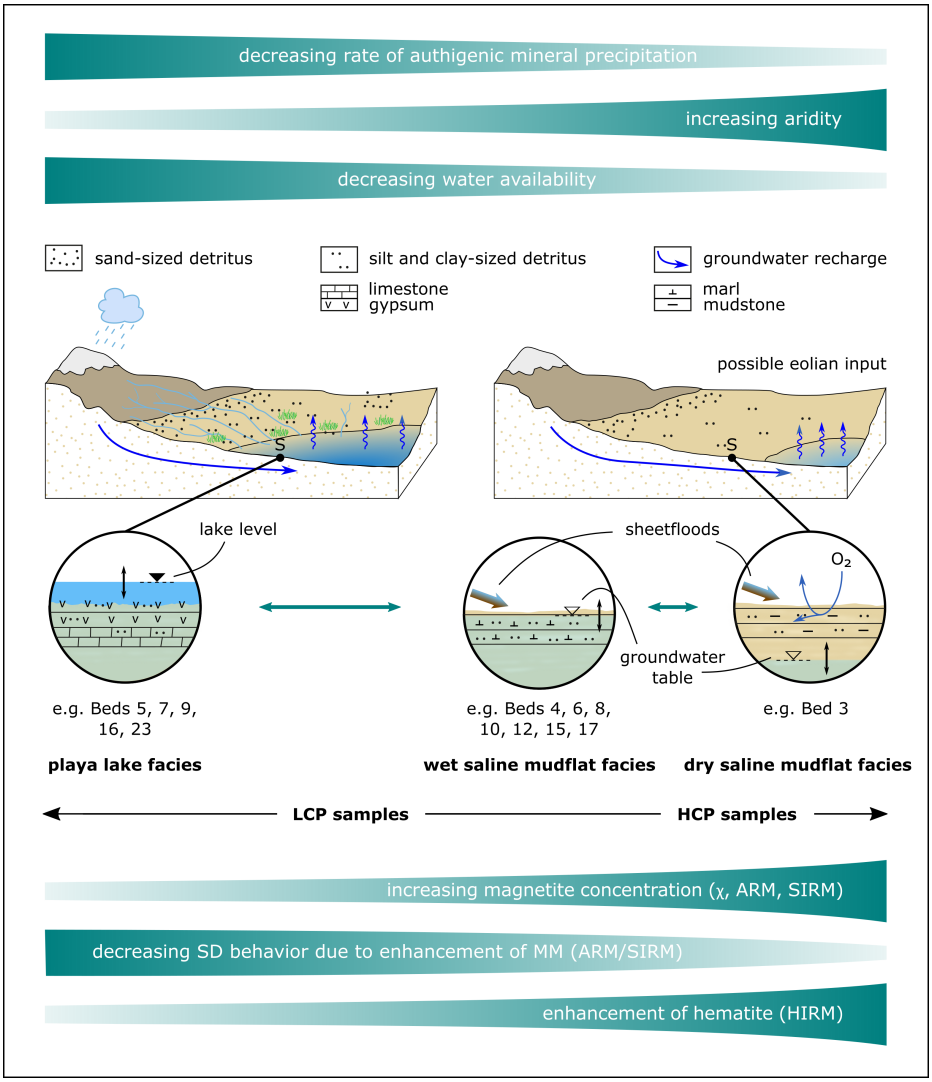

Figure 7: Summarizing sketch of the depositional conditions in the Ili basin and rock magnetic signature of the playa cycle. The schematic position of the studied sequence within the Ili Basin is marked by an S. In the presented scenario, the variations in the magnetic record are controlled by enhancement of authigenic magnetite formation (MM fraction) and increased hematite concentrations due to LTO. The higher MM/HM ratio in HCP samples causes the decreasing single domain (SD) behavior. In the playa cycle, rock magnetic properties reflect not only water availability and aridity changes but allow for a more detailed interpretation of the hydrologic conditions, in particular during increased aridity

8 Conclusions

The studied playa cycle of middle Miocene age from the Aktau Mountains in the Ili Basin, SE Kazakhstan, shows a distinct magnetic signature. In this study, we present detailed rock magnetic data of the continuously sampled playa cycle together with geochemical element contents.

A complex interplay of various processes during and after deposition likely controlled the rock magnetic mineralogy in the playa cycle. The magnetic signal is carried by two magnetite fractions and a hematite phase in varying relative and absolute contributions. A biogenic origin of the HM fraction, post-depositional formation of the MM fraction and hematite formation by LTO are the most likely scenario explaining the observed magnetic variations.

The magnetic concentration dependent parameters, i.e. χ, ARM, SIRM and HIRM, do not only mirror the lithofacies of the playa cycle but allow a more differentiated interpretation of the water availability during deposition and thus aridity changes in the Aktau Mountains. The s-ratio is linked to the groundwater table. Low s-ratio values point to enhanced oxidation due to infiltration of atmospheric oxygen during groundwater table lowstands when the top of the capillary fringe sinks below the sediment surface. These parameters together with the magnetic grain size dependent ratios (χ_{fd}, χ_{ARM}/χ and ARM/SIRM) and geochemical element contents are effective proxies for a detailed paleo-environmental reconstruction of the middle Miocene Ili Basin. This study further suggests that rock magnetic parameters are potentially effective proxies for similar floodplain/playa lake settings.

Acknowledgments

We wish to thank the administration and rangers of the State National Park Altyn Emel for providing access to the Aktau Mountains, and gratefully acknowledge Konstantin Kossov and Julia Zhilkina for their support in the field. This study was financed by the Deutsche Forschungsgemeinschaft (DFG grant AP 34/41-1 and VO 687/16-1).

References

Abdul Aziz, H., Hilgen, F., Krijgsman, W., Sanz, E., Calvo, J. P. 2000. Astronomical forcing of sedimentary cycles in the middle to late Miocene continental Calatayud Basin (NE Spain). Earth Planet. Sci. Lett. 177(1-2), 9-22, doi: 10.1016/S0012-821X(00)00035-2.

Ahmed, I., Maher, B. A. 2018. Identification and paleoclimatic significance of magnetite nanoparticles in soils. Proc. Natl. Acad. Sci. USA 115(8), 1736-1741. doi: 10.1073/pnas.1719186115.

Amante, C., Eakins, B. W. 2009. ETOPO1 1 Arc-Minute Global Relief Model: Procedures, Data Sources and Analysis. NOAA Technical Memorandum NESDIS NGDC-24, Nat. Geophys. Data Center, NOAA. doi: 10.7289/v5c8276m.

Ao, H., Dekkers, M. J., Deng, C. L., Zhu, R. X. 2009. Paleoclimatic significance of the Xiantai fluvio-lacustrine sequence in the Nihewan Basin (North China), based on rock magnetic properties and clay mineralogy. Geophys. J. Int. 177, 913-924. doi: 10.1111/j.1365-246X.2008.04082.x.

Appel, E., Soffel, H. C. 1985. Domain state of Ti-rich titanomagnetites deduced from domain structure observations and susceptibility measurements. J. Geophys. 56, 121-132.

Appel, E. 1987. Stress anisotropy in Ti-rich titanomagnetites. Phys. Earth Planet. Inter. 46 (1-3), 233-240. doi: 10.1016/0031-9201(87)90185-3

Arenas, C., Alonso Zarza, A. M., Pardo, G. 1999. Dedolomitization and other early diagenetic processes in Miocene lacustrine deposits, Ebro Basin (Spain). Sed. Geol. 125, 23-45. doi: 10.1016/S0037-0738(98)00146-8.

Bazhanov, V. S., Kostenko, N. N. 1961. "Geologicheskiy razrez Dzhungarskogo Alatau i ego paleozoologicheskoye obosnovanie [Geological section of Dzhungarian Alatau and its paleontological basis]," in Materialy po Istorii Fauny i Flory Kazakhstana, ed I. G. Galuzo (Alma Ata: Akademia Nauk Kazakhskoy SSR), 47-52.

Beske-Diehl, S. J., Soroka, W. L. 1984. Magnetic properties of variably oxidized pillow basalt. Geophys. Res. Lett. 11, 225-228. doi: 10.1029/GL011i003p00217

Bloemendal, J., King, J., Hall, F. R., Doh, S.-J. 1992. Rock magnetism of Late Neogene and Pleistocene deep-sea sediments: relationship to sediment source, diagenetic processes, and sediment lithology. J. Geophys. Res. 97, 4361-4375. doi: 10.1029/91JB03068.

Bowler, J. M., Teller, J. T. 1986. Quaternary evaporites and hydrological changes, Lake Tyrrell, North-West Victoria. Aust. J. Earth Sci. 33, 43-63. doi: 10.1080/08120098608729349

Bowles, J., Jackson, M., Chen, A., Solheid, P. 2009. Interpretation of low-temperature data, part 1: Superparamagnetism and paramagnetism. IRM Quart. 19, 7-11.

Briere, P. R. 2000. Playa, playa lake, sabkha: Proposed definitions for old terms. J. Arid Environ. 45, 1-7, doi: 10.1006/jare.2000.0633.

Canfield, D. E., Berner, R. A. 1987. Dissolution and pyritization of magnetite in anoxic marine sediments. Geochim. Cosmochim. Acta 51, 645-659. doi: 10.1016/0016-7037(87)90076-7.

Caves, J. K., Winnick, M. J., Graham, S. A., Sjostrom, D. J., Mulch, A., Chamberlain, C. P. 2015. Role of the westerlies in Central Asia climate over the Cenozoic. Earth Planet. Sci. Lett. 428, 33-43. doi: 10.1016/j.epsl.2015.07.023

Chang, L., Winklhofer, M., Roberts, A. P., Heslop, D., Florindo, F., Dekkers, M. J., Krijgsman, W., Kodama, K., Yamamoto, Y. 2013. Low-temperature magnetic properties of pelagic carbonates: Oxidation of biogenic magnetite and identification of magnetosome chains. J. Geophys. Res. 118, 6049-6065. doi: 10.1002/2013JB010381.

Channell, J. E. T., Hodell, D. A., Margari, V., Skinner, L. C., Tzedakis, P. C., Kesler, M. S. 2013. Biogenic magnetite, detrital hematite, and relative paleointensity in Quaternary sediments from the Southwest Iberian Margin. Earth Planet. Sci. Lett. 376, 99-109. doi: 10.1016/j.epsl.2013.06.026.

Crusius, J., Calvert, S., Pedersen, T., Sage, D. 1996. Rhenium and molybdenum enrichments in sediments as indicators of oxic, suboxic and sulfidic conditions of deposition. Earth Planet. Sci. Let. 145, 65-78. doi: 10.1016/S0012-821X(96)00204-X.

Cumberland, S. A., Douglas, G., Grice, K., Moreau, J. W. 2016. Uranium mobility in organic matter-rich sediments: A review of geological and geochemical processes. Earth Sci. Rev. 159, 160-185. doi: 10.1016/j.earscirev.2016.05.010.

Dean, W. E., Gardner, J. V., Piper, D. Z. 1997. Inorganic geochemical indicators of glacial-interglacial changes in productivity and anoxia on the California continental margin. Geochim. Cosmochim. Ac. 61, 4507-4518. doi: 10.1016/S0016-7037(97)00237-8.

Demory, F., Oberhänsli, H., Nowaczyk, N. R., Gottschalk, M., Wirth, R., Naumann, R. 2005. Detrital input and early diagenesis in sediments from Lake Baikal revealed by rock magnetism. Glob. Planet. Change 46, 145-166. doi: 10.1016/j.gloplacha.2004.11.010.

Deng, C. L., Liu, Q. S., Wang, W., Liu, C. C. 2007. Chemical overprint on the natural remanent magnetization of a subtropical red soil sequence in the Bose Basin, southern China. Geophys. Res. Lett. 34, L22308. doi: 10.1029/2007GL031400.

Deocampo, D. M., Cuadros, J., Wing-Dudek, T., Olives, J., Amouric, M. 2009. Saline Lake diagenesis as revealed by coupled mineralogy and geochemistry of multiple ultrafine clay phases: Pliocene Olduvai Gorge, Tanzania. Am. J. Sci. 309, 834-868. doi: 10.2475/09.2009.03.

Deotare, B. C., Kajale, M. D., Rajaguru, S. N., Basavaiah, N. 2004. Late Quaternary geomorphology, palynology and magnetic susceptibility of playas in western margin of the Indian Thar Desert. J. Ind. Geophys. Union 8(1), 15-25.

Dinarès-Turell, J., Hoogakker, B. A. A., Roberts, A. P., Rohling, E. J., Sagnotti, L. 2003. Quaternary climatic control of biogenic magnetite production and eolian dust input in cores from the Mediterranean Sea. Palaeogeogr. Palaeoclimatol. Palaeoecol. 190, 195-209. doi: 10.1016/S0031-0182(02)00605-3.

Dzhamangaraeva, A. K. 1997. Pliocene charophytes from Aktau Mountain, southeastern Kazakhstan. Geobios 30, 475-479. doi: 10.1016/S0016-6995(97)80115-5.

Erickson, B. E., Helz, G. R. 2000. Molybdenum(VI) speciation in sulfidic waters: Stability and lability of thiomolybdates. Geochim. Cosmochim. Ac. 64(7), 1149-1158. doi: 10.1016/S0016-7037(99)00423-8.

Eugster, H. P., Hardie, L. A. 1978. Saline Lakes. In: Lakes: Chemistry, Geology, Physics. Learman, A. (Editor), pp. 237-293. Springer, New York, Heidelberg, Berlin. doi: 10.1007/978-1-4757-1152-3_8.

Evans, M. E., Heller, F. 2003. Environmental Magnetism: Principles and Applications of Environmagnetics. Academic Press, New York.

Fang, X. M., Zan, J. B., Appel, E., Lu, Y., Song, C. H., Dai, S., Tuo, S. B. 2015. An Eocene-Miocene continuous rock magnetic record from the sediments in the Xining Basin, NW China: indication for Cenozoic persistent drying driven by global cooling and Tibetan Plateau uplift. Geophys. J. Int. 201(1), 78-89, 1 doi: 10.1093/gji/ggv002.

Florindo, F., Roberts, A., Palmer, M. R. 2003. Magnetite dissolution in siliceous sediments. Geochem. Geophys. Geosyst. 4(7):1053. doi: 10.1029/2003GC000516.

Frisch, K., Voigt, S., Voigt, T., Hellwig, A., Verestek, V., Weber, Y. 2018. Extreme aridity prior to lake expansion deciphered from facies evolution in the Miocene Ili Basin, SE Kazakhstan. Sedimentology, accepted. doi: 10.1111/sed.12556.

Geiss, C. E., Zanner, C. W. 2006. How abundant is pedogenic magnetite? Abundance and grain size estimates for loessic soils based on rock magnetic analyses. J. Geophys. Res. 111, B12S21. doi: 10.1029/2006jb004564.

Guo, Z. T., Ruddiman, W. F., Hao, Q. Z., Wu, H. B., Qiao, Y. S., Zhu, R. X., Peng, S. Z., Wei, J. J., Yuan, B. Y., Liu, T. S. 2002. Onset of Asian desertification by 22 Myr ago inferred from loess deposits in China. Nature 416, 159-163. doi: 10.1038/416159a

Hardie, L. A., Smoot, J. P., Eugster, H. P. 1978. Saline lakes and their deposits: a sedimentological approach. In: Modern and ancient lake sediments. Matter, A., Tucker, M.E. (Editors), Int. Assoc. Sedimentol. Spec. Publ. 2, 7-41. doi: 10.1002/9781444303698.ch2.

Hellwig, A., Voigt, S., Mulch, A., Frisch, K., Bartenstein, A., Pross, J., Gerdes, A., Voigt, T. 2018. Late Oligocene to early Miocene humidity change recorded in terrestrial sequences in the Ili Basin (south-eastern Kazakhstan, Central Asia. Sedimentology 65, 517-539. doi: 10.1111/sed.12390.

Herb, C., Zhang, W., Koutsodendris, A., Appel, E., Fang, X., Pross, J. 2013. Environmental implications of the magnetic record in Pleistocene lacustrine sediments of the Qaidam Basin, NE Tibetan Plateau. Quater. Int. 313, 218-229. doi: 10.1016/j.quaint.2013.06.015.

Herb, C., Koutsodendris, A., Zhang, W., Appel, E., Fang, X., Voigt, S., Pross, J., 2015. Late Plio-Pleistocene humidity fluctuations in the western Qaidam Basin (NE Tibetan Plateau) revealed by an integrated magnetic-palynological record from lacustrine sediments. Quarter. Res. 84, 457-466. doi: 10.1016/j.yqres.2015.09.009.

Housden, J., O'Reilly, W. 1990. On the intensity and stability of the natural remanent magnetization of ocean floor basalts. Phys. Earth Planet. Inter. 64, 261-278. doi: 10.1016/0031-9201(90)90042-V.

Hu, S., Deng, C., Appel, E., Verosub, K. L. 2002. Environmental magnetic studies of lacustrine sediments. Chin. Sci. Bull. 47(7), 613-616. doi: 10.1360/02tb9141.

Hu, S., Goddu, S., Herb, C., Appel, E., Gleixner, G., Wang, S., Yang, X., Zhu, X. 2015. Climate variability and its magnetic response recorded in a lacustrine sequence in Heqing basin at the SE Tibetan Plateau since 900 ka. Geophys. J. Int. 201, 444-458. doi: 10.1093/gji/ggv033.

Huerta, P., Armenteros, I., Recio, C., Blanco, J. A. 2010. Palaeogroundwater evolution in playa-lake environments: Sedimentary facies and stable isotope record (Palaeogene, Almazán basin, Spain). Palaeogeogr. Palaeoclimatol. Palaeoecol. 286, 135-148. doi: 10.1016/j.palaeo.2009.12.008.

Huggett, J. M. 2005. Low-temperature illitization of smectite in the late Eocene and early Oligocene of the Isle of Wight (Hampshire basin), U.K. Am. Mineral. 90, 1192-1202. doi: 10.2138/am.2005.1674.

Jelinek, V. 1981. Characterization of the magnetic fabrics of rocks. Tectonophysics 79, 63-67. doi: 10.1016/0040-1951(81)90110-4.

Karlin, R., Levi, S. 1985. Geochemical and sedimentological control of the magnetic properties of hemipelagic sediments. J. Geophys. Res. 90, 10373-10392. doi: 10.1029/JB090iB12p10373.

Katz, B., Elmore, R. D., Engel, M. H. 1998. Authigenesis of magnetite in organic-rich sediment next to a dike: implications for thermoviscous and chemical remagnetizations. Earth Planet. Sci. Lett. 163, 221-234. doi: 10.1016/S0012-821X(98)00189-7.

Katz, B., Elmore, R. D., Cogoini, M., Engel, M. H., Ferry, S. 2000. Associations between burial diagenesis of smectite, chemical remagnetization, and magnetite authigenesis in the Vocontian trough, SE France. J. Geophys. Res. 105, 851-868. doi: 10.1029/1999JB900309.

Kodama, K. P. 2012. Paleomagnetism of Sedimentary Rocks: Process and Interpretation. Wiley-Blackwell, Oxford. doi: 10.1002/9781118384138.

Kordikova, E. G. 2000. Insectivora (Mammalia) from the Lower Miocene of the Aktau Mountains, South-Eastern Kazakhstan. Senckenb. Lethaea 80, 67-79. doi: 10.1007/BF03043665.

Kordikova, E. G., de Bruijn, H. 2001. Early Miocene Rodents from the Aktau Mountains (South-Eastern Kazakhstan). Senckenb. Lethaea 81, 391-405. doi: 10.1007/BF03042791.

Kordikova, E. G., Mavrin, A. V. 1996. Stratigraphy and Oligocene-Miocene mammalian biochronology of the Aktau Mountains, Dzhungarian Alatau range, Kazakhstan. Palaeovertebrata 25, 141-174.

Kröner, A., Kovach, V., Belousova, E., Hegner, E., Armstrong, R., Dolgopolova, A., Seltmann, R., Alexeiev, D. V., Hoffmann, J. E., Wong, J., Sun, M., Cai, K., Wang, T., Tong, Y., Wilde, S. A., Degtyarev, K. E., Rytsk, E. 2014. Reassessment of continental growth during the accretionary history of the Central Asian Orogenic Belt. Gondwana Res., 25, 103-125. doi: 10.1016/j.gr.2012.12.023.

Kruiver, P. P., Krijgsman, W., Langereis, C. G., Dekkers, M. J. 2005. Cyclostratigraphy and rock-magnetic investigation of the NRM signal in late Miocene palustrine-alluvial deposits of the Librilla section (SE Spain). J. Geophys. Res. 107(B12), 2334. doi: 10.1029/2001JB000945.

Larson, E. D., Walker, T. R. 1975. Development of chemical remanent magnetization during early stages of red-bed formation in Late Cenozoic sediments, Baja, California. Geol. Soc. Am. Bull. 86, 639-650. doi: 10.1130/0016-7606(1975)86<639:DOCRMD>2.0.CO;2

Li, Y.-X., Yu, Z. C., Kodama, K. P. 2006a. Sensitive moisture response to Holocene millennial-scale climate variations in the Mid-Atlantic region, USA. The Holocene, 17(1), 3-8. doi: 10.1177/0959683606069386.

Li, Y.-X., Yu, Z. C., Kodama, K. P., Moeller, R. E. 2006b. A 14,000-year environmental change history revealed by mineral magnetic data from White Lake, New Jersey, USA. Earth Planet. Sci. Lett. 2006, 27-40. doi: 10.1016/j.epsl.2006.03.052.

Liddicoat, J. C., Opdyke, N. D., Smith, G. I. 1980. Palaeomagnetic polarity in a 930-m core from Searles Valley, California, Nature, 286, 22-25. doi: 10.1038/286022a0.

Liu, J., Zhu, R., Roberts, A. P., Li, S., Chang, J.-H. 2004. High-resolution analysis of early diagenetic effects on magnetic minerals in post-middle-Holocene continental shelf sediments from the Korea Strait. J. Geophys. Res. 109, B03103, doi: 10.1029/2003JB002813.

Lowenstein, T. K., Hardie, L. A. 1985. Criteria for the recognition of salt-pan evaporites. Sedimentology 32, 627-644. doi:10.1111/j.1365-3091.1985.tb00478.x

Lucas, S. G., Bayshashov, B. U., Tyutkova, L. A., Zhamangara, A. K., Aubekerov, B. Z. 1997. Mammalian biochronology of the Paleogene-Neogene boundary at Aktau Mountain, eastern Kazakhstan. Paläontol. Z. 71, 305-314. doi: 10.1007/BF02988498.

Lucas, S. G., Aubekerov, B. Z., Dzhamangaraeva, A. K., Bayshashov, B. U., Tyutkova, L. A. 2000. Cenozoic lacustrine deposits of the Ili basin, southeastern Kazakhstan, in Lake Basins Through Space and Time. E. Gierlowski-Kordesch, K. R. Kelts (Editors), AAPG Studies in Geology, 59-64. doi: 10.1306/St46706C3.

Maher, B. A., Taylor, R. M. 1988. Formation of ultrafine-grained magnetite in soils. Nature, 336, 368-370. doi: 10.1038/336368a0.

Maher, B. A. 1998. Magnetic properties of modern soils and Quaternary loessic paleosols: Paleoclimatic implications. Palaeogeogr. Palaeoclimatol. Palaeoecol. 137(1-2), 25-54. doi: 10.1016/S0031-0182(97)00103-X.

Maher, B. A., Alekseev, A. O., Alekseeva, T. 2003. Magnetic mineralogy of soils across the Russian steppe: Climate dependence of pedogenic magnetite formation. Palaeogeogr. Palaeoclimatol. Palaeoecol., 201, 321-341. doi: 10.1016/S0031-0182(03)00618-7.

Maher, K., Bargar, J. R., Brown, G. E. 2013. Environmental Speciation of Actinides. Inorg. Chem. 52 (7), 3510-3532. doi: 10.1021/ic301686d

Maxbauer, D. P., Feinberg, J. M., Fox, D. L. 2016a. Magnetic mineral assemblages in soils and paleosols as the basis for paleoprecipitation proxies: A review of magnetic methods and challenges. Earth Sci. Rev. 155, 28-48. doi: 10.1016/j.earscirev.2016.01.014.

Maxbauer, D. P., Feinberg, J. M., Fox, D. L. 2016b. MAX UnMix: A web application for unmixing magnetic coercivity distributions. Comput. Geosci. 95, 140-145. doi: 10.1016/j.cageo.2016.07.009.

McCabe, C., Elmore, R.D. 1989. The occurrence and origin of Late Paleozoic remagnetization in the sedimentary rocks of North America. Rev. of Geophys. 27, 471-494. doi: 10.1029/RG027i004p00471.

McCabe, C., Jackson, M., Saffer, B. 1989. Regional patterns of magnetite authigenesis in the Appalachian Basin; implications for the mechanism of late Paleozoic remagnetization. J. Geophys. Res. 94, 10429-10443. doi: 10.1029/JB094iB08p10429.

McNeill, D. F. 1990. Biogenic magnetite from surface Holocene carbonate sediments, Great Bahama Bank, J. Geophys. Res. 95, 4363-4371. doi:10.1029/JB095iB04p04363.

Miao, Y., Herrmann, M., Wu, F., and Yan, X., Yang, S. 2012. What controlled Mid-Late Miocene long-term aridification in Central Asia? - Global cooling or Tibetan Plateau uplift: a review. Earth Sci. Rev. 112, 155-172. doi: 10.1016/j.earscirev.2012.02.003.

Miot, J., Li, J., Benzerara, K., Sougrati, M. T., Ona-Nguema, G., Bernard, S., Jumas, J.-C., Guyot, F. 2014. Formation of single domain magnetite by green rust oxidation promoted by microbial anaerobic nitrate-dependent iron oxidation. Geochim Cosmochim Acta 139, 327-343. doi: 10.1016/j.gca.2014.04.047.

Moreau, M. G., Ader, M., Enkin, R. J. 2005. The magnetization of clay-rich rocks in sedimentary basins: low-temperature experimental formation of magnetic carriers in natural samples. Earth Planet. Sci. Lett 230, 193-210. doi: 10.1016/j.epsl.2004.11.013.

Moskowitz, B. M., Frankel, R. B., Bazylinski, D. A. 1993. Rock magnetic criteria for the detection of biogenic magnetite. Earth Planet. Sci. Lett., 120, pp. 283-300. doi: 10.1016/0012-821X(93)90245-5.

Negrini, R. M., Erbes, D. B., Faber, K., Herrera, A., Roberts, A. P., Cohen, A. S., Wigand, P. E., Foit, F. F. 2000. A paleoclimate record for the past 250,000 years from Summer Lake, Oregon, USA: I. Chronology and magnetic proxies for lake level. Jour. Paleolim. 24, 125-149. doi: 10.1023/A:1008144025492.

Nichols, G.J., Fisher, J.A. 2007. Processes, facies and architecture of fluvial distributary system deposits. Sed. Geol. 195, 75-90. doi: 10.1016/j.sedgeo.2006.07.004.

Oldfield, F. 1994. Toward the discrimination of fine-grained ferrimagnets by magnetic measurements in lake and near-shore marine sediments. J. Geophys. Res., 99, 9045-9050. doi: 10.1029/93JB03137.

Orgeira, M., Egli, R., Compagnucci, R. 2011. A Quantitative Model of Magnetic Enhancement in Loessic Soils. In: The Earth's Magnetic Interior 1. Petrovsky, E., Ivers, D., Harinarayana, T., Herrero-Bervera, E. (Editors), Springer, 361-397. doi: 10.1007/978-94-007-0323-0_25.

Peck, J. A., King, J. W., Colman, S. M., Kravchinsky, V. A. 1994. A rock-magnetic record from Lake Baikal, Siberia: evidence for Late Quaternary climate change. Earth Planet. Sci. Lett. 122, 221-238. doi: 10.1016/0012-821X(94)90062-0.

Pluhar, C. J., Holt, J., Kirschvink, J., Adams, R. 1992. Magnetostratigraphy of the Confidence Hills formation, Southern Death Valley, California. San Bernardino County Museum Association Quarterly 39(2), p. 12-19.

Ramstein, G., Fluteau, F., Besse, J., Joussaume, S. 1997. Effect of orogeny, plate motion and land-sea distribution on Eurasian climate change over the past 30 million years. Nature 386, 788-795. doi: 10.1038/386788a0.

Roberts, A. P. 2015. Magnetic mineral diagenesis. Earth Sci. Rev. 151, 1-47. doi: 10.1016/j.earscirev.2015.09.010.

Rosen, M. R. 1991. Sedimentologic and geochemical constraints on the evolution of Bristol Dry Lake Basin, California, U.S.A. Palaeogeogr., Palaeoclimatol., Palaeoecol. 84, 229-257. doi: 10.1016/0031-0182(91)90046-T.

Rosen, M. R. 1994. The importance of groundwater in playas: A review of playa classifications and the sedimentology and hydrology of playas. In: Paleoclimate and Basin Evolution of Playa Systems. Rosen, M. R. (Editor), Geol. Soc. Am. Spec. Pap. 289, 1-18. doi: 10.1130/SPE289-p1.

Rosenbaum, J. G., Reynolds, R. L., Adam, D. P., Drexler, J., Sarna-Wojcicki, A. M., Whitney, G. C. 1996. Record of middle Pleistocene climate change from Buck Lake, Cascade Range, southern Oregon - Evidence from sediment magnetism, trace element geochemistry, and pollen. Geol. Soc. Amer. Bull. 108, 1328-1341. doi: 10.1130/0016-7606(1996)108<1328:ROMPCC>2.3.CO;2.

Rosenbaum, J. G., Reynolds, R. L. 2004. Basis for paleoenvironmental interpretation of magnetic sediment from Upper Klamath Lake (Oregon): effects of weathering and mineralogical sorting. J. Paleolimnol. 31, 253-265. doi: 10.1023/B:JOPL.0000019228.46421.f4.

Rowan, C. J., Roberts, A. P. 2006. Magnetite dissolution, diachronous greigite formation, and secondary magnetizations from pyrite oxidation: unravelling complex magnetizations in Neogene marine sediments from New Zealand. Earth Planet. Sci. Lett. 241, 119-137. doi: 10.1016/j.epsl.2005.10.017.

Roy, P. D., Sinha, R., Smykatz-Kloss, W., Singhvi, A. K., Nagar, Y. C. 2008. Playas of the Thar Desert: mineralogical and geochemical Archives of Late Holocene Climate. Asian. J. Earth Sci. 1, 43-61. doi: 10.3923/ajes.2008.43.61.

Sagnotti, L., Florindo, F., Wilson, G. S., Roberts, A. P., Verosub, K. L. T 1998. Environmental Magnetism of Lower Miocene Strata from the CRP-1 Core, McMurdo Sound, Antarctica. Terra Ant. 5(3), 661-667.

Sandgren, P., Risberg, J. 1990. Magnetic mineralogy of the sediments in Lake Ådran, eastern Sweden, and an interpretation of early Holocene water level changes. Boreas 19, 57-68. doi: 10.1111/j.1502-3885.1990.tb00422.x.

Schütt, B. 2000. Holocene paleohydrology of playa lakes in northern and central Spain: a reconstruction based on the mineral composition of lacustrine sediments. Quarter. Int. 73-74, 7-27. doi: 10.1016/S1040-6182(00)00062-8.

Smith, B. M. 1987. Consequences of the maghemitization on the magnetic properties of submarine basalts: synthesis of previous works and results concerning basement rocks from mainly D.S.D.P. Legs 51 and 52. Phys. Earth Planet. Inter. 46 (1-3), 206-226. doi: 10.1016/0031-9201(87)90183-X.

Snowball, I. F., Thompson, R. 1988. The occurrence of Greigite in sediments from Loch Lomond. J. Quarter. Sci. 3, 121-125. doi:10.1002/jqs.3390030203

Snowball, I. F. 1993. Geochemical control of magnetite dissolution in subarctic lake sediments and the implications for environmental magnetism. J. Quat. Sci., 8, 339-346, doi: 10.1002/jqs.3390080405.

Tang, Z., Ding, Z., White, P. D., Dong, X., Ji, J., Jiang, H., Luo, P., Wang, X. 2011. Late Cenozoic central Asian drying inferred from a palynological record from the northern Tian Shan. Earth Planet. Sci. Lett. 302, 439-447. doi: 10.1016/j.epsl.2010.12.042.

Tohver, E., Weil, A. B., Solum, J. G., Hall, C. M. 2008. Direct dating of carbonate remagnetization by ^{40}Ar/^{39}Ar analysis of the smectite-illite transformation. Earth Planet. Sci. Lett. 274, 524-530. doi: 10.1016/j.epsl.2008.08.002.

Vasconcelos, C., McKenzie, J. A., Bernasconi, S., Grujic, D., Tien, A. J. 1995. Microbial mediation as a possible mechanism for natural dolomite formation at low temperatures. Nature 377, 220-222. doi: 10.1038/377220a0.

van Velzen, A. J., Dekkers, M. J. 1999. Low-temperature oxidation of magnetite in loess-paleosol sequences: A correction of rock magnetic parameters. Stud. Geophys. Geod. 43, 357-375. doi: 10.1023/A:1023278901491.

van Velzen, A. J., Zijderveld, J. D. A. 1995. Effects of weathering on single-domain magnetite in Early Pliocene marine marls. Geophys. J. Int. 121, 267-278. doi: 10.1111/j.1365-246X.1995.tb03526.x.

Verestek, V., Appel, E., Voigt, S., Frisch, K. 2018. Constrained Magnetostratigraphic Dating of a Continental Middle Miocene Section in the Arid Central Asia. Front. Earth Sci. 6(49). doi: 10.3389/feart.2018.00049.

Voigt, S., Weber, Y., Frisch, K., Bartenstein, A., Hellwig, A., Petschick, R., Bahr, A., Pross, J., Koutsodendris, A., Voigt, T., Verestek, V., Appel, E. 2017. Climatically forced moisture supply, sediment flux and pedogenesis in Miocene mudflat deposits of south-east Kazakhstan, Central Asia. Deposit. Rec. 3. doi: 10.1002/dep2.34.

Wang, X. S., Yang, Z. Y., Lovlie, R., Min, L. R. 2004. High-resolution magnetic stratigraphy of fluvio-lacustrine succession in the Nihewan Basin, China. Quat. Sci. Rev. 23, 1187-1198. doi: 10.1016/j.quascirev.2003.11.007.

Warthmann, R., Vasconcelos, C., Sass, H., McKenzie, J. A. 2005. Desulfovibrio brasiliensis sp. nov., a moderate halophilic sulfate-reducing bacterium from Lagoa Vermelha (Brazil) mediating dolomite formation. Extremophiles 9, 255-261. doi: 10.1007/s00792-005-0441-8.

Watson, A. 1985. Structure, chemistry and origins of gypsum crusts in southern Tunisia and the central Namib Desert. Sedimentology 32, 855-875. doi: 10.1111/j.1365-3091.1985.tb00737.x.

Wei, Z., Zhong, W., Shang, S., Ye, S., Tang, X., Xue, J., Ouyang, J., Smol, S. P. 2018. Lacustrine mineral magnetic record of postglacial environmental changes from Dahu Swamp, southern China. Global Planet. Change 170, 62-75. doi: 10.1016/j.gloplacha.2018.08.010.

Woods, S. D., Elmore, R. D., Engel, M. H. 2002. Paleomagnetic dating of the smectite-to-illite conversion: Testing the hypothesis in Jurassic sedimentary rocks, Skye, Scotland. J. Geophys. Res. 107(B5). doi: 10.1029/2000JB000053.

Zhang, W. L., Appel, E., Fang, X. M., Song, C. H., Cirpka, O. 2012. Magnetostratigraphy of deep drilling core SG-1 in the western Qaidam Basin (NE Tibetan Plateau) and its tectonic implications. Quat. Res. 78, 139-148. doi: 10.1016/j.yqres.2012.03.011.

Zhou, L. P., Oldfield, F., Wintle, A.G., Robinson, S.G., Wang, J.T. 1990. Partly pedogenic origin of magnetic variations in Chinese loess. Nature, 346, 737-739. doi: 10.1038/346737a0.

Chapter 5

Climatically forced moisture supply, sediment flux and pedogenesis in Miocene mudflat deposits of south-east Kazakhstan, Central Asia

Author	Author position	Scientific ideas	Data generation	Analysis & interpretation	Paper writing
Silke Voigt	1	100%	25%	25%	70%
Yuki Weber	2	-	40%	40%	26%
Konstantin Frisch	3	-	2%	5%	-
Alexander Bartenstein	4	-	5%	2%	-
Alexandra Hellwig	5	-	-	2%	-
Rainer Petschick	6	-	2%	2%	-
André Bahr	7	-	2%	2%	-
Jörg Pross	8	-	15%	5%	2%
Andreas Koutsodendris	9	-	5%	2%	-
Thomas Voigt	10	-	-	5%	2%
Verena Verestek	11	-	2%	5%	-
Erwin Appel	12	-	2%	5%	-
Status in publication process:		published			

The Depositional Record
The journal of the International Association of Sedimentologists
Open Access

ORIGINAL RESEARCH ARTICLE

Climatically forced moisture supply, sediment flux and pedogenesis in Miocene mudflat deposits of south-east Kazakhstan, Central Asia

SILKE VOIGT*, YUKI WEBER*,†, KONSTANTIN FRISCH*, ALEXANDER BARTENSTEIN*, ALEXANDRA HELLWIG*, RAINER PETSCHICK*, ANDRÉ BAHR*,‡, JÖRG PROSS*,‡, ANDREAS KOUTSODENDRIS‡, THOMAS VOIGT§, VERENA VERESTEK¶ and ERWIN APPEL¶

*Institute of Geosciences, Goethe University Frankfurt, Altenhöferallee 1, 60438 Frankfurt, Germany (E-mail: s.voigt@em.uni-frankfurt.de)
†Department of Earth and Planetary Sciences, Harvard University, 20 Oxford Street, Cambridge, MA 02138, USA
‡Institute of Earth Sciences, Heidelberg University, Im Neuenheimer Feld 234-236, 69120 Heidelberg, Germany
§Institute of Geosciences, Friedrich Schiller University Jena, Burgweg 11, 07749 Jena, Germany
¶Institute of Geosciences, University Tübingen, Sigwartstrasse 10, Hölderlinstrasse 12, 72074 Tübingen, Germany

Keywords
Central Asia, climate, Miocene, pedogenesis, sediment flux, terrestrial sedimentation.

Manuscript received: 3 May 2017; Accepted: 29 August 2017

The Depositional Record 2017; 3(2): 209–232

doi: 10.1002/dep2.34

ABSTRACT

The continental settings of Central Asia witnessed increased desertification during the Cenozoic as a result of mountain uplift and the Paratethys retreat. The interaction of these tectonic-scale processes with orbitally forced climate change and their influence on Asia's atmospheric moisture distribution are poorly constrained. A Miocene succession of continental mudflat deposits, exposed in the Aktau Mountains (Ili Basin, south-east Kazakhstan), has great potential as a terrestrial palaeoclimate archive. About 90 m of the 1700 m thick succession comprise alluvial mudflat deposits and appear as cyclic alternation of coarse sheet floods, mudflat fines and semi-arid hydromorphic soils. In this study, bulk-sediment mineralogy and geochemistry, magnetic susceptibility, sediment colour and palynology are used to reconstruct environmental conditions by determining changes and forcing mechanisms in the intensity of sediment discharge, weathering and pedogenesis. The results presented here indicate four major periods of arid soil formation and one palustrine interval characterized by higher evaporation rates under highly alkaline/saline conditions. A positive correlation between weathering indices and the Mg/Al ratio suggest that these horizons correspond to maximum rates of evapotranspiration and aridity. The formation of mudflat fines is, instead, interpreted as representing higher detrital sediment production by more intense alluvial fan activity during times of higher precipitation. Time series analysis of weathering indices, colour and magnetic susceptibility data yields cycle-to-frequency ratios with the potential to represent Milankovitch cyclicity with short and long eccentricity as dominant periodicities. Periods of pronounced aridity, paced by long eccentricity forcing, reflect changes in moisture availability. On longer tectonic timescales, the persistent appearance of gypsum indicates a shift towards more arid conditions. This trend in climate is considered to result from the closure of the eastern gateway of the Mediterranean to the Indian Ocean that restricted circulation and enhanced salinity within the Eastern Paratethys.

INTRODUCTION

The evolution of Cenozoic climate is characterized by global cooling, increased meridional temperature gradients and the expansion of polar ice sheets in Antarctica and the Northern Hemisphere since *ca* 35 Ma and *ca* 15 Ma, respectively (Zachos *et al.*, 2008; De Vleeschouwer *et al.*, 2017). The mechanisms behind this global cooling, its

regional differentiation and the feedbacks involved are still a matter of debate. Continental settings of Central Asia witnessed increased desertification and the establishment of a monsoonal climate during the Cenozoic as a result of India's collision with Asia and the Paratethys retreat (Molnar & Tapponnier, 1975; Ramstein *et al.*, 1997). However, the timing of this continent-scale climate shift relative to global climate evolution, the interplay between regional and global factors and the effects of orbital-scale processes are not yet well constrained.

Based on loess deposits in China, the existence of energetic winter monsoon winds and large source areas for aeolian dust in the interior of Asia has been traced back to 22 Ma (Guo *et al.*, 2002). Alternatively, desert areas in inner Asia north of the uplifting Pamir and Tian Shan mountain chains may have been mainly influenced by westerly wind flow since Eocene to Oligocene times (Sun *et al.*, 2010; Caves *et al.*, 2015). A variety of proxy records suggests a temporally differentiated pattern for the onset of desertification in Central Asia, ranging from the Eocene/Oligocene transition in north-east Tibet and south-western Mongolia (Dupont-Nivet *et al.*, 2007; Sun & Windley, 2015) to the mid-to-late Miocene north of Tibet (Dettman *et al.*, 2003; Kent-Corson *et al.*, 2009; Sun *et al.*, 2015), and the mid-Pliocene on the Chinese Loess Plateau (Wang, 2006). Mammal diversity changes in Oligocene–Miocene successions in Mongolia provide evidence for intermittent episodes of increased precipitation (Harzhauser *et al.*, 2016) and the aeolian origin of the Valley of Lakes successions was questioned by results of clay mineralogy (Richoz *et al.*, 2017). The relative intensities of the westerlies and monsoonal wind systems played an important role in transporting moisture into Asia's continental interior (Caves *et al.*, 2015). Climate modelling results suggest reduced moisture transport to inner Asia by weakened westerlies and monsoonal winds after the global shift to cooler climate conditions in the Oligocene (Licht *et al.*, 2014).

The mid-Miocene (17 to 14 Ma) was one of the last warm periods of the Neogene (Zachos *et al.*, 2008; Holbourn *et al.*, 2014, 2015). While the proxy evidence for a warm and relatively humid mid-Miocene world is clear, the mechanisms responsible for this climate state are not. Atmospheric pCO_2 variations are supposed to drive changes in the global carbon reservoirs, implying changing rates of silicate weathering and global carbon sequestration (Holbourn *et al.*, 2015). A factor recently invoked to explain mid-Miocene warmth is a lower continental topography than today promoting a more zonal atmospheric circulation with a westerly flow over lowered mid-latitude plateaus (Henrot *et al.*, 2010). However, available proxy data yield somewhat contradictory climate scenarios for the mid-Miocene of Central Asia. While records from Mongolia and China indicate increased desertification since Oligocene to early Miocene times (Guo *et al.*, 2002; Sun & Windley, 2015), the regionally widespread formation of lacustrine deposits in eastern/south-eastern Kazakhstan and the Tarim Basin during the Miocene, described as "the great lacustrine stage", suggest increased atmospheric moisture transport to Central Asia (Akhmetyev *et al.*, 2005; Liu *et al.*, 2014). Palynological data of mid-Miocene age indicate warm-temperate conditions for the Junggar Basin and the north-east Tibetan Plateau (Hui *et al.*, 2011; Miao *et al.*, 2011; Tang *et al.*, 2011b) pointing towards a transient episode of increased humidity.

A terrestrial alluvial floodplain succession of mid-Miocene age, exposed in the Aktau Mountains of the Ili Basin, south-eastern Kazakhstan, has the potential to provide insights into the Miocene climate evolution in Central Asia (Fig. 1). In this study, bulk-sediment mineralogy and geochemistry (element geochemistry, $CaCO_3$/$CaSO_4$ content), magnetic susceptibility (MS), sediment colour and palynological data are used to decipher the regional response of sedimentary particle supply, chemical weathering intensity and pedogenesis to changes in regional moisture supply by precipitation and subsurface aquifer recharge. Furthermore, the results provide insights into climate and environmental conditions in the context of atmospheric moisture transport to Central Asia. Time series analysis of chemical weathering indices, (MS) and sediment colour data are used to decipher potential orbital forcing mechanisms.

GEOLOGICAL SETTING

The Ili Basin is a closed (endorheic) basin within the intracontinental Tian Shan mountain system. It is surrounded by continuously uplifting mountain ranges of the Zailiysky and Dzungarian Alatau and became progressively contracted by N-S shortening and fragmented due to the activation of intrabasinal basement uplifts (Kober *et al.*, 2013; Macaulay *et al.*, 2014). The basin fill covers a time span from the late Eocene to present. The Tian Shan mountain ranges grew as a result of India's collision with Asia with current crustal shortening (*ca* 20 mm y^{-1}) accounting for nearly half of India's convergence with Eurasia (Abdrakhmatov *et al.*, 1996). Exhumation and unroofing ages indicate the initial uplift of the Tian Shan to have occurred in the Oligocene to early Miocene (Hendrix *et al.*, 1994; Sobel *et al.*, 2003, 2006; Macaulay *et al.*, 2014). During these times, the central Ili Basin mainly accommodated distal, low-energy sediments on a regionally extensive peneplain while the basin margins were accompanied by alluvial fans (Kober *et al.*, 2013).

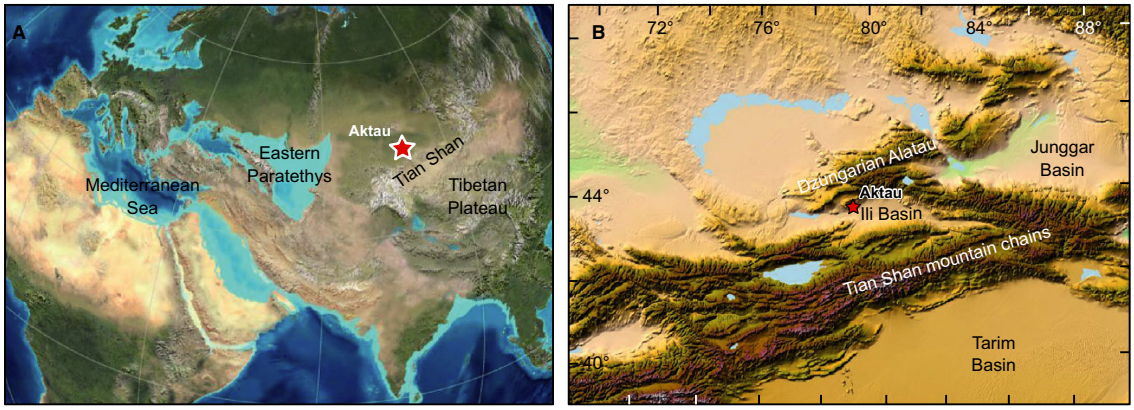

Fig. 1. Map showing the position of the Aktau succession (A) on a palaeogeographic reconstruction of the Miocene (Deep Time Maps™) and (B) on the present-day topography (Amante & Eakins, 2009).

In the Aktau Mountains, a Neogene exposure of Ili Basin sediments south of the Dzungarian Alatau (44°0′9.58″N, 79°14′56.94″E; Fig. 1), a 1700 m thick succession of fine-grained deposits forms an asymmetric anticline with a steeply to vertical dipping southern limb and a gently dipping northern flank (Bazhanov & Kostenko, 1961). Alluvial sediments of Pleistocene age disconformably overlie the succession and are involved in very young folding activity. Aktau means "White Mountains" in the Kazakh language and the succession is characterized by spectacular colour banding of its deposits (Fig. 2). The overall succession and its facies have been documented in a series of earlier studies and expose a quasi-continuous Eocene/Oligocene to Pliocene terrestrial record (Bazhanov & Kostenko, 1961; Bodina, 1961; Lucas *et al.*, 1997; Kordikova & Mavrin, 1996). Previous authors have introduced diverging lithostratigraphic schemes that are summarized by Kober *et al.* (2013). Here, the formation names of Bodina (1961) are followed together with thicknesses given by Bazhanov & Kostenko (1961) and Kordikova & Mavrin (1996), as both yield the best agreement with field observations (Fig. 3).

The succession is based in red-coloured clays and sandstones of a river system (Arasan Formation, 63 m) that grade into reddish to brown-red mud-dominated deposits, which contain distal alluvial, meandering river deposits and gypsum beds of a saline mudflat with evidence of an ephemeral playa lake (Alakul Fm, 115 m). Higher up the succession, a transition to cross-bedded fluvial sandstones of a meandering river occurs above a significant disconformity (Aidarly Fm, 130 to 140 m) overlain by cyclically bedded, reddish-brown mudflat deposits (Bastau Fm, 90 m). The upper part of the succession consists of greenish grey gypsisols and ephemeral playa lake deposits, as well as perennial lacustrine limestones with freshwater charophytes, ostracods and gastropods, and intercalated coal seems (Koktal and Kokterek Fms, 460 m). The top of the succession is represented by silty mudflat deposits with intercalations of lacustrine, fossil-rich fresh water limestones and channel sandstones indicative of a permanent river system with an adjacent fresh water lake (Ili Fm, *ca* 880 m; Fig. 2). Parent rocks for the alluvial plain deposits of the Arasan, Alakul, Bastau and Koktal formations are Permo-Carboniferous volcanics exposed in the Katutau and Dzungarian Alatau mountain ranges at the northern edge of the Ili Basin today. They comprise andesites, rhyolites and trachytes that belong to the Palaeozoic accretionary arc complex of the Central Asian Orogenic belt (Jahn *et al.*, 2000, 2004; Li *et al.*, 2015). The provenance of major parts of the basin fill from these sources is proven by proximal alluvial fan deposits close to the basin margins. In contrast, sandstones of the Arasan, Aidarly and Ili formations were mainly derived from a distant quartz-rich and mica-rich source often mixed with volcanics derived from local sources (Lucas *et al.*, 1997; Kober *et al.*, 2013).

Biostratigraphic ages are available from the fluvial Arasan and Aidarly formations and lacustrine floodplain deposits of the Ili Formation. Dating of the late Eocene (Ergilian) Arasan Formation is based on mammal bones of Brontotheriidae and the hyracodontid *Ardynia* sp. (Gromova, 1952; Lucas *et al.*, 1997). The lower Aidarly Formation is of late Oligocene age based on occurrences of the giant rhinoceros *Indricotherium* (Lucas *et al.*, 1997), while the upper Aidarly Formation is placed into the late Burdigalian to Langhian mammal zones MN4 to MN5 based on records of plants and mammals (rodents, carnivores, insectivores, the odd-toed *Gomphotherium* and early deers such as *Stephanocemas* and *Lagomeryx*) (Fig. 3; Lucas *et al.*, 1997; Kordikova, 2000; Kordikova & de Bruijn, 2001). The lower Ili Formation yields charophytes

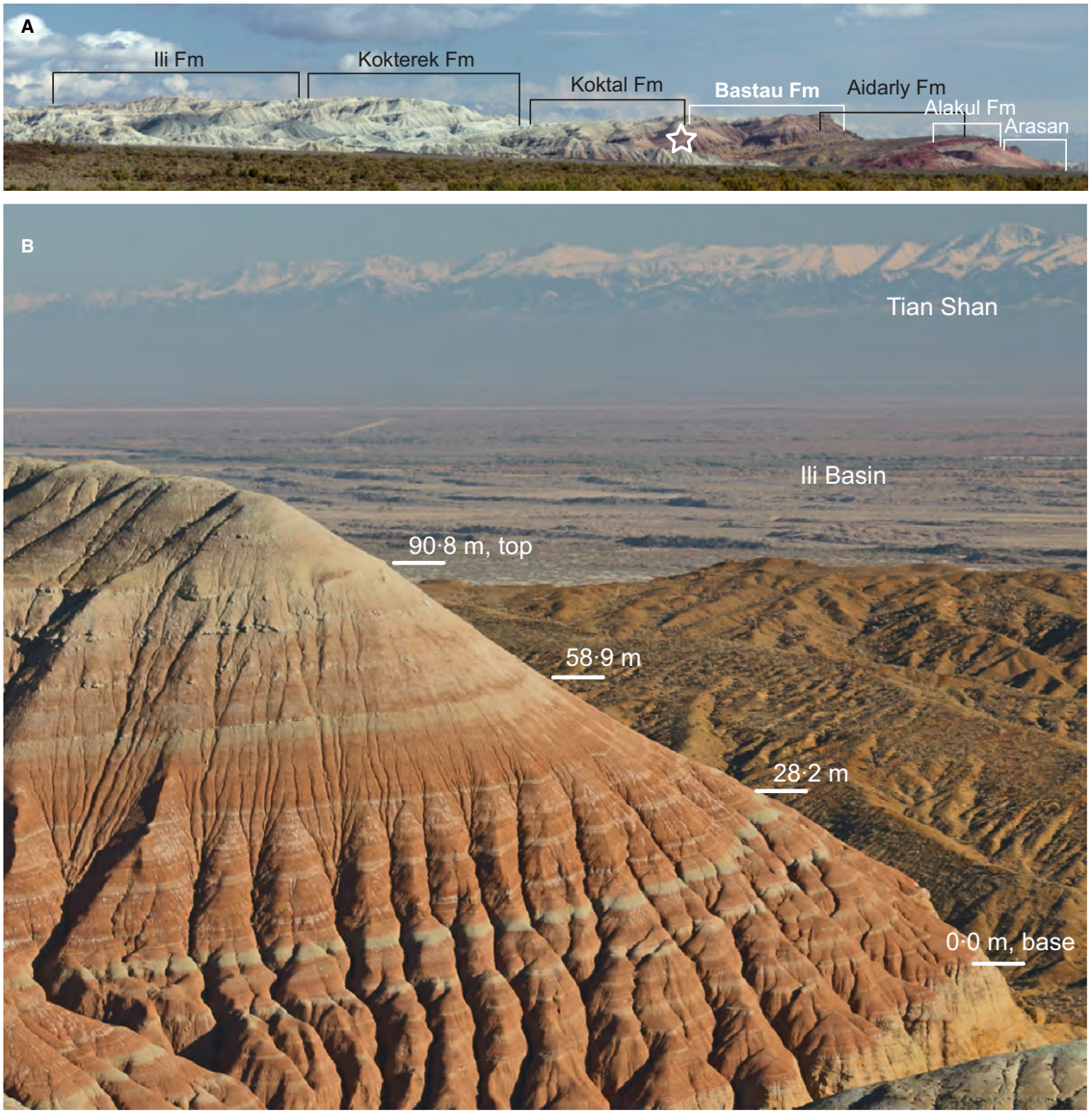

Fig. 2. Outcrop images showing the Aktau succession. (A) View of the western flank of the Aktau Hills with the range of lithostratigraphic formations. Length of exposure is *ca* 5 km. The hill in (B) is marked by a star. (B) Southward view from the studied Bastau Formation (Fm) with the Ili Basin and Tian Shan Mountains in the background.

typical for the late Miocene to early Pliocene (Dzhamangaraeva, 1997). Early palaeontological excavations in the Ili Formation provided records of the gomphotere *Anancus avernensis*, an extinct elephant living 7 to 1·8 Ma ago (Bazhanov & Kostenko, 1961). Based on these biostratigraphic data, the age of the here studied Bastau Formation is constrained to the mid-Miocene between 17 and 14 Ma (Fig. 3).

METHODS

During field work in 2011 and 2015, the 91 m thick Bastau Formation was logged in centimetre-to-decimetre-scale resolution. Direct measurements of bed-thickness were adjusted to the total thickness of the sedimentary succession determined with a laser distance and angle meter to correct for erroneous thickness measurements related to variable slope

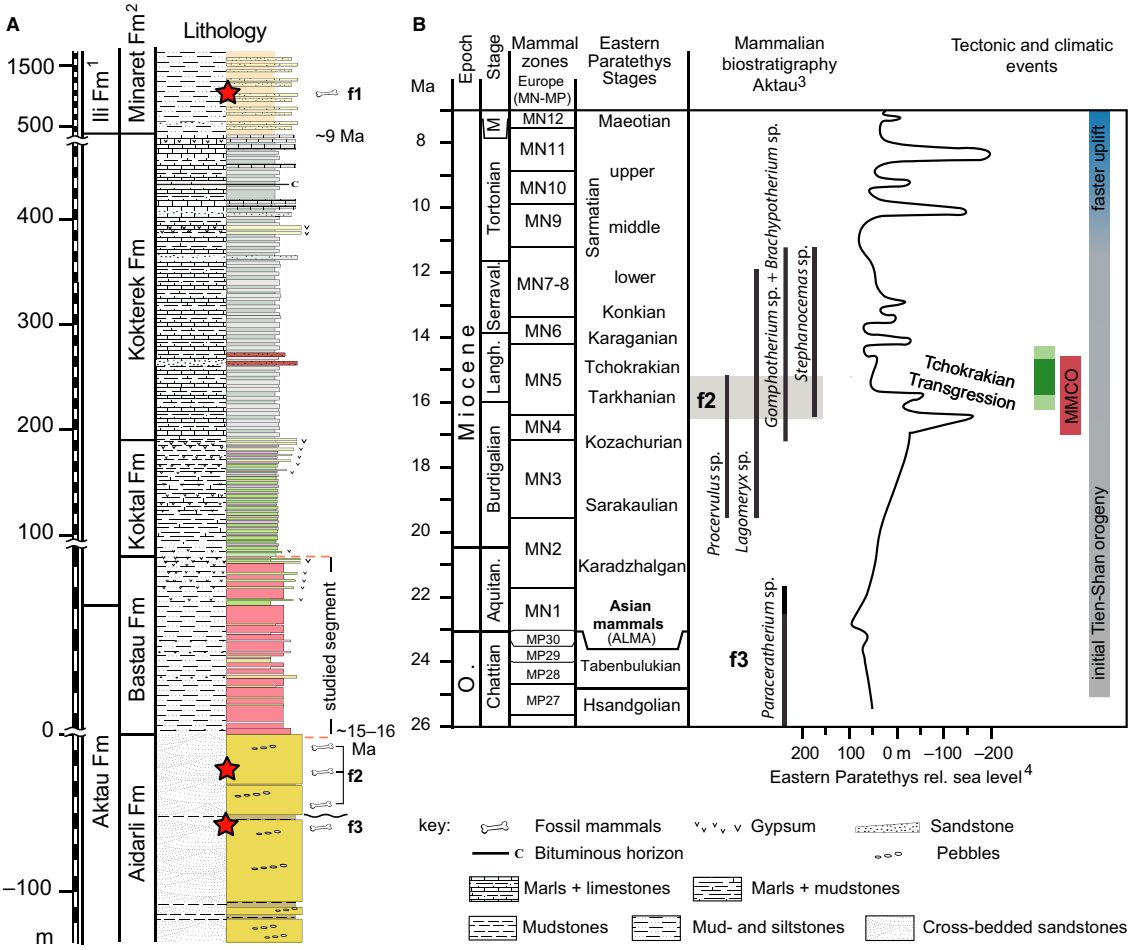

Fig. 3. Stratigraphic overview of parts of the Aktau Mountains succession with (A) the lithology and position of biostratigraphic marker beds (stars) in the Miocene (f2, f3, Lucas *et al.*, 1997) and Late Miocene to Pliocene (f1, Bazhanov & Kostenko, 1961; Dzhamangaraeva, 1997), and (B) an overview of regional divisions, biozonations, tectonic and climate events in Europe and Central Asia and the estimated age for the Bastau Formation (green bar). Ages are after GTS12. Lithostratigraphic formations are from Bazhanov & Kostenko (1961)[1] and Bodina (1961)[2]. Mammalian biostratigraphy[3] is from Bazhanov & Kostenko (1961) and Lucas *et al.* (1997), and the relative Paratethys sea-level curve[4] is after Popov *et al.* (2010). Uplift ages of the Tian Shan are from Sobel *et al.* (2003, 2006) and Macaulay *et al.* (2014). MMCO, Middle Miocene Climatic Optimum.

angles. The succession was sampled in 20 to 25 cm spacing for bulk-sediment geochemistry. Potentially prospective strata were also sampled for palynology. Sediment colour scans were performed in 5 to 8 cm spacing with a Konica Minolta CM-700d spectrophotometer, and volume-specific magnetic susceptibility (MS) was measured every 10 cm with a hand-held SM 30 magnetic susceptibility meter (ZH Instruments, Brno, Czech Republic).

Element geochemistry

To account for the different components of Bastau Formation sediments (silicates, carbonates, sulphates and salts) and to isolate the silicate fraction, the geochemical composition of powdered sediment samples was analysed in two steps, by separating the acetic acid-leachable fraction from the non-leachable fraction. Following the method of Goldberg & Humayun (2010) 400 to 600 mg of sample powder was treated with 4·5 ml of 50% acetic acid at 50 to 75°C for *ca* 18 h; 250 µl of the leached solvent was then analysed by ICP-OES. The remaining sediment was repeatedly washed to ensure complete removal of dissolved ions from the sediment pore water. The 100 mg of decalcified sample powder was then digested in HF-enhanced agua regia with the microwave Multiwave 3000™ by Anton Paar.

An internal reference material and a blank were included in each session.

Geochemical analyses were carried out by ICP-OES on an iCAP6300 Duo™ by Thermo Scientific. Matrix concentrations were reduced by diluting the primary preparation solutions by a factor of three. Yttrium was added to all samples as an internal reference. Calibration solutions were prepared separately for the leached and bulk-digested samples using certified single and multi-element standards (SPEXCertiPrep). Acetic acid-leached and bulk samples were then analysed in separate sessions. Reproducibility of repeated sample and standard measurements was within 5% (2σ) for most elements.

The weight loss caused by leaching of the rock powders ranged from 3·8% to 75%. As not only calcite was removed from the sediment, the carbonate content (calcite) was calculated by using the Ca concentration in the leachable fraction (Calcite [wt%] = mCa*100·1). Gypsum abundances were assessed using the sulphur content of totally dissolved samples, which show a strong correlation of sulphate (SO_4) and Ca for sulphate concentrations above 1 wt%. The content of gypsum was determined by assuming that all sulphur in the non-leachable fraction is related to gypsum (Gypsum [wt%] = mS (silicate) * 172·14). Some samples experienced a mass loss during the washing process after leaching. Stoichiometric calculations of the Ca content in the leachable fraction and the bulk sediment show the mass loss to be related to dissolution of gypsum. This mass loss has been added to the calculated gypsum content from the non-leachable fraction. Element concentrations of the non-leachable fraction are used to calculate indices of chemical weathering (see below).

Grain size and sediment mineralogy

Grain-size and X-ray diffractometry (XRD) analyses were performed on a subset of samples of the Bastau (n = 14) and Alakul formations (n = 10) and from stratigraphic equivalent horizons (n = 18) from the more proximal Kendyrlisay Valley section (Hellwig *et al.*, 2017). For grain-size analyses, 20 mg of each sample was decalcified with 20% formic acid, and after neutralization and homogenization wet sieved to remove grain sizes >100 μm. The fine fraction (<100 μm) was held in suspension in a Na-polyphosphate solution before 5 ml of the suspension was measured using a HORIBA LA-950 laser particle analyzer.

For XRD analyses, powdered rock samples were mounted on sample holders using the back-loading technique to reveal poor orientation and texturation. The measurements were performed on a PANALYTICAL X'Pert Bragg-Brentano diffractometer, using a copper beam powered by 30 mA and 40 KV generator current, Ni filter, programmable divergence slit, sample spinning and X'Celerator 1D detector. The characteristic diffraction maxima of each identified mineral phase was determined using MacDiff software. Intensities were converted to fixed 1° divergence characteristics and weighted by reference intensity ratios (RIR) to calculate the relative contribution from each mineral phase. Samples with a clay mineral composition containing palygorskite and/or mixed layer structures with expandable layers were treated for 24 h with ethylene glycol to aid in the identification of such phases. Palygorskite needles were also identified by Scanning Electron Microscopy.

The following phases were detected (in brackets: main diffraction maxima positions and RIR value as used for semiquantitative data calculation): mixed layer illite–smectite (around 12 to 13 Å, 0·4), palygorskite (10·35 Å, 0·52), illite/muscovite (10 Å, 0·43), chlorite/clinochlore (14, 7·1, and 3·54 Å, 1·0), quartz (4·26 and 3·34 Å, 3·03), K-feldspar (3·23 to 3·25 Å, 0·6), albite (3·18 to 3·2 Å, 0·64), calcite (3·04 Å, 3·32), ankerite (2·91, 3·15), dolomite (2·9 Å, 2·51), gypsum (7·6 Å, 1·7), halite (2·82 Å, 4·71).

Scanning electron microscopy (SEM)

Single samples from the Bastau Formation were prepared for SEM with a Zeiss Sigma VP. The suspended sediment was mounted on a slice, dried at 40° and afterwards sputtered with platinum. SEM microscopy was performed with a voltage of 10 to 15 kV.

Palynology

Six samples from the Bastau Formation were processed for palynological analysis using standard techniques previously applied to lake sediments from Central Asia including freeze-drying, weighing, HCl (30%) and HF (40%) treatment, and sieving through a 10 μm nylon mesh (Herb *et al.*, 2015). At least 300 pollen grains were counted per sample under 400 × magnification. Identification of taxa and nomenclature followed Hoorn *et al.* (2012), Han *et al.* (2016) and Miao *et al.* (2016).

Time series analysis

Time series of colour data, MS and element geochemistry were used for spectral analysis. In particular, the time series of the Red/Blue colour ratio (700/480 nm), the chemical proxy of alteration (CPA) and the Ti/Al ratio are used because of its high sensitivity to variations in the detrital sediment flux, redox conditions and degree of weathering (Salminen *et al.*, 2005; Buggle *et al.*, 2011). Spectral analysis was performed on each time series

following the method of Weedon (2003) in order to identify dominant cycle lengths. Prior to the algorithm, each record was normalized by mean value subtraction and sampled evenly by linear interpolation. The record of MS was plotted on a logarithmic scale to achieve variance stabilization. Redfit power spectra were calculated with the "PAST" software (Hammer *et al.*, 2001) following the algorithm by Schulz & Mudelsee (2002). Dominant cycle frequencies were used for Gaussian band-pass filtering in order to identify potential cycle-frequency ratios typical for orbital forcing in the Miocene Bastau Formation. In addition, average spectral misfit (ASM) calculations and evolutive harmonic analysis (EHA) was performed with the Mg/Al time series using the astrochron software package by Meyers (2014). For ASM analysis, candidate frequencies which reflect possible Milankovitch forcing were identified from the Mg/Al redfit power spectrum at 90% confidence level. Miocene orbital target frequencies and their uncertainties are derived from Laskar *et al.* (2004) following the approach in Meyers *et al.* (2012).

WEATHERING INDICES

Chemical weathering indices rely on the concept that mobile elements are selectively removed from weathering profiles relative to rather immobile elements. A number of element indices have been applied to different terrestrial sediments as palaeoenvironmental indicators. Here, a modified Ca-free version of the chemical index of alteration (CIA; Nesbitt & Young, 1982), the CPA (Buggle *et al.*, 2011), and the molar Mg/Al ratio were chosen as an analogue for magnesium-bearing minerals (Maynard, 1992).

The CIA, derived from the silicate fraction, is a quantitative measure of feldspar weathering by relating Al, enriched in the residues, to Na, Ca and K removed from a soil profile by plagioclase and K-feldspar weathering ($CIA = [Al_2O_3/(Al_2O_3 + Na_2O + CaO^* + K_2O)]^*100$; Nesbitt & Young, 1982). Changes in sediment provenance, hydraulic sorting and post-depositional processes lead to K^+ addition, as for instance, diagenetic illitization. Illitization is also reported as pedogenic process in soils forming under arid climates (Singer, 1988) when smectite is altered during repeated wetting and drying cycles in the presence of K^+ (Eberl *et al.*, 1986). The most interfering element for Bastau Formation sediments, however, is Ca, which is commonly present both in detrital plagioclase and pedogenic carbonates and sulphates. Some of the Ca content of the acid insoluble fraction is related to gypsum, therefore we used a Ca-free version CIA-Ca of the CIA.

The CPA, defined as the molar ratio of Al and Na ($CPA = [Al_2O_3/(Na_2O + Al_2O_3)]^*100$), is a weathering index for carbonate-rich shales, siltstones and sandstones because of the small ionic radius of Na and its interference with non-silicate minerals in non-saline soils (Buggle *et al.*, 2011). The paired elements, Na and Al, minimize biases due to variable mineralogical composition of the parent material.

Climates with low to moderate precipitation reduce the intensity of weathering. Soluble cations such as Mg^{2+} can accumulate in soil pore waters by the limited flux of water through the soil profile which leads to the formation of alkaline and alkaline earth-rich secondary minerals (e.g. smectite and carbonates; Calvo *et al.*, 1999; Sheldon & Tabor, 2009; Torres & Gaines, 2013). In highly alkaline/saline solutions, rich in dissolved silica, Mg^{2+} is incorporated into trioctahedral clay minerals as Mg-smectite and sepiolite (Deocampo, 2004, 2015; Cuadros *et al.*, 2016). Here, the molar Mg/Al ratio from the total dissolved fraction is used as a measure of clay authigenesis in times of elevated rates of evaporation and higher groundwater table.

In addition, the molar ratio of Ti/Al from the non-leachable fraction (Ti*100/Al) is used as a geochemical index for palaeoenvironmental interpretation. The Ti/Al ratio is a classical indicator for sediment provenance, the more Ti present the more mafic the parent rock is (Salminen *et al.*, 2005; Sheldon & Tabor, 2009). Higher Ti/Al ratios indicate higher abundances of heavy minerals such as rutile, anatase, brookite, titanite and/or ilmenite (titanomagnetite) or detrital Ti-rich pyroxenes and amphibols in the catchment area. If the chemical composition of the parent rock in the source area remains unchanged through time, the Ti/Al ratio can be interpreted as an indicator of weathering intensity and sedimentary discharge from the catchment area (Sheldon & Tabor, 2009). Physical weathering readily removes Ti from igneous and metamorphic rocks where it subsequently becomes enriched in the fine fractions of floodplain sediments (Salminen *et al.*, 2005; Taboada *et al.*, 2006; Minyuk *et al.*, 2014). The Ti/Al ratio is used here as a proxy for the intensity of alluvial sediment discharge in times of unchanged provenance.

DATA AND RESULTS

Sedimentary facies

The Bastau Formation consists of reddish-brown mudstones with intercalated greyish-green and reddish sandstones that appear cyclically throughout the succession (Figs 2B and 4A). A typical sedimentary cycle begins with thin (5 to 20 cm) beds of medium-grained to coarse-grained sandstones, composed of several units separated by thin pelitic layers, finally grading into several metres thick mudstones. The base of the single sandstone beds

may be slightly erosive or channelized. Although sandstone units can be traced over hundreds of metres, individual layers pinch out over short distances (10 to 50 m). Grain size varies in different layers from well-rounded granules to medium-grained sand of moderate roundness. Especially, thin lobate units have significant matrix content, pointing to hyper-concentrated flows. The topmost centimetres of single sandstone layers often show secondary clay infiltration. The poorly sorted sandstones, rich in unweathered volcanic rock fragments and plagioclase grains, are interpreted as representing distal lobes of sheet flood deposits of terminal splays and their related feeder channels (Fig. 4C).

The mudstones are homogeneous, structureless rocks on average with less than 1% to 2% sand content. Often, they display a mottled texture or polyedric fracturing. They yield secondary carbonates and salts and the grain-size distribution (<100 μm) is bimodal with modal peaks at 0·2 to 0·3 μm and 9 to 10 μm, respectively (Fig. 5). The small grain-size fraction is mainly represented by authigenic components while the larger modal peak is indicative of detrital silt particles. The grain-size pattern is supported by

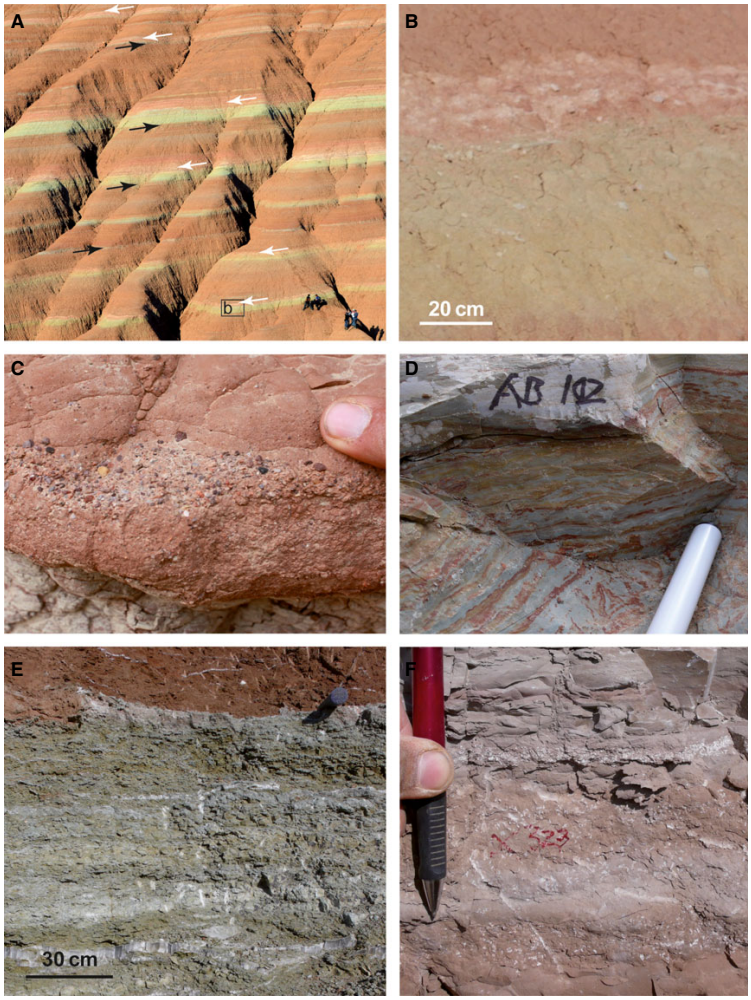

Fig. 4. Outcrop images showing the Bastau Formation facies types: (A) alternation of greyish sandstones and reddish-brown mudstones between 9 and 32 m representing sheet flood deposits (black arrows) and phreatic carbonates (white arrows) in a mudflat, (B) detail of (A) showing nodular phreatic carbonates on top of a bleached sandstone at 9 m, (C) enrichment of unweathered rock fragments in badly sorted sandstones, (D) reddish mottled grey gleysol at 16·2 m, (E) well-bedded calcareous marl with gypsum deposited in a playa lake system overlain by reddish mudstones at 61·4 m, and (F) abundant occurrence of displacive gypsum in mudstone deposits above the first lake (Horizon IV). Note people in bottom right corner of A.

the results of powder XRD analyses (Fig. 5). Relatively high abundances of unweathered minerals (quartz + albite + K-feldspar) sum up to 60% of the mudstone's composition. The mean clay mineral content is 29% and comprises mixed layer illite/smectite (0·7%), palygorskite (7·8%), illite (15·1%) and chlorite (5·0%). The relatively high abundance and needle-like preservation of palygorskite underlines its authigenic formation under arid to semi-arid depositional conditions (Fig. 5). At some horizons, distinct nodular calcareous horizons occur (Fig. 4A and B). Mostly, they form 5 to 10 cm thick beds above massive sheet flood deposits. The nodular appearance of carbonates demonstrates its phreatic origin from saturated solutions in times of elevated groundwater table. Episodes of elevated groundwater table and pedogenic reworking are also evident from reddish or greyish mottling structures (Fig. 4D). Accordingly, the mudstones are interpreted as dry mudflat deposits, homogenized by plant growth and bioturbation and, in part, overprinted by in situ weathering and authigenesis.

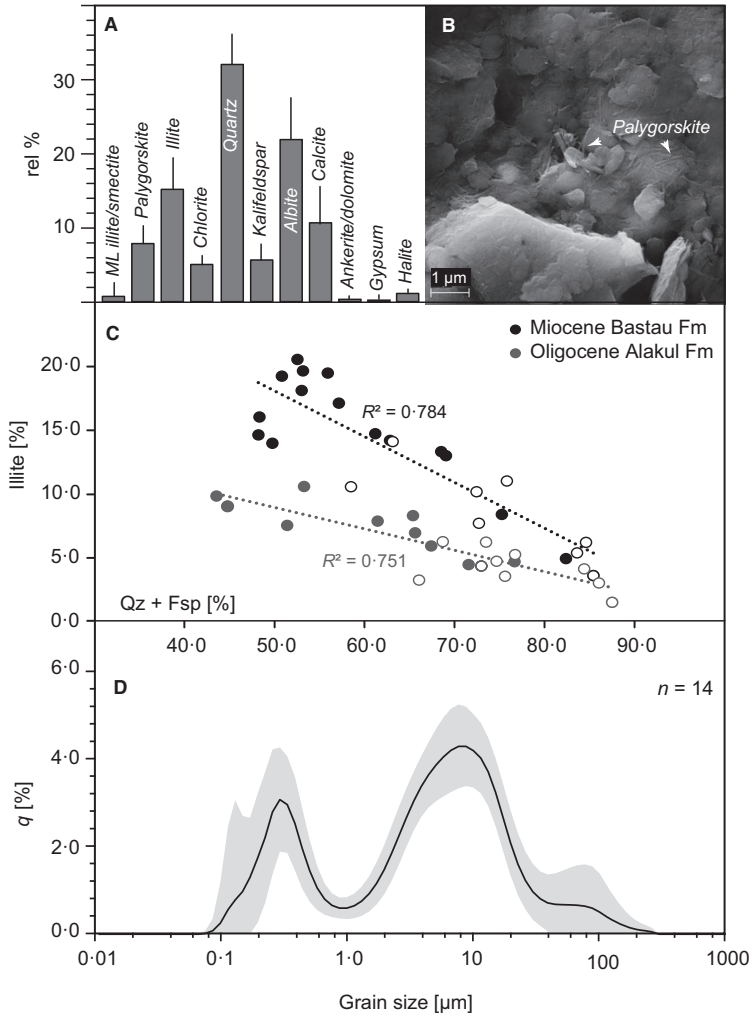

Fig. 5. Overview of the mineralogical composition and grain size of Bastau Formation sediments, (A) mean relative abundance of mineral phases estimated by powder X-ray diffractometry (XRD), (B) Scanning electron microscopy (SEM) image of sample AB 133, (C) relation of relative percentages of illite to quartz and feldspar in the Bastau and Alakul formations (closed circles) in comparison to a more proximal site (open circles, see text), (D) mean grain-size distribution of the <100 µm fraction with the 1 σ standard deviation (grey area). Unweathered source rock minerals sum up to 60% (albite + kalifeldspar + quartz). Abundant occurrence of small palygorskite needles in the mudstones refer to their authigenic formation. The bimodal grain-size distribution shows the grain-size separation of authigenic and detrital components.

Above 59 m, a prominent change in sedimentary facies occurs with a 3 m thick green horizon ("green band", GB) of calcareous mudstones (Fig. 4E). It consists of bedded nodular carbonates in its lower part and increased contents of gypsum towards the top (Fig. 6). This horizon is interpreted as the first occurrence of prolonged palustrine conditions in the Aktau succession. The shift from carbonates to gypsum represents an increase in salinity from almost freshwater to hypersaline conditions indicative of high rates of evaporation. Higher up, the succession consists again of alternations of sandstones and mudstones, however, with abundant gypsum (Fig. 4F). Gypsum is present as single idiomorphic lenticular crystals within the sediment and forms up to 1 m thick crusts of chicken wire gypsum on top of the Bastau Formation (Fig. 2B). Thin sections show the gypsum also as secondary precipitates in the pore space suggesting a phreatic zone origin. Lenticular gypsum crystals and chicken wire-textured massive gypsum indicate mechanical replacement of soft, water-saturated mud. The abrupt appearance of gypsum above 60 m corresponds to elevated rates of evaporation in a progressively hydrologic restricted basin and indicates a facies shift from dry to saline mudflat and playa lake environments (Fig. 6).

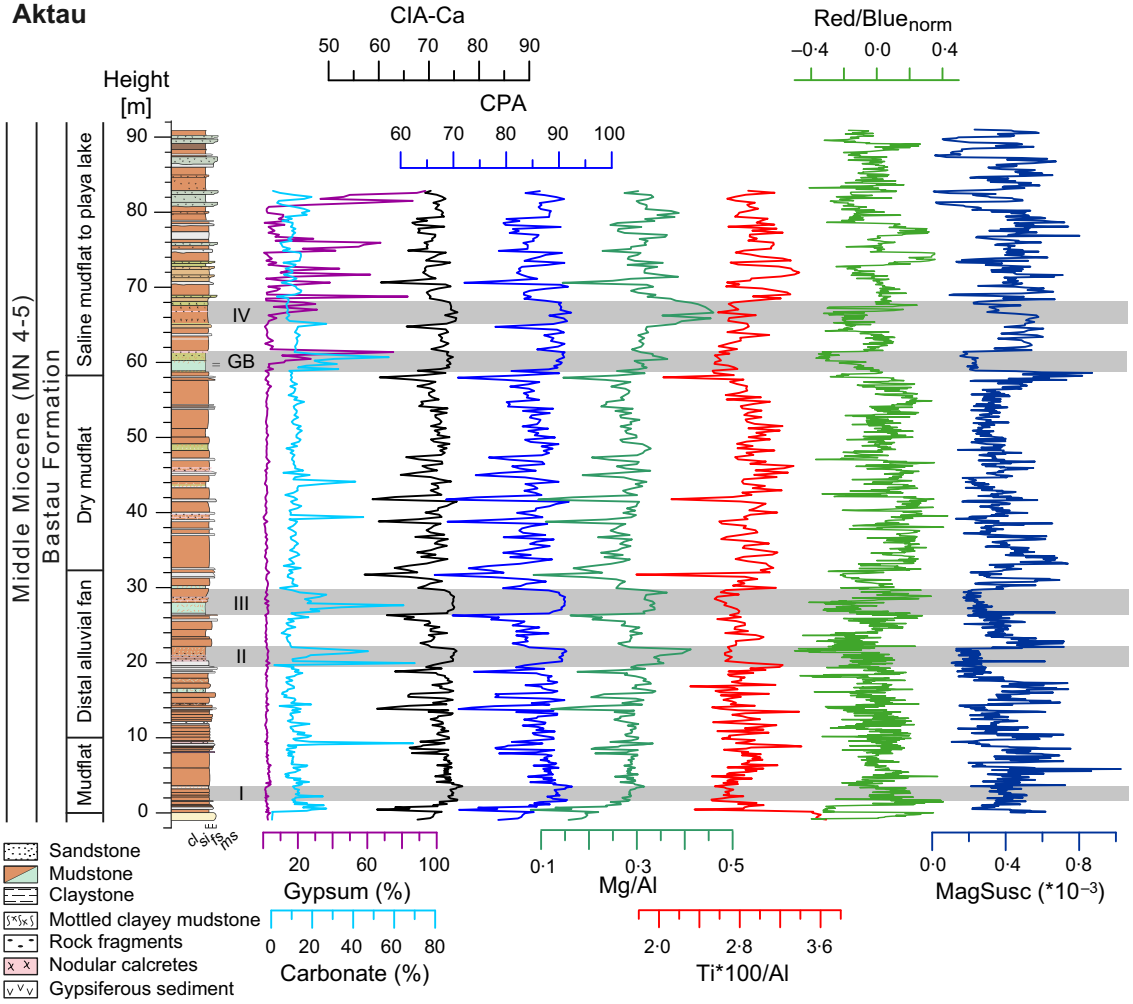

Fig. 6. Lithologic log of the Bastau Formation with carbonate and gypsum content, weathering indices in the acid-leachable fraction (CPA, CIA-Ca, Mg/Al; see text), Ti/Al ratio, sediment colour (normalized Red/Blue ratio) and MS. Numbered grey bars mark horizons of intensified weathering and clay mineral authigenesis. Arrows mark the position of productive palynological samples.

Element geochemistry, sediment colour and magnetic susceptibility

The carbonate content of mudstones in the Bastau Formation is on the order of 10% to 15% (Fig. 6). Elevated values between 20% and 30%, with single maximum values up to 60%, occur in beds with phreatic cementation above sheet flood deposits and in the palustrine horizon between 58·2 m and 61·4 m. The gypsum content is negligibly small below 60 m. A first significant occurrence of 10% to 75% at 60·0 to 61·4 m is associated with the upper part of the lacustrine horizon.

The weathering indices CIA-Ca, CPA and Mg/Al have mean values of 71 ± 3, 86 ± 5 and 0·29 ± 0·05, respectively, typical for sustained chemical weathering conditions. In addition, the three indices show relatively similar variations (Fig. 6). Elevated values occur in four horizons characterized by pedogenic reworking evident from mottling and associated colour changes. Namely these horizons occur at 1 to 3 m (I), 19 to 23 m (II), 27 to 30 m (III) and 65 to 68 m (IV). A fifth horizon is marked by the palustrine horizon GB (58 to 61·4 m). Very low weathering indices are associated with coarse sheet flood deposits rich in unweathered rock fragments. The CPA shows an almost identical pattern of variability as the CIA-Ca but differs from it by having higher amplitude variations. The Mg/Al ratio shows similar relative trends as the CPA and CIA-Ca but displays pronounced maxima which are caused by additional Mg enrichment in horizons of elevated pedogenesis (Figs 6 and 7). Prominent Mg enrichment occurs in Horizon IV.

Median concentrations of TiO_2 are 0·7 ± 0·1% and the Ti*100/Al ratio displays small variations around a mean value of 2·8 to 2·9, typical for a source rock with rather uniform chemistry (Fig. 6). Elevated values at the base of the succession are the only exception and refer to a different provenance for the fluvial Aidarly Formation sediments. Throughout the remainder of the succession, low Ti/Al ratios occur in the horizons of pedogenic reworking, and chemical weathering paces the more elevated values into 20 to 30 m long depositional cycles. A similar pattern exposes the Red/Blue colour ratio with low and high frequency variations indicative of changes in lithology and redox conditions of the sediment. The low frequency variations display 20 to 30 m long cycles separated by lower values in horizons of elevated weathering. Superimposed variations of higher frequency are associated with colour banding.

The MS displays cyclic variations with significant drops in the more weathered horizons. The minima are stratigraphically more expanded and include horizons of mudstone mottling reflecting changes in iron mobility and thus the sediment redox state after deposition. Elevated values occur mainly in the lower and upper part of the succession (e.g. at 7 to 8 m and 22 to 23 m or beneath the palustrine horizon (GB) associated with enhanced detrital input.

Palynology

Only two of the six analysed samples (KAZ-10 and KAZ-11 at 62·20 m and 62·55 m, respectively) yielded moderately preserved palynological assemblages consisting predominantly of pollen and spores; in addition, the assemblages contain abundant non-pollen palynomorphs, including algal cysts of unknown affinity, rare organic-walled dinoflagellate cysts of presumably freshwater origin and fungal spores (Fig. 8).

The pollen and spore assemblages extracted from samples KAZ-10 and KAZ-11 contain substantial numbers of conifer-derived bisaccate pollen grains (i.e. *Pinuspollenites*, *Piceapollenites* and *Abiespollenites* in order of decreasing abundance). They make up 70·2% and 14·2% of the assemblages, respectively; *Taxodiaceapollenites* reaches 0·6% and 7·3%. With regard to pollen from deciduous trees, the assemblages are dominated by (in order of decreasing abundance) *Ulmipollenites* (9·9% and 55·0%, respectively) and *Pterocaryapollenites* (1·4% and 3·3%); other deciduous tree-pollen taxa occurring in low (i.e. ≤2%) percentages are *Alnuspollenites*, *Carpinuspollenites*, cf. *Caryapollenites*, *Fraxinoipollenites*, cf. *Juglanspollenites*, *Quercoidites*, *Striaticolpites*, *Tiliaepollenites* and *Triporopollenites.* Non-arboreal pollen grains are mainly from *Cyperaceaepollis* (6·8% and 4·8%, respectively) and *Graminidites* (5·1% and 13·0%); other non-arboreal pollen taxa occurring in low (i.e. ≤2%)

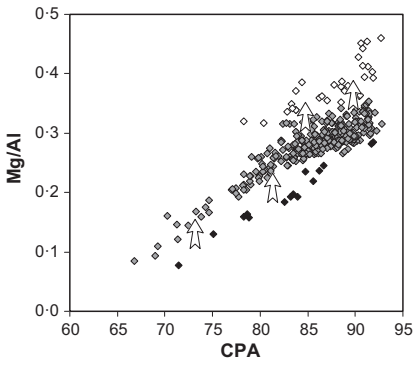

Fig. 7. Cross plot of CPA and Mg/Al ratios for Bastau Fm sediments that demonstrates the process of Mg enrichment during early diagenetic authigenic clay formation (white arrows). Black symbols represent the lowermost 2 m of the succession; white symbols mark horizons of phreatic carbonate precipitation and evaporative enrichment, and grey diamonds all other samples (see text).

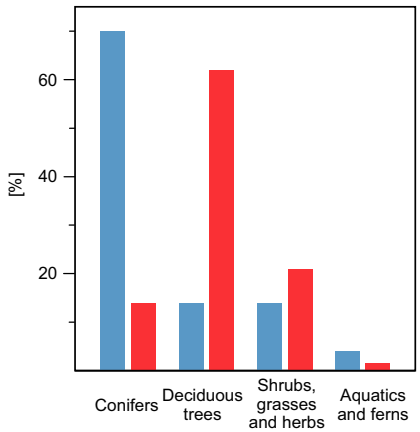

Fig. 8. Percentages of the different pollen and spore groups identified in samples KAZ-10 (blue bars) and KAZ-11 (red bars).

percentages are *Chenopodipollis*, *Compositoipollenites* and *Ephedripites* spp. Fern spores account for 3·7% of the pollen and spore assemblage of sample KAZ-10, and pollen from aquatic plants (i.e. *Sparganiaceaepollenites*) account for 1·5% of the pollen and spore assemblage of sample KAZ-11.

Time series analysis

Average Middle to Late Miocene sedimentation rates of the Aktau succession (bases Bastau to Ili formations) are on the order of 5·0 to 8·5 cm ka^{-1} based on its overall thickness of 530 ± 40 m and biostratigraphic age (8 ± 1 Ma; Bazhanov & Kostenko, 1961; Bodina, 1961). The prevalence of fine-grained sediments indicates rather stable subsidence without tectonically enhanced deepening of the Ili Basin.

Time series analysis was performed on the records of CPA, Ti/Al, Mg/Al, Red/Blue and MS. Spatial resolution of the CPA and Ti/Al time series (25 ± 6 cm, 1σ) is not sufficient for a robust detection of precession periods. Spatial resolutions of MS and the Red/Blue ratio are higher (6 ± 2 cm and 9 ± 5 cm, 1σ), however, both time series are measured directly on rock fragments in the field and can be inaccurate because the lack of plain surfaces may cause signal noise and distortion. Redfit spectra were calculated to identify cycle lengths of dominant periodicities and filter outputs of significant cycles were generated to identify cycle-frequency ratios diagnostic for orbital forcing. ASM was calculated for the Mg/Al time series (Meyers, 2014). The method offers a statistical test to reject the null hypothesis (no orbital signal) at a certain significance level. If the null hypothesis can be rejected, the ASM metric estimates the most probably sedimentation rate for a stratigraphic interval by comparing candidate frequencies to the fixed target frequencies from the orbital solution for a given range of sedimentation rates (Meyers & Sageman, 2007). In addition, EHA was performed to test the stability of sedimentation rate.

Redfit spectra of the four studied time series display different dominant cycle lengths (Fig. 9). The Ti/Al ratio has only one dominant cycle 27 to 28 m in length, with more than 99% significance. Similar periodicities are also visible in the logMS (22 to 30 m, >95%) and the Red/Blue (20 to 40 m, >99%) time series. While the Ti/Al ratio shows a clear peak, the broad range of cycle lengths of the logMS and Red/Blue time series refers to the amalgamation of different cycles, which cannot be addressed because of the short length of the time series. The CPA, MS and Red/Blue ratio show dominant peaks between 6·4 to 7·3 m (>90 to 95%) and 5·0 to 5·4 m (>95%). Their common occurrence in different time series with different spatial resolution argues for a common forcing. Further significant peaks (>95%) occur at variable cycle lengths between 1·5 m and 2·5 m, with the four time series lacking consistency.

Results from the ASM calculation of the Mg/Al time series show that for a sedimentation rate of 5·1 cm kyr^{-1} the null hypothesis can be rejected with a H_0 significance level of 0·18% (Fig. 10A and B). This sedimentation rate would assign the 5·0 to 5·4 m cycle to the periodicity of short eccentricity. Furthermore, the EHA normalized amplitude spectrum shows spectral power for the frequencies of long and short eccentricity and obliquity (Fig. 10C). A shift towards higher sedimentation rates higher occurs above 27 m and explains the increased cycle length of 6·4 to 7·3 m for the short eccentricity signal (Fig. 10C). Short eccentricity is weakly developed between 35 m and 55 m where the dominance of a *ca* 3 m cycle suggests a stronger control by obliquity. Gaussian bandpass filter outputs were generated for the 6·4 m cycle in the CPA, the 27 m, 22 m and 7·3 m cycle in the MS, the 27 m cycle in the Ti/Al, and the 30 m, 20 m, 7 m and 5·1 m cycle in the Red/Blue ratio (Fig. 9). The long 22 to 30 m cycle displays minima in the horizons of elevated weathering intensity. Here, the 6·4 to 7·3 m cycle has its highest amplitudes (grey bars in Fig. 9) while it weakens in the intervals between. The 6·4 to 7·3 m filters of MS and CPA display anti-phase correlated cycles. The filter output of the 5·1 m cycle in the Red/Blue ratio shows the 5·0 to 5·4 m cycle closely related to the 6·4 to 7·3 m cycle representing similar sedimentary cycles in horizons of lower sedimentation rate.

The arrangement of spectral peaks (frequency ratios), such as the 1 : 4 relationship between long (405 ka) and short (*ca* 100 ka) eccentricity is robustly expressed by the 20 to 22 m and 5·0 to 5·4 m cycles in the lower part of

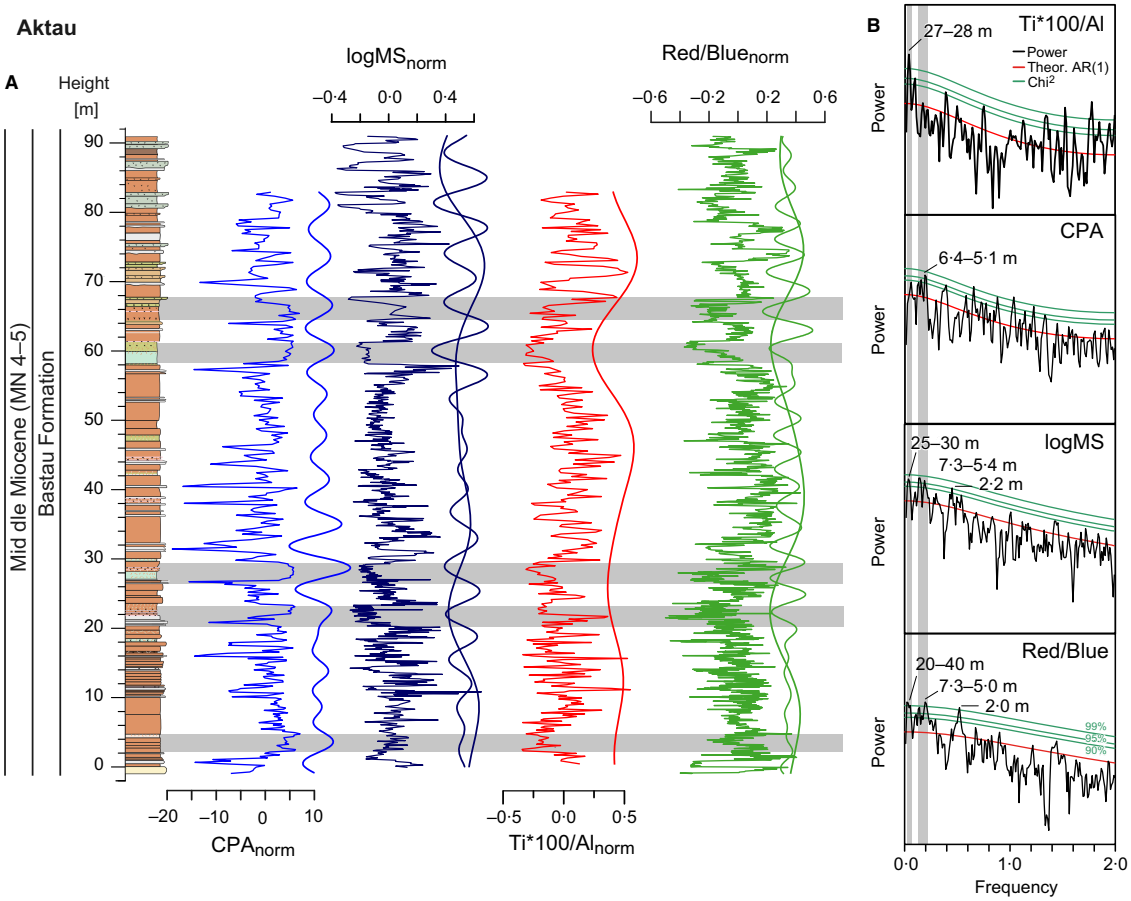

Fig. 9. Gaussian filter outputs (A) and Redfit spectra (B) for dominant frequencies of CPA, logMS, Ti/Al and the Red/Blue colour ratio. Filter frequencies for the time series are 0·037 ± 0·015 cycles m^{-1} for logMS, Ti/Al and Red/Blue, 0·155 ± 0·047 cycles m^{-1} for CPA, 0·137 ± 0·041 cycles m^{-1} for logMS and 0·191 ± 0·057 cycles m^{-1} for Red/Blue. The 6·4 to 7·3 m and 5·0 to 5·4 m cycles, probably related to the 100 ka short eccentricity cycle, are prominently developed in the CPA, MS and Red/Blue time series. The 27 to 30 m cyclicity is significantly developed in the logMS, Ti/Al and Red/Blue data and is interpreted as representing the 405 ka long eccentricity cycle. Further subsidiary cycles occur between 1·5 m and 2·5 m in the CPA, logMS and Red/Blue data.

the succession and the 27 to 30 m and the 6·4 to 7·3 m cycles in the upper part evident in the different studied times series. The resolution of the MS and Red/Blue time series is high enough to detect precession and obliquity periods. However, no clear signal could be identified in the Redfit spectra of both records because of signal noise at higher frequencies. Given the low temporal resolution of biostratigraphy and the limitations of the presented data sets, we caution against explicit development of an astrochronology for this interval. This work motivates the development of improved independent age controls for the entire Aktau succession, such as palaeomagnetic stratigraphy and radiometric dating. There is limited discussion below on the identification of potential orbital frequencies and the assessment of their effects on climatically forced sedimentation.

DISCUSSION

Weathering and authigenic clay mineral formation

Chemical weathering under arid and semi-arid conditions responds sensitively to changes in the hydrologic system of the basin, either through tectonically driven changes in the discharge system, or by climatically driven changes in the hydrological balance. A plot of the Bastau Formation sediment chemistry in the A-CN-K diagram (Fig. 11;

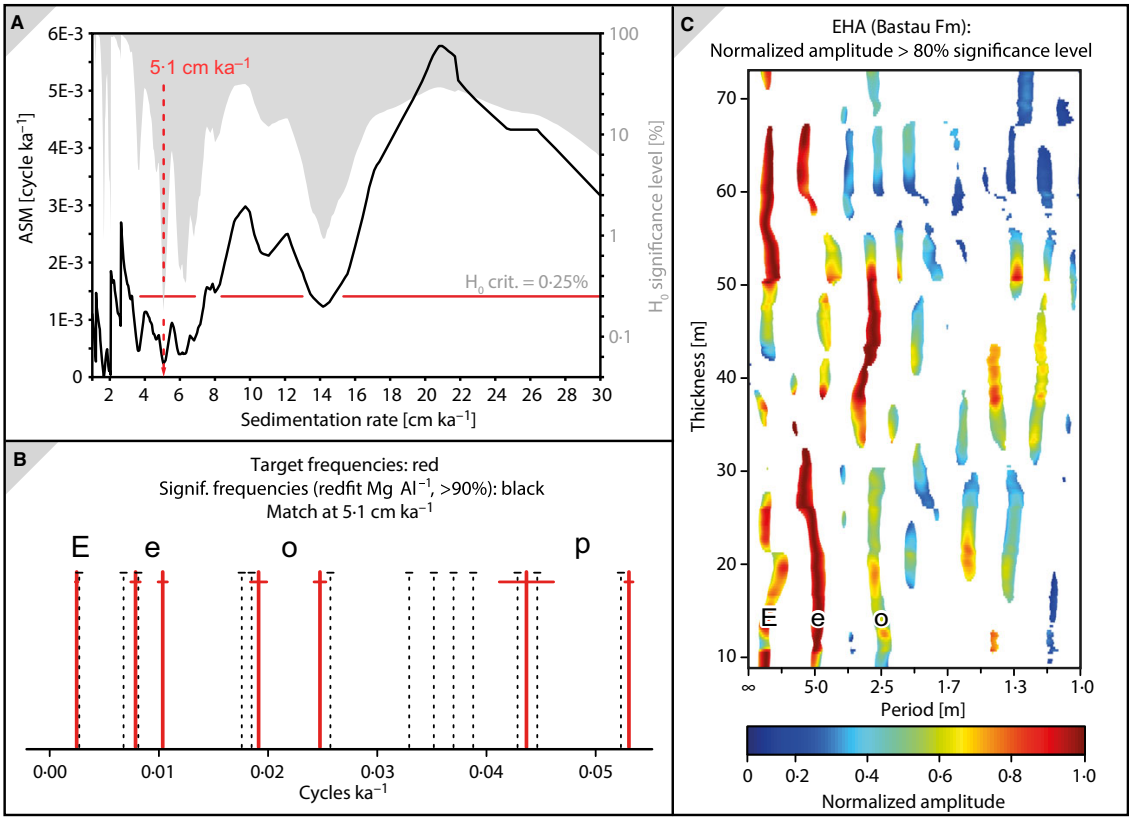

Fig. 10. (A) ASM of the Mg/Al time series calculated for sedimentation rates between 1 and 30 cm kyr^{-1} with 400 sedimentation rates investigated, resulting in a critical significance level H_0 for null hypothesis rejection of 0·25%. (B) Significant spectral peaks from Mg/Al redfit >90% CL (=candidate frequencies, black) and their match with seven orbital target frequencies (0·00247, 0·00786, 0·01035, 0·01913, 0·02475, 0·04366, 0·05305, red). The null hypothesis of no orbital forcing can be rejected for a mean sedimentation rate of 5·1 cm kyr^{-1}. (C) EHA amplitude spectrum of the Mg/Al time series at the 80% significance level.

Nesbitt & Young, 1984, 1989) shows the sediments to derive from source rocks with a composition typical for the upper continental crust in accordance with their origin from volcanic arc complexes (Jahn *et al.*, 2000). Mean CIA-Ca values of 71 ± 3 indicate that Bastau Formation sediments underwent sustained chemical weathering. Plagioclase weathering is the main mineral reaction causing the preferential removal of Ca and Na. Furthermore, the sediment chemistry data display in agreement with results of XRD analyses a trend towards elevated K concentrations, typical for the formation of illite. Illite can be directly formed from weathering of K-feldspar and muscovite or by post-depositional processes as diagenetic illitization. Illite can also be formed by low-temperature illitization of smectite (Baldermann *et al.*, 2015; Cuadros *et al.*, 2016) when K is fixed during repeated wetting and drying processes in the soil (Singer & Stoffers, 1980). In the Bastau Formation, the relative abundance of illite is negatively correlated with those of quartz and feldspar indicating a predominant detrital origin of illite, additionally supported by stratigraphic equivalent XRD data from a proximal site 40 km distant (Fig. 5C; Hellwig *et al.*, 2017). Illite formation by post-depositional alteration, as observed for Oligocene sediments in south-western Mongolia (Richoz *et al.*, 2017), is not considered a relevant process here. Illite percentages of mudflat sediments in the Bastau Formation are about 10% higher than those of the underlying Alakul Formation which underwent higher burial temperatures, but show a similar proximal-distal relationship in the abundance of unweathered quartz and feldspar to illite typical for detrital transport (Fig. 5C).

Sedimentary facies and geochemical indices in the Bastau Formation refer to five horizons of elevated weathering intensity (Figs 5 and 6). The horizons are characterized by hydromorphic features of soil formation (mottling), phreatic carbonate precipitation close to the

groundwater table or by palustrine sedimentation, typical features in distal parts of endorheic basins. The higher abundance of clay minerals together with elevated CIA, CPA and Mg/Al, and low Ti/Al values suggest that these beds formed in times of low detrital sediment supply and landscape stability.

Intensified weathering can be explained either by (1) elevated water/moisture supply to the vadose zone by precipitation and/or surface and subsurface discharge; (2) longer periods of landscape stability with lower rates of sediment discharge from the hinterland; and (3) elevated rates of evaporation and capillary groundwater rise. An important feature of Bastau Formation sediments in addressing these processes is the covariance of CPA/CIA and Mg/Al which refers to more intense weathering under highly evaporative conditions (Fig. 7).

Magnesium fixation in silicates requires Mg enrichment in the aqueous environment by either by Ca removal by the early formation of carbonates and sulphates or by evaporative capillary groundwater rise (Calvo *et al.*, 1999; Deocampo, 2015). Primary controls for the authigenic formation of Mg-rich clays (e.g. smectite, palygorskite) are high magnesia and silica activities and elevated pH (Deocampo, 2004; Deocampo *et al.*, 2009). Studies in modern arid environments have shown that a strong enrichment of elements in pore waters takes place in areas sheltered from detrital input and subjected to strong evaporation as in marginal lacustrine settings, in interdune clay pans and ponds where groundwater is discharging (Calvo *et al.*, 1999). The K, Mg and Si are extracted from supersaturated solutions to form interstratified illite and trioctahedral Mg-rich smectite (Jones & Weir, 1983; Banfield *et al.*, 1991). The presence of palygorskite in calcic soils results from incongruent dissolution precipitation (Jones & Galan, 1988), direct precipitation from oversaturated solutions or from transformation of inherited clay precursers (Cuadros *et al.*, 2016). Badaut & Risacher (1983) observed authigenic Mg-smectite formation under conditions of silica saturation where the pH was above 8·2 in lakes in Bolivia. High salinity/alkalinity, dissolved silica enrichment and high pH values (>9·5 to 10) also favour Mg enrichment and trioctahedral clay formation in palaeolake Olduvai, Tanzania (Deocampo, 2004). Fibrous clays such palygorskite and chlorite degrade to smectite when the climate is more humid and annual rainfall exceeds 300 mm (Calvo *et al.*, 1999).

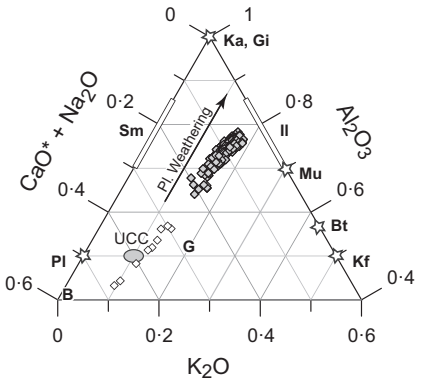

Fig. 11. A-CN-K ($Al_2O_3 - CaO^* + Na_2O - K_2O$) ternary diagram according to Nesbitt & Young (1984). The position of the upper continental crust (UCC), basalt (B), granite (G), plagioclase (Pl), kalifeldspar (Kf), muscovite (Ms), biotite (Bt), smectite (Sm), illite (Il) and kaolinite (Ka) is given for orientation. Data points of the Bastau Fm plot on a line typical for plagioclase weathering because of preferential removal of Ca and Na (grey diamonds) with a shift towards increased K-content (see text). The weathering line is distorted with respect to CaO* due to an overestimation of CaO* in the gypsum-rich upper Bastau Fm (white diamonds).

The source of K, Mg and Si needed for clay mineral formation in Bastau Formation sediments is derived from feldspar weathering of the volcanic source rocks in the catchment area. The presence of fibrous palygorskite and abundant chlorite argue for their authigenic formation under more arid conditions. This process is most intense in the intervals of elevated Mg/Al ratios. Accordingly, it is possible to state that the highest degrees of weathering were achieved when the regional climate was at its driest and elevated rates of potential evapotranspiration supported capillary groundwater rise. On the other hand, hydromorphic soil features and phreatic carbonate precipitation argue for a higher groundwater table in the weathered horizons and thus for higher water supply to the vadose zone. The most probably explanation for this water supply is an elevated subsurface discharge from montane areas in the surroundings of the Ili Basin. In an analogue to modern observations, the highest weathering intensities probably occurred when mean annual precipitation values were at or below 300 mm, soil water pH reached values above 8·5 and the phreatic zone was at or close to the surface. Regarding the interpretation of weathering indices as proxies in palaeoclimatology, we can state, if covariance with CPA and/or CIA is achieved, the Mg/Al ratio serves as an aridity index.

Regional hydrology

The primary water source for arid to semi-arid basins is precipitation, and in a long-term steady-state system, precipitation is balanced by the water loss to evapotranspiration, underlying aquifer recharge, surface runoff and vadose infiltration of soil moisture (Maliva & Missimer, 2012). In the distal depositional setting of the Ili Basin,

water supply is provided either by rainfall or by surface and subsurface discharge from the head of the alluvial systems of the Tian Shan mountain system (Hellwig *et al.*, 2017). Orogenic uplift reinforced in the late Oligocene to early Miocene at rather low and continuous rates (4 to 5 cm ka^{-1}) and created a hilly landscape (Burtman, 2012). Sedimentological and geochemical data of this study provide evidence for variable water availability with wetter and more arid phases within the alluvial plain of the Ili Basin.

Deposition of medium-grained to coarse-grained sandstones indicates episodes of rapid unchannelled surface drainage with transport of coarser detritus from local source areas. Episodes of distal sheet flood deposition are characterized by low CIA, CPA and Mg/Al ratios, larger grain sizes and poorly sorted fine-sized to medium-sized sandstones. These beds have the lowest Ti/Al ratios, characteristic of unweathered source rock. Sheet flood deposits are overlain by mudstones with hydromorphic features of soil formation (mottling) and phreatic carbonate precipitation close to the groundwater table. Mottling results from reduction of ferrous iron to ferric iron during periods of waterlogging and is indicative of pronounced seasonal wetting (Huggett & Cuadros, 2005; Gale *et al.*, 2006). In addition, high CIA, CPA and Mg/Al ratios and the occurrence of palygorskite indicate arid soil formation by capillary groundwater rise as well as starvation of detrital sediment supply. Elevated groundwater inflow was probably maintained through the underlying relatively permeable sandstones, an effective mechanism described for semi-arid alluvial systems in Miocene basins of Spain (Sanz *et al.*, 1995). Furthermore, incongruent dissolution of detrital Ti-oxides by reducing ground waters and alteration to anatase, as observed for the Jurassic Morrison Formation in Colorado (Adams *et al.*, 1974; Sanford, 1994), is a probably process which led to the observed lowering of Ti/Al ratios. The several metres thick structureless mudstones, instead, are well drained and represent higher rates of vertical mudflat accretion when ongoing detrital sediment production at moderate weathering rates occurred. The well-drained mudflat deposits show the highest Ti/Al ratios. It has been shown by several studies that Ti can be enriched in the fine fraction of detrital sediments (Taboada *et al.*, 2006; Yang *et al.*, 2006; Minyuk *et al.*, 2014). Detrital Ti enrichment occurred by fluvio-aeolian processes when heavy Ti-bearing minerals were concentrated by episodic flooding events and aeolian blowout of ancient surfaces (Figs 5 and 6). Furthermore, successive Ti enrichment in mudflats occurs by in situ weathering and oxidation and the formation of sedimentary anatase (Bestland, 1997).

The Ti/Al ratio is considered as a proxy for sedimentary discharge here. The average TiO_2 concentration ($0{\cdot}7 \pm 0{\cdot}1\%$) in the Bastau Formation is typical for sediments sourced by weathering of igneous and metamorphic parent materials (Salminen *et al.*, 2005). The rather small variability in Ti/Al does not indicate significant provenance changes in the catchment. Climate exerts a major control on sediment supply and fan activity. Ahlborn *et al.* (2015) found a strong relationship between precipitation and sediment supply in a small catchment area on the southern-central Tibetan Plateau. Modelling results have shown that climate variability, in particular precipitation, produce extremely fast responses throughout the catchment–fan system and overprint lower frequency tectonic variations (Allen & Densmore, 2000). Higher rates of alluvial fan activity are directly linked to higher hinterland precipitation and water availability. A similar pattern emerges for sediment accumulation in the Ili Basin. Horizons with elevated Ti/Al correspond to periods of higher detrital sediment supply and thus to overall wetter conditions. Lowered Ti/Al ratios represent intervals of reduced detrital influx and intensified soil formation under more arid conditions (Horizons I to IV and GB).

Accordingly, sheet flood deposition with subsequent pedogenic mottling and deposition of unstructured mudflats represent two climate end-members in the water balance of the local hydrologic system. Flash floods, formed when the water supply exceeds the soil infiltration capacity, allow for the formation of short-term ponds and ground water recharge (Amiaz *et al.*, 2011). At a later stage, evaporative capillary ground water rise led to pore water enrichment and intensified authigenic clay mineral formation under arid conditions. Such a scenario is supported by strong seasonal gradients in both discharge and evaporation. Instead, periods of rather steady detrital supply during mudflat accretion represents a balance of continuous sediment production and in situ weathering without the formation of hydromorphic soil features during periods of less extreme climate. Such a scenario is supported by less pronounced seasonality of discharge and evaporation.

Vegetation

The palynological assemblages from samples KAZ-10 and KAZ-11 yield a consistent picture of the vegetation and environment characterizing the study site at the time of sediment deposition. Based on the ecological preferences of their nearest living parent plants, the identified pollen and spores can be attributed to different vegetation units.

The occurrences of *Sparganiaceaepollenites* (nearest living relative: *Sparganium* – common name: bur-reed) and *Cyperaceaepollis* (Cyperaceae – sedges) along with dinoflagellate cysts of presumably freshwater origin

indicate the existence of perennial marshland and at least temporary open-water bodies. This aquatic/marshland setting was surrounded by riparian forests as documented by the occurrences of substantial amounts of *Alnuspollenites* (*Alnus* – alder) and *Ulmipollenites* (*Ulmus* – elm), and the co-occurrences of *Carpinuspollenites* (*Carpinus* – hornbeam), *Fraxinoipollenites* (*Fraxinus* – ash), *Pterocaryapollenites* (*Pterocarya* – wingnut) and notably *Taxodiaceapollenites* (*Taxodium* – swamp cypress). Ferns and Poaceae (grasses), represented by fern spores and *Graminidites*, respectively, thrived as part of the forest understorey.

Further away from the marshland and under drier conditions, a steppe vegetation prevailed that was characterized by Poaceae along with Asteraceae (represented by *Compositoipollenites*) and xerophytic herbs such as chenopods (goosefoot – represented by *Chenopodipollis*), and different taxa of *Ephedra* (joint-pine – represented by *Ephedripites* spp.).

Finally, the slopes of higher altitude settings in the surroundings supported – possibly patchy – montane, conifer-dominated forests represented by *Pinuspollenites* (*Pinus* – pine), *Piceapollenites* (*Picea* – spruce) and *Abiespollenites* (*Abies* – fir); they may have benefitted from enhanced soil moisture and air humidity in comparison to that available to the lower elevation steppe vegetation.

The palynological results derived from samples KAZ-10 and KAZ-11 are in excellent agreement with other palaeobotanical evidence from the upper Middle to lowermost Upper Miocene of Central Asia, such as from eastern Kazakhstan (Akhmetyev *et al.*, 2005) and the Qaidam Basin of the north-eastern Tibetan Plateau (Miao *et al.*, 2011).

Orbital control on mudflat deposition

The period of the Bastau Formation sediment deposition falls into the juvenile stage of Tian Shan's orogeny of weak crustal deformation and low uplift rates (Burtman, 2012). Corresponding sedimentation rates were in the range of 6 to 13 cm ka^{-1} in the inner and outer basins of the Tian Shan (Huang *et al.*, 2006; Heermance *et al.*, 2007; Charreau *et al.*, 2008). Estimates of average sedimentation rates in the Aktau succession (5·0 to 8·5 cm kyr^{-1}) based on biostratigraphic data presented here fall into this range. The spectral analysis results show two dominant cycle lengths (5·0 to 5·4 m and 20 to 22 m, 6·4 to 7·3 m and 27 to 30 m) at different levels in the Bastau Formation, which we interpret as the signals of short and long eccentricity based on its cycle-to-frequency ratio. The very significant 27 to 28 m cycle in the Ti/Al time series argues for the presence of roughly three 405 kyr cycles (Fig. 9) with an overall duration of deposition of the Bastau Formation of 1·0 to 1·2 Myr. However, lower sedimentation rates in the lower Bastau together with the filter outputs of the 5·0 to 5·4 m and 20 to 22 m cycles show the presence of four 405 kyr cycles, which would extend the duration to 1·4 to 1·6 Myr.

Filter outputs of the two dominant frequencies appear noisy with the highest amplitudes of the 6·4 to 7·3 m cycle at horizons, where the 27 to 30 m cycle displays minima and a very weak signal in the intervals between (Fig. 9). Changes in the sedimentation rate, for example, by elevated/lowered clastic supply or by the longer presence of stable landscapes, can lead to signal distortion (Abels *et al.*, 2009, 2014; Hilgen *et al.*, 2014). Complex interactions between climate and depositional processes as described above involve non-linear feedbacks, which affect the significance of spectral peaks. Together with the low resolution of biostratigraphic age control, cyclostratigraphy is therefore not developed for the Bastau succession, instead the discussion is centred on cycle pattern and amplitudes, which might have been forced by orbitally controlled climate change.

Of interest here is the anti-phase correlation of MS and CPA. Maxima in MS correspond to higher supply rates of unweathered detrital components. Following the notion that higher rates of alluvial activity correspond to higher rates of precipitation and *vice versa*, maximum amplitudes of the 6·4 to 7·3 m cycle should represent the intervals of highest climate variability by recording the most pronounced extremes between evaporation and precipitation in the hydrological balance. The long 27 to 30 m cycle is best expressed in the Ti/Al ratio. The filter output shows minima in the horizons of most elevated climate extremes between pronounced water supply and aridity (Horizons I-IV, GB) and maxima in the interval where the 6·4 to 7·3 m cycle is hard to detect in CPA and MS (Fig. 9). Long-term variability of the Ti/Al paced by the 405 ka cycle describes variations between two climate stages. Minima in Ti/Al correspond to high amplitude climate shifts expressed by abundant discharge of sheet floods during times of elevated precipitation alternating with periods of low detrital supply and alkaline weathering in times of high evaporation. Maxima in Ti/Al reflect periods of more stable sediment production and moderate weathering intensity in times of less extreme climate change. Insolation-driven climate changes strongly affect seasonality, and the observed pattern argues for changes in the seasonal contrast as driving force.

The biostratigraphic age control for the Bastau succession does not allow for direct comparison of the observed orbitally driven climate pattern with the orbital solution (Laskar *et al.*, 2004). However, based on the observations presented here it is possible to speculate that maxima in

the Ti/Al filter output could correspond to long eccentricity minima and the Ti/Al minima to long eccentricity maxima. Individual horizons of maximum aridity represent individual short eccentricity or obliquity cycles. Long eccentricity minima represent periods of higher precipitation and fan activity, corresponding to overall wetter conditions as a result of lower seasonality of precipitation in both the catchment area and the site of deposition. Long eccentricity maxima, instead, refer to lower rates of fine-grained sediment supply and drier periods. At the same time, there is a higher probability for the deposition of coarse-grained sheet floods. This is best expressed around the GB horizon. Stronger seasonal gradients promote seasonally intensified precipitation in the catchment area which discharged into the basin by surface and subsurface flow. Higher MS values and a lower CPA (56 to 58 m) refer to the accumulation of coarser and less weathered clastic material. More subsurface discharge resulted in a groundwater table rise until the formation of palustrine conditions. Parallel to increased water supply, seasonally elevated rates of evaporation led to drying, capillary groundwater rise and gypsum formation. Evidence from palynology describe the low-lying landscape as dry steppe with patchy conifer-dominated forests at higher elevations. Such an open landscape without closed vegetation cover does not provide favourable conditions for the formation of thick soil horizons in the catchment area which could stabilize the erosion of freshly weathered material.

The observation provides support for the hypothesis of Zachos *et al.* (2010) who suggested that the long eccentricity variations in the global carbon cycle are controlled by seasonality of precipitation on land. More year-round precipitation favours the areal spread of humid conditions and wetlands during times of long eccentricity minima, which in turn led to increased terrestrial carbon sequestration. More seasonal precipitation, instead, supports monsoonal and dry climates and increased steppe and dry grasslands. Abels *et al.* (2014) observed a well-developed cyclicity in fluvial sediments of the lower Eocene Willwood Formation of the Bighorn Basin in North America and showed precessional control for overbank avulsion. Furthermore, at the 100 kyr and 405 kyr scales, the bundling of well-developed simple pedofacies cycles can be linked to eccentricity maxima and, thus, to intervals of mature palaeosol development. The 405 kyr cyclicity may have originated from subsequent relatively wet conditions related to high amplitude precession cycles during eccentricity maxima. Such a pattern is also similar to that observed in the Bastau succession. Although it is not possible to discuss phase relationships in terms of the orbital solution, based on the observed pattern, it is possible to suggest that arid to semi-arid terrestrial mudflat sedimentation in the mid-Miocene Ili Basin in Central Asia was strongly controlled by seasonal changes in moisture availability paced by long eccentricity.

Mid-Miocene palaeoenvironment

Proxy records from various basins provide evidence that Central Asia's climate was warmer and wetter in the mid-Miocene in comparison to the long-term Cenozoic average that displayed pronounced aridity and desertification from the Oligocene to early Miocene (Guo *et al.*, 2002; Sun & Windley, 2015; Zheng *et al.*, 2015). Sedimentary facies in the northern Junggar Basin (Fig. 12) comprise fluvial and lacustrine deposits between 17·5 and 13·5 Ma with the onset of aeolian red clay deposition after 13·5 Ma (Sun *et al.*, 2010). Evidence for the presence of perennial fluvial drainage and lakes comes also from the southern Junggar Basin with the development of modern-like desert vegetation after 13·5 Ma (Tang *et al.*, 2011b; Charreau *et al.*, 2012). South of the Tian Shan, reddish mudstones of the Jidike Formation indicate the prevalence of arid conditions since 13·5 Ma (Sun *et al.*, 2015), and palynological evidence from basins in the north-eastern Tibetan Plateau, such as Qaidam and Tianshui, argue for a warmer, moister period between 14 and 15 Ma with substantial cooling and drying afterwards (Hui *et al.*, 2011; Miao *et al.*, 2011). These findings are consistent with the assumption that on longer timescales mid-Miocene warming and late Miocene cooling correspond to the global climate evolution (Zachos *et al.*, 2008; De Vleeschouwer *et al.*, 2017).

Results from climate modelling with Miocene boundary conditions and lower than present topography suggest significant warming in Inner Asia compared to today (Henrot *et al.*, 2010; Tang *et al.*, 2011a). Climate warming is most pronounced in the winter with more zonal climate and increased moisture supply by westerly winds. Strong low-level westerlies were generated as a result of a strong N-S pressure gradient between atmospheric high pressure above the Tibetan Plateau and a low-pressure cell above the northern lowlands (Tang *et al.*, 2011a; Fig. 12). Westerly wind-driven moisture supply is documented for many sites in Inner Asia based on the oxygen isotopic composition of pedogenic carbonates (Caves *et al.*, 2015). In addition, the lack of oxygen isotopic fractionation along the trajectories argues for a high degree of regional moisture recycling by evapotranspiration (Caves *et al.*, 2015).

The palynological results from the Bastau Formation presented here describe an open landscape covered by steppe vegetation with small riparian forests around smaller ponds typical of semi-arid climates. The geochemical data show a strong sedimentary response to regional surface and subsurface water availability relative to orbital

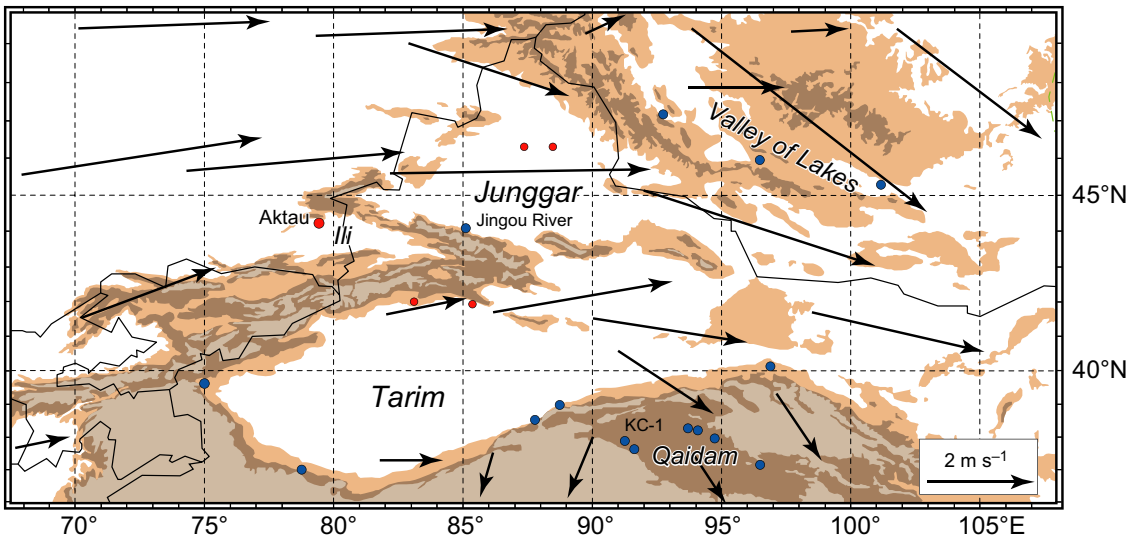

Fig. 12. Topographic map of Inner Asia showing present-day mountain ranges together with results of a regional Miocene climate simulation with lower topography than at present (Tang *et al.*, 2011a). Also shown are localities with Miocene palaeoclimate proxy data from literature and this study (Sun *et al.*, 2010, 2015; Miao *et al.*, 2011; Tang *et al.*, 2011b; Charreau *et al.*, 2012; Caves *et al.*, 2015). Black arrows are modelled vectors of low level winter winds at 850 hPa. Blue sites show localities with pedogenic oxygen isotopic evidence for westerly wind sourced moisture supply (Caves *et al.*, 2015). Topographic colour coding represents the current 1500 m (light brown), 2500 m (dark brown) and 4000 m (grey) isoheights.

extremes. Insolation changes affect the length of the seasons and, thus, the intensity of winter precipitation. Most of the precipitation is probably trapped by the low-relief mountain ranges of the Tian Shan, which served as a regional source for runoff, aquifer recharge and detrital sediment supply. The intensity of westerly winter winds are assumed to have responded sensitively to orbital forcing, hence controlling the amount of moisture available for regional recycling in both the catchment area and the aquifers. In times of pronounced regional evapotranspiration, a stronger summer–winter gradient of westerly wind intensity probably reduced the amount of precipitation within the basin and additionally increased the probability for heavy rain storms and flash flood deposition due to more intense precipitation events in the catchment area. In times of wetter conditions, a lower summer–winter gradient of westerly intensity increased the amounts of year-round surface runoff and activated mudflat aggradation.

The overall successions of both sedimentary facies and geochemical data of the Bastau Formation represent enhancement of aridity on longer time scales. The establishment of alkaline palustrine conditions marks a transition in the Miocene evolution of the Ili Basin when hypersaline conditions prevailed in the basin with limited runoff. Incoming water from floods evaporated and as the brine concentrates gypsum precipitated either directly from solution or by forming pedogenic crystallites and crusts on top of the playa floor. The appearance of gypsum occurred rather abruptly and could be explained either by the formation of endorheic conditions or by climate change. Since endorheic conditions were already prevalent from the onset of mudflat deposition in the Bastau Formation, the first accumulation of gypsum is related to a severe change in the regional climate system from wetter semi-arid conditions to more pronounced aridity. A dry climate persisted from this time onwards.

The sudden appearance of gypsum in the Miocene Ili Basin is difficult to explain and the source of the sulphur is questionable since gypsum is completely absent in the succession below the palustrine GB horizon. There are no local sulphur sources in the catchment area since it consists entirely of rhyolitic and andesitic volcanic rocks (Jahn *et al.*, 2000, 2004). It is possible that the sulphur originated from a marine source. Deposition of Bastau Formation sediments lasted for about 1·0 to 1·2 Myr with the biostratigraphic data indicating a middle Miocene, possibly Langhian age (Fig. 3). At this time, extensive evaporites were deposited at the margins of the Eastern Paratethys (Rögl, 1999; Popov *et al.*, 2004; Bruch *et al.*, 2007). Although, this area is located more than 500 km

west of the Ili Basin based on palaeogeographic reconstructions (Popov *et al.*, 2004), the precise position of the Eastern Paratethys shoreline is not well constrained from geological data because of the absence of Neogene sediments in central Kazakhstan. However, assuming the prevalence of westerly winds evident from Miocene climate modelling (Henrot *et al.*, 2010; Tang *et al.*, 2011a), the high degree of regional moisture recycling by evapotranspiration evident from the low fractionation of pedogenic oxygen isotopes (Caves *et al.*, 2015), sulphur could have been transported via several precipitation/infiltration/deflation steps from the Eastern Paratethys. Such a mechanism is also supported by oceanographic box modelling results, which show increased salinity and lowered temperature in the Mediterranean–Eastern Paratethys system as a result of gateway closure to the Indian Ocean in the late Langhian to early Serravallian (Karami *et al.*, 2009). Furthermore, the rather sudden occurrence of gypsum could be related to transgressive eastward extension of the Eastern Paratethys (Popov *et al.*, 2004). Although a precise dating of the facies shift is not yet possible, the mid-Miocene Tchokrakian transgression is a good candidate.

CONCLUSIONS

Middle Miocene mudflat and marginal playa lake sediments were deposited at the margin of low-gradient alluvial systems in the endorheic Ili Basin, south-east Kazakhstan within the Tian Shan mountain system. The 91 m thick Bastau Formation exposed in the Aktau Mountains was studied for its bulk-sediment geochemistry, MS and sediment colour to characterize its composition and to determine changes in weathering, pedogenesis and alluvial fan activity. A positive correlation between weathering indices (CIA, CPA) and the Mg/Al ratio documents evaporative enrichment and authigenic Mg fixation by clay mineral formation in the vadose zone in highly alkaline/saline settings. Four major periods of arid soil formation and one palustrine interval represent the highest degrees of weathering in periods when pedogenesis exceeded sedimentary discharge. Periods of higher moisture availability and higher rates of hinterland precipitation are indicated by successive mudflat accretion by higher alluvial fan activity recorded by elevated Ti/Al ratios and MS.

Time series analysis of chemical weathering indices, MS and sediment colour data show cycle-to-frequency ratios typical of Milankovitch cyclicity, with dominant periodicities interpreted as representing short and long eccentricity cycles. In particular, the Ti/Al ratio demonstrates a pacing of pedogenic mottling and detrital mudflat accretion by long eccentricity, thus suggesting an orbital control on regional moisture availability and mudflat deposition. It is assumed that more frequent bundling of sheet flood deposition and subsequent pedogenic alteration correspond to long eccentricity maxima, and longer lasting periods of elevated fan activity to long eccentricity minima. However, a better-constrained age model is necessary to relate these changes to the orbital solution.

The overall sedimentary succession shows a long-lasting increase in aridity in the studied area. Of particular interest is the abrupt onset of gypsum formation at the time the GB horizon was deposited. The sudden appearance of gypsum beds indicates a climate and possibly orbital trigger analogous to the initiation of the Messinian salinity crisis in the Mediterranean. Such a trigger could have been the transition to the mid-Miocene cooling. On longer timescales, the closure of the eastern gateway of the Mediterranean to the Indian Ocean enhanced restriction within Eastern Tethys, providing the necessary boundary conditions.

In light of the results above, the quasi-continuous, terrestrial Miocene succession of the Aktau Hills emerges as a sensitive recorder of changes in atmospheric moisture supply. This makes it a highly promising terrestrial archive for palaeoclimate research, ideally located in order to address the role of Central Asia in the global climate evolution during the Miocene.

ACKNOWLEDGEMENTS

We thank the Deutsche Forschungsgemeinschaft for granting several field campaigns (DFG grants VO 687/13, VO 687/16 and PR 651/13). In particular, we thank Konstantin Kossov, Julia Zhilkina and Marat Ainsonow for logistical support and their warm and friendly company in the field. The administration and rangers of the State National Park Altyn Emel are thanked for providing access to the Aktau Mountains for geological field work. We thank André Baldermann and an anonymous reviewer for their constructive and insightful reviews of this work.

References

Abdrakhmatov, K.Y., Aldazhanov, S.A., Hager, B.H., Hamburger, M.W., Herring, T.A., Kalabaev, K.B., Makarov, V.I., Molnar, P., Panasyuk, S.V., Prilepin, M.T., Reilinger, R.E., Sadybakasov, I.S., Souter, B.J., Trapeznikov, Y.A., Tsurkov, V.Y. and **Zubovich, A.V.** (1996) Relatively recent construction of the Tien Shan inferred from GPS measurements of present-day crustal deformation rates. *Nature*, **384**, 450–453.

Abels, H.A., Aziz, H.A., Ventra, D. and **Hilgen, F.J.** (2009) Orbital climate forcing in mudflat to marginal lacustrine

deposits in the Miocene Teruel Basin (Northeast Spain). *J. Sed. Res.*, **79**, 831–847.

Abels, H.A., Kraus, M.J. and **Gingerich, P.** (2014) Precession-scale cyclicity in the fluvial lower Eocene Willwood Formation of the Bighorn Basin, Wyoming (USA). *Sedimentology*, **60**, 1467–1483.

Adams, S.S., Curtis, H.S. and **Hafen, P.L.** (1974) Alteration of detrital magnetite-ilmenite in continental sandstones of the Morrison Formation, New Mexico. In: *Symposium on the Formation of Uranium Ore Deposits*, International Atomic Energy Agency, Vienna, Proceedings series, 219–252.

Ahlborn, M., Haberzettl, T., Wang, J.B., Alivernini, M., Schlutz, F., Schwarz, A., Su, Y.L., Frenzel, P., Daut, G., Zhu, L.P. and **Mäusbacher, R.** (2015) Sediment dynamics and hydrologic events affecting small lacustrine systems on the southern-central Tibetan Plateau – the example of TT Lake. *Holocene*, **25**, 508–522.

Akhmetyev, M.A., Dodoniv, A.E., Sornikova, M.V., Spasskaya, I.I., Kremenetsky, K.V. and **Klimanov, V.A.** (2005). Kazakhstan and Central Asia (Plains and Foothills). In: *Cenozoic Climatic and Environmental Changes in Russia* (Eds A.A. Velichko and V.P. Nechaev), *Geol. Soc. Am. Spec. Paper*, **382**, 139–161.

Allen, P.A. and **Densmore, A.L.** (2000) Sediment flux from an uplifting fault block. *Basin Res.*, **12**, 367–380.

Amante, C. and **Eakins, B.W.** (2009) *ETOPO1 1 Arc-Minute Global Relief Model: Procedures, Data Sources and Analysis*. NOAA Technical Memorandum NESDIS NGDC-24, Nat. Geophys. Data Center, NOAA. https://doi.org/10.7289/v5c8276m.

Amiaz, Y., Sorek, S., Enzel, Y. and **Dahan, O.** (2011) Solute transport in the vadose zone and groundwater during flash floods. *Water Resour. Res.*, **47**, W10513. https://doi.org/10.1029/2011wr010747.

Badaut, D. and **Risacher, F.** (1983) Authigenic smectite on diatom frustules in Bolivian saline lakes. *Geochim. Cosmochim. Acta*, **47**, 363–375.

Baldermann, A., Warr, L.N., Letofsky-Papst, I. and **Mavromatis, V.** (2015) Substantial iron sequestration during green-clay authigenesis in modern deep-sea sediments. *Nat. Geosci.*, **8**, 885–890.

Banfield, J.F., Jones, B.F. and **Veblen, D.R.** (1991) An AEM-TEM Study of Weathering and Diagenesis, Abert Lake, Oregon. 2. Diagenetic Modification of the Sedimentary Assemblage. *Geochim. Cosmochim. Acta*, **55**, 2795–2810.

Bazhanov, V.S. and **Kostenko, N.N.** (1961) Geologicheskiy razrez Dzhungarskogo Alatau i ego paleozoologicheskoye obosnovanie [Geological section of Dzhungarian Alatau and its paleontological basis]. In: *Materialy po istorii fauny i flory Kazakhstana* (Ed. I.G. Galuzo), *Akademia Nauk Kazakhskoy SSR, Alma Ata*, **3**, 47–52.

Bestland, E.A. (1997) Alluvial terraces and paleosols as indicators of early Oligocene climate change (John Day Formation, Oregon). *J. Sed. Res.*, **67**, 840–855.

Bodina, L.E. (1961) Ostrakody tretichnykh otlozhenii Zaisanskoi I Iliiskoi depressi [Ostracods of Tertiary deposits in the Zaisan and Ili depressions]. *Trudy VNIGRI*, **170**, 43–153.

Bruch, A.A., Uhl, D. and **Mosbrugger, V.** (2007) Miocene climate in Europe – patterns and evolution – a first synthesis of NECLIME. *Palaeogeogr. Palaeoclimatol. Palaeoecol.*, **253**, 1–7.

Buggle, B., Glaser, B., Hambach, U., Gerasimenko, N. and **Markovic, S.** (2011) An evaluation of geochemical weathering indices in loess-paleosol studies. *Quatern. Int.*, **240**, 12–21.

Burtman, V.S. (2012) Geodymanics of Tibet, Tarim, and the Tien Shan in the Late Cenozoic. *Geotectonics*, **46**, 185–211.

Calvo, J.P., Blanc-Valleron, M.M., Rodríguez-Arandía, J.P., Rouchy, J.M. and **Sanz, M.E.** (1999) Authigenic clay minerals in continental evaporitic environments. In: *Paleoweathering, Palaeosurfaces and Related Continental Deposits* (Eds M. Thiry and R. Simon-Coincon), *Spec. Publ. Int. Ass. Sedimentol.*, **27**, 129–151.

Caves, J.K., Winnick, M.J., Graham, S.A., Sjostrom, D.J., Mulch, A. and **Chamberlain, C.P.** (2015) Role of the westerlies in Central Asia climate over the Cenozoic. *Earth Planet. Sci. Lett.*, **428**, 33–43.

Charreau, J., Avouac, J.P., Chen, Y., Dominguez, S. and **Gilder, S.** (2008) Miocene to present kinematics of fault-bend folding across the Huerguosi anticline, northern Tianshan (China), derived from structural, seismic, and magnetostratigraphic data. *Geology*, **36**, 871–874.

Charreau, J., Kent-Corson, M.L., Barrier, L., Augier, R., Ritts, B.D., Chen, Y., France-Lannord, C. and **Guilmette, C.** (2012) A high-resolution stable isotopic record from the Junggar Basin (NW China): implications for the paleotopographic evolution of the Tianshan Mountains. *Earth Planet. Sci. Lett.*, **341**, 158–169.

Cuadros, J., Diaz-Hernandez, J.L., Sanchez-Navas, A., Garcia-Casco, A. and **Yepes, J.** (2016) Chemical and textural controls on the formation of sepiolite, palygorskite and dolomite in volcanic soils. *Geoderma*, **271**, 99–114.

De Vleeschouwer, D., Vahlenkamp, M., Crucifix, M. and **Pälike, H.** (2017) Alternating Southern and Northern Hemisphere climate response to astronomical forcing during the past 35 m.y. *Geology*, **45**, 375–378.

Deocampo, D.M. (2004) Authigenic clays in East Africa: regional trends and paleolimnology at the Plio-Pleistocene boundary, Olduvai Gorge, Tanzania. *J. Paleolimnol.*, **31**, 1–9.

Deocampo, D.M. (2015) Authigenic clay minerals in lacustrine mudstones. In: *Paying Attention to Mudrocks* (Eds D. Larsen, S.O. Egenhoff and N.S. Fishman), *Geol. Soc. Am. Spec. Paper*, **515**, 45–64.

Deocampo, D.M., Cuadros, J., Wing-Dudek, T., Olives, J. and **Amouric, M.** (2009) Saline Lake diagenesis as revealed by coupled mineralogy and geochemistry of multiple

ultrafine clay phases: pliocene Olduvai Gorge, Tanzania. *Am. J. Sci.*, **309**, 834–868.

Dettman, D.L., Fang, X.M., Garzione, C.N. and **Li, J.J.** (2003) Uplift-driven climate change at 12 Ma: a long delta O-18 record from the NE margin of the Tibetan plateau. *Earth Planet. Sci. Lett.*, **214**, 267–277.

Dupont-Nivet, G., Krijgsman, W., Langereis, C.G., Abels, H.A., Dai, S. and **Fang, X.M.** (2007) Tibetan plateau aridification linked to global cooling at the Eocene-Oligocene transition. *Nature*, **445**, 635–638.

Dzhamangaraeva, A.K. (1997) Pliocene charophytes from Aktau Mountain, southeastern Kazakhstan. *Geobios*, **30**, 475–479.

Eberl, D.D., Srodon, J. and **Northrop, H.R.** (1986) Potassium fixation in smectite by wetting and drying. *ACS Sym. Ser.*, **323**, 296–326.

Gale, A.S., Huggett, J.M., Pälike, H., Laurie, E., Hailwood, E.A. and **Hardenbol, J.** (2006) Correlation of Eocene-Oligocene marine and continental records: orbital cyclicity, magnetostratigraphy and sequence stratigraphy of the Solent Group, Isle of Wight, UK. *J. Geol. Soc. London*, **163**, 401–415.

Goldberg, K. and **Humayun, M.** (2010) The applicability of the Chemical Index of Alteration as a paleoclimatic indicator: an example from the Permian of the Parana Basin, Brazil. *Palaeogeogr. Palaeoclimatol. Palaeoecol.*, **293**, 175–183.

Gromova, V. (1952) Primitívnye tapiroobrazye iz Paleogena Mongolij [Primitive tapirs from the Paleogene of Mongolia]. *Akad. Nauk SSSR Trud. Paleontolog. Inst.*, **41**, 99–119.

Guo, Z.T., Ruddiman, W.F., Hao, Q.Z., Wu, H.B., Qiao, Y.S., Zhu, R.X., Peng, S.Z., Wei, J.J., Yuan, B.Y. and **Liu, T.S.** (2002) Onset of Asian desertification by 22 Myr ago inferred from loess deposits in China. *Nature*, **416**, 159–163.

Hammer, Ø., Harper, D.A.T. and **Ryan, P.D.** (2001) PAST: paleontological Statistics software package for education and data analysis. *Palaeontol. Electr.*, **4**, 9.

Han, F., Rydin, C., Bolinder, K., Dupont-Nivet, G., Abels, H.A., Koutsodendris, A., Zhang, K.X. and **Hoorn, C.** (2016) Steppe development on the Northern Tibetan Plateau inferred from Paleogene ephedroid pollen. *Grana*, **55**, 71–100.

Harzhauser, M., Daxner-Höck, G., López-Guerrero, P., Maridet, O., Oliver, A., Piller, W.E., Richoz, S., Erbajeva, M.A., Neubauer, T.A. and **Göhlich, U.B.** (2016) Stepwise onset of the Icehouse world and its impact on Oligo-Miocene Central Asian mammals. *Sci. Rep.*, **6**, 36169.

Heermance, R.V., Richard, V., Chen, J., Burbank, D.W., Douglas, W. and **Wang, C.** (2007) Chronology and tectonic controls of late Tertiary deposition in the Southwestern Tian Shan Foreland, NW China. *Basin Res.*, **19**, 599–632.

Hellwig, A., Voigt, S., Mulch, A., Frisch, K., Bartenstein, A., Pross, J., Gerdes, A. and **Voigt, T.** (2017) Late Oligocene–early Miocene humidity change recorded in terrestrial sequences in the Ili Basin (SE Kazakhstan, Central Asia). *Sedimentology*. https://doi.org/10.1111/sed.12390.

Hendrix, M.S., Dumitru, T.A. and **Graham, S.A.** (1994) Late Oligocene Early Miocene unroofing in the Chinese Tien-Shan – an early effect of the India-Asia collision. *Geology*, **22**, 487–490.

Henrot, A.J., Francois, L., Favre, E., Butzin, M., Ouberdous, M. and **Munhoven, G.** (2010) Effects of CO_2, continental distribution, topography and vegetation changes on the climate at the Middle Miocene: a model study. *Clim. Past*, **6**, 675–694.

Herb, C., Koutsodendris, A., Zhang, W.L., Appel, E., Fang, X.M., Voigt, S. and **Pross, J.** (2015) Late Plio-Pleistocene humidity fluctuations in the western Qaidam Basin (NE Tibetan Plateau) revealed by an integrated magnetic-palynological record from lacustrine sediments. *Quatern. Res.*, **84**, 457–466.

Hilgen, F.J., Hinnov, L.A., Aziz, H.A., Abels, H.A., Batenburg, S., Bosmans, J.H.C., De Boer, B., Husing, S.K., Kuiper, K.F., Lourens, L.J., Rivera, T., Tuenter, E., Van De Wal, R.S.W., Wotzlaw, J.F. and **Zeeden, C.** (2014) Stratigraphic continuity and fragmentary sedimentation: the success of cyclostratigraphy as part of integrated stratigraphy. *Geol. Soc. Spec. Publ.*, **404**, 157–197.

Holbourn, A., Kuhnt, W., Lyle, M., Schneider, L., Romero, O. and **Andersen, N.** (2014) Middle Miocene climate cooling linked to intensification of eastern equatorial Pacific upwelling. *Geology*, **42**, 19–22.

Holbourn, A., Kuhnt, W., Kochhann, K.G.D., Andersen, N. and **Meier, K.J.S.** (2015) Global perturbation of the carbon cycle at the onset of the Miocene Climatic Optimum. *Geology*, **43**, 123–126.

Hoorn, C., Straathof, J., Abels, H.A., Xu, Y.D., Utescher, T. and **Dupont-Nivet, G.** (2012) A late Eocene palynological record of climate change and Tibetan Plateau uplift (Xining Basin, China). *Palaeogeogr. Palaeoclimatol. Palaeoecol.*, **344**, 16–38.

Huang, B.C., Piper, J.D.A., Peng, S.T., Liu, T., Li, Z. and **Zhu, R.X.** (2006) Magneto stratigraphic study of the Kuche Depression, Tarim Basin, and Cenozoic uplift of the Tian Shan Range, Western China. *Earth Planet. Sci. Lett.*, **251**, 346–364.

Huggett, J.M. and **Cuadros, J.** (2005) Low-temperature illitization of smectite in the late Eocene and early Oligocene of the Isle of Wight (Hampshire basin), UK. *Am. Mineral.*, **90**, 1192–1202.

Hui, Z.C., Li, J.J., Xu, Q.H., Song, C.H., Zhang, J., Wu, F.L. and **Zhao, Z.J.** (2011) Miocene vegetation and climatic changes reconstructed from a sporopollen record of the Tianshui Basin, NE Tibetan Plateau. *Palaeogeogr. Palaeoclimatol. Palaeoecol.*, **308**, 373–382.

Jahn, B.M., Wu, F.Y. and **Chen, B.** (2000) Massive granitoid generation in Central Asia: Nd isotope evidence and implication for continental growth in the Phanerozoic. *Episodes*, **23**, 82–92.

Jahn, B.M., Windley, B., Natal'in, B. and **Dobretsov, N.** (2004) Phanerozoic continental growth in central Asia – Preface. *J. Asian Earth Sci.*, **23**, 599–603.

Jones, B.F. and **Galan, E.** (1988) Sepiolite and Palygorskite. *Rev. Mineral.*, **19**, 631–674.

Jones, B.F. and **Weir, A.H.** (1983) Clay-Minerals of Lake Abert, an alkaline, saline lake. *Clays Clay Miner.*, **31**, 161–172.

Karami, M.P., Meijer, P.T., Dijkstra, H.A. and **Wortel, M.J.R.** (2009) An oceanic box model of the Miocene Mediterranean Sea with emphasis on the effects of closure of the eastern gateway. *Paleoceanography*, **24**, PA4203. https://doi.org/10.1029/2008pa001679.

Kent-Corson, M.L., Ritts, B.D., Zhuang, G.S., Bovet, P.M., Graham, S.A. and **Chamberlain, C.P.** (2009) Stable isotopic constraints on the tectonic, topographic, and climatic evolution of the northern margin of the Tibetan Plateau. *Earth Planet. Sci. Lett.*, **282**, 158–166.

Kober, M., Seib, N., Kley, J. and **Voigt, T.** (2013) Thick-skinned thrusting in the northern Tien Shan foreland, Kazakhstan: structural inheritance and polyphase deformation. *Geol. Soc. Spec. Publ.*, **377**, 19–42.

Kordikova, E.G. (2000) Insectivora (Mammalia) from the Lower Miocene of the Aktau Mountains, South-Eastern Kazakhstan. *Senckenb. Lethaea*, **80**, 67–79.

Kordikova, E.G. and **de Bruijn, H.** (2001) Early Miocene Rodents from the Aktau Mountains (South-Eastern Kazakhstan). *Senckenb. Lethaea*, **81**, 391–405.

Kordikova, E.G. and **Mavrin, A.V.** (1996) Stratigraphy and Oligocene-Miocene mammalian biochronology of the Aktau Mountains, Dzhungarian Alatau range, Kazakhstan. *Palaeovertebrata*, **25**, 141–174.

Laskar, J., Robutel, P., Joutel, F., Gastineau, M., Correia, A.C.M. and **Levrard, B.** (2004) A long-term numerical solution for the insolation quantities of the Earth. *Astron. Astrophys.*, **428**, 261–285.

Li, D., He, D., Maa, D., Tang, Y., Kong, Y. and **Tang, J.** (2015) Carboniferous-Permian tectonic framework and its later modifications to the area from eastern Kazakhstan to southern Altai: insights from the Zaysan-Jimunai Basin evolution. *J. Asian Earth Sci.*, **113**, 16–35.

Licht, A., Van Cappelle, M., Abels, H.A., Ladant, J.B., Trabucho-Alexandre, J., France-Lanord, C., Donnadieu, Y., Vandenberghe, J., Rigaudier, T., Lecuyer, C., Terry, D., Adriaens, R., Boura, A., Guo, Z., Soe, A.N., Quade, J., Dupont-Nivet, G. and **Jaeger, J.J.** (2014) Asian monsoons in a late Eocene greenhouse world. *Nature*, **513**, 501–506.

Liu, W.G., Liu, Z.H., An, Z.S., Sun, J.M., Chang, H., Wang, N., Dong, J.B. and **Wang, H.Y.** (2014) Late Miocene episodic lakes in the arid Tarim Basin, western China. *Proc. Natl Acad. Sci. USA*, **111**, 16292–16296.

Lucas, S.G., Bayshashov, B.U., Tyutkova, L.A., Zhamangara, A.K. and **Aubekerov, B.Z.** (1997) Mammalian biochronology of the Paleogene-Neogene boundary at Aktau Mountain, eastern Kazakhstan. *Paläontol. Z.*, **71**, 305–314.

Macaulay, E.A., Sobel, E.R., Mikolaichuk, A., Kohn, B. and **Stuart, F.M.** (2014) Cenozoic deformation and exhumation history of the Central Kyrgyz Tien Shan. *Tectonics*, **33**, 135–165.

Maliva, R. and **Missimer, T.** (2012) *Arid Lands Water Evaluation and Management, Environmental Science and Engineering*. Springer-Verlag, Berlin, Heidelberg, 148 pp.

Maynard, J.B. (1992) Chemistry of modern soils as a guide to Interpreting Precambrian Paleosols. *J. Geol.*, **100**, 279–289.

Meyers, S.R. (2014) Astrochron: an R package for astrochronology. Available at: https://cran.r-project.org/package=astrochron.

Meyers, S.R. and **Sageman, B.B.** (2007) Quantification of deep-time orbital forcing by average spectral misfit. *Am. J. Sci.*, **307**, 773–792.

Meyers, S.R., Bradley, B.S. and **Michael, A.A.** (2012) Obliquity forcing of organic matter accumulation during Oceanic Anoxic Event 2. *Paleoceanography*, **27**, PA3212. https://doi.org/10.1029/2012PA002286.

Miao, Y.F., Fang, X.M., Herrmann, M., Wu, F.L., Zhang, Y.Z. and **Liu, D.L.** (2011) Miocene pollen record of KC-1 core in the Qaidam Basin, NE Tibetan Plateau and implications for evolution of the East Asian monsoon. *Palaeogeogr. Palaeoclimatol. Palaeoecol.*, **299**, 30–38.

Miao, Y.F., Fang, X.M., Liu, Y.S., Yan, X.L., Li, S.Y. and **Xia, W.M.** (2016) Late Cenozoic pollen concentration in the western Qaidam Basin, northern Tibetan Plateau, and its significance for paleoclimate and tectonics. *Rev. Palaeobot. Palynol.*, **231**, 14–22.

Minyuk, P.S., Borkhodoev, V.Y. and **Wennrich, V.** (2014) Inorganic geochemistry data from Lake El'gygytgyn sediments: marine isotope stages 6-11. *Clim. Past*, **10**, 467–485.

Molnar, P. and **Tapponnier, P.** (1975) Cenozoic tectonics of Asia – effects of a continental collision. *Science*, **189**, 419–426.

Nesbitt, H.W. and **Young, G.M.** (1982) Early proterozoic climates and plate motions inferred from major element chemistry of lutites. *Nature*, **299**, 715–717.

Nesbitt, H.W. and **Young, G.M.** (1984) Prediction of some weathering trends of plutonic and volcanic-rocks based on thermodynamic and kinetic considerations. *Geochim. Cosmochim. Acta*, **48**, 1523–1534.

Nesbitt, H.W. and **Young, G.M.** (1989) Formation and diagenesis of weathering profiles. *J. Geol.*, **97**, 129–147.

Popov, S.V., Rögl, F., Rozanov, A.Y., Steiniger, F.F., Shcherba, I.G. and **Kovac, M.** (eds.) (2004) Lithological-Paleogeographical maps of Paratethys. *Cour. Forsch.-Inst. Senckenberg*, **250**, 1–46.

Popov, S.V., Antipov, M.P., Zastrozhnov, A.S., Kurina, E.E. and **Pinchuk, T.N.** (2010) Sea-level fluctuations on the northern shelf of the Eastern Paratethys in the Oligocene-Neogene. *Stratigr. Geo. Correl.*, **18**, 200–224.

Ramstein, G., Fluteau, F., Besse, J. and **Joussaume, S.** (1997) Effect of orogeny, plate motion and land sea distribution on

Eurasian climate change over the past 30 million years. *Nature*, **386**, 788–795.

Richoz, S., Baldermann, A., Frauwallner, A., Harzhauser, M., Daxner-Höck, G., Klammer, D. and **Piller, W.E.** (2017) Geochemistry and mineralogy of the Oligo-Miocene sediments of the Valley of Lakes, Mongolia. *Palaeobio. Palaeoenv.*, **97**, 233–258.

Rögl, F. (1999) Mediterranean and Paratethys. Facts and hypotheses of an Oligocene to Miocene paleogeography (short overview). *Geol. Carpathica*, **50**, 339–349.

Salminen, R. (Chief-editor), Batista, M.J., Bidovec, M., Demetriades, A., De Vivo, B., De Vos, W., Duris, M., Gilucis, A., Gregorauskiene, V., Halamic, J., Heitzmann, P., Lima, A., Jordan, G., Klaver, G., Klein, P., Lis, J., Locutura, J., Marsina, K., Mazreku, A., O'Connor, P.J., Olsson, S., Ottesen, R.T., Petersell, V., Plant, J.A., Reeder, S., Salpeteur, I., Sandström, H., Siewers, U., Steenfeldt, A. and **Tarvainen, T.** (2005) *FOREGS Geochemical atlas of Europe, Part 1: Background Information, Methodology and Maps*. Geological Survey of Finland, Espoo, 525 pp, 36 figures, 362 maps.

Sanford, R.F. (1994) Hydrogeology of Jurassic and Triassic wetlands in the Colorado Plateau and the origin of tabular sandstone uranium deposits. *U.S. Geol. Surv. Prof. Paper*, **1548**, 1–40.

Sanz, M.E., Alonsozarza, A.M. and **Calvo, J.P.** (1995) Carbonate pond deposits related to semiarid alluvial systems – examples from the Tertiary Madrid Basin, Spain. *Sedimentology*, **42**, 437–452.

Schulz, M. and **Mudelsee, M.** (2002) REDFIT: estimating red-noise spectra directly from unevenly spaced paleoclimatic time series. *Comput. Geosci.*, **28**, 421–426.

Sheldon, N.D. and **Tabor, N.J.** (2009) Quantitative paleoenvironmental and paleoclimatic reconstruction using paleosols. *Earth-Sci. Rev.*, **95**, 1–52.

Singer, A. (1988) Illite in aridic soils, desert dusts and desert loess. *Sed. Geol.*, **59**, 251–259.

Singer, A. and **Stoffers, P.** (1980) Clay mineral diagenesis in two East-African Lake-Sediments. *Clay Miner.*, **15**, 291–307.

Sobel, E.R., Hilley, G.E. and **Strecker, M.R.** (2003) Formation of internally drained contractional basins by aridity-limited bedrock incision. *J. Geophys. Res.-Soil Earth*, **108**, 2344. https://doi.org/10.1029/2002jb001883.

Sobel, E.R., Chen, J. and **Heermance, R.V.** (2006) Late Oligocene-Early Miocene initiation of shortening in the Southwestern Chinese Tian Shan: implications for Neogene shortening rate variations. *Earth Planet. Sci. Lett.*, **247**, 70–81.

Sun, J.M. and **Windley, B.F.** (2015) Onset of aridification by 34 Ma across the Eocene-Oligocene transition in Central Asia. *Geology*, **43**, 1015–1018.

Sun, J.M., Ye, J., Wu, W.Y., Ni, X.J., Bi, S.D., Zhang, Z.Q., Liu, W.M. and **Meng, J.** (2010) Late Oligocene-Miocene mid-latitude aridification and wind patterns in the Asian interior. *Geology*, **38**, 515–518.

Sun, J.M., Gong, Z.J., Tian, Z.H., Jia, Y.Y. and **Windley, B.** (2015) Late Miocene stepwise aridification in the Asian interior and the interplay between tectonics and climate. *Palaeogeogr. Palaeoclimatol. Palaeoecol.*, **421**, 48–59.

Taboada, T., Cortizas, A.M., Garcia, C. and **Garcia-Rodeja, E.** (2006) Particle-size fractionation of titanium and zirconium during weathering and pedogenesis of granitic rocks in NW Spain. *Geoderma*, **131**, 218–236.

Tang, H., Micheels, A., Eronen, J. and **Fortelius, M.** (2011a) Regional climate model experiments to investigate the Asian monsoon in the Late Miocene. *Clim. Past*, **7**, 847–868.

Tang, Z.H., Ding, Z.L., White, P.D., Dong, X.X., Ji, J.L., Jiang, H.C., Luo, P. and **Wang, X.** (2011b) Late Cenozoic central Asian drying inferred from a palynological record from the northern Tian Shan. *Earth Planet. Sci. Lett.*, **302**, 439–447.

Torres, M.A. and **Gaines, R.R.** (2013) Paleoenvironmental and Paleoclimatic Interpretations of the Late Paleocene Goler Formation, Southern California, USA, Based on Paleosol Geochemistry. *J. Sed. Res.*, **83**, 591–605.

Wang, B. (2006) *The Asian Monsoon*. Springer Praxis Books, Berlin, 788 pp.

Weedon, G. (2003) *Time-series Analysis and Cyclostratigraphy*. Cambridge University Press, Cambridge, 259 pp.

Yang, S.L., Ding, F. and **Ding, Z.L.** (2006) Pleistocene chemical weathering history of Asian arid and semi-arid regions recorded in loess deposits of China and Tajikistan. *Geochim. Cosmochim. Acta*, **70**, 1695–1709.

Zachos, J.C., Dickens, G.R. and **Zeebe, R.E.** (2008) An early Cenozoic perspective on greenhouse warming and carbon-cycle dynamics. *Nature*, **451**, 279–283.

Zachos, J.C., Mccarren, H., Murphy, B., Röhl, U. and **Westerhold, T.** (2010) Tempo and scale of late Paleocene and early Eocene carbon isotope cycles: implications for the origin of hyperthermals. *Earth Planet. Sci. Lett.*, **299**, 242–249.

Zheng, H.B., Wei, X.C., Tada, R.J., Clift, P.D., Wang, B., Jourdan, F., Wang, P. and **He, M.Y.** (2015) Late Oligocene-early Miocene birth of the Taklimakan Desert. *Proc. Natl Acad. Sci. USA*, **112**, 7662–7667.

Supporting Information

Additional Supporting Information may be found online in the supporting information tab for this article:

Data S1. Magnetic susceptibility, geochemistry and colour data of Bastau Formation sediments.

Chapter 6

Further paleoclimatic studies

The established magnetostratigraphy of the Bastau Fm (Verestek et al., 2018, Chapter 3) provided a robust temporal framework for further studies on the Miocene paleoenvironment in the Ili Basin. In collaboration with the team from the Goethe University Frankfurt, further publications emerged from sedimentological and geochemical studies on the terrestrial Miocene succession of the Aktau Mountains. These publications are not included in this doctoral thesis because they do not deal with rock magnetic properties of the sedimentary succession but highly benefited from joint discussions and comparisons with rock magnetic records. In the following, the main findings are summarized.

Studying the middle to late Miocene alluvial-lacustrine deposits, Frisch et al. (2019) reconstructed the hydrological evolution of the Ili Basin and attributed the long-term evolution of a terminal lake to a climatic control. Based on the age model developed in Verestek et al. (2018) (Chapter 3), the onset and enhancement of the salinization could be correlated to the first major cooling step of the Miocene Climate Transition (Holbourn et al., 2013). In the Ili Basin, this is marked by a period of pronounced aridity and increased seasonality. The periods of extreme aridity in the Ili Basin are suggested to be a continental counterpart to the Badenian Salinity Crisis (13.8 Ma to approx. 13.4 Ma) in the Paratethys (Palcu et al., 2017; Frisch et al., 2019). This highlights the contribution of atmospheric forcing to the widespread occurrences of high evaporation environments across Eurasia during the Middle Miocene (Frisch et al., 2019).

Further studies on element geochemistry and stable isotopes ($\delta^{13}C$ and $\delta^{18}O$) of the middle to late Miocene succession were combined with time series analyses to assess the forcing mechanisms. For cyclostratigraphic interpretation the Ti/Al ratio, sulphate content, $\delta^{13}C$ and water level were used. The hydrological budget of the closed basin shows a link to the obliquity modulation as well as a response to long and short eccentricity forcing. The salinity is correlated to obliquity, with salinization during low obliquity amplitude modulation. The most severe drought from 13.8 to 13.5 Ma probably occurred during enhanced evaporation due to high eccentricity. The recurring droughts during obliquity nodes are possibly related to weakened westerly winds over the Ili Basin in response to high latitude cooling and polar ice sheet expansion. The corresponding publication is in preparation (Frisch et al., in preparation).

References

Frisch, K., Voigt, S., Voigt, T., Hellwig, A., Verestek, V., and Weber, Y. 2019. Extreme aridity prior to lake expansion deciphered from facies evolution in the Miocene Ili Basin, south-east Kazakhstan. *Sedimentology*, accepted. doi: 10.1111/sed.12556.

Frisch, K., Voigt, S., Voigt, T., Verestek, V., Appel, E., Albert, R., Gerdes, A., Raddatz, J., Weber, Y., and Arndt, I. in preparation. Astronomical forced aridity during the Miocene Climate Transition in Central Asia.

Holbourn, A., Kuhnt, W., Clemens, S., Prell, W., and Andersen, N. 2013. Middle to late Miocene stepwise climate cooling: Evidence from a high-resolution deep water isotope curve spanning 8 million years. *Paleoceanography*, 28:688–699. doi: 10.1002/2013PA002538.

Palcu, D., Golovina, L., Vernyhorova, Y., Popov, S., and Krijgsman, W. 2017. Middle Miocene paleoenvironmental crises in Central Eurasia caused by changes in marine gateway configuration. *Global Planet. Change*, 158:57–71. doi: 10.1016/j.gloplacha.2017.09.013.

Verestek, V., Appel, E., Voigt, S., and Frisch, K. 2018. Constrained Magnetostratigraphic Dating of a Continental Middle Miocene Section in the Arid Central Asia. *Front. Earth Sci.*, 6:49. doi: 10.3389/feart.2018.00049.

Chapter 7

Conclusions

In the present doctoral thesis, the Miocene environmental evolution in the Ili Basin (southeast Kazakhstan) is investigated with a focus on the use of magnetic properties in lacustrine sediments for magnetostratigraphic dating and as high-resolution climate proxies. In the following, the main findings and conclusions are presented.

Magnetostratigraphic dating of the Aktau Mountains

The rock magnetic mineralogy of a middle to late Miocene sedimentary succession in the Ili Basin was studied. In the alluvial and lacustrine deposits of the Aktau Mountains, magnetite and hematite were identified as the main magnetic carriers with stable remanences. The determined paleo-directions are consistent with those expected for the Miocene in Central Asia. Furthermore, a lithofacies dependence of the rock magnetic parameters was revealed (Verestek et al., 2018, Chapter 3; Verestek et al., in review, Chapter 4). The observed magnetic properties are controlled by the depositional variability and indicate magneto-mineralogical alteration effects, including significant secondary magnetization. The lithofacies dependent remagnetization effects can be attributed to dissolution of magnetite and hematite and secondary magnetite (Verestek et al., 2018, Chapter 3). Widespread remagnetization constrained the established magnetostratigraphy to the Bastau Fm. Except for this formation, reverse paleo-directions are rare and

scattered inhibiting further magnetostratigraphic dating. For the Bastau Fm, rock magnetic properties were used to discriminate remanence directions that have been affected by secondary magnetization to provide a reliable magnetostratigraphy. The presented magnetostratigraphy dates the Bastau Formation to the middle Miocene with an age from 15.3 to 13.9 Ma (Verestek et al., 2018, Chapter 3). The results are in good agreement with estimates based on biostratigraphic markers as well as time-series analysis of magnetic susceptibility and chemical weathering indices. With this age model, the middle Miocene succession can be put in the context of the Middle Miocene Climate Transition. Changes of magneto-mineralogical properties above 55 m in the Bastau Formation concomitant with increasing salinization and lithology changes towards saline mudflats and later to an ephemeral playa lake are associated with global cooling.

Paleoenvironment reconstruction in the Ili Basin

The rock magnetic signature of a middle Miocene playa cycle in the Koktal Fm was investigated in high resolution (Verestek et al., in review, Chapter 4). Additional geochemical element contents and sedimentological aspects indicate that the rock magnetic parameters such as the magnetic concentration dependent parameters, ARM/SIRM and s-ratio are sensitive recorders of (ground)water availability and aridity changes in the Ili Basin. Higher magnetic concentrations occur in times of lower water availability and the highest concentration dependent parameters are further associated with increased aridity. A scenario for the origin of the ferro(i)magnetic minerals and possible magnetic alteration processes is presented, in which authigenic formation of magnetite and low temperature oxidation are the main factors controlling the variations in the magnetic record. The rock magnetic parameters provide an effective proxy record for a high resolution reconstruction of the paleo-environment not only in the middle Miocene Ili Basin but also in comparable floodplain/playa lake settings.

Moisture availability, the intensity of sediment discharge, weathering and pedogenesis in the middle Miocene Ili Basin are climatically forced (Voigt et al., 2017, Chapter 5). The combined study of bulk-sediment mineralogy, geochemistry, magnetic susceptibility, sediment color and palynology revealed four main intervals of arid soil formation and one palustrine phase in the Bastau Fm with higher evaporation rates under highly alka-

line/saline conditions. Higher moisture supply and higher precipitation rates resulted in the deposition of accumulated mudflat fines. Time series analysis of chemical weathering indices such as the Ti/Al ratio suggest that the changes in moisture availability and the mudflat deposits are orbital forced by long eccentricity cycles.

The established magnetostratigraphy of the Bastau Fm (Verestek et al., 2018, Chapter 3) provided a robust temporal framework for further studies on the middle to late Miocene paleoenvironment in the Ili Basin. Frisch et al. (2019) reconstructed the hydrological evolution of the Ili Basin and attributed the long-term evolution of a terminal lake to a climatic control. Further cyclostratigraphic studies showed that from 15.4 to 11.0 Ma the hydrological budget responded sensitively to obliquity modulation as well as to long and short eccentricity forcing (Frisch et al., in preparation).

References

Frisch, K., Voigt, S., Voigt, T., Hellwig, A., Verestek, V., and Weber, Y. 2019. Extreme aridity prior to lake expansion deciphered from facies evolution in the Miocene Ili Basin, south-east Kazakhstan. *Sedimentology*, accepted. doi: 10.1111/sed.12556.

Frisch, K., Voigt, S., Voigt, T., Verestek, V., Appel, E., Albert, R., Gerdes, A., Raddatz, J., Weber, Y., and Arndt, I. in preparation. Astronomical forced aridity during the Miocene Climate Transition in Central Asia.

Verestek, V., Appel, E., Voigt, S., and Frisch, K. 2018. Constrained Magnetostratigraphic Dating of a Continental Middle Miocene Section in the Arid Central Asia. *Front. Earth Sci.*, 6:49. doi: 10.3389/feart.2018.00049.

Verestek, V., Appel, E., Frisch, K., and Voigt, S. in review. Rock magnetic signature of a playa cycle in Central Asia and environmental implications. *Int. J. Earth Sci.*

Voigt, S., Weber, Y., Frisch, K., Bartenstein, A., Hellwig, A., Petschick, R., Bahr, A., Pross, J., Koutsodendris, A., Voigt, T., Verestek, V., and Appel, E. 2017. Climatically forced moisture supply, sediment flux and pedogenesis in Miocene mudflat deposits of south-east Kazakhstan, Central Asia. *Deposit. Rec.*, 3(2):209–232. doi: 10.1002/dep2.34.

Chapter 8

Open research questions

During the research for this doctoral thesis, many new research questions arose. While some could be answered with this thesis, some still remain open. The most important open research questions are addressed below.

Remagnetization

Throughout the middle to late Miocene succession in the Aktau Mountains, post-depositional alteration effects are observed constraining the magnetostratigraphic dating of the Neogene sediments. Despite remagnetizations and secondary overprints, a magnetostratigraphy could be established for the Bastau Formation. Based on this age model, reverse paleo-directions should occur in the overlying Koktal and Kokterek formation, in particular the reverse polarity dominated chrons C3B, C3A and C2. However, reverse paleo-directions (determined from more than 400 samples collected from these two formations) are rare and scattered inhibiting further magnetostratigraphic dating and indicating widespread remagnetization. Verestek et al. (2018) (Chapter 3) and Verestek et al. (in review) (Chapter 4) link alteration processes to secondary formation of magnetite and the acquisition of a CRM by the magnetite grains. A large remagnetization event can be excluded because of the rare but scattered occurrence of reverse paleo-directions. A common post-depositional process of magnetite formation would also result in more

reverse directions and in particular in reverse polarity intervals. Consequently, a complex mechanism must have caused the remagnetizations. Further rock magnetic studies could deal with the prevalent remagnetization effects and investigate the driving mechanisms behind the loss of the primary magnetization and the acquisition of secondary magnetizations using and enhancing the paleomagnetic and geochemical methods elaborated in Verestek et al. (2018) (Chapter 3) and Verestek et al. (in review) (Chapter 4).

Authigenic magnetite

Authigenic formation of magnetite is suggested before, during and after deposition in both the Bastau Fm and a playa cycle in the Koktal Fm (Verestek et al., 2018, Chapter 3; Verestek et al., in review, Chapter 4). In both sequences, two magnetite fractions could be identified based on rock magnetic data such as IRM acquisition curves. Verestek et al. (in review) (Chapter 4) suggest a scenario where both magnetite fractions are of authigenic origin formed at different stages before and after deposition. The exact mechanisms controlling the formation processes remain unclear. Further investigations could focus on authigenic formation processes including the iron sources and favorable conditions for biogenic and inorgnaic formation of magnetite, e.g. transmission electron microscope observations would be helpful to assess the structure of the fine magnetite particles and elucidate their origin.

Extending the proxy record

The Aktau Mountains expose Eocene/Oligocene to early Pleistocene terrestrial sediments. Using the methods and proxies presented in this doctoral thesis all formations in the Aktau Mountains could be studied to reconstruct Central Asia's climate and its forcing mechanisms from the late Paleogene to the early Quaternary. For instance, the oldest formations of the Aktau Mountains (Arasan Fm and Alakul Fm, ~180 m) bear the potential to elucidate the link of global cooling at the Eocene/Oligocene transition with significant aridification and cooling in the Asian interior as suggested by e.g. Dupont-Nivet et al. (2007); Kraatz and Geisler (2010); Xiao et al. (2010). The late Neogene was marked by an extensive environmental change in both marine and continental ecosystems and an onset of aridification in Central Asia (Miao et al., 2012; Herbert et al., 2016;

Holbourn et al., 2018). The ~880 m-thick deposits of a connected river-freshwater-lake system in the Ili Fm could be further investigated to assess the paleoenvironment of the late Miocene and early Pleistocene in the Ili Basin. Sampling all formations in the Aktau Mountains in a dense sampling scheme (with distances of several decimeters) and investigating the rock magnetic and geochemical properties as in Verestek et al. (in review) (Chapter 4) could provide a long proxy record of the Eocene/Oligocene to early Pleistocene succession, with the potential of further cyclostratigraphic studies.

Clay authigenesis

Clay diagenesis of smectite and illitization are suggested as possible processes resulting in secondary formation of magnetite and secondary chemical remanent magnetizations (Verestek et al., 2018, Chapter 3; Verestek et al., in review, Chapter 4). Both repeated drying and wetting processes and pedogenesis favor slow illitization of smectite at low temperatures (Huggett, 2005). The fluctuating groundwater table as well as the saline mudflat and ephemeral playa deposits in the Aktau Mountains are favorable conditions for the diagenesis of smectite and illitization. Detailed studies of the clay mineralogy could help to investigate this hypothesis.

References

Dupont-Nivet, G., Krijgsman, W., Langereis, C., Abels, H., Dai, S., and Fang, X. 2007. Tibetan Plateau aridification linked to global cooling at the Eocene-Oligocene transition. *Nature*, 445:635–638. doi: 10.1038/nature05516.

Herbert, T. D., Lawrence, K. T., Tzanova, A., Peterson, L. C., Caballero-Gill, R., and Kelly, C. S. 2016. Late Miocene global cooling and the rise of modern ecosystems. *Nat. Geosci.*, 9:843–847. doi: 10.1038/ngeo2813.

Holbourn, A. E., Kuhnt, W., Clemens, S. C., Kochhann, K. G. D., Jöhnck, J., Lübbers, J., and Andersen, N. 2018. Late Miocene climate cooling and intensification of southeast Asian winter monsoon. *Nat. Commun.*, 9:1584. doi: 10.1038/s41467-018-03950-1.

Huggett, J. M. July 2005. Low-temperature illitization of smectite in the late eocene and early oligocene of the Isle of Wight (Hampshire basin), U.K. *Am. Mineral.*, 90: 1192–1202. doi: 10.2138/am.2005.1674.

Kraatz, B. P. and Geisler, J. H. 2010. Eocene-Oligocene transition in Central Asia and its effects on mammalian evolution. *Geology*, 38:111. doi: 10.1130/G30619.1.

Miao, Y., Herrmann, M., Wu, F., Yan, X., and Yang, S. 2012. What controlled Mid-Late Miocene long-term aridification in Central Asia?– Global cooling or Tibetan Plateau uplift: A review. *Earth Sci. Rev.*, 112:155–172. doi: 10.1016/j.earscirev.2012.02.003.

Verestek, V., Appel, E., Voigt, S., and Frisch, K. 2018. Constrained Magnetostratigraphic Dating of a Continental Middle Miocene Section in the Arid Central Asia. *Front. Earth Sci.*, 6:49. doi: 10.3389/feart.2018.00049.

Verestek, V., Appel, E., Frisch, K., and Voigt, S. in review. Rock magnetic signature of a playa cycle in Central Asia and environmental implications. *Int. J. Earth Sci.*

Xiao, G., Abels, H. A., Yao, Z., Dupont-Nivet, G., and Hilgen, F. J. 2010. Asian aridification linked to the first step of the Eocene-Oligocene Climate Transition (EOT) in obliquity-dominated terrestrial records in Xining Basin, China. *J. Earth Sci.*, 21:219–220. doi: 10.1007/s12583-010-0216-8.

Appendix

During the research for this thesis over 900 oriented samples have been collected from the sedimentary succession at the Aktau Mountains and have been subjected to rock magnetic measurements. Since the measured data is only partly published, the magnetic susceptibility (χ), natural remanent magnetization (NRM), anhysteretic remanent magnetization (ARM), saturation remanent magnetization (SIRM), s-ratio, NRM/ARM ratio and the virtual geomagnetic pole latitude (VGP lat) of all samples are shown in the following table.

Sample	Height [m]	χ [m³/kg]	NRM [Am²/kg]	ARM [Am²/kg]	SIRM [Am²/kg]	s-ratio [-]	NRM/ARM [-]	VGP lat [°]
C004	-2.72	1.06E-07	1.52E-06	9.30E-06			0.16	-52.62
C005	-2.56	9.81E-08	8.76E-07	9.89E-06	1.22E-03	0.71	0.09	-39.92
C006	-2.38	2.71E-07	3.64E-06	2.16E-05	5.11E-03	0.86	0.17	-47.29
C007	-2.16	1.39E-07	1.37E-06	1.29E-05	1.87E-03	0.84	0.11	-46.10
C008	-1.97	1.46E-07	9.58E-07	1.42E-05	2.21E-03	0.81	0.07	-61.34
C009	-1.74	9.66E-08	9.07E-07	9.82E-06	1.04E-03	0.74	0.09	-45.69
C010	-1.50	9.48E-08	2.04E-06	1.03E-05	1.23E-03	0.74	0.20	-63.21
C011	-1.30	8.81E-08	8.85E-07	8.70E-06	8.92E-04	0.74	0.10	-54.90
C012	-0.99	8.76E-08	6.51E-07	8.31E-06	9.71E-04	0.76	0.08	-63.96
C013	-0.79	8.85E-08	9.23E-07	7.21E-06	1.12E-03		0.13	53.53
C014	-0.59	9.10E-08	5.58E-07	8.43E-06	1.06E-03	0.70	0.07	-29.12
C015	-0.37	7.20E-08	6.72E-07	6.99E-06	8.07E-04	0.74	0.10	
C016	-0.20	7.40E-08	5.40E-07	5.37E-06	5.78E-04	0.82	0.10	-58.69
C017	0.00	1.29E-07	1.95E-06	3.73E-06	1.69E-03	0.69	0.52	-45.59
C018	0.12	1.32E-07	2.27E-06		2.99E-03	0.59		-39.47
C019	0.24	1.35E-07	1.77E-06	3.68E-06	2.75E-03	0.54	0.48	-22.99
C020	0.36	1.38E-07	1.27E-06	2.64E-06	3.47E-03	0.52	0.48	-53.12
C021	0.48	2.01E-07	3.35E-06	1.60E-05	2.65E-03	0.73	0.21	64.76
C022	0.60	1.17E-07	1.63E-06	1.13E-05	1.02E-03	0.85	0.14	
C023	0.90	9.25E-08	7.94E-07	1.30E-05			0.06	21.07
C024	1.03	3.10E-07	6.11E-06	3.19E-05	5.52E-03	0.89	0.19	
C025	1.28	3.91E-07	4.93E-06	4.94E-05	6.82E-03	0.90	0.10	71.97
B001	1.37	1.94E-07	1.76E-06	2.46E-05	2.58E-03	0.79	0.07	
C026	1.54	2.31E-07	5.66E-06	1.21E-05	3.95E-03	0.77	0.47	46.71
C027	1.79	1.33E-07	2.00E-06	5.37E-06			0.37	55.38
C028	2.04	1.45E-07	2.82E-06	5.37E-06			0.53	74.26
C029	2.22	2.26E-07	2.33E-06	3.36E-05	3.00E-03	0.82	0.07	
C030	2.40	1.71E-07	8.51E-07	1.24E-05	2.11E-03	0.76	0.07	-57.81
C031	2.58	1.86E-07	2.84E-06	1.33E-05	3.19E-03	0.82	0.21	-81.61
C032	2.76	2.38E-07	4.86E-07	3.34E-05	2.82E-03	0.81	0.01	-33.51
B002	2.88		1.51E-06					-48.59
C033	2.93	3.50E-07	4.40E-07	4.06E-05	3.37E-03	0.83	0.01	-59.98
C034	3.11	3.22E-07	1.85E-07	4.09E-05	3.50E-03	0.83	0.00	-43.60
C035	3.29	3.02E-07	1.05E-06	3.88E-05	2.93E-03	0.84	0.03	-45.15
B003	3.45	3.01E-07	8.27E-07	3.73E-05	3.02E-03	0.81	0.02	-62.83
C036	3.47	2.87E-07	1.16E-06	3.43E-05	2.74E-03	0.83	0.03	-50.58
C037	3.64	2.84E-07	9.23E-07	3.24E-05	2.62E-03	0.82	0.03	-49.58
C038	3.81	3.05E-07	1.55E-06	3.33E-05	3.07E-03	0.82	0.05	-65.51
B004	3.87		2.25E-06	3.50E-05			0.06	-58.84
C039	3.99	2.73E-07	1.93E-06	3.29E-05	2.64E-03	0.82	0.06	-62.19
C040	4.16	3.07E-07	4.01E-06	4.29E-05	3.04E-03	0.84	0.09	-73.85
C041	4.33	3.41E-07	8.62E-07	4.15E-05	3.14E-03	0.85	0.02	-64.66
B005	4.38	3.28E-07	7.00E-06	4.12E-05	3.06E-03	0.82	0.17	-53.42
C042	4.42	3.50E-07	5.63E-06	4.13E-05	2.74E-03		0.14	-57.77
C043	4.50	2.96E-07	8.74E-06	4.94E-05	2.81E-03	0.85	0.18	-60.71
C044	4.59	2.59E-07	5.22E-06	3.55E-05	2.32E-03	0.84	0.15	-69.33
C045	4.67	3.03E-07	9.35E-07	4.08E-05	2.98E-03		0.02	-41.71
C046	5.04	2.53E-07	7.18E-07	2.51E-05	2.39E-03	0.81	0.03	-22.64
B006	5.20	3.15E-07	8.18E-06	4.97E-05	2.78E-03		0.16	-53.25
C047	5.41	2.70E-07	5.70E-07	2.97E-05	2.55E-03	0.83	0.02	-58.62
C048	5.78	3.33E-07	1.30E-06	3.69E-05	3.26E-03	0.84	0.04	-72.38
B007	5.80	2.27E-07	6.37E-07	2.61E-05	2.16E-03	0.80	0.02	-47.25
C049	6.15	3.04E-07	1.05E-06	4.30E-05	2.96E-03	0.82	0.02	-44.66
B008	6.40		7.12E-07	3.21E-05			0.02	-41.32
C050	6.52	4.15E-07	6.29E-07	5.19E-05	4.49E-03	0.85	0.01	-41.39

Sample	Height [m]	χ [m³/kg]	NRM [Am²/kg]	ARM [Am²/kg]	SIRM [Am²/kg]	s-ratio [-]	NRM/ARM [-]	VGP lat [°]
C051	6.89	2.70E-07	2.86E-07	3.62E-05	3.00E-03	0.83	0.01	-52.22
B009	7.10	3.00E-07	8.37E-07	4.18E-05	2.65E-03	0.78	0.02	-78.71
C052	7.26	2.97E-07	1.49E-06	3.47E-05	2.65E-03	0.82	0.04	-70.08
C053	7.64	2.91E-07	1.46E-06	3.58E-05	2.65E-03	0.84	0.04	-70.35
B010	7.70	2.54E-07	1.95E-06	3.19E-05	3.03E-03	0.80	0.06	-54.85
C054	8.01	2.72E-07	2.93E-06	3.40E-05	2.34E-03	0.83	0.09	-83.10
C055	8.38	3.16E-07	8.36E-07	3.56E-05	2.81E-03	0.81	0.02	-55.12
B011	8.45	2.97E-07	2.74E-06	3.89E-05	2.83E-03	0.85	0.07	-44.12
C056	8.75	2.96E-07	1.18E-06	3.75E-05	2.46E-03	0.85	0.03	-37.65
C057	9.12	3.40E-07	1.57E-07	3.89E-05	3.00E-03	0.85	0.00	-42.45
B012	9.12	3.38E-07	1.90E-06	3.88E-05	3.25E-03	0.82	0.05	-59.11
C058	9.49	3.57E-07	1.21E-06	4.65E-05	3.23E-03	0.85	0.03	-64.61
C059	9.86	3.41E-07	7.83E-07	4.89E-05	3.07E-03	0.84	0.02	-41.99
B013	10.00	3.48E-07	1.58E-06	4.46E-05	3.44E-03	0.81	0.04	-35.89
C060	10.23	1.68E-07	1.96E-06	1.64E-05			0.12	77.20
C061	10.37	3.28E-07	2.22E-06	3.71E-05	3.16E-03	0.83	0.06	52.67
D00	10.47	7.73E-07	1.38E-06	6.35E-05	1.02E-02	0.86	0.02	-45.73
C062	10.52	3.90E-07	1.87E-06	4.34E-05	4.31E-03	0.85	0.04	30.53
B014	10.60		2.73E-06					
C063	10.66	2.94E-07	7.19E-07	3.70E-05	2.93E-03	0.82	0.02	
D01	10.77	2.43E-07	9.41E-07	2.67E-05	5.67E-03	0.84	0.04	-22.95
C064	10.81	3.59E-07	1.40E-06	3.90E-05	4.66E-03	0.86	0.04	
C065	10.95	2.39E-07	1.48E-06	2.46E-05	9.98E-03	0.86	0.06	-52.34
D02	11.04	2.95E-07	1.42E-06	3.57E-05	4.76E-03	0.88	0.04	-50.24
C066	11.09	1.27E-07	1.01E-06	1.21E-05	8.53E-04	0.90	0.08	28.95
B015	11.20	1.02E-07	4.71E-07	1.02E-05	5.59E-04	0.86	0.05	-39.97
C067	11.24	1.23E-07	1.10E-06	1.15E-05	7.35E-04	0.95	0.10	
C068	11.38	1.72E-07	1.47E-06	1.15E-05	1.32E-03	0.92	0.13	-54.82
C069	11.53	1.42E-07	2.82E-06	6.80E-06			0.41	77.61
D03	11.60	1.76E-07	1.59E-06	8.31E-06	1.05E-03	0.89	0.19	
C070	11.67	6.56E-08	8.50E-07	2.73E-06	7.34E-04	0.85	0.31	64.88
C071	11.80	3.91E-07	3.73E-06	6.62E-05	3.90E-03	0.86	0.06	-40.49
C072	11.93	4.51E-07	2.77E-06	5.79E-05	5.12E-03	0.86	0.05	-87.70
B016	11.95	4.83E-07	5.37E-06	7.17E-05	5.05E-03	0.87	0.07	61.55
C073	12.06	3.08E-07	1.97E-06	5.06E-05	2.96E-03	0.83	0.04	-44.55
C074	12.19	3.38E-07	3.74E-06	4.63E-05	3.21E-03	0.84	0.08	-34.85
C075	12.32	3.59E-07	5.23E-06	4.56E-05	3.57E-03	0.84	0.11	47.65
B017	12.40	3.09E-07	4.05E-06	4.51E-05	2.86E-03	0.86	0.09	-25.38
C076	12.45	3.90E-07	3.09E-06	4.65E-05	4.61E-03	0.85	0.07	48.24
C077	12.64	3.24E-07	3.48E-06	4.18E-05			0.08	39.83
C078	12.81	3.38E-07	3.91E-06	5.38E-05	3.62E-03	0.84	0.07	51.25
B018	12.90	3.17E-07	3.40E-06	5.48E-05	2.76E-03	0.84	0.06	82.10
C079	12.98	3.26E-07	4.68E-06	5.06E-05	3.09E-03	0.84	0.09	72.56
C080	13.15	3.24E-07	4.89E-06	4.63E-05	3.06E-03	0.83	0.11	44.79
C081	13.32	3.93E-07	3.60E-06	5.23E-05	4.28E-03	0.86	0.07	77.26
B019	13.37	3.23E-07	1.07E-05	4.96E-05	5.09E-03	0.89	0.22	70.39
C082	13.49	4.43E-07	4.61E-06	5.02E-05	4.43E-03	0.87	0.09	63.45
C083	13.66	1.56E-07	1.48E-06	1.16E-05	3.64E-03	0.81	0.13	83.99
C084	13.83	1.86E-07	2.28E-06	1.45E-05	7.18E-03	0.82	0.16	68.61
B020	13.90	1.95E-07	3.61E-06	2.30E-05	5.94E-03	0.85	0.16	52.84
C085	14.00	1.25E-07	7.21E-07	7.88E-06	8.34E-04	0.79	0.09	82.49
C086	14.15	1.15E-07	9.43E-07	9.84E-06	8.83E-04	0.89	0.10	70.00
C087	14.30	1.50E-07	1.47E-06	6.29E-06	1.39E-03	0.84	0.23	77.57
B021	14.40	1.36E-07	4.48E-07	8.40E-06	7.16E-04	0.83	0.05	31.40
C088	14.44	1.46E-07	9.58E-07	7.62E-06	7.44E-04	0.86	0.13	33.84

Sample	Height [m]	χ [m³/kg]	NRM [Am²/kg]	ARM [Am²/kg]	SIRM [Am²/kg]	s-ratio [-]	NRM/ARM [-]	VGP lat [°]
C089	14.59	2.58E-07	1.57E-06	3.70E-05	2.69E-03	0.83	0.04	29.41
C090	14.74	2.76E-07	8.68E-06	4.38E-05	5.90E-03	0.90	0.20	75.79
C091	14.89	3.34E-07	1.57E-06	4.27E-05	3.73E-03	0.84	0.04	
B022	14.90	4.11E-07	3.51E-06	5.49E-05	4.28E-03	0.84	0.06	38.96
C092	15.04	3.86E-07	2.28E-06	4.47E-05	4.08E-03	0.86	0.05	
C093	15.19	2.54E-07	3.97E-06	2.85E-05	4.58E-03	0.87	0.14	59.77
C094	15.33	4.06E-07	2.74E-06	4.62E-05	4.78E-03	0.86	0.06	
B023	15.40	2.38E-07	5.45E-06	4.48E-05	3.32E-03	0.86	0.12	72.30
C095	15.48	2.80E-07	2.91E-06	4.47E-05	2.50E-03	0.83	0.07	35.74
C096	15.63	1.81E-07	1.27E-06	1.33E-05	4.31E-03	0.83	0.10	52.26
C097	15.78	1.96E-07	6.30E-06	2.26E-05	3.49E-03	0.87	0.28	50.14
B024	15.84	2.21E-07	5.49E-06	4.30E-05	3.43E-03	0.83	0.13	60.15
C098	15.93	2.50E-07	7.65E-06	3.06E-05	7.81E-03	0.87	0.25	80.64
C099	16.14	3.05E-07	6.68E-06	4.52E-05	9.09E-03	0.89	0.15	70.43
C100	16.34	2.17E-07	6.63E-07	2.13E-05	6.11E-03	0.91	0.03	-40.17
C101	16.55	2.67E-07	2.41E-06	4.10E-05	2.64E-03	0.81	0.06	-70.67
B025	16.70		3.46E-06	4.53E-05			0.08	-42.83
C102	16.95	2.23E-07	1.56E-06	2.01E-05	3.15E-03	0.81	0.08	-52.28
C103	17.34	1.68E-07	6.24E-07	1.11E-05	4.77E-03	0.79	0.06	-31.83
B026	17.57	2.00E-07	1.81E-06		8.91E-03	0.74		-47.89
C104	17.74	1.76E-07	1.45E-06	1.41E-05	6.30E-03	0.84	0.10	-43.19
C105	18.13	2.02E-07	2.07E-06	2.10E-05			0.10	
C106	18.22	3.21E-07		5.07E-05	7.60E-03	0.88		
C107	18.32	1.42E-07	4.83E-07	8.80E-06	5.82E-04	0.83	0.05	
C108	18.41	1.36E-07	4.83E-07	7.22E-06	2.18E-03	0.66	0.07	65.54
C109	18.50	1.34E-07	6.55E-07	5.51E-06			0.12	34.75
B027	18.60	1.31E-07	3.30E-07	8.46E-06	1.35E-03		0.04	-50.79
C110	18.64	2.99E-07	5.43E-07	3.63E-05	3.97E-03	0.83	0.01	-50.48
C111	18.78	3.66E-07	8.18E-07	4.89E-05	4.18E-03	0.85	0.02	-61.95
C112	18.92	2.46E-07	2.59E-06	2.35E-05	8.31E-03	0.88	0.11	-53.42
C113	19.05	2.48E-07	4.15E-06	2.48E-05	4.72E-03	0.89	0.17	-54.09
C114	19.19	2.30E-07	3.86E-06	2.42E-05	5.44E-03	0.90	0.16	-49.73
B028	19.20	2.74E-07	5.20E-06	4.27E-05	3.05E-03	0.83	0.12	-56.34
C115	19.33	2.03E-07	2.67E-07	1.82E-05	2.69E-03	0.83	0.01	-59.18
C116	19.47	3.54E-07	6.97E-06	3.89E-05	3.27E-03	0.87	0.18	-60.31
C117	19.56	3.73E-07	7.41E-06	4.76E-05	3.46E-03	0.87	0.16	-67.20
B029	19.63		6.23E-06					-54.50
C118	19.64	3.71E-07	7.73E-06	4.78E-05	3.59E-03	0.86	0.16	-60.69
C119	19.89	3.31E-07	1.44E-05	4.47E-05	3.37E-03	0.84	0.32	-38.93
C120	19.98	3.20E-07	3.16E-05	4.24E-05	3.34E-03	0.84	0.75	-27.87
C121	20.15	3.68E-07	1.87E-06	4.04E-05	4.84E-03	0.86	0.05	
B030	20.20	1.69E-07	2.53E-06	1.66E-05	4.41E-03	0.83	0.15	-80.42
C122	20.36	2.52E-07	1.13E-06	2.24E-05	4.28E-03	0.84	0.05	
D04	20.50	2.60E-07	8.33E-07	3.62E-05	3.77E-03	0.82	0.02	-58.96
C123	20.58	2.56E-07	1.71E-06	4.18E-05	7.12E-03	0.88	0.04	-62.68
B031	20.63	9.22E-08	1.69E-06	6.99E-05	1.61E-03	0.62	0.02	-34.29
C05	20.68	1.69E-07	1.12E-06	1.93E-05	2.18E-03	0.74	0.06	-63.26
C124	20.75	2.30E-07	2.64E-06	3.22E-05	5.12E-03	0.65	0.08	-42.94
C125	21.02	1.27E-07	2.17E-07	7.06E-06	2.90E-04	0.92	0.03	-66.32
C126	21.28	1.19E-07	7.80E-07	9.10E-06	4.29E-04	0.98	0.09	-50.03
B032	21.30	1.26E-07	1.17E-06	1.16E-05	8.14E-04	0.96	0.10	24.40
D06	21.55	1.69E-07	1.60E-06	1.24E-05	8.34E-04	0.97	0.13	-20.24
C127	21.81	1.71E-07	1.50E-06	1.62E-05	1.49E-03	0.96	0.09	36.33
B033	21.90	6.15E-08	5.39E-07	1.28E-06	2.82E-04	0.75	0.42	
D07	21.96	1.12E-07	6.06E-07	6.66E-06	1.15E-03	0.79	0.09	-42.04

Sample	Height [m]	χ [m³/kg]	NRM [Am²/kg]	ARM [Am²/kg]	SIRM [Am²/kg]	s-ratio [-]	NRM/ARM [-]	VGP lat [°]
C128	22.07	1.35E-07	1.99E-06	6.88E-06			0.29	68.70
D08	22.20	8.64E-08	5.49E-07	3.74E-06	4.97E-04	0.84	0.15	-56.26
C129	22.34	1.48E-07	1.02E-06	5.59E-06	1.24E-03	0.78	0.18	80.86
C130	22.60	1.59E-07	1.44E-06	4.29E-06	9.69E-04	0.71	0.34	62.48
D09	22.65	1.15E-07	9.78E-07	5.37E-06	4.84E-04	0.78	0.18	-74.68
C131	22.69	1.33E-07	7.34E-07	4.25E-06	5.17E-04	0.78	0.17	81.48
C132	22.78	1.20E-07	5.82E-07	3.53E-06	6.08E-04	0.91	0.16	65.12
B034	22.90		5.13E-07					
C133	22.91	1.03E-07	3.05E-06	2.46E-06	6.85E-04	0.77	1.24	62.03
C134	23.00	1.05E-07	5.85E-07	2.70E-06	6.27E-04	0.62	0.22	
C135	23.12	1.13E-07	1.16E-06	2.71E-06			0.43	78.09
C136	23.24	1.26E-07	2.23E-06	2.97E-06	8.11E-04	0.64	0.75	-48.91
C137	23.37	1.09E-07	1.33E-06	5.29E-06	8.07E-04	0.66	0.25	
C138	23.49	2.63E-07	4.69E-06	4.26E-05	5.49E-03	0.87	0.11	37.72
C139	23.58	3.88E-07	1.53E-06	5.01E-05	3.96E-03	0.85	0.03	-40.84
C140	23.70	3.36E-07	2.60E-05	4.75E-05	3.91E-03	0.84	0.55	
B035	23.80	2.43E-07	6.40E-06	2.97E-05	4.78E-03	0.85	0.22	-24.07
C141	23.93	3.14E-07	5.50E-06	4.09E-05	3.33E-03	0.82	0.13	-40.27
C142	24.22	2.28E-07	2.91E-06	2.56E-05	5.44E-03	0.87	0.11	-37.84
C143	24.44	2.32E-07	2.32E-06	2.57E-05	6.98E-03	0.89	0.09	-44.82
C144	24.67	2.02E-07	3.43E-06	2.33E-05	6.37E-03	0.89	0.15	-65.18
B036	24.75	2.81E-07	2.72E-06	3.59E-05	4.57E-03	0.85	0.08	-34.77
C145	24.84	2.10E-07	4.02E-06	2.60E-05	6.29E-03	0.89	0.15	-70.12
C146	25.07	2.31E-07	5.84E-06	2.22E-05	4.72E-03	0.87	0.26	-54.53
C147	25.19	2.23E-07	1.41E-05	3.08E-05	7.36E-03	0.87	0.46	-77.04
C148	25.36	2.11E-07	2.88E-06	1.80E-05	4.64E-03	0.86	0.16	-52.60
C149	25.62	2.77E-07	1.49E-06	2.81E-05	6.17E-03	0.85	0.05	
B037	25.70	2.02E-07	4.09E-06	2.26E-05	3.30E-03		0.18	-69.18
C150	25.89	2.66E-07	3.65E-07	4.08E-05	3.11E-03	0.83	0.01	-42.52
C151	26.15	1.88E-07	6.88E-07	1.85E-05	5.80E-03	0.77	0.04	-61.38
C152	26.51	2.09E-07	1.77E-06	2.20E-05	5.67E-03	0.96	0.08	
B038	26.54	2.25E-07	8.38E-07	2.82E-05	2.90E-03	0.87	0.03	-60.61
C153	26.69	1.69E-07	1.88E-07	1.27E-05	3.36E-03	0.84	0.01	-55.29
C154	26.86	2.17E-07	1.43E-06	3.57E-05	7.05E-03	0.86	0.04	-51.59
C155	27.10	2.98E-07	6.14E-06	4.88E-05	6.48E-03	0.86	0.13	60.20
D10	27.15	1.31E-07	1.04E-06	5.82E-06	5.60E-04	0.78	0.18	29.26
C156	27.21	1.37E-07	1.88E-06	1.78E-05	2.26E-03	0.86	0.11	-43.88
B039	27.25	1.38E-07	3.20E-06	2.47E-05	1.60E-03	0.85	0.13	-36.07
D11	27.35	1.55E-07	7.97E-07	8.49E-06	6.45E-04	0.97	0.09	-44.13
C157	27.44	1.26E-07	6.28E-07	5.99E-06	3.57E-04	0.92	0.10	
D12	27.58		8.11E-07					
C158	27.65	9.58E-08	1.78E-07	2.84E-06	1.98E-04	0.96	0.06	-46.08
C159	27.85	1.22E-07	4.22E-07	3.86E-06	2.68E-04	0.95	0.11	
B040	27.90	1.65E-07	1.52E-06	3.56E-05	9.76E-04	0.90	0.04	
D13	28.00	1.41E-07	1.34E-06	4.21E-06	2.82E-04	0.88	0.32	-25.43
C160	28.09	9.37E-08	3.78E-07	2.81E-06	2.44E-04	0.92	0.13	-68.05
C161	28.15	1.39E-07	5.27E-07	4.70E-06	3.59E-04	0.93	0.11	
C162	28.20	1.31E-07	3.83E-07	3.85E-06	2.30E-04	0.93	0.10	-34.75
C163	28.26	1.40E-07	2.19E-06	4.25E-06	6.90E-04	0.75	0.51	77.88
D14	28.33	1.41E-07	1.62E-06					
B041	28.40	1.27E-07	4.18E-07	1.01E-06	5.62E-04	0.78	0.42	-70.10
C164	28.43	1.15E-07	1.83E-06	3.04E-06	8.09E-04	0.68	0.60	69.73
C165	28.55	1.28E-07	1.93E-06	3.75E-06	6.64E-04	0.71	0.51	80.05
D15	28.60	1.14E-07	2.65E-06	3.40E-06	6.60E-04	0.62	0.78	-66.89
C166	28.67	1.44E-07	1.14E-06	4.12E-06			0.28	56.56

Sample	Height [m]	χ [m³/kg]	NRM [Am²/kg]	ARM [Am²/kg]	SIRM [Am²/kg]	s-ratio [-]	NRM/ARM [-]	VGP lat [°]
C167	28.78	1.32E-07	1.46E-06	3.82E-06	8.00E-04	0.63	0.38	
C168	28.94	1.31E-07	2.27E-06	2.39E-06			0.95	-75.34
B042	29.00	1.75E-07		4.39E-06	7.03E-04	0.65		
C169	29.11	1.17E-07	1.62E-06	2.29E-06	6.06E-04	0.65	0.71	72.77
C170	29.27	1.49E-07	6.60E-07	1.44E-05	2.91E-03	0.89	0.05	30.91
C171	29.43	2.50E-07	5.83E-07	3.47E-05	2.88E-03	0.82	0.02	-53.80
D16	29.47	2.84E-07	3.87E-06	4.09E-05	2.87E-03	0.85	0.09	-16.60
B043	29.50	1.02E-07	4.99E-07	5.12E-06	7.09E-04	0.61	0.10	14.36
C172	29.60	2.44E-07	3.85E-06	3.81E-05	4.42E-03	0.87	0.10	68.76
B044	29.86	2.73E-07	5.13E-07	3.90E-05	2.93E-03	0.83	0.01	-72.52
C173	29.90	1.86E-07	2.60E-07	1.98E-05	4.97E-03	0.89	0.01	
C174	30.03	1.26E-07	1.03E-06	1.10E-05	1.23E-03	0.87	0.09	51.24
D17	30.10	2.98E-07	5.23E-06	3.63E-05	3.92E-03	0.83	0.14	-44.13
C175	30.23	2.19E-07	3.84E-06	2.94E-05	3.59E-03	0.85	0.13	76.03
B045	30.45		4.40E-06					
C176	30.58	3.58E-07	3.05E-06	4.74E-05	3.63E-03	0.84	0.06	45.82
C177	30.92	3.53E-07	2.38E-06	4.98E-05	3.70E-03	0.83	0.05	
C178	31.03	3.15E-07	2.69E-06	4.64E-05	3.50E-03	0.83	0.06	
B046	31.13	1.31E-07	1.46E-06	1.22E-05	3.00E-03	0.78	0.12	55.53
C179	31.14	1.85E-07	1.39E-06	1.86E-05	6.56E-03	0.87	0.07	69.23
C180	31.68	1.95E-07	2.12E-06	1.94E-05	7.30E-03	0.87	0.11	58.79
B047	31.96	2.01E-07	8.05E-06	2.70E-05	5.56E-03	0.84	0.30	84.37
C181	32.23	2.00E-07	4.73E-06	2.03E-05	7.28E-03	0.88	0.23	72.89
C182	32.34	2.13E-07	7.30E-06	3.00E-05	6.69E-03	0.87	0.24	57.93
B048	32.39	1.92E-07	3.14E-06	1.71E-05	5.13E-03	0.85	0.18	39.22
C183	32.46	2.29E-07	7.09E-06	3.27E-05	4.49E-03	0.85	0.22	72.31
C184	32.57	2.40E-07	7.19E-06	3.18E-05	4.69E-03	0.84	0.23	56.49
C185	32.74	2.37E-07	4.94E-06	2.94E-05	7.99E-03	0.85	0.17	78.07
C186	32.90	1.79E-07		1.64E-05	5.69E-03	0.86		
B049	32.95	4.51E-07	3.94E-06		4.46E-03	0.84		84.32
C187	33.07	2.50E-07	8.19E-06	5.53E-05	3.27E-03	0.87	0.15	79.32
C188	33.23	4.14E-07	5.72E-06	4.84E-05	4.79E-03	0.85	0.12	59.05
C189	33.39	3.00E-07	4.12E-06	4.29E-05	3.10E-03	0.83	0.10	54.54
B050	33.55	1.83E-07	2.10E-05		5.09E-03	0.85		
C190	33.55	3.65E-07	5.04E-06	4.46E-05	4.36E-03	0.84	0.11	68.28
C191	33.72	3.68E-07	5.44E-06	4.61E-05	4.38E-03	0.85	0.12	68.98
C192	33.88	3.15E-07		3.73E-05	3.12E-03	0.83		
B051	34.04	2.89E-07	2.96E-06	3.63E-05	2.62E-03	0.82	0.08	58.00
C193	34.08	2.21E-07	5.67E-06	1.54E-05	3.25E-03	0.84	0.37	76.97
C194	34.28	2.38E-07	4.20E-06	1.74E-05	5.40E-03	0.86	0.24	76.40
C195	34.45	2.83E-07	3.18E-06	2.94E-05	3.64E-03	0.84	0.11	83.73
C196	34.62	2.86E-07	2.85E-06	3.39E-05	2.84E-03	0.83	0.08	68.60
B052	34.64		2.16E-06					-65.53
C197	34.74	3.27E-07	1.82E-06	3.23E-05	3.88E-03	0.84	0.06	57.05
C198	34.85	1.91E-07	3.69E-06	1.88E-05	3.10E-03	0.87	0.20	78.36
C199	35.08	2.41E-07	2.17E-06	2.46E-05			0.09	81.11
C200	35.25	1.84E-07	1.59E-06	1.15E-05	4.63E-03	0.86	0.14	72.42
B053	35.32	1.71E-07	1.00E-06	1.33E-05	5.54E-03	0.87	0.07	-67.86
C201	35.42	2.52E-07	1.15E-06	2.60E-05	3.34E-03	0.81	0.04	-27.03
C202	35.59	2.66E-07	1.69E-06	4.01E-05	2.77E-03	0.76	0.04	-70.24
C203	35.76	3.55E-07	2.97E-06	3.06E-05	4.58E-03	0.81	0.10	-63.74
B054	35.87	1.65E-07	9.92E-07	1.64E-05	3.89E-03	0.85	0.06	
C204	35.93	2.59E-07	1.16E-06	2.94E-05	2.59E-03	0.82	0.04	-56.30
C205	36.10	1.60E-07	1.20E-06	1.15E-05	4.34E-03	0.85	0.10	-77.43
C206	36.42	1.72E-07	2.23E-06	1.54E-05	6.02E-03	0.89	0.15	-61.61

Sample	Height [m]	χ [m³/kg]	NRM [Am²/kg]	ARM [Am²/kg]	SIRM [Am²/kg]	s-ratio [-]	NRM/ARM [-]	VGP lat [°]
C207	36.67	1.63E-07	2.89E-06	1.77E-05	5.76E-03	0.85	0.16	
C208	36.92	1.75E-07	1.33E-06	1.67E-05	5.47E-03	0.85	0.08	-21.82
C209	37.16	1.66E-07	4.98E-07	1.36E-05	4.54E-03	0.84	0.04	-70.54
B055	37.20	1.33E-07	1.14E-06	7.12E-06	9.69E-04	0.87	0.16	
C210	37.41	1.70E-07	6.30E-07	1.38E-05	4.50E-03	0.84	0.05	
C211	37.66	2.23E-07	3.35E-06	4.08E-05	4.75E-03	0.83	0.08	64.42
C212	38.01	1.43E-07	2.55E-06	1.04E-05			0.24	78.91
D18	38.18	1.34E-07	1.09E-06	2.02E-05	1.34E-03	0.86	0.05	-35.64
B056	38.28	1.26E-07	1.27E-06	1.25E-05	1.11E-03	0.72	0.10	67.20
C213	38.36	9.27E-08	1.36E-06	3.64E-06	9.96E-04		0.37	74.87
D19	38.40	1.39E-07	3.20E-06	8.79E-06	1.17E-03	0.68	0.36	
D20	38.65		1.25E-06					
C214	38.71	1.39E-07	2.66E-06	3.41E-06	1.46E-03		0.78	
C215	39.06	2.06E-07	6.89E-07	1.91E-05			0.04	49.00
D21	39.12	2.85E-07	5.49E-07	2.18E-05	4.88E-03	0.93	0.03	-71.30
C216	39.20	2.05E-07	6.80E-07	1.76E-05	4.96E-03	0.85	0.04	87.43
C217	39.34	2.76E-07	2.48E-06	2.88E-05	4.02E-03	0.83	0.09	74.31
B057	39.36	1.97E-07	1.42E-06	6.44E-06	1.44E-03	0.75	0.22	-33.70
C218	39.48	1.88E-07	8.35E-07	2.02E-05	1.60E-03	0.78	0.04	63.87
D22	39.52	2.92E-07	2.47E-06	2.78E-05	3.36E-03	0.84	0.09	62.79
C219	39.62	1.95E-07	1.15E-06	1.53E-05	2.53E-03	0.85	0.08	
C220	39.76	1.86E-07	1.43E-06	1.43E-05	1.94E-03	0.82	0.10	29.81
C221	39.96	1.66E-07	1.96E-06	1.35E-05			0.14	60.16
C222	40.15	2.09E-07	2.90E-06	2.84E-05	2.66E-03	0.84	0.10	77.75
B058	40.28		6.22E-07					26.06
C223	40.31	2.59E-07	6.31E-06	5.65E-05	3.45E-03	0.87	0.11	57.25
C224	40.46	1.66E-07	1.97E-06	1.10E-05	1.85E-03	0.80	0.18	67.01
C225	40.71	2.54E-07	6.69E-06	4.16E-05			0.16	79.29
C226	40.95	2.26E-07	5.94E-06	3.34E-05	3.90E-03	0.84	0.18	71.80
C227	41.11	1.59E-07	2.00E-06	9.49E-06	2.85E-03	0.84	0.21	66.70
C228	41.29	1.79E-07	2.59E-06	1.58E-05	4.72E-03	0.88	0.16	78.26
B059	41.40	2.52E-07	5.14E-06	1.84E-05	4.28E-03	0.86	0.28	74.48
C229	41.48	2.19E-07	3.94E-06	1.84E-05	3.78E-03	0.87	0.21	67.26
C230	41.66	1.71E-07	4.09E-06	1.27E-05	4.91E-03	0.90	0.32	73.28
C231	41.93	1.57E-07	3.49E-06	9.81E-06	3.10E-03	0.85	0.36	77.37
C232	42.00	1.25E-07	1.93E-06	9.60E-06	7.95E-04	0.83	0.20	72.04
C233	42.24	1.37E-07	2.04E-06	8.25E-06	1.01E-03	0.83	0.25	64.63
C234	42.49	1.01E-07	1.72E-06	2.72E-06	6.96E-04	0.53	0.63	54.71
B060	42.53	2.48E-07	2.29E-06	2.58E-05	2.74E-03	0.83	0.09	66.33
C235	42.73	8.85E-08	1.44E-06	2.32E-06	5.00E-04	0.57	0.62	72.22
C236	42.96	1.39E-07	1.99E-06	1.19E-05	2.81E-03	0.86	0.17	64.77
C237	43.25	2.60E-07	2.99E-06	2.21E-05	4.68E-03	0.87	0.14	72.44
C238	43.50	1.80E-07	4.02E-06	1.22E-05	5.26E-03	0.87	0.33	76.93
B061	43.75	1.71E-07	2.09E-06	1.29E-05	4.34E-03	0.88	0.16	70.28
C239	43.76	2.10E-07	3.88E-06	1.90E-05	3.52E-03	0.84	0.20	69.48
C240	43.83	1.99E-07	6.56E-06	2.52E-05	4.84E-03	0.88	0.26	84.42
C241	44.10	2.64E-07	7.02E-06	3.73E-05	6.07E-03	0.89	0.19	64.22
B062	44.30	9.03E-08	3.24E-07	5.95E-06	5.30E-04	0.76	0.05	42.66
C242	44.36	2.07E-07	5.42E-06	2.58E-05	2.77E-03	0.85	0.21	44.11
C243	44.53	2.02E-07	3.57E-06	1.95E-05	2.62E-03	0.86	0.18	68.02
B063	45.07	2.02E-07	3.61E-06		5.08E-03	0.90		79.65
C244	45.10	2.13E-07	3.55E-06	2.04E-05	7.07E-03	0.88	0.17	81.38
B064	45.58	1.73E-07	1.75E-06	1.68E-05	4.89E-03	0.86	0.10	59.25
C245	45.86	1.93E-07	4.36E-06	1.54E-05	6.04E-03	0.88	0.28	81.33
B065	45.87	2.95E-07	6.09E-06	4.42E-05	7.38E-03	0.86	0.14	65.62

Sample	Height [m]	χ [m³/kg]	NRM [Am²/kg]	ARM [Am²/kg]	SIRM [Am²/kg]	s-ratio [-]	NRM/ARM [-]	VGP lat [°]
C246	46.09	2.05E-07	4.34E-06	1.83E-05	6.55E-03	0.88	0.24	77.90
B066	46.17	1.87E-07	1.76E-06	2.39E-05	4.97E-03	0.88	0.07	74.99
C247	46.32	1.59E-07	2.32E-06	9.15E-06	3.48E-03	0.85	0.25	70.70
C248	46.62	1.92E-07	4.34E-06	1.66E-05	4.91E-03	0.88	0.26	75.77
B067	46.64	1.63E-07	1.94E-06	8.77E-06	3.60E-03	0.86	0.22	55.58
C249	46.91	2.09E-07	4.76E-06	2.26E-05	3.19E-03	0.80	0.21	82.66
C250	47.04	1.78E-07	4.55E-06	1.67E-05	3.21E-03	0.84	0.27	67.01
B068	47.05	2.32E-07	6.27E-06	2.70E-05	6.23E-03	0.84	0.23	63.68
C251	47.21	1.90E-07	4.29E-06	2.17E-05	4.00E-03	0.86	0.20	76.48
C252	47.37	2.41E-07	7.39E-06	3.33E-05	3.91E-03	0.86	0.22	68.09
B069	47.42	2.52E-07	5.21E-06	5.12E-05	2.53E-03	0.83	0.10	72.18
C253	47.57	2.51E-07	6.77E-06	3.51E-05	3.42E-03	0.86	0.19	81.98
C254	47.83	1.42E-07	1.43E-06	7.74E-06	8.02E-04	0.86	0.18	69.55
C255	48.00	1.34E-07	1.19E-06	6.43E-06	6.85E-04	0.75	0.19	70.88
B070	48.14	2.54E-07	5.16E-06	4.23E-05	3.47E-03	0.87	0.12	86.13
C256	48.17	2.49E-07	7.46E-06	3.91E-05	3.22E-03	0.86	0.19	85.57
C257	48.34	2.76E-07	7.35E-06	4.12E-05	4.03E-03	0.87	0.18	77.09
C258	48.64	2.05E-07	4.54E-06	2.30E-05	3.59E-03	0.86	0.20	67.44
B071	48.85	1.54E-07	8.43E-07	1.25E-05	2.88E-03	0.85	0.07	87.40
C259	48.86	1.66E-07	2.02E-06	1.22E-05	4.32E-03	0.87	0.16	82.86
C260	49.08	1.55E-07	1.72E-06	8.63E-06	3.15E-03	0.84	0.20	63.91
C261	49.22	1.36E-07	1.43E-06	6.23E-06	2.08E-03	0.80	0.23	73.71
C262	49.41	1.65E-07	2.78E-06	1.04E-05	2.44E-03	0.85	0.27	69.02
C263	49.59	1.55E-07	1.31E-06	8.93E-06	3.26E-03	0.85	0.15	64.56
B072	49.78	1.50E-07	7.22E-07	1.16E-05	2.83E-03	0.85	0.06	66.70
C264	49.85	1.78E-07	2.48E-06	1.21E-05	2.13E-03	0.83	0.20	64.92
C265	50.10	1.63E-07	8.92E-07	8.92E-06	3.73E-03	0.86	0.10	53.65
C266	50.36	1.67E-07	2.55E-06	9.89E-06	4.46E-03	0.86	0.26	57.00
C267	50.62	1.49E-07	1.20E-06	8.48E-06	3.23E-03	0.85	0.14	68.28
B073	50.63	1.37E-07	7.71E-07	2.90E-06			0.27	63.14
C268	50.84	1.51E-07	2.24E-06	7.39E-06	3.10E-03	0.84	0.30	76.97
C269	51.06	1.40E-07	1.72E-06	6.21E-06	2.30E-03	0.82	0.28	74.49
C270	51.28	1.61E-07	2.51E-06	1.04E-05	4.12E-03	0.87	0.24	79.83
C271	51.46	1.66E-07	2.71E-06	1.01E-05	4.75E-03	0.86	0.27	78.65
B074	51.47	1.96E-07	3.91E-06	2.12E-05	3.30E-03	0.84	0.18	76.88
C272	51.64	1.64E-07	2.24E-06	1.01E-05	4.42E-03	0.86	0.22	81.71
C273	51.86	1.69E-07	1.56E-06	1.01E-05	4.20E-03	0.86	0.16	77.15
C274	52.08	1.57E-07	2.09E-06	8.93E-06	3.73E-03	0.85	0.23	71.03
C275	52.30	2.10E-07	4.31E-06	1.63E-05	3.46E-03	0.85	0.26	79.14
C276	52.52	1.58E-07	2.17E-06	9.36E-06	4.27E-03	0.86	0.23	59.41
B075	52.60	1.67E-07	2.28E-06	1.39E-05	4.76E-03	0.87	0.16	65.87
C277	52.74	1.58E-07	2.64E-06	7.95E-06	3.29E-03	0.85	0.33	63.65
C278	52.89	2.18E-07	4.32E-06	1.97E-05	4.61E-03	0.85	0.22	77.55
C279	53.11	1.79E-07	5.09E-06	1.41E-05	3.51E-03	0.87	0.36	88.06
C280	53.33	1.84E-07	7.70E-06	1.46E-05	2.79E-03	0.88	0.53	72.40
B076	53.42	1.59E-07	2.08E-06	2.06E-05	3.26E-03	0.86	0.10	68.87
C281	53.55	1.95E-07	4.63E-06	1.86E-05	3.11E-03	0.86	0.25	77.42
C282	53.83	2.04E-07	5.02E-06	2.10E-05	3.24E-03	0.85	0.24	49.16
C283	54.11	2.32E-07	5.15E-06	2.61E-05	4.65E-03	0.86	0.20	75.84
C284	54.44	1.96E-07	4.46E-06	1.85E-05	2.92E-03	0.83	0.24	85.77
C285	54.66	1.89E-07	3.79E-06	1.65E-05	2.66E-03	0.83	0.23	72.92
C286	54.89	1.85E-07	6.06E-06	1.96E-05	2.29E-03	0.83	0.31	63.58
C287	55.11	2.11E-07	4.78E-06	2.56E-05	3.00E-03	0.85	0.19	77.57
C288	55.33	2.75E-07	6.38E-06	3.65E-05	5.34E-03	0.85	0.17	80.89
B077	55.43	1.92E-07	3.80E-06	2.18E-05	3.48E-03	0.84	0.17	72.89

Sample	Height [m]	χ [m³/kg]	NRM [Am²/kg]	ARM [Am²/kg]	SIRM [Am²/kg]	s-ratio [-]	NRM/ARM [-]	VGP lat [°]
C289	55.77	2.74E-07	6.36E-06	3.70E-05	4.34E-03	0.86	0.17	82.00
C290	56.10	2.95E-07	6.29E-06	4.50E-05	4.21E-03	0.87	0.14	85.28
C291	56.37	3.36E-07	1.02E-05	4.59E-05	5.34E-03	0.90	0.22	77.65
B078	56.38	2.33E-07	4.62E-06	3.63E-05	4.15E-03	0.85	0.13	82.46
C292	56.66	2.99E-07	5.80E-06	3.47E-05	5.04E-03	0.89	0.17	86.31
C293	56.99	3.86E-07	7.48E-06	3.96E-05	8.01E-03	0.88	0.19	70.91
B079	57.00		1.04E-05	4.59E-05			0.23	85.56
C294	57.17	3.55E-07	9.66E-06	3.90E-05	6.64E-03	0.88	0.25	84.57
C295	57.43	4.42E-07	6.43E-06	4.46E-05	9.02E-03	0.88	0.14	82.36
C296	57.55	3.42E-07	1.04E-05	4.26E-05	5.56E-03	0.89	0.24	49.23
B080	57.66	3.50E-07	8.70E-06	4.35E-05	8.34E-03	0.89	0.20	79.52
C297	57.68	2.82E-07	1.13E-05	3.57E-05	3.51E-03	0.87	0.32	59.61
C298	57.80	3.61E-07	1.03E-05	4.35E-05	6.95E-03	0.87	0.24	79.83
C299	57.94	3.26E-07	1.48E-05	4.71E-05	5.03E-03	0.88	0.31	74.73
C300	58.16	3.19E-07	1.08E-05	4.13E-05	5.17E-03	0.88	0.26	72.20
B081	58.37	3.76E-07	1.00E-05	4.96E-05	6.79E-03	0.87	0.20	69.64
C301	58.49	1.44E-07	3.44E-07	3.12E-06	1.69E-04	0.75	0.11	85.39
C302	58.81	1.49E-07	8.29E-07	4.85E-06	6.97E-04	0.97	0.17	77.07
C303	59.14	1.14E-07	3.45E-07	3.04E-06	1.19E-04	0.96	0.11	69.81
B082	59.23	1.40E-07	6.85E-07	5.85E-06	5.86E-04	0.99	0.12	75.24
C304	59.53	1.03E-07	4.18E-07	2.45E-06	4.55E-04	0.61	0.17	62.69
C305	60.30	8.97E-08	3.35E-07	2.30E-06	2.17E-04	0.97	0.15	
C306	61.06	9.95E-08	3.25E-07	2.11E-06	2.08E-04	0.81	0.15	44.70
C307	61.40	1.08E-07	3.72E-07	3.45E-06	2.65E-04	0.82	0.11	80.74
C308	61.50	3.64E-07	8.34E-06	5.12E-05	5.82E-03	0.89	0.16	69.09
B083	61.53	3.50E-07	9.66E-06	4.69E-05	4.76E-03	0.89	0.21	77.56
C309	61.80	3.21E-07	8.08E-06	5.36E-05	4.43E-03	0.89	0.15	71.29
C310	62.00	2.72E-07	7.83E-06	4.84E-05	3.45E-03	0.88	0.16	68.71
C312	62.15	3.14E-07	1.01E-05	5.90E-05	4.69E-03	0.90	0.17	79.78
C311	62.20	3.05E-07	8.09E-06	5.53E-05	4.19E-03	0.90	0.15	86.56
C313	62.46	3.29E-07	1.07E-05	4.04E-05	4.77E-03	0.91	0.26	79.72
B084	62.54	2.94E-07	1.24E-05	4.78E-05	3.87E-03	0.91	0.26	64.37
C314	62.77	3.53E-07	9.66E-06	5.47E-05	5.77E-03	0.91	0.18	76.58
C315	63.08	2.98E-07	1.21E-05	4.59E-05	4.63E-03	0.92	0.26	74.24
C316	63.39	3.52E-07	9.40E-06	5.08E-05	5.52E-03	0.92	0.19	59.30
B085	63.46	3.69E-07	1.34E-05	4.84E-05	5.28E-03	0.91	0.28	71.04
C317	63.59	3.27E-07	1.35E-05	3.38E-05	5.66E-03	0.93	0.40	67.87
C318	63.89	2.80E-07	9.95E-06	4.24E-05	4.19E-03	0.92	0.23	68.40
B086	64.13	3.54E-07	1.63E-05	4.36E-05	6.66E-03	0.94	0.37	71.77
C319	64.26	3.02E-07	1.58E-05	3.78E-05	4.86E-03	0.92	0.42	80.53
C320	64.45	1.65E-07	1.83E-06	8.53E-06	1.15E-03	0.73	0.21	73.47
C321	64.73	3.97E-07	1.14E-05	4.97E-05	6.33E-03	0.91	0.23	84.07
B087	65.50	3.25E-07	8.56E-06	5.26E-05	4.13E-03	0.91	0.16	51.45
C322	65.82	4.47E-07	1.21E-05	5.61E-05	8.28E-03	0.91	0.22	89.39
B088	67.10	4.48E-07	1.24E-05	5.47E-05	7.99E-03	0.92	0.23	
C323	68.04	4.01E-07	9.81E-06	5.27E-05	5.99E-03	0.91	0.19	70.61
C324	68.38	3.72E-07	1.30E-05	4.93E-05	5.64E-03	0.91	0.26	76.31
B089	68.55	3.24E-07	1.19E-05	5.19E-05	4.03E-03	0.89	0.23	67.68
C325	68.88	3.09E-07	1.23E-05	5.63E-05	3.75E-03	0.88	0.22	78.50
C326	69.38	3.11E-07	1.08E-05	5.40E-05	3.97E-03	0.85	0.20	67.66
C327	69.80	3.56E-07	8.01E-06	4.99E-05	5.78E-03	0.92	0.16	78.21
C328	70.13	3.76E-07	1.10E-05	4.61E-05	6.31E-03	0.93	0.24	75.29
B090	70.17	3.13E-07	7.97E-06	3.78E-05	5.93E-03	0.93	0.21	80.91
B091	70.90	4.44E-07	9.88E-06	4.89E-05	8.01E-03	0.95	0.20	74.03
C330	71.10	7.70E-08	4.07E-07	2.23E-06	1.18E-04	0.79	0.18	72.49

Sample	Height [m]	χ [m³/kg]	NRM [Am²/kg]	ARM [Am²/kg]	SIRM [Am²/kg]	s-ratio [-]	NRM/ARM [-]	VGP lat [°]
C331	71.40	1.45E-07	1.58E-06	1.91E-06	1.30E-03	0.91	0.83	72.04
D23	71.75	2.57E-07	7.49E-06	3.24E-05	4.30E-03	0.93	0.23	72.50
C332	71.95	4.49E-07	9.49E-06	5.45E-05	7.52E-03	0.93	0.17	72.56
D24	72.25	3.43E-07	9.31E-06	5.08E-05	3.71E-03	0.89	0.18	76.25
C333	72.41	3.73E-07	7.24E-06	4.80E-05	5.22E-03	0.92	0.15	72.47
C334	72.87	3.02E-07	7.77E-06	4.79E-05	3.78E-03	0.88	0.16	59.97
B092	73.00	4.62E-07	9.62E-06	5.88E-05	8.34E-03	0.93	0.16	51.85
C335	73.32	3.45E-07	8.00E-06	4.83E-05	4.63E-03	0.91	0.17	81.94
D25	73.35	3.04E-07	9.70E-06	4.68E-05	4.30E-03	0.88	0.21	75.51
C336	73.78	3.01E-07	8.65E-06	4.55E-05	3.79E-03	0.88	0.19	82.94
B093	73.86	3.11E-07	9.91E-06	5.24E-05	4.10E-03	0.90	0.19	66.92
D26	74.00	3.21E-07	5.45E-06	4.53E-05	5.66E-03	0.90	0.12	-56.91
C337	74.23	3.41E-07	6.10E-06	5.22E-05	5.03E-03	0.89	0.12	-26.03
C338	74.69	3.36E-07	5.98E-06	4.92E-05	4.99E-03	0.95	0.12	39.01
B094	74.73	3.79E-07	5.93E-06	5.00E-05	5.43E-03	0.91	0.12	-37.22
D27	75.00	4.90E-07	7.54E-06	5.46E-05	6.41E-03	0.89	0.14	-62.57
C339	75.25	4.41E-07	6.59E-06	4.77E-05	8.14E-03	0.93	0.14	66.75
B095	75.72	3.36E-07	4.40E-06	5.39E-05	5.90E-03	0.92	0.08	35.65
C340	75.81	4.81E-07	8.01E-06	5.50E-05			0.15	76.25
D28	75.90	3.87E-07	3.99E-06	5.20E-05	7.11E-03	0.92	0.08	-68.93
C341	76.36	4.43E-07	6.15E-06	4.66E-05	6.68E-03	0.91	0.13	89.79
D29	76.60	4.24E-07	6.92E-06	4.94E-05	7.73E-03	0.92	0.14	
C342	76.92	4.01E-07	6.25E-06	4.44E-05	5.66E-03	0.90	0.14	76.51
D30	77.00	3.82E-07	6.19E-06	5.15E-05	5.93E-03	0.91	0.12	-79.15
B096	77.10	1.50E-07	4.64E-06	5.15E-05			0.09	-41.89
D31	77.15	4.62E-07	7.64E-06		6.48E-03	0.87		-33.43
D32	77.30	3.64E-07	6.83E-06	4.40E-05	6.66E-03	0.87	0.16	
C343	77.48	3.87E-07	6.74E-06	4.18E-05			0.16	-9.87
D33	77.60	4.25E-07	5.50E-06	4.97E-05	7.33E-03	0.90	0.11	-50.71
D34	77.80	3.99E-07	3.80E-06	5.49E-05	5.02E-03	0.87	0.07	-48.69
C344	78.04	4.23E-07	6.45E-06	4.28E-05	6.51E-03	0.91	0.15	54.64
C345	78.60	3.80E-07	3.73E-06	4.60E-05	6.16E-03	0.90	0.08	-40.13
B097	78.77	3.90E-07	6.01E-06	5.80E-05	5.60E-03	0.91	0.10	-53.04
C346	79.15	3.04E-07	4.03E-06	3.82E-05	5.22E-03	0.92	0.11	-38.87
C347	79.71	1.65E-07	2.59E-06	1.71E-05	2.83E-03	0.93	0.15	-74.59
D35	80.10	4.15E-07	6.63E-06	4.04E-05	7.08E-03	0.91	0.16	-39.94
B098	80.18	4.02E-07	5.60E-06	5.78E-05	6.84E-03	0.91	0.10	-39.75
C348	80.27	3.69E-07	5.87E-06	4.53E-05	6.13E-03	0.91	0.13	68.15
C349	80.83	2.85E-07	3.68E-06	1.90E-05			0.19	63.75
C350	81.39	3.56E-07	6.64E-06	3.56E-05	6.52E-03	0.93	0.19	74.10
B099	81.83	3.57E-07	6.49E-06	5.21E-05	5.82E-03	0.92	0.12	43.90
C351	81.94	3.21E-07	4.15E-06	2.99E-05	6.46E-03	0.93	0.14	
C352	82.50	4.81E-08	2.20E-07	1.10E-06	8.96E-05	0.96	0.20	74.72
C353	83.06	3.38E-07	9.31E-06	3.07E-05	5.47E-03	0.91	0.30	68.32
Z092	83.18	4.56E-07	1.02E-05	5.29E-05	8.11E-03	0.91	0.19	
C354	83.53	3.45E-07	9.84E-06	2.80E-05	4.84E-03	0.94	0.35	73.14
Z094	83.88	3.45E-07	7.92E-06	2.55E-05	5.22E-03	0.91	0.31	65.83
C355	83.99	3.90E-07	1.10E-05	3.59E-05	6.21E-03	0.92	0.31	63.40
Z093	84.18	2.62E-07	7.15E-06	2.80E-05	4.58E-03	0.91	0.26	77.15
C356	84.69	3.46E-07	1.12E-05	3.51E-05	5.32E-03	0.89	0.32	59.44
Z095	85.02	4.00E-07	1.06E-05	4.03E-05	6.87E-03	0.91	0.26	82.29
C357	85.06	3.01E-07	5.91E-06	2.01E-05			0.29	65.77
C358	85.32	3.22E-07	7.30E-06	1.83E-05	4.70E-03	0.93	0.40	70.45
Z096	85.89	4.16E-07	8.92E-06	3.45E-05	6.80E-03	0.91	0.26	67.74
C359	85.99	5.33E-07	1.18E-05	3.79E-05	9.83E-03	0.94	0.31	55.31

Sample	Height [m]	χ [m³/kg]	NRM [Am²/kg]	ARM [Am²/kg]	SIRM [Am²/kg]	s-ratio [-]	NRM/ARM [-]	VGP lat [°]
Z097	87.74	2.67E-08	3.20E-07	8.08E-06	1.96E-04	0.93	0.04	49.49
C360	87.86	3.76E-07	7.72E-06	3.87E-05	6.06E-03	0.89	0.20	63.79
C361	88.53	4.26E-07	4.73E-06	3.72E-05	6.94E-03	0.87	0.13	65.21
Z098	89.12	4.77E-08	6.94E-07	5.79E-06	4.73E-04	0.83	0.12	78.34
C362	89.19	1.13E-07	2.46E-06	9.39E-06	1.85E-03	0.89	0.26	71.55
C363	89.82	8.26E-08	4.87E-07	3.09E-06	2.28E-04	0.80	0.16	79.32
Z099	89.88	7.90E-08	5.98E-07	4.64E-06	1.38E-04	0.66	0.13	72.96
C364	90.39	4.15E-07	6.98E-06	4.31E-05	6.96E-03	0.91	0.16	81.46
C365	90.66	2.43E-07	3.66E-06	1.43E-05			0.26	59.58
C366	91.00	1.18E-07	2.28E-07	3.33E-06	1.49E-04	0.90	0.07	-33.90
C367	91.58	8.39E-08	2.99E-07	2.37E-06	1.46E-04	0.97	0.13	54.17
K100	91.74	5.94E-08	2.89E-07	4.99E-06			0.06	
C368	92.15	8.99E-08	2.58E-07	2.25E-06	8.51E-05	0.91	0.11	67.84
K101-2	92.27	8.13E-08	2.70E-07	1.88E-05	9.92E-05	0.94	0.01	
C369	92.64	7.51E-08	4.36E-07	2.55E-06	2.44E-04	0.99	0.17	80.04
K102	93.12	5.81E-08	1.89E-07	1.50E-06			0.13	
C370	93.13	5.82E-08	1.98E-07	1.30E-06	9.04E-05	0.97	0.15	
K103	94.06	1.12E-07	6.72E-07	2.51E-06			0.27	71.40
C371	94.11	1.20E-07	4.70E-07	3.97E-06	2.51E-04	0.97	0.12	57.44
C372	94.91	6.46E-08	4.29E-07	2.78E-06	1.54E-04	0.94	0.15	
K104	95.22	1.12E-07	4.17E-07	5.32E-06			0.08	
C374	95.71	3.44E-07	3.54E-06	3.97E-05			0.09	54.50
C373	95.79	3.91E-07	5.54E-06	4.59E-05	6.48E-03	0.90	0.12	-35.67
K105	96.20		1.01E-06	4.82E-05			0.02	-66.02
C375	96.25	3.17E-07	3.54E-06	4.65E-05	5.06E-03	0.89	0.08	-21.39
C376	96.63	2.85E-07	5.13E-06	2.99E-05			0.17	76.38
C377	97.07	1.58E-07	1.62E-06	1.05E-05	1.64E-03	0.84	0.15	74.29
C378	97.40	3.34E-07	7.18E-06	3.76E-05	5.08E-03	0.88	0.19	74.23
K106	97.48	3.07E-07	6.92E-06	4.26E-05			0.16	77.50
C379	97.84	4.39E-07	9.24E-06	3.74E-05	7.61E-03	0.90	0.25	61.63
C380	98.06	6.98E-07	1.22E-05	4.37E-05	1.28E-02	0.91	0.28	69.19
K107	98.72		1.14E-05	2.35E-05	2.19E-03	0.92	0.49	78.29
C381	98.45		5.87E-06	4.99E-05			0.12	72.40
C383	99.19	4.62E-07	1.09E-05	5.51E-05	6.60E-03	0.91	0.20	64.48
C382	99.27	4.34E-07	1.30E-05	4.65E-05	7.38E-03	0.90	0.28	63.45
C384	99.54	3.41E-07	9.46E-06	3.03E-05	5.36E-03	0.93	0.31	63.54
C385	99.72	2.29E-07	6.48E-06	2.15E-05	3.32E-03	0.93	0.30	82.26
C386	99.90	2.95E-07	6.88E-06	2.73E-05	4.92E-03	0.93	0.25	82.90
C387	100.08	1.94E-07	3.66E-06	1.37E-05	3.14E-03	0.89	0.27	77.61
K108	100.62	1.20E-07	1.03E-06	4.63E-06			0.22	75.56
K109	101.44	9.51E-08	3.98E-07	4.27E-06	1.55E-04		0.09	51.09
K112	105.65	1.22E-07	3.00E-07	7.51E-06			0.04	67.68
K113	107.72	1.87E-07	3.65E-06	1.36E-05			0.27	56.47
K114	108.72	9.47E-08	7.66E-07	4.81E-06			0.16	78.15
K115	109.22	1.07E-07		3.10E-06				
K116	109.41	1.24E-07	7.67E-07	7.50E-06			0.10	53.13
K117	109.90	6.14E-08	3.46E-07	1.94E-06			0.18	87.69
K118	110.75	8.30E-08	5.69E-07	3.46E-06	1.30E-04	0.97	0.16	85.28
K119	111.61	5.23E-08	2.95E-07	1.97E-06			0.15	60.68
K120	112.47	9.01E-08	1.61E-07	5.95E-06			0.03	67.34
K121	114.62	6.32E-08	4.13E-07	1.16E-06			0.36	79.09
K122	115.30	7.22E-08	5.38E-07	1.81E-06			0.30	70.18
K123	115.98	7.34E-08	6.22E-07	2.27E-06			0.27	61.82
K124	116.73	1.03E-07	5.15E-07	3.28E-06			0.16	63.75
K125	117.73	4.48E-08	1.98E-07	1.07E-06			0.19	64.24

Sample	Height [m]	χ [m³/kg]	NRM [Am²/kg]	ARM [Am²/kg]	SIRM [Am²/kg]	s-ratio [-]	NRM/ARM [-]	VGP lat [°]
K126	118.09	6.72E-08	1.29E-06	4.54E-06			0.28	83.99
K127	119.34		2.42E-07	8.63E-06	6.98E-05	0.94	0.03	55.96
K128	120.51	7.31E-08	2.31E-07	5.20E-07			0.44	
K129	121.82	1.12E-07	4.87E-07	2.03E-06			0.24	77.51
K130	123.12	6.69E-08	2.11E-07	1.93E-06			0.11	79.33
K131	124.47	7.99E-08	6.25E-07	1.02E-06			0.61	-53.91
K132	125.96	9.00E-08	3.75E-07	1.32E-06			0.28	70.18
K133	126.76	6.28E-08	5.85E-08	3.54E-06			0.02	
K134	127.72	1.11E-07	3.08E-07	2.74E-06			0.11	75.96
K135	128.57		2.04E-07	1.88E-06	5.88E-05	0.86	0.11	47.34
K136	129.94	6.92E-08	2.79E-07	2.85E-06			0.10	62.46
K137	130.91	8.29E-08	4.78E-07	2.54E-06			0.19	48.45
K138	131.87	7.80E-08	3.25E-07	2.12E-06	1.08E-04	0.76	0.15	56.44
K139	132.47	1.12E-07	4.05E-07	4.74E-06			0.09	
K140	134.81	7.50E-08	2.11E-07	8.71E-07			0.24	78.82
K141	135.65	9.49E-08	7.49E-07	5.46E-06			0.14	37.58
K142	138.02	4.64E-08	2.14E-07	2.46E-06			0.09	64.11
K143	139.03	7.77E-08	4.01E-07	1.20E-06			0.33	80.91
K144	139.82	1.04E-07	4.77E-07	2.72E-06			0.18	52.14
K145	141.47	4.37E-08	2.64E-07	1.98E-06			0.13	63.63
K146	142.31	6.16E-08	6.90E-07	3.55E-06			0.19	3.82
K147	143.10	5.69E-08	3.84E-07	9.38E-07			0.41	68.32
K148	144.36	6.71E-08	2.01E-07	1.74E-06			0.12	83.47
K149	145.23	9.74E-08	4.25E-07	2.10E-06			0.20	67.73
K150	145.99	9.97E-08	5.63E-07	2.77E-06			0.20	56.29
K151	146.86	6.55E-08	3.04E-07	6.52E-06	6.92E-05	0.95	0.05	79.30
K152	147.80	1.13E-07	3.59E-07	5.43E-06			0.07	49.65
K153	148.37	6.22E-08	2.97E-07	1.79E-06			0.17	43.47
K154	149.42	4.87E-08	2.95E-07	1.27E-06			0.23	86.42
K155	150.38	6.59E-08	1.89E-07	2.51E-06			0.08	63.61
K156	151.19	1.33E-08	5.43E-08	1.21E-07	2.03E-05		0.45	
K157	151.64		6.66E-07	2.08E-06			0.32	-20.36
K158	152.62	7.12E-08	1.91E-07	1.98E-06			0.10	74.02
K159	153.90	4.04E-08	2.49E-07	2.17E-06	6.93E-05	0.99	0.11	54.58
L160	155.10	6.34E-08	1.88E-07	1.01E-06			0.19	
L161	156.01	7.37E-08	3.25E-07	2.02E-06			0.16	
L162	156.67	4.38E-08	1.74E-07	6.21E-07			0.28	50.15
L164	158.92	6.17E-08	4.03E-07	2.83E-06	1.07E-04	0.95	0.14	-14.38
L165	159.86	6.62E-08	1.32E-07	9.71E-07			0.14	71.80
L166	160.23	7.99E-08	6.39E-07	4.81E-06			0.13	56.84
L167	161.34	5.80E-08	2.27E-07	1.65E-06	3.14E-05	0.97	0.14	77.27
L168	161.87	8.00E-08	4.36E-07	3.22E-06			0.14	47.08
L170	162.92	7.47E-08	4.54E-07	5.31E-06			0.09	43.32
L171	164.06	5.46E-08	6.47E-07	1.65E-06	4.22E-05	0.97	0.39	58.55
L172	164.83	7.99E-08	3.61E-07	4.74E-06			0.08	62.22
L173	165.58	4.26E-08	1.96E-07	2.44E-06	5.79E-05	0.95	0.08	24.73
L174	166.70	8.47E-08	2.57E-07	3.29E-06			0.08	64.81
L175	167.20	4.85E-08	1.68E-07	9.13E-07	4.60E-05	0.63	0.18	78.62
L176	168.40	9.98E-08	3.31E-07	1.57E-06			0.21	
L177	169.20	4.30E-08	1.19E-07	1.13E-05	3.16E-05	0.96	0.01	
L178	170.10	7.19E-08	8.40E-07	3.72E-06			0.23	-6.46
L179	171.38	5.24E-08	1.43E-07	1.84E-06			0.08	
L180	172.66	5.20E-08	5.84E-08	7.67E-07			0.08	51.72
L181	173.15	6.56E-08	1.37E-07	2.37E-06			0.06	
L183	175.44	8.70E-08	2.49E-07	2.17E-06	1.31E-04	0.93	0.12	60.50

Sample	Height [m]	χ [m³/kg]	NRM [Am²/kg]	ARM [Am²/kg]	SIRM [Am²/kg]	s-ratio [-]	NRM/ARM [-]	VGP lat [°]
L184	176.24	9.92E-08	2.68E-07	6.01E-06			0.04	52.24
L185	176.56	9.72E-08	3.85E-07	1.51E-06			0.26	
L186	178.20	9.48E-08	6.68E-07	3.11E-06			0.21	-24.74
L187	179.03	5.05E-08	1.29E-07	2.29E-06			0.06	69.30
L188	179.92	4.66E-08	1.48E-07	1.41E-06	5.42E-05	0.95	0.11	75.62
L189	181.21	5.01E-08	1.70E-07	3.28E-06	4.42E-05	0.96	0.05	
L190	182.51	6.97E-08	4.97E-07	4.65E-06			0.11	74.24
L191	183.47	6.82E-08	3.30E-07	2.75E-06			0.12	
L192	184.13	5.21E-08	1.82E-07	2.52E-06	8.06E-05	0.95	0.07	
L193	184.97	7.90E-08	3.95E-07	4.07E-06	1.77E-04	0.96	0.10	55.41
L194	186.04	7.31E-08	4.67E-07	3.53E-06	1.08E-04	0.96	0.13	66.89
L195	187.03	8.96E-08	5.55E-07	3.14E-06	2.73E-04	0.97	0.18	60.60
L196	187.32	7.53E-08	2.25E-07	3.69E-06	9.40E-05	0.96	0.06	-4.32
L197	187.99	8.70E-08	1.86E-07	1.03E-05	7.78E-05	0.96	0.02	79.06
L198	189.16	8.35E-08	2.23E-07	3.23E-06	7.82E-05	0.96	0.07	30.54
L199	191.08	5.14E-08	2.59E-07	1.94E-06	9.93E-05	0.81	0.13	51.16
L200	191.69	6.34E-08	3.35E-07	3.28E-06	5.47E-05	0.96	0.10	72.40
L201	192.05	7.25E-08	1.05E-07	3.61E-06	8.99E-05	0.88	0.03	-63.99
L202	192.83	6.52E-08	2.65E-07	7.83E-06	6.60E-05	0.95	0.03	-22.54
L203	193.63		1.74E-07		5.86E-05	0.94		65.80
L204	194.49	5.37E-08	2.53E-07	4.74E-06	1.28E-04	0.95	0.05	72.10
L205	195.34		2.55E-07	4.82E-06			0.05	
L206	196.03	8.84E-08	1.77E-07	1.22E-06	6.64E-05	0.97	0.14	51.67
L207	196.89	1.06E-07	4.03E-07	8.19E-07			0.49	67.34
L208	197.93	1.03E-07	3.19E-07	2.70E-06	1.04E-04	0.93	0.12	71.87
L209	199.15		2.84E-07	3.37E-06	7.80E-05	0.96	0.08	56.84
L210	200.20	1.05E-07	3.21E-07	2.23E-06	1.11E-04	0.81	0.14	
L211	201.16	6.63E-08	1.70E-07	2.24E-06	1.20E-04	0.95	0.08	
L213	203.32	8.82E-08	3.83E-07	5.80E-07	1.57E-04	0.88	0.66	
L214	204.21	9.57E-08	3.26E-07	6.66E-07	7.55E-05	0.94	0.49	52.97
L215	205.60	6.39E-08	6.42E-07	8.74E-07	1.00E-04	0.92	0.74	
L218	209.40	6.64E-08	1.99E-07	2.82E-06	4.90E-05	0.93	0.07	34.77
L219	210.98		5.60E-07	4.09E-06	3.72E-04	0.88	0.14	80.19
L221	213.84	8.56E-08	6.84E-07	4.69E-06			0.15	57.21
L222	215.03	7.77E-08	4.92E-07	4.79E-06	1.15E-04		0.10	84.45
L223	217.66	8.21E-08	4.36E-07	2.37E-06	1.29E-04		0.18	-20.03
L224	221.62	6.53E-08	2.05E-07	2.08E-06	6.65E-05	0.91	0.10	-62.67
L225	228.65	1.08E-07	1.92E-07	6.53E-06	6.60E-05	0.94	0.03	58.11
L226	230.72	6.06E-08	4.70E-07	2.33E-06	1.26E-04	0.91	0.20	81.64
L228	238.11	9.40E-08	2.19E-07	2.86E-06	6.12E-05	0.98	0.08	59.29
L229	240.49	5.20E-08	1.34E-07	5.57E-06	4.63E-05	0.94	0.02	
L230	241.80	9.06E-08	2.87E-07	5.70E-06			0.05	65.62
L231	243.86	8.27E-08	3.61E-07	1.48E-06	8.90E-05	0.85	0.24	50.78
L232	246.75	7.00E-08	3.98E-07	3.10E-06	1.43E-04	0.98	0.13	43.84
L233	248.50	7.82E-08	3.43E-07	6.15E-07	1.14E-04	0.93	0.56	
L234	250.57	8.00E-08	4.84E-07	2.25E-06	1.11E-04	0.93	0.21	
L235	252.73	6.97E-08	1.98E-07	9.53E-07			0.21	17.99
L236	255.13	8.91E-08	1.44E-06	1.25E-05			0.12	
L237	257.91	1.16E-07	1.65E-06	3.67E-06	6.56E-04	0.86	0.45	59.40
L239	262.17	1.36E-07	5.28E-07	5.00E-06	2.00E-04	0.72	0.11	88.44
N001	263.72		1.70E-06					65.87
N002	263.94		8.75E-06					72.31
L240	264.10	3.47E-07	1.45E-05	4.13E-05	4.97E-03	0.92	0.35	70.29
N003	264.23		1.76E-05					25.62
N004	265.46		1.08E-05					65.23

Sample	Height [m]	χ [m³/kg]	NRM [Am²/kg]	ARM [Am²/kg]	SIRM [Am²/kg]	s-ratio [-]	NRM/ARM [-]	VGP lat [°]
N005	266.15		1.03E-06					59.37
N006	266.73		1.00E-06					78.07
L241	267.07	8.17E-08	7.14E-07	5.38E-06	2.14E-04	0.84	0.13	24.13
N007	267.09		5.00E-06					73.80
N008	267.44		2.00E-06					55.54
N009	267.89		4.59E-06					73.76
N010	268.14		2.15E-06					71.54
N011	268.51		6.83E-07					83.50
N012	268.97		9.78E-06					76.99
N013	269.62		2.23E-06					67.33
N014	270.10		9.68E-07					71.79
N015	270.62		7.87E-07					78.49
N016	271.18		4.96E-07					83.23
N017	271.51		4.61E-06					50.12
N018	271.98		3.54E-07					75.97
L243	272.43		7.77E-07	5.47E-06	1.66E-04	0.93	0.14	-59.47
N019	273.05		2.51E-07					79.21
N020	273.66		1.34E-05					70.32
N021	273.87		1.51E-06					64.43
L244	273.95		4.34E-07	2.90E-06	5.80E-05	0.92	0.15	77.25
N022	274.76		4.24E-07					-47.74
N023	275.35		3.09E-07					67.87
N026	275.67		1.83E-06					58.97
N024	275.99		4.02E-07					57.88
L245	276.10	1.29E-07	4.97E-07	5.68E-06	1.24E-04	0.82	0.09	82.91
N027	276.23		7.93E-07					66.64
N025	276.46		1.26E-06					68.29
N028	276.71		1.00E-06					46.65
N029	277.29		6.45E-07					68.59
N030	278.00		5.26E-07					69.51
N031	278.21		1.99E-07					71.31
N03	278.41		1.54E-05					70.02
N033	278.73		2.24E-06					73.35
N034	279.24		4.57E-07					78.31
N035	279.49		4.90E-07					59.13
N036	280.43		8.31E-07					-70.30
N037	281.63		7.81E-07					-49.08
N038	281.84		4.16E-07					54.73
N039	282.14		3.92E-07					-37.89
N040	282.42		5.70E-07					-6.75
N041	282.68		2.81E-07					
N042	282.87		4.57E-07					63.64
N043	283.06		6.36E-07					79.42
N044	283.37		3.19E-07					62.29
N045	283.74		4.24E-07					81.65
N046	284.62		4.75E-07					-45.66
N047	285.63		7.84E-07					
N048	285.97		1.11E-06					-32.19
N049	286.30		4.28E-07					
N050	286.46		3.83E-06					65.42
N051	286.69		3.35E-07					-14.01
N052	287.63		9.27E-07					35.07
N053	288.58		5.65E-07					75.25
L249	289.23	1.17E-07	3.37E-07	7.68E-07	1.21E-04	0.94	0.44	85.00
N054	289.24		7.13E-07					72.12
N055	290.15		9.42E-06					70.34
N056	290.60		2.49E-06					43.17
N057	290.80		4.28E-07					78.08
N058	291.73		3.08E-07					-62.03
N059	292.81		7.91E-07					54.66
N060	293.12		4.82E-07					-30.98
N061	294.01		2.57E-07					
L251	294.06	6.68E-08	3.68E-07	3.65E-07	6.97E-05	0.93	1.01	74.37
N062	294.67		3.63E-07					65.81
N063	295.20		2.68E-07					-76.03
N064	295.43		2.87E-07					64.23
N068	296.47		3.52E-07					-60.93
N065	296.48		5.25E-07					
N066	296.91		2.16E-07					79.63
N069	297.10		4.58E-07					77.68
N070	297.59		1.06E-05					81.32
N067	297.60		6.95E-06					68.04
N071	297.95		1.35E-06					56.05
L253	298.30	1.02E-07	6.92E-07	3.50E-06	2.73E-04	0.78	0.20	77.21
N072	298.55		2.64E-07					-48.36
N073	299.01		6.18E-07					-17.98
N074	299.47		2.02E-07					61.18
L254	300.00	7.01E-08	2.98E-07	2.05E-06	7.21E-05	0.94	0.15	57.72
N075	301.26		3.20E-07					48.02
N076	301.90		4.87E-07					65.50
N077	302.45		4.55E-07					66.88
N078	303.19		4.29E-07					51.06
N079	303.87		9.59E-07					
L255	304.25	1.12E-07	3.52E-07	3.70E-06	1.13E-04	0.86	0.10	-60.00
N080	304.58		3.62E-07					67.41
N081	304.97		5.57E-07					61.82
N082	305.89		4.34E-07					
L256	306.01	1.00E-07	1.51E-06	7.36E-06	2.79E-04	0.91	0.21	
N083	306.21		2.17E-07					-48.39
N084	306.87		5.53E-07					
N085	307.20		4.74E-07					
L257	307.30	1.46E-07	3.60E-06	4.59E-06			0.78	78.28
N086	307.70		8.50E-07					88.20
N087	308.10		2.84E-06					84.74
N088	308.81		5.55E-07					74.56
L258	309.16	8.48E-08	4.52E-07	4.68E-06	1.32E-04	0.89	0.10	
N089	309.59		2.94E-07					
N090	310.05		2.57E-07					-46.22
L259	310.33	6.96E-08	2.70E-07	5.46E-06	1.48E-04	0.94	0.05	38.58
N091	310.41		6.87E-07					
N092	310.99		7.11E-07					-38.55
L260	311.93	9.00E-08	2.69E-07	7.15E-06	1.01E-04	0.91	0.04	65.04
N093	312.39		2.82E-07					87.13
N094	312.73		1.63E-07					47.34
N095	313.21		4.85E-07					74.60
L261	313.78	1.24E-07	1.28E-06	1.22E-05	8.09E-04	0.90	0.11	84.07
N096	314.44		5.24E-07					61.95
N097	314.77		2.33E-07					
N098	315.11		2.42E-07					-75.98
L26	315.47	6.38E-08	1.48E-07	5.58E-07	7.10E-05	0.93	0.27	

Sample	Height [m]	χ [m³/kg]	NRM [Am²/kg]	ARM [Am²/kg]	SIRM [Am²/kg]	s-ratio [-]	NRM/ARM [-]	VGP lat [°]
N099	315.54		7.57E-07					-35.27
N100	316.05		9.35E-07					
N101	316.98		4.37E-07					43.02
N102	317.44		5.07E-07					18.50
L263	317.54	7.82E-08	2.93E-07	5.37E-06	1.00E-04	0.91	0.05	
N103	317.74		1.51E-07					
N104	318.20		3.21E-07					
N105	318.57		3.09E-07					-86.96
N106	319.84		6.32E-07					-19.62
L264	320.20	1.34E-07	5.46E-07	2.49E-06	1.45E-04	0.93	0.22	
N107	320.44		1.93E-06					
N108	321.17		2.52E-06					58.85
N109	322.13		7.35E-07					
L26	322.38	1.06E-07	3.79E-07	7.81E-06	1.28E-04	0.97	0.05	-68.62
N110	322.74		2.71E-07					
N111	323.18		4.29E-07					69.35
L266	323.52		4.89E-07	2.29E-06	1.19E-04	0.93	0.21	
N112	324.00		1.71E-07					76.85
N113	324.35		5.58E-06					35.01
L26	324.72	9.57E-08	1.21E-06	5.50E-06	2.14E-04	0.98	0.22	
N114	325.01		6.72E-07					
N115	325.75		4.59E-07					81.69
N116	326.99		3.73E-07					84.24
N117	328.06		6.64E-07					45.07
N118	328.75		4.40E-07					83.82
N119	329.10		2.66E-07					75.79
N120	329.33		1.51E-06					87.52
L270	329.74	8.54E-08	7.81E-07	1.73E-06			0.45	
N121	330.15		7.21E-07					
N122	330.52		1.04E-06					81.41
N123	330.83		5.78E-06					85.61
N124	331.41		6.25E-07					-52.49
N125	331.58		1.84E-06					-56.33
N126	331.87		2.81E-07					-59.41
L271	331.91	1.24E-07	3.80E-07	1.24E-05	1.61E-04	0.92	0.03	60.96
N127	332.59		6.82E-07					39.54
N128	333.51		2.27E-07					-14.90
N129	334.23		2.96E-07					81.38
L273	334.40	8.16E-08	7.24E-07	8.35E-06	1.11E-04	0.98	0.09	53.52
N130	335.03		2.95E-07					64.24
N131	335.96		6.44E-07					21.38
L274	335.97	1.41E-07	1.68E-06	4.23E-06	4.99E-04		0.40	52.39
N132	336.34		4.43E-07					28.27
N133	336.82		5.18E-07					13.15
L275	337.37	9.79E-08	4.59E-07	1.61E-05	1.54E-04	0.96	0.03	69.54
N134	337.48		6.30E-07					69.18
N135	338.30		6.04E-07					60.34
N136	338.64		2.98E-07					-34.71
L276	339.25	1.05E-07	3.98E-07	2.95E-06	1.30E-04	0.92	0.13	
N137	339.35		8.04E-06					77.13
N138	339.65		5.79E-06					79.69
N139	340.07		2.52E-06					88.88
N140	340.29		2.02E-06					85.05
N141	340.69		3.09E-06					73.35
L277	340.99		1.26E-06	4.95E-06			0.26	

Sample	Height [m]	χ [m³/kg]	NRM [Am²/kg]	ARM [Am²/kg]	SIRM [Am²/kg]	s-ratio [-]	NRM/ARM [-]	VGP lat [°]
N142	341.08		5.45E-07					86.12
N143	341.55		3.28E-07					
N144	341.78		5.28E-07					83.72
N145	342.31		6.57E-07					78.54
N146	342.80		4.57E-07					60.00
N147	343.46		2.28E-07					48.57
L278	343.51	9.60E-08	8.08E-07	4.23E-06	5.06E-04	0.92	0.19	
N148	343.77		1.16E-06					48.05
N149	344.10		6.32E-07					
N150	344.60		4.87E-07					70.61
N151	345.09		1.20E-06					70.72
N152	345.83		5.13E-07					78.62
L279	346.23		5.52E-07	7.54E-06	4.57E-04	0.93	0.07	
N153	346.37		3.94E-07					80.77
N154	347.11		6.26E-07					77.14
N155	347.49		2.66E-06					27.40
N156	347.64		9.63E-07					83.33
N157	347.88		9.20E-07					77.83
N158	348.30		7.94E-07					73.34
N159	348.67		1.17E-07					37.28
N160	348.85		4.13E-07					73.37
L280	348.91	3.47E-08	7.79E-08	1.31E-06	1.87E-05	0.86	0.06	-58.99
N161	349.01		5.22E-07					-34.04
N162	349.33		1.23E-06					80.35
N163	349.60		3.94E-06					76.00
N164	349.95		4.60E-07					-28.31
N165	350.48		5.06E-07					74.13
L281	350.51	8.74E-08	4.08E-07	3.19E-06	8.28E-05	0.95	0.13	-65.99
N166	350.71		3.31E-07					74.59
N167	351.08		2.76E-07					75.02
N168	351.33		5.38E-07					59.67
N169	351.57		4.99E-07					67.47
N170	351.85		1.50E-06					85.13
L282	352.21	8.08E-08	1.25E-06	1.05E-06	7.68E-05	0.97	1.19	52.50
N171	352.26		6.73E-07					55.20
N172	352.69		1.29E-06					-18.34
N173	353.06		7.45E-07					75.15
N174	353.24		7.27E-07					-50.21
N175	353.88		5.78E-07					66.51
N176	354.39		3.60E-07					78.33
L283	354.43	1.13E-07		2.75E-06	7.72E-05	0.99		79.26
N177	354.53		5.93E-07					59.08
N178	354.80		4.59E-06					-43.77
N179	355.65		7.76E-07					-34.23
L284	356.46	9.23E-08	4.47E-07	1.94E-06	2.12E-04	0.97	0.23	
N180	357.11		3.58E-07					
N181	357.52		3.17E-07					27.84
N182	359.12		1.25E-06					70.76
L286	359.17	7.29E-08	1.02E-07	1.40E-06	4.00E-05	0.95	0.07	
N183	359.44		5.41E-07					36.84
N184	360.16		4.53E-07					67.56
L287	360.56	1.11E-07	6.06E-07	3.57E-06	1.28E-04	0.97	0.17	43.95
N185	360.57		2.10E-06					83.69
N186	361.18		2.07E-06					-31.01
N187	361.62		6.32E-07					-71.62

Sample	Height [m]	χ [m³/kg]	NRM [Am²/kg]	ARM [Am²/kg]	SIRM [Am²/kg]	s-ratio [-]	NRM/ARM [-]	VGP lat [°]
N188	362.62		4.53E-06					74.03
N189	363.37		1.79E-07					-65.93
L289	363.38	1.13E-07	6.89E-07	3.52E-06	1.26E-04	0.87	0.20	
L290	364.93		2.66E-07	4.34E-06	2.76E-04	0.76	0.06	-72.91
L291	366.53	8.40E-08	4.47E-07	2.54E-06	6.74E-05	0.79	0.18	
L292	367.89	5.96E-08	1.29E-07	1.32E-06	4.67E-05	0.96	0.10	-17.51
N190	368.89		5.94E-07					60.55
L293	368.98	8.71E-08	2.57E-07	2.38E-06	1.14E-04	0.93	0.11	71.19
N191	369.26		1.33E-06					-19.91
N192	369.94		6.74E-07					67.91
L294	370.20	3.42E-08	1.26E-07	1.51E-06	4.61E-05	0.93	0.08	54.38
N193	370.50		3.67E-07					-67.14
L295	370.97	8.06E-08	4.37E-07	9.76E-07			0.45	
N194	371.19		2.11E-07					
L296	372.67	6.42E-08	2.16E-07	2.69E-06	6.59E-05	0.97	0.08	
L298	374.90	7.48E-08	2.19E-07	8.06E-07	4.23E-05	0.97	0.27	77.39
L299	375.88	1.01E-07	3.37E-07	2.48E-06	1.33E-04	0.96	0.14	56.83
L300	377.79	8.82E-08	1.41E-07	4.81E-06	3.06E-05	0.94	0.03	54.68
L301	379.39	1.00E-07	5.61E-07	2.17E-06	7.95E-05	0.98	0.26	
L302	380.58	1.98E-08	6.14E-07	8.85E-06	3.33E-05		0.07	
L303	381.38	1.30E-07	2.48E-05		6.47E-04	0.78		-4.11
L304	382.18	2.83E-08	1.61E-06	8.42E-06	1.52E-04	1.03	0.19	-48.31
L305	383.70		6.41E-07	3.95E-06	3.43E-05	0.99	0.16	
L306	385.70	2.51E-08	6.95E-07	2.70E-05	1.72E-04	0.99	0.03	-76.92
L307	387.70	1.48E-08	2.73E-07	2.46E-06	2.28E-05	0.98	0.11	-37.59
L308	389.70	8.96E-08	4.25E-07	1.94E-05	1.18E-04	0.88	0.02	
L309	391.70	1.08E-07	3.82E-07	2.07E-06	6.84E-05	0.97	0.18	80.68
L310	393.70		6.36E-07	8.34E-06			0.08	66.12
L311	395.70	6.65E-08	5.16E-07	2.98E-06	7.78E-05	0.95	0.17	71.04
L312	397.70	1.55E-08	5.33E-07	9.26E-07	3.28E-05	0.95	0.58	75.84
L313	399.70		4.26E-07	2.26E-06	5.73E-05	0.98	0.19	61.28
L314	401.70		2.06E-07	4.45E-06			0.05	74.87
L315	403.70	5.23E-08	6.16E-07	1.64E-06	7.48E-05	0.94	0.37	66.22
L316	405.70	1.75E-08	4.65E-07	3.53E-05	2.77E-05		0.01	
L317	407.70	1.43E-07	3.56E-06	5.18E-06			0.69	62.58
L319	411.70	3.69E-08	1.23E-07	8.52E-07	2.86E-05	0.98	0.14	87.15
L320	413.70	9.06E-08	3.42E-07	3.60E-06	6.08E-05	0.96	0.10	77.97
L321	415.70	9.47E-08	5.16E-07	6.66E-06			0.08	
L322	417.70	8.63E-08	9.50E-07	3.15E-05	1.12E-04	0.96	0.03	
L323	419.70	1.31E-07	1.72E-06	8.23E-06	1.12E-03	0.93	0.21	88.50
L324	421.70	1.13E-07	5.20E-07	1.81E-06	1.64E-04		0.29	61.56

Danksagung

Ganz herzlich möchte ich mich bei Prof. Dr. Erwin Appel bedanken, der es mir ermöglichte in diesem großartigen Kasachstan-Projekt mitzuarbeiten. Durch seine tolle Betreuung und Unterstützung sowie das Vertrauen in mein selbstständiges Arbeiten, konnte ich über mich hinauswachsen.

Ohne Prof. Dr. Silke Voigt hätte es das ganze Projekt nicht gegeben. Vielen Dank dafür sowie für die wunderbare Betreuung, die Diskussionen und Impulse, und den großen Einsatz bei den Geländekampagnen.

Konstantin Frisch möchte ich vor allem für die tolle gemeinsame Zeit in Kasachstan, die anregenden Diskussionen, Hilfe bei geologischen Fragestellungen und das sorgfältige Kommentieren meiner Manuskripte bedanken.

Ein großer Dank geht auch an Konstantin Kossov und Julia Zhilkina für ihren unermüdlichen Einsatz und die schöne Zeit während unserer Geländearbeit in Kasachstan. Die Geländekampagnen bleiben unvergessen.

Allen Mitgliedern der Geophysik-Arbeitsgruppe danke ich herzlich für die tolle Zeit, aber auch für die wertvollen Diskussionen und Anregungen! Ein besonderer Dank geht an Wolfgang Rösler für seine allzeit offenen Ohren und die Mithilfe beim Reparieren von Messgeräten. Danke auch an Martin Dersch für die Hilfe bei den vielen Messungen.

Eine weitere wichtige Voraussetzung für mein wissenschaftliches Arbeiten war die Finanzierung des Projektes durch die Deutsche Forschungsgemeinschaft (DFG).

Ein großes Dankeschön für die Unterstützung in den letzten Jahren geht an meine Familie und besonders an Fabian.